博士論文

Comprehensive Study of Anti-neutrino Signals at KamLAND

(カムランドにおける反ニュートリノ信号の包括的研究)

渡辺　寛子

平成 23 年

Abstract

KamLAND is marked by the ability to detect anti-neutrino signals at 1,000 ton of ultra pure liquid scintillator. This thesis presents the comprehensive studies covering reactor anti-neutrinos, geo anti-neutrinos and extraterrestrial anti-neutrinos. The data set includes data acquired following a radio purity upgrade and amounts to 2296.0 days livetime. The number of the anti-neutrino candidates is estimated to be 2,249 events.

From a three-flavor analysis of reactor anti-neutrino, new constraints on the neutrino oscillation parameters Δm^2_{12}, θ_{12} and θ_{13} are presented. Under the assumption of *CPT* invariance, a two-flavor analysis ($\theta_{13} = 0$) of the KamLAND and solar data yields the best-fit values $\tan^2\theta_{12} = 0.444^{+0.031}_{-0.029}$ and $\Delta m^2_{21} = 7.48^{+0.20}_{-0.22} \times 10^{-5}$ eV^2; a three-flavor analysis with θ_{13} as a free parameter yields the best-fit values $\tan^2\theta_{12} = 0.452^{+0.034}_{-0.030}$, $\Delta m^2_{21} = 7.48^{+0.19}_{-0.19} \times 10^{-5}$ eV^2, and $\sin^2\theta_{13} = 0.020^{+0.015}_{-0.018}$. Furthermore, the global analysis for different combination of data is presented, and the significance of nonzero θ_{13} is higher than 3 σ C.L.

KamLAND experiment presented the first experimental study of geo-neutrinos, in 2005. In this thesis, the Rate + Shape + Time analysis estimates geo-neutrino events of 117^{+29}_{-28} and excludes zero signal at 4.5 σ C.L. The result has the consequence that the radiogenic heat contribution is evidently smaller than the heat emission rate from the Earth surface, even adding the expected contribution form ^{40}K and ^{238}U decays. This is the first practical direct estimates of the radiogenic heat with geo-neutrinos and it excluded a homogeneous, fully radiogenic model at 98.3 % C.L., revealing a partial radiogenic model for the Earth.

Lastly, the result of the extraterrestrial anti-neutrino analysis in the energy range 8.3 MeV $< E_{\bar{\nu}_e} <$ 30.8 MeV are presented. All of the candidate events can be attributed to background, most importantly neutral current atmospheric neutrino interaction, setting as upper limit on the probability of ^{8}B solar ν_e's converting into $\bar{\nu}_e$'s at 5.3×10^{-5} (90% C.L.).

Acknowledgments

First and foremost I would like to thank Professor Kunio Inoue, the spokesperson of the KamLAND experiment. I would not have the opportunity to take part in the KamLAND experiment without hearing his lecture. He always gave me significant advice, guidance, chances and creative ideas over the years. Without his continuous suggestions and encouragement, this dissertation would never have been completed.

I also would like to thank Asso. Prof. Junpei Shirai, Asso. Prof. Tadao Mitsui, and Asso. Prof. Masayuki Koga.s I often had useful discussion and helpful advice. These were very valuable and always educational for me.

I owe my special thanks to Dr. Itaru Shimizu for his constant and clear advice to analyze the KamLAND data. I also would like to deeply thank Dr. Haruo Ikeda, who has been continuously my primary adviser from my 1st grade in the master course. Thanks to all the member of KamLAND group for all the interesting discussions and useful meetings related to this analysis; Dr. Kengo Nakamura, Dr. Yoshihito Gando, Dr. Satoru Yamada, and Dr. Kota Ueshima. Special appreciation goes to Dr. Yasuhiro Kishimoto and Dr. Sei Yoshida, the past KamLAND collaborators. I would like to thank all members of the secretarial, technical and other staffs for their kindly support.

I would like to thank my peers, Yasuhiro Takemoto and Azusa Terashima for their friendship. Many thanks to all of people in RCNS, Kyoko Tamae, Hisashi Takahashi, Hisataka Yoshida, Xu Benda, Yohei Ono, Ryo Kato, Takahiro Nakada, Ayumu Oki, Sayuri Matsuda, Hiromu Hanakago, Akira Obata, and other postgraduate students. I very enjoyed school life with them.

Finally, but certainly not least, I would like to thank my parents, Tsuneo and Noriko Watanabe, brother Shoichiro Watanabe, grandparent Yoshinori and Kikuko Watanabe and Yoshiko Otake for their unfailing support over my life. I also appreciate the encouragement my late grandfather, Shoji Otake.

Contents

List of Figures

List of Tables

Part I

Introduction and KamLAND Experiment

Chapter 1

Introduction

The existence of the neutrino was introduced by W. Pauli [1] for more than 20 years before F. Reines and C. Cowan detected the first electron anti-neutrinos at the Savannah River nuclear reactor via inverse-β decay, $\bar{\nu}_e + n \rightarrow e^+ + n$ in 1956 [2] [3]. Furthermore, it took another 10 years to succeed in detections the electron neutrino from the sun by R. Davis Jr. and his colleagues in the Homestake gold mine in 1968 [4]. They have observed solar neutrino about 30 years, but this result raised an unresolved problem between the theoretically predicted and experimentally measured solar neutrino flux. The number of observed neutrino was only one third of the theoretical prediction, and this disagreement was the dawn of the "Solar Neutrino Problem" which fostered the growth and interest in neutrinos over the next 30 years.

The most possible solution for this neutrino anomaly is the neutrino oscillation, which indicates the flavor changing of neutrinos. This idea was suggested by Maki, Nakagawa and Sakata [5] in 1962. As the massless particle cannot change its state, the neutrinos with oscillation are massive.

From the late 1990s, the real time measurement become possible, by Kamiokande (1983-1996), Super-Kamiokande (1996-) and the Subdury Neutrino Observatory (SNO, 1999-2006). These experiments have provided precise measurements of the solar neutrinos. The Kamiokande experiment was the first to measure the composite ^{8}B and HEP solar neutrino spectrum above 5 MeV [6]. Furthermore, they were capable of determining the direction of the neutrinos; providing the first evidence that those events were definitively coming from the Sun. Super-Kamiokande can also measure atmospheric neutrinos, and its report of their anomalous zenith angle distribution [7] is considered the first definitive observation of neutrino flavor transformation. However, the oscillatory function of the flavor changing probability which is the most characteristic for the neutrino oscillation has not been observed yet. In 2002, the first result of KamLAND [8] observed the significant deficit of the electron anti-neutrinos from distance power reactors and excluded all solar neutrino solutions.

The neutrino flavor oscillation is now well established by the convergence of results from experiments involving solar, reactor, atmospheric, and accelerator neutrinos. It has recently been widely recognized that providing the value of mixing angle θ_{13} is a subject of intense ongoing activity. If θ_{13} is nonzero, future oscillation experiments may explore leptonic CP violation and probe the neutrino mass hierarchy.

While we continue to explore the neutrino properties , we have began to use neutrinos as "probe". For example, KamLAND reported the results of the first study of electron anti-neutrinos produced within the Earth in 2005 [9], and Borexino also reported an excess of events they attribute to geo-neutrinos in 2010 [10]. The anti-neutrinos from the Earth's interior are used for discussing the Earth's models.

As a neutrino interacts with other particles only via week interaction, its cross section is very small. Such property of neutrinos provides observation of those from distance sources, such as distance reactors, Earth's interior, and extraterrestrial sources. KamLAND is a multi-purpose detector with ultra pure organic liquid scintillator that can address a variety of scientific topics and a wide range of anti-neutrino energy. This dissertation presents the comprehensive study of anti-neutrinos using KamLAND's own special characteristics. The main discussion is divided by energy range of target anti-neutrinos into main two parts. The contents are organized as follows :

- **Part I : Introduction and KamLAND Experiment**
  - Chapter 1 : Introduction
    The neutrino properties and the recent topics of neutrino physics are described.
  - Chapter 2 : KamLAND Experiment
    The overview of the detector of KamLAND, and the detection method of anti-neutrinos are described. The liquid scintillator purification system are also summarized.
  - Chapter 3 : Event Reconstruction and Detector Calibration
    The procedure of event reconstruction in the detector is listed, and its quality is checked using calibration sources. The detector related systematic uncertainty is also described.
- **Part II : Low Energy Anti-Neutrino**
  - Chapter 4 : Low Energy Anti-Neutrino Sources
    The anti-neutrino sources for low energy region, such as reactor $\bar{\nu}_e$ and geo $\bar{\nu}_e$ are described. The method of reactor $\bar{\nu}_e$ flux calculation and the geophysical models are given.
  - Chapter 5 : Event Selection
    Selection criteria of $\bar{\nu}_e$ are described from the viewpoint of background rejection. To improve the selection efficiency, the likelihood selection is applied for $\bar{\nu}_e$ selection. The details of this selection are also described.
  - Chapter 6 : Background Estimation
    The backgrounds for low energy anti-neutrino measurement are listed and estimated these rates.
  - Chapter 7 : Analysis; Reactor Neutrino
    The method and results of reactor $\bar{\nu}_e$ oscillation analysis are described. Oscillation parameters are measured precisely, and global θ_{13} analysis using recent experimental results is also discussed.
  - Chapter 8 : Analysis; Geo Neutrino
    The geo neutrino analysis using event rate, spectrum shape and time

information are described. Constraints on the geophysical models are also given.

- **Part III : High Energy Anti-Neutrino**
  - Chapter 9 : High Energy Anti-Neutrino Sources
    The anti-neutrino sources for high energy region, such as extraterrestrial $\bar{\nu}_e$ is discussed.
  - Chapter 10 : Background Estimation
    The estimated results of major backgrounds for high energy $\bar{\nu}_e$ are summarized.
  - Chapter 11 : Analysis
    From the analysis of high energy $\bar{\nu}_e$, the limits of some parameters are improved using the present data. These analysis results are listed.
- **Part IV : Discussion and Conclusions**
  Summary of this thesis.

1.1 Neutrino Oscillation

It is now well-established that neutrinos are massive and mixed, and that these properties lead to the oscillations observed in measurements of neutrinos produced in the Sun, in the atmosphere, by accelerators, and by reactors. These measurements have established neutrino oscillation parameters precisely. However, there are still some issues in neutrino oscillation physics; providing the value of mixing angle θ_{13} and leptonic CP phase δ is a subject of intense ongoing activity, and neutrino mass hierarchy and θ_{23} degeneracy (octant degeneracy) are at the center of particle physics agenda.

1.1.1 Vacuum Oscillation

Neutrino oscillations are a quantum mechanical consequence of the existence of nonzero neutrino masses and neutrino (lepton) mixing, and of the relatively small splitting between the neutrino masses. The neutrino oscillation was suggested by Maki, Nakagawa and Sakata in 1962 [5]. The neutrino flavor eigenstates $|\nu_\alpha\rangle$ (α = e, μ, τ) can be expressed as a linear combination of the mass eigenstates $|\nu_i\rangle$ (i = 1, 2, 3) as follows :

$$|\nu_\alpha\rangle = \sum_{i=1}^{3} U^*_{\alpha i}|\nu_i\rangle, \tag{1.1}$$

where U^* is a complex conjugate of a 3×3 unitary mixing matrix known as Pontecorvo-Maki-Nakagawa-Sakata (PMNS) matrix U ($U^\dagger = U$). Conversely, one can write the mass eigenstates with respect to the flavor eigenstates :

$$|\nu_i\rangle = \sum_{\alpha=e,\mu,\tau} U_{\alpha i}|\nu_\alpha\rangle \tag{1.2}$$

Introducing a Dirac CP-violating phase δ in the form

$$D = \begin{pmatrix} 1 & 0 & 0 \\ 0 & 1 & 0 \\ 0 & 0 & e^{i\delta} \end{pmatrix} \tag{1.3}$$

and two Majorana phases α_1, α_2

$$M = \begin{pmatrix} e^{i\frac{\alpha_1}{2}} & 0 & 0 \\ 0 & e^{i\frac{\alpha_2}{2}} & 0 \\ 0 & 0 & 1 \end{pmatrix} \tag{1.4}$$

the three flavor mixing matrix is written as

$$\begin{aligned} U &= \begin{pmatrix} 1 & 0 & 0 \\ 0 & c_{23} & s_{23} \\ 0 & -s_{23} & c_{23} \end{pmatrix} D \begin{pmatrix} c_{13} & 0 & s_{13} \\ 0 & 1 & 0 \\ -s_{13} & 0 & c_{13} \end{pmatrix} D^\dagger \begin{pmatrix} c_{12} & s_{12} & 0 \\ -s_{12} & c_{12} & 0 \\ 0 & 0 & 1 \end{pmatrix} M \\ &= \begin{pmatrix} c_{12}c_{13} & s_{12}c_{13} & s_{13}e^{-i\delta} \\ -s_{12}c_{23} - c_{12}s_{23}s_{13}e^{i\delta} & c_{12}c_{23} - s_{12}s_{23}s_{13}e^{i\delta} & s_{23}c_{13} \\ s_{12}s_{23} - c_{12}c_{23}s_{13}e^{i\delta} & -c_{12}s_{23} - s_{12}s_{23}s_{13}e^{i\delta} & c_{23}c_{13} \end{pmatrix} \begin{pmatrix} e^{i\frac{\alpha_1}{2}} \\ e^{i\frac{\alpha_2}{2}} \\ 1 \end{pmatrix}, \end{aligned} \tag{1.5}$$

where $s_{ij} = \sin\theta_{ij}$, $c_{ij} = \cos\theta_{ij}$ $(i, j = 1, 2, 3)$. The 3×3 matrix containing the Majorana phases drops out when calculating the inner product. Each mass eigenstate has a definite mass and energy, hence its propagation can be described by the time-dependence Schrödinger equation. In vacuum, with $\hbar = 1$:

$$i\frac{d}{dt}|\nu_i(t)\rangle = \hat{H}|\nu_i(t)\rangle = E_i|\nu_i(t)\rangle \tag{1.6}$$

where $\hat{H}$ is the Hamiltonian operator in vacuum and E_i is the energy of ν_i. The wave function can be written as follows :

$$|\nu_i(t)\rangle = e^{-iE_it}|\nu_i(0)\rangle. \tag{1.7}$$

Consequently, using Eq.(1.1) and Eq.(1.7), the flavor eigenstate propagate is written as follows :

$$|\nu_\alpha(t)\rangle = \sum_{i=1}^{3} U^*_{\alpha i} e^{-iE_it}|\nu_i(0)\rangle. \tag{1.8}$$

Inserting Eq.(1.2),

$$|\nu_\alpha(t)\rangle = \sum_{\beta=e,\mu,\tau}\sum_{i=1}^{3} U^*_{\alpha i}U_{\beta i}e^{-iE_it}. \tag{1.9}$$

The transition amplitude from $|\nu_\alpha(t)\rangle$ to $|\nu_\beta\rangle$ is given by

$$\langle\nu_\beta|\nu_\alpha\rangle = \sum_{i=1}^{3} U^*_{\alpha i}U_{\beta i}e^{-E_it}. \tag{1.10}$$

Then, the transition probability is

$$\begin{aligned} P(\nu_\alpha \to \nu_\beta) &= |\langle\nu_\beta|\nu_\alpha(t)\rangle|^2 \\ &= \left|\sum_{i=1}^{3} U^*_{\alpha i}U_{\beta i}e^{E_it}\right| \left|\sum_{i=1}^{3} U^*_{\alpha i}U_{\beta i}e^{-E_it}\right| \\ &= \sum_{i=1}^{3}\sum_{j=1}^{3} U^*_{\alpha i}U_{\beta i}U^*_{\alpha j}U_{\beta j}e^{i(E_i-E_j)t}. \end{aligned} \tag{1.11}$$

There are some approximations which will simplify the oscillation equation. Imagine now that ν_α has been produced with a definite momentum p, so that all of its mass-eigenstate components have this common momentum. Then, with c = 1 and assuming that all neutrino masses m_i are small compared to the neutrino momentum, the energy of ν_i (E_i) is

$$\begin{aligned} E_i &= \sqrt{p^2 + m_i^2} \\ &= p + \frac{m_i^2}{2p} \qquad (\text{with } p_i \gg m_i) \\ &\approx E_\nu + \frac{m_i^2}{2E_\nu} \quad (\text{with } p \approx E_\nu), \end{aligned} \tag{1.12}$$

where E_ν is the neutrino energy. Using $t \gg L$ (L is distance from source) and

$$E_i - E_j = \frac{m_i^2 - m_j^2}{2E_\nu} = \frac{\Delta m_{ij}^2}{2E_\nu}, \tag{1.13}$$

Eq. (1.11) is

$$P(\nu_\alpha \to \nu_\beta)(E_\nu, L) = \sum_{i=1}^{3}\sum_{j=1}^{3} U^*_{\alpha i} U_{\beta i} U^*_{\alpha j} U_{\beta j} \exp\left(i\frac{\Delta m^2_{ij}}{2E_\nu}L\right). \tag{1.14}$$

From Eq. (1.12), the phase factor of this function is then approximately

$$\exp\left(i\frac{\Delta m^2_{ij}}{2E_\nu}L\right) = 1 - 2\sin^2\left(\frac{\Delta m^2_{ij}}{4E_\nu}L\right) + i\sin\left(\frac{\Delta m^2_{ij}}{2E_\nu}\right). \tag{1.15}$$

Furthermore, using

$$\sum_{i=1}^{3}\sum_{j\neq i, j=1}^{3} = 2\sum_{i>j}, \tag{1.16}$$

Eq. (1.14) can be written as

$$\begin{aligned} P(\nu_\alpha \to \nu_\beta)(E_\nu, L) = \delta_{\alpha\beta} &- 4\sum_{i>j} \mathrm{Re}(U^*_{\alpha i}\ U_{\beta i}\ U^*_{\alpha j}\ U_{\beta j})\ \sin^2\left(\frac{\Delta m^2_{ij}}{4E_\nu}L\right) \\ &+ 2\sum_{i>j} \mathrm{Im}(U^*_{\alpha i}\ U_{\beta i}\ U^*_{\alpha j}\ U_{\beta j})\ \sin^2\left(\frac{\Delta m^2_{ij}}{2E_\nu}L\right), \end{aligned} \tag{1.17}$$

where $\delta_{\alpha\beta} = 1$ when $\alpha = \beta$, and 0 when $\alpha \neq \beta$. For example, when $\alpha = \beta$, this third term disappears and the survival probability of ν_α is simply written as

$$P(\nu_\alpha \to \nu_\alpha) = 1 - \sum_{i>j} 4|U_{\alpha i}|^2\ |U_{\alpha j}|^2\ \sin^2\left(\frac{\Delta m^2_{ij}}{4E_\nu}L\right). \tag{1.18}$$

In the natural system of units, since the phase unit is non-dimensional,

$$\begin{aligned} \frac{\Delta m^2_{lj}[\mathrm{eV}^2]}{4E_\nu[\mathrm{MeV}]}\ L[\mathrm{m}] &= \frac{\Delta m^2_{lj}[\mathrm{eV}^2]\ L[\mathrm{m}]}{4E_\nu[\mathrm{MeV}]\ \hbar c[\mathrm{MeV}\cdot\mathrm{fm}]} \\ &= 1.267\frac{\Delta m^2_{lj}[\mathrm{eV}^2]L[\mathrm{m}]}{E_\nu[\mathrm{MeV}]}. \end{aligned} \tag{1.19}$$

Here $\hbar c = 197.3$ [MeV $\cdot$ fm] is applied.

Assuming that CPT invariance holds,

$$P(\bar\nu_\alpha \to \bar\nu_\beta) = P(\nu_\alpha \to \nu_\alpha). \tag{1.20}$$

But, from Eq.(1.17), we see that

$$P(\nu_\alpha \to \nu_\alpha; U) = P(\nu_\alpha \to \nu_\alpha; U^*). \tag{1.21}$$

Thus, when CPT holds,

$$P(\bar\nu_\alpha \to \bar\nu_\beta; U) = P(\nu_\alpha \to \nu_\alpha; U^*). \tag{1.22}$$

That is, the probability for oscillation of an anti-neutrino is the same as that for a neutrino, except that the mixing matrix U is replaced by its complex conjugate.

Thus, if U is not real, the neutrino and anti-neutrino oscillation probabilities can differ by having opposite value of the last term of Eq. (1.17). When CPT holds, any difference between these probabilities indicates a violation of CP invariance.

To simplify the discussion, only two flavors are considered, the unitary mixing U is written as

$$U = \begin{pmatrix} \cos\theta_{12} & \sin\theta_{12} \\ -\sin\theta_{12} & \cos\theta_{12} \end{pmatrix} \tag{1.23}$$

The survival probability of ν_α in two flavor oscillation is written as

$$\begin{aligned} P(\nu_\alpha \to \nu_\alpha) &= 1 - 4\cos^2\theta_{12}\sin^2\theta_{12}\sin^2\left(\frac{\Delta m^2_{21}}{4E_\nu}L\right) \\ &= 1 - \sin^2 2\theta_{12}\sin^2\left(\frac{\Delta m^2_{21}}{4E_\nu}L\right) \\ &= 1 - \sin^2 2\theta_{12}\sin^2\left(\frac{1.267\ \Delta m^2_{21}[\mathrm{eV}^2]L[\mathrm{m}]}{E_\nu[\mathrm{MeV}]}\right) \end{aligned} \tag{1.24}$$

In the case of three flavor generations, there are three pairs of $(i, j) = (2, 1)$, $(3, 1)$, $(3, 2)$ in Eq. (1.17). The survival probability of ν_α is written as follows :

$$\begin{aligned} P(\nu_\alpha \to \nu_\alpha) = 1 - 4\Bigg[& |U_{\alpha 2}|^2|U_{\alpha 1}|^2\ \sin^2\left(\frac{\Delta m^2_{21}}{4E_\nu}L\right) \\ & + |U_{\alpha 3}|^2|U_{\alpha 1}|^2\ \sin^2\left(\frac{\Delta m^2_{31}}{4E_\nu}L\right) \\ & + |U_{\alpha 3}|^2|U_{\alpha 2}|^2\ \sin^2\left(\frac{\Delta m^2_{32}}{4E_\nu}L\right)\Bigg] \end{aligned} \tag{1.25}$$

The survival probability of ν_e for three flavor oscillation is written as

$$P(\nu_e \to \nu_e) = 1 - \sin^2 2\theta_{13}\sin^2\left(\frac{\Delta m^2_{32}}{4E_\nu}\right) - \cos^4\theta_{13}\sin^2\left(\frac{\Delta m^2_{21}}{4E_\nu}\right) \tag{1.26}$$

The oscillation probability is characterized by the mixing angle, the mass squared difference Δm^2_{ij}, the neutrino flight length L and the neutrino energy E_ν. So the oscillation amplitude is maximum when $\Delta m^2_{ij}L = \pi/2$. In Table 1.1, the sensitivities of difference oscillation experiments are listed calculated by this relation.

Table 1.1: Sensitivity of difference oscillation experiments.

Source	Type of ν	E_ν [MeV]	L [km]	min(Δm^2) [eV^2]
Reactor	$\bar{\nu}_e$	~ 1	1	$\sim 10^{-3}$
Reactor	$\bar{\nu}_e$	~ 1	100	$\sim 10^{-5}$
Accelerator	ν_μ, $\bar{\nu}_\mu$	$\sim 10^3$	1	$\sim$1
Accelerator	ν_μ, $\bar{\nu}_\mu$	$\sim 10^3$	1000	$\sim 10^{-3}$
Atmospheric	$\nu_{\mu,e}$, $\bar{\nu}_{\mu,e}$	$\sim 10^3$	10^4	$\sim 10^{-4}$
Sun	ν_e	~ 1	1.5×10^8	$\sim 10^{-11}$

1.1.2 Matter Oscillation

When neutrinos travel through matter (e.g. in the Sun, Earth, or a supernova), their coherent forward scattering from particles they encounter along the way can significantly modify their propagation [11]. Based on this theory, Mikheyev and Smirnov suggest that the probability for changing flavor can be rather different than it is in vacuum [12]. Flavor change that occurs in matter, and that grouse out of the interplay between flavor-nonchanging neutrino-matter interactions and neutrino mass and mixing, is known as the Mikheyev-Smirnov-Wolfenstein (MSW) effect. While all three neutrino flavors interact with electrons, protons, and neutrinos via Z_0 exchange (neutral current), only electron neutrinos interact with electrons via W^- or W^+ exchange (charged current) as shown in Figure 1.1. Hence ν_e has a different potential from ν_μ and ν_τ.

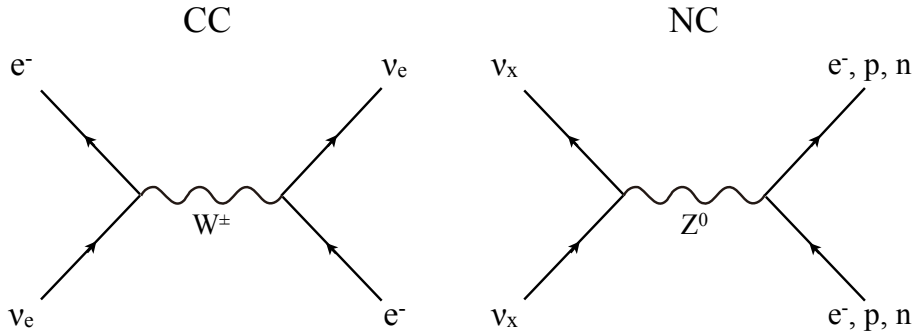

Figure 1.1: Coherent forward scattering Feynman diagrams which give rise to the MSW effect. All neutrino flavors interact via NC channel while only ν_e interact with the W boson.

To simplify the discussion, only two flavors are considered from here. The time evolution of the neutrino wave function is given by

$$\begin{aligned} i\frac{d}{dt}\begin{pmatrix}\nu_e(t)\\ \nu_\mu(t)\end{pmatrix} &= H_{\text{eff}}\begin{pmatrix}\nu_e(t)\\ \nu_\mu(t)\end{pmatrix} \\ &= \left[U\begin{pmatrix}E_1 & 0\\ 0 & E_2\end{pmatrix}U^\dagger + \begin{pmatrix}V_C+V_N & 0\\ 0 & V_N\end{pmatrix}\right]\begin{pmatrix}\nu_e(t)\\ \nu_\mu(t)\end{pmatrix}, \end{aligned} \tag{1.27}$$

where H_{eff} is the effective Hamiltonian, U us the unitary mixing matrix given in Eq. (1.23), E_i is the neutrino energy given by Eq. (1.12), and V_C (V_N) is the effective potential on charged (neutral) current interaction, respectively.

The phase factor propagation of neutrino is modified from ipx to $ipnx$, where n us a refractive index,

$$-p(n-1) = -\frac{2\pi N_e}{p^2}f(0) = \pm\sqrt{2}G_{\text{F}}N_e = V_C, \tag{1.28}$$

where N_e is electron density, $f(0)$ is the forward scattering amplitude in $\nu_e e \to \nu_e e$, and G_{F} is the Fermi coupling constant ($G_{\text{F}}/(\hbar c)^3 = 1.166 \times 10^{-5}$ GeV^{-2}). The neutral current term V_N also changes the effective neutrino mass, but it does not so equally for both flavors. Since it does not modify the mass difference between ν_e and

ν_μ, it has no effect on the oscillation pattern. After omitting the neutral current, H_{eff} becomes

$$H_{\text{eff}} = \left(E + \frac{m_1^2 + m_2^2}{4E} + \frac{V_C}{2} \right) I + \frac{1}{2} \begin{pmatrix} -\Delta_V \cos 2\theta + V_C & \Delta_V \sin 2\theta \\ \Delta_V \sin 2\theta & \Delta_V \cos 2\theta - V_C \end{pmatrix}, \quad (1.29)$$

where $\Delta_V = (m_2^2 - m_1^2) \ / \ 2E$. The first diagonal term of Eq. (1.29) does not contribute to the oscillation pattern. The eigenstates of the second term are regarded as the effective masses of the two eigenstates in matter, giving an effective mass difference Δ_M of

$$\Delta_M = \sqrt{(\Delta_V \cos 2\theta - V_C)^2 + (\Delta_V \sin 2\theta)^2}. \quad (1.30)$$

These eigenstates are

$$\begin{pmatrix} \nu_{1M} \\ \nu_{2M} \end{pmatrix} = \begin{pmatrix} \cos\theta_M & -\sin\theta_M \\ \sin\theta_M & \cos\theta_M \end{pmatrix} \begin{pmatrix} \nu_e \\ \nu_\mu \end{pmatrix}, \quad (1.31)$$

where θ_M is the mixing angle defined as

$$\begin{aligned} \tan 2\theta_M &= \frac{H_{\text{eff}}^{e\mu}}{H_{\text{eff}}^{\mu\mu} H_{\text{eff}}^{ee}} \\ &= \frac{\Delta_V \sin 2\theta}{\Delta_V \cos 2\theta - V_C}, \end{aligned} \quad (1.32)$$

or, equivalently

$$\sin^2 \theta_M = \frac{(\Delta_V \sin 2\theta_V)^2}{\Delta_M^2}. \quad (1.33)$$

From above equation, a large electron density provides a large mixing angle in the matter, as shown in Table 1.2. When a electron density satisfies

$$N_e^{\text{resonance}} = \frac{\Delta_V \cos 2\theta_V}{\sqrt{2} G_{\text{F}}}, \quad (1.34)$$

the resonance occurs and neutrino mixing is a maximum.

Table 1.2: Relation between the electron density and the mixing angle in the matter.

N_e	0	$\cdots$	$N_e^{\text{resonance}}$	$\cdots$	∞
θ_M	θ_V	$\cdots$	$\pi/4$	$\cdots$	$\pi/2$

1.2 Neutrino Oscillation Parameters and Recent Topics

1.2.1 Neutrino Oscillation Parameters

Neutrino oscillation has been firmly established by a series of experiments with neutrinos from the Sun, the Earth's atmosphere, nuclear reactors, and accelerates. All these data can be described within a three-flavor neutrino oscillation framework, characterized by two mass-squared differences (Δm^2_{21}, Δm^2_{31}), three mixing angles (θ_{12}, θ_{13}, θ_{23}), and one complex phase (δ). Together with the mass-squared differences the angles θ_{12}, θ_{23} are well determined by the oscillation data. In contrast, the value of θ_{13}, the sign of Δm^2_{13}, and CP phase δ are the remaining issues of the neutrino oscillation physics.

The global best fit results of neutrino oscillation parameters are summarized in Table 1.3. There results are given by T. Schwetz *et al.* in 2010.

Table 1.3: Best-fit values with 1σ errors for the three-flavor neutrino oscillation parameters from global data in 2010[13].

Parameter	best fit
Δm^2_{21} $[10^{-5}$ eV$^2]$	$7.59^{+0.23}_{-0.18}$
$\lvert\Delta m^2_{31}\rvert$ $[10^{-3}$ eV$^2]$	$2.40^{+0.12}_{-0.11}$
$\sin^2\theta_{12}$	$0.318^{+0.019}_{-0.016}$
$\sin^2\theta_{23}$	$0.50^{+0.07}_{-0.016}$
$\sin^2\theta_{13}$	$0.013^{+0.013}_{-0.009}$

1.2.2 Experiments for Mixing Angle θ_{13}

CHOOZ

The third mixing angle θ_{13} was tested by the CHOOZ reactor experiment [14]. The experiment looked for distortions in the energy spectrum of $\bar{\nu}_e$ produced by a neuter reactor 1 km away from the detector containing liquid scintillator. $\bar{\nu}_e$ survival probability can be expressed as follows :

$$P(\bar{\nu}_e \to \bar{\nu}_e) = 1 - \sin^2 2\theta_{13} \sin^2 \left(\frac{1.27 \Delta m^2_{13} L}{E} \right). \tag{1.35}$$

The CHOOZ experiment ended without any evidence for $\bar{\nu}_e$ oscillation in large mass splittings $\Delta m^2 = 10^{-2} \sim 10^{-3}$. Thus, it implies that the ν_e fraction in ν_3 mass eigenstate would have been too small to be detected. The upper limit on θ_{13} was given by the CHOOZ experiment

$$\sin^2 \theta_{13} < 0.04 \tag{1.36}$$

at 90 % C.L. (assuming $\Delta m^2_{23} = 2.0 \times 10^{-3}$ eV^2).

T2K

T2K experiment use a neutrino beam consisting mainly of muon neutrinos, produced at the J-PARK accelerator facility and observed at a distance of 295 km and an off-axis angle 2.5°by the Super-Kamiokande detector. The survival probability can be written as

$$\begin{aligned} P_{\nu_\mu \to \nu_e} \simeq & \sin^2 2\theta_{13} \sin^2 \theta_{23} \sin^2 \left(\frac{\Delta m^2_{31} L}{4E} \right) \\ & \mp \alpha \sin 2\theta_{13} \sin \delta \sin 2\theta_{12} \sin 2\theta_{23} \left(\frac{\Delta m^2_{31} L}{4E} \right) \sin^2 \left(\frac{\Delta m^2_{31} L}{4E} \right) \\ & - \alpha \sin 2\theta_{13} \cos \delta \sin 2\theta_{12} \sin 2\theta_{23} \left(\frac{\Delta m^2_{31} L}{4E} \right) \cos \left(\frac{\Delta m^2_{31} L}{4E} \right) \sin \left(\frac{\Delta m^2_{31} L}{4E} \right) \\ & + \alpha^2 \cos^2 \theta_{23} \sin^2 2\theta_{12} \left(\frac{\Delta m^2_{31} L}{4E} \right)^2, \end{aligned} \tag{1.37}$$

where the sign of the second term refers to neutrinos (minus) to anti-neutrinos (plus). The full oscillation probability is complicates, but when neglecting the CP violation terms and matter effects, the oscillation probability becomes

$$P_{\nu_\mu \to \nu_e} \simeq \sin^2 \theta_{23} \sin^2 2\theta_{13} \sin^2 \left(\frac{\Delta m^2_{31} L}{4E} \right) \tag{1.38}$$

It is noticed that the amplitude of the oscillation is proportional to $\sin^2 2\theta_{13}$. The measurement of this oscillation channel will give a direct measurement of the mixing angle θ_{13}.

The present data releases corresponds to 1.43×10^{20} protons on target [15]. Six events pass all selection criteria for an electron neutrino events. In a three-flavor neutrino oscillation scenario with $\theta_{13} = 0$ the except number of such events is 1.5 ±

0.3 (syst.). Under this hypothesis, the probability to observe six or more candidates is 7×10^{-3}, equivalent to 2.5 σ significance. At 90 % C.L., the data are consistent with

$$0.03(0.04) < \sin^2 2\theta_{13} < 0.28(0.34) \tag{1.39}$$

for $\delta = 0$ and a normal (inverted) hierarchy. Figure 1.2 shows the allowed regions for $\sin^2 2\theta_{13}$.

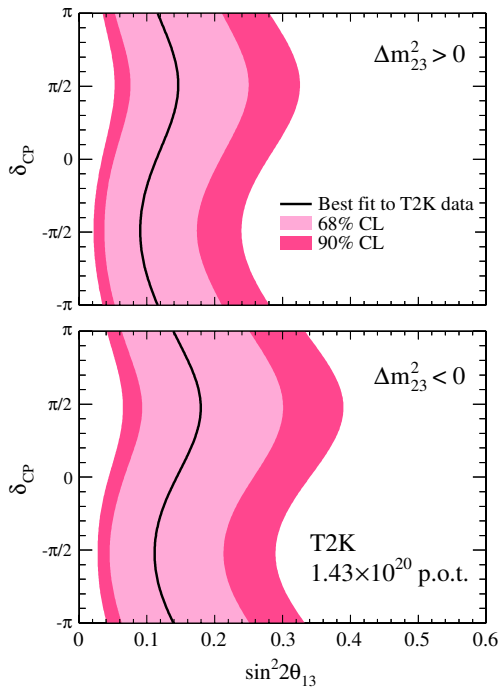

Figure 1.2: Allowed regions for $\sin^2 2\theta_{13}$ by T2K experiment for normal (top) and inverted (bottom) mass hierarchy [15].

MINOS

The MINOS (the Main Inject Neutrino Oscillation Search) experiment has been designed to study flavor composition of a beam of muon neutrinos, produced at NuMI neutrino baseline. The 0.98-kton near detector is located on-site at Fermilab, 1.04 km downstream of the NuMI target. The 5.4-kton far detector is located 735 km downstream in the Soudan Underground Laboratory. In Ref. [16], a search for $\nu_\mu \to \nu_\mu$ appearance has been presented, based on $8.2{\times}10^{20}$ protons on the NuMI target. The survival probability also can be written as Eq. (1.37) or Eq. (1.38). 62 events have been observed in the far detector with a background of 49.5 $\pm$ 2.8 (syst.) $\pm$ 7.0 (stat.) events predicted by the measurement in the near detector. This corresponds to an excess of about 1.7 σ. They find that

$$2\sin^2\theta_{23}\sin^2 2\theta_{13} < 0.12(0.20) \tag{1.40}$$

at 90 % C.L. for $\delta = 0$ and a normal (inverted) hierarchy. Figure 1.3 shows the allowed regions for $2\sin^2\theta_{23}\sin^2 2\theta_{13}$.

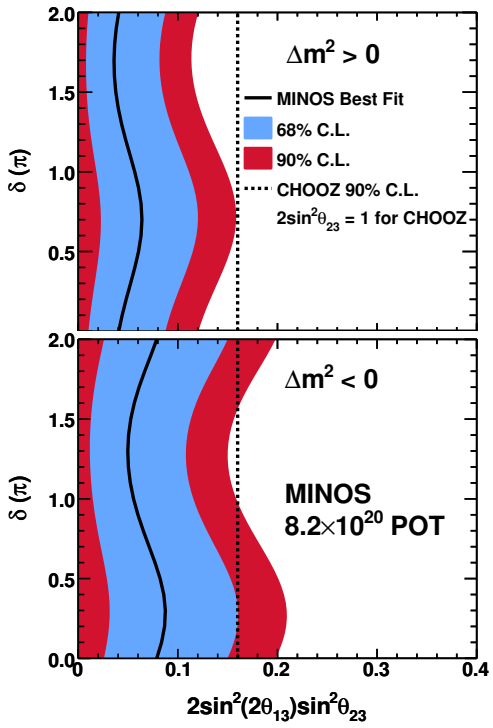

Figure 1.3: Allowed regions for $2\sin^2 2\theta_{13}\sin^2\theta_{23}$ by MINOS experiment. The upper (lower) panel assumes the normal (inverted) neutrino mass hierarchy.

Double Chooz

The latest measurements result of θ_{13} is presented by Double CHOOZ experiment at the last of 2011 [17]. They present their first results with a detector located ~1050 m from the two 4.25 GW_{th} thermal power reactors of the Chooz Nuclear Power Plant and under a 300 m.w.e. rock overburden. The detector has 10^m Gd loaded liquid scintillator, and $\bar{\nu}_e$ events are identified by Gd's emission of ~8 MeV in γ rays. Assuming the normal hierarchy, the $\bar{\nu}_e$ survival probability can be written

$$\begin{aligned} P_{\bar{\nu}_e\to\bar{\nu}_e} &= 1 - 2\sin^2\theta_{13}\cos^2\theta_{13}\sin^2\left(\frac{\Delta m^2_{31}L}{4E}\right) \\ &\quad - \frac{1}{2}\cos^4\theta_{13}\sin^2(2\theta_{12})\sin^2\left(\frac{\Delta m^2_{12}L}{4E}\right) \\ &\quad + 2\sin^2\theta_{13}\cos^2\theta_{13}\sin^2\theta_{12}\left(\cos\left(\frac{\Delta m^2_{31}L}{2E} - \frac{\Delta m^2_{12}L}{2E}\right) - \cos\left(\frac{\Delta m^2_{31}L}{2E}\right)\right). \end{aligned} \tag{1.41}$$

The first two terms contain respectively the atmospheric driven and solar driven contributions, while the third term, absent from any two-neutrino mixing model, is an interference between solar and atmospheric driven oscillations which amplitude is a function of θ_{13}. Therefore, up to second order in $\sin^2\theta_{13}$ and $\alpha \equiv \frac{\Delta m^2_{21}}{\Delta m^2_{31}}$, the

survival probability can be expressed as

$$P_{\bar{\nu}_e \to \bar{\nu}_e} \simeq 1 - \sin^2 2\theta_{13} \left(\frac{\Delta m^2_{31} L}{4E} \right) + \alpha^2 \left(\frac{\Delta m^2_{31} L}{4E} \right)^2 \cos^4 \theta_{13} \sin^2 2\theta_{12} \qquad (1.42)$$

, where the third term can safety be neglected given the current range of mixing parameters found in neutrino experiments. Thus reactor experiments provide a clean measurement of the mixing angle θ_{13}.

Figure 1.4 shows the energy spectrum based on 110 days of data. An observed-to-predicted ratio of events of 0.944 ± 0.016 (stat.) $\pm$ 0.040 (syst.). Analyzing both the rate of the prompt positrons and their energy spectrum, they found

$$\begin{aligned} \sin^2 2\theta_{13} &= 0.086 \pm 0.041(\text{stat.}) \pm 0.030(\text{syst.}) \\ 0.017 &< \sin^2 2\theta_{13} < 0.16 \quad (90\%\text{C.L.}). \end{aligned} \qquad (1.43)$$

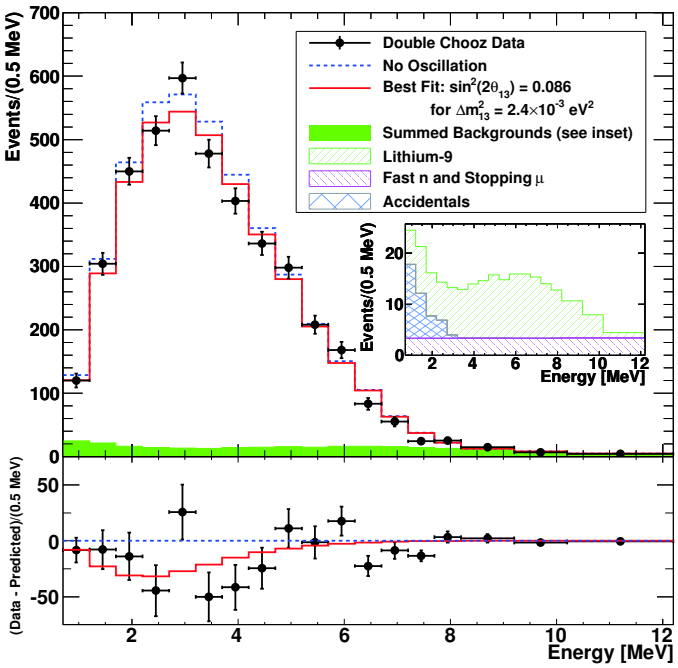

Figure 1.4: Expected energy spectrum of Double Chooz experiment (top) [17]. The bottom panel shows the difference between the data and no-oscillation spectrum.

Chapter 2

KamLAND Experiment

KamLAND (**Kam**ioka **L**iquid scintillator **A**nti-**N**eutrino **D**etector) is located in a rock cavern in the Kamioka mine, ∼1000m below the summit of Mt. Ikenoyama in Gifu, Japan. The 2,700 meter water equivalent overburden reduces the cosmic ray flux by a factor of roughly 10^{-5} with respected to the surface flux. The cosmic muon rate is about 0.34 Hz in the inner detector. The KamLAND detector is marked by the ability to detect low energy anti-neutrino signals at liquid scintillator compared with water Cherenkov detector.

The structure of KamLAND detector and the detection method are described in this chapter.

2.1 KamLAND Detector

The KamLAND detector occupies the former site of the Kamiokande [18] experiment in the Kamioka mine. The construction began in 1997, and data has been corrected from 2002. Figure 2.1 shows overview of the KamLAND detector and experimental site. The KamLAND area is 3km from the Kamoika mine entrance. There are 2 types of systems for liquid scintillator purification. The 1st purification system was designed and built at the beginning of KamLAND construction phase based on liquid-liquid extraction method. On the other hand, the 2nd purification system was newly constructed in Fall 2006 with the aim of reducing radioactive backgrounds for solar neutrino measurement. In this system, KamLAND liquid scintillator was first distilled to remove radioactive material elements such as ^{210}Pb and ^{40}K, and then sent to a nitrogen purge tower in order to remove radioactive nobel gas elements such as ^{222}Rn and ^{85}Kr. A high purity nitrogen gas was supplied from high purity nitrogen system, which were newly constructed in 2006. The purified water is produced at water purification system, and it is filled in the inner detector.

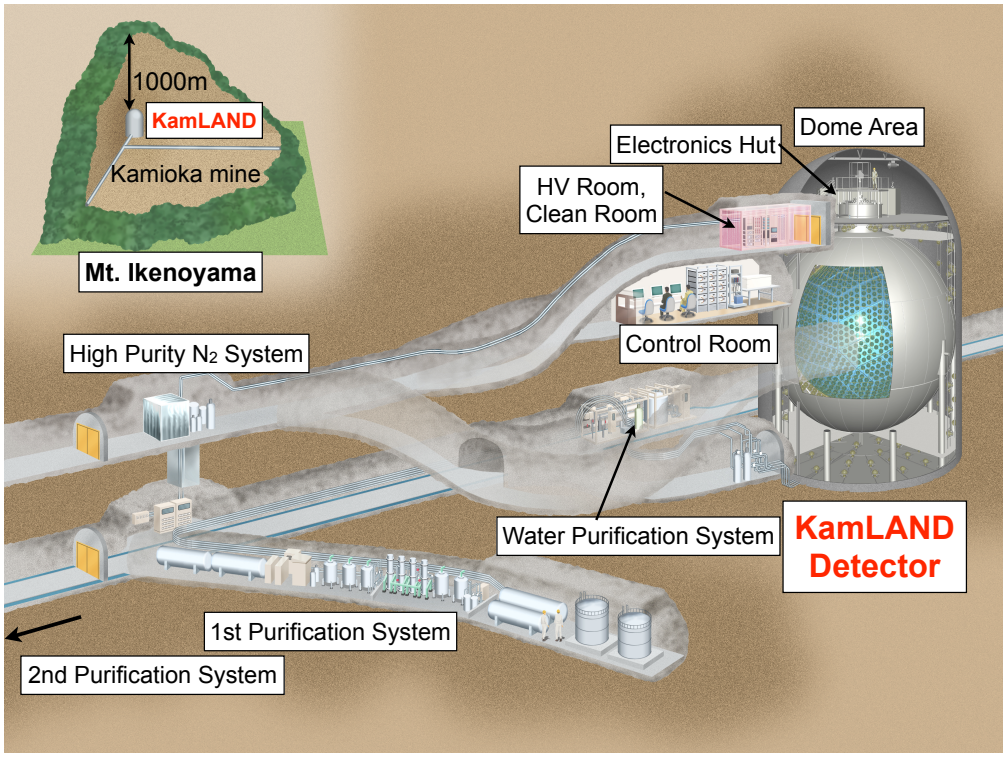

Figure 2.1: KamLAND detector and experimental site.

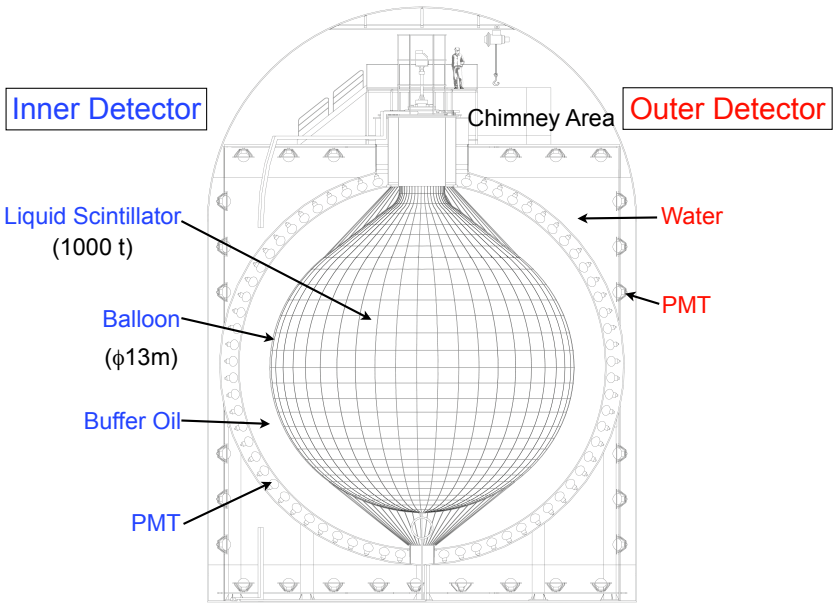

Figure 2.2: Schematic diagram of the KamLAND detector

2.2 Detector Components

Figure 2.2 shows a schematic of the KamLAND detector, which consists of two major sections, the inner detector (ID) and the outer detector (OD), separated by a spherical stainless steel tank of 18.0m diameter. The ID section is designed for detection of $\bar{\nu}_e$, and the OD section acts as a cosmic ray active veto while also attenuating γ radiation from the surrounding rock. Light produced in the ID and OD is detected by photo multiplier tubes (PMT), which convert photons that hit their photo-cathodes into an electrical signal. Waveforms from PMTs, readout as voltage as a function of tome, are recorded and later used to reconstruct the energies and positions of events. To test the performance of the algorithms in finding the energy and position, radioactive calibration sources with known energies are deployed at exactly known positions.

2.2.1 Inner Detector (ID)

Liquid Scintillator and Buffer Oil

A spherical balloon of 13.0 m diameter is suspended inside the stainless steel tank and filled with 1000 tons $\left(1171 \pm 25\mathrm{m}^3\right)$ [1] of ultra pure liquid scintillator (LS). To detect anti-neutrinos with energy as low as 1 MeV, the detector is required to have excellent high output, optical transparency, and low level of radioactivity. In addition, the large number of target make it possible to improve statistics. Liquid scintillator suites these requirements, and KamLAND is the largest liquid scintillator detector in the world.

The LS consists of 80.2 % dodecane ($C_{12}H_{26}$) and 19.8 % pseudecumene (1,2,4-trimethylbenzene, C_9H_{12}) by volume, with 1.36 ± 0.03 g/L of PPO (2,5-diphenyloxazole, $C_{15}H_{11}NO$) as a primary fluor. The property of each components of liquid scintillator is summarized in Table 2.1.

Table 2.1: The property of each components of liquid scintillator

parameter	Pseudocumene	Dodecane	PPO
molecular structure	C_9H_{12}	$C_{12}H_{26}$	$C_{15}H_{11}NO$
density [g/cm^3] at 15°C	0.8796	0.7526	-
boiling point [°C] at 1 atm	169	216	360
melting point [°C] at 1 atm	-44	-10	72
flashing point [°C]	54	83	-

[1] The total volume of the LS was measured during detector filling.

Table 2.2: The target and actual parameters of liquid scintillator [20]

parameter	design value	actual value
temperature [°C]	~ 12	11.5
specific density [g/cm^3] at 15°C	0.778	0.77754± 0.00010
H/C ratio	1.902	1.969
refractive index at λ=590nm, 14°C	1.44	1.44087 ± 0.00015
light yield [p.e./MeV]		
(i) 17inch PMT only	∼250	∼300 (at center)
(ii) 17inch + 20inch PMT	∼400	-
time response parameters [nsec]		
R(t)=a/$\tau_a$exp(-t/τ_a) + b/$\tau_b$exp(-t/τ_b)		
a	0.86	0.69
b	0.14	0.31
τ_a	6.9	4.0
τ_b	8.8	8.6
neutron capture tim [μsec]	∼212	212.5±8.1
radiation length [cm]	18	-
flashing point [°C]	64	-
thermal expansion coefficient [/°C]	-0.00095	-
kinetic viscosity [cSt] at 30°C	1.4	-

The light yield depends on the light transparency of the LS as well as the light output. The composition ration of decane and pseudocumene is adjusted to get maximum light yield for central events. The actual light yield for events at the center of detector is about 300 p.e./MeV using for only 17-inch PMTs, and about 500 p.e./MeV using for 17-inch and 20-inch PMTs. The measured attenuation length of the LS is about 10 m at 400 nm wavelength by using a dye-laser [19]. The light output is 49% anthracene (8,300 photons/MeV). The designed parameters and actual values of LS are shown in Table 2.2.

The KamLAND detector also has the buffer oil surrounding to prevent from external γ-ray background, which comes from the radioactive impurities in the detector material such like stainless steal tank, or in surrounding rock containing ^{208}Tl and ^{40}K. To keep the spherical shape of balloon, the specific gravity of the buffer oil is adjusted to be 0.04 % lower than the LS. For this purpose, the components and mixture ratio of buffer oil is optimized. The buffer old consists of 53 % normal paraffin ($C_{12}H_{26}$) and isoparaffin ($C_nH_{2n+2}, n \sim 14$).

Balloon and Kevlar Rope

A spherical balloon of 13.0 m diameter is suspended by a netting of high strength Kevlar ropes from the top of the detector. The balloon is the key component of the detector which isolates the LS from the external buffer oil. Therefore, the requirements of the balloon are as follows: high transparency to light in 350 to 500 nm wavelength range, chemical compatibility with the LS and buffer oil, low radioactivity, impermeability to Rn, and mechanical strength to maintain the spherical shape of the LS. Among numerous candidate material, the balloon is made of fivefold layer film, EVOH (25μ m) / Nylon (15μ m) / Nylon / Nylon / EVOH , with a total thickness is 135 μm. EVOH is an effective material to prevent the permeation of Rn and Oxygen, so Rn concentration ratio across the film can be s low as 1.8×10^{-6}. Then, Nylon is used as a strength reinforcement. The balloon consists of 44 gores welded together, and the light transparency is more than 90%.

The balloon is suspended by 44-longitudinal and 30-lateral Kevlar braid ropes to maintain its spherical shape. The Kevlar is made of par amid fiber whose excellent features are suitable for KamLAND, and is five times stronger than on an equal weight basis.

The radioactivities in the balloon and Kevlar rope are summarized in Table 2.4. When KamLAND construction, the Kevlar ropes were washed with alcohol to remove the radioactive impurities. However, the Kevlar rope still contains 8.3×10^{-10} g/g of ^{40}K, whose decay rate corresponds to 31 Bq.

Table 2.3: Radioactivities in the balloon film and the Kevlar ropes

balloon film	U	Th	^{40}K
concentration [ppb]	0.018	0.014	0.27
decay [Bq]	0.02	0.006	7.2

Kevlar roles	U	Th	^{40}K
concentration [ppb]	0.08	0.8	1.2
decay [Bq]	0.1	0.33	31

2.2.2 Outer Detector (OD)

The OD is a cylindrical water-Cherenkov cosmic ray veto detector, which surrounds the stainless steal tank and contains approximately 3000 m^3 of pure water. Hamamatsu R3600 PMTs detect Cherenkov light produced by muons going through the OD. The OD also acts as an attenuator for neutrons and γ by reducing the number of these particles entering the IF from outside the detector. The water in the OD is circulated constantly to remove excess heat produced by PMTs in the ID and OD.

In order to increase light counting efficiency and utilize muon tracking, the OD is separated by reflective Tyvek into 4 sections: top, upper, lower, and bottom. The stainless steel containment sphere separates to the top and upper sections from the lower and bottom sections. The PMTs in the top (50 PMTs) and bottom (60 PMTs) sections are attached on the ceiling and the floor of the OD, facing downward

and upward, respectively. On the other hand, The PMTs in the upper (60 PMTs) and lower (55 PMTs) sections are attached on the wall of the OD facing towards the cylindrical axis of the detector. Tyvek sheets optically separate each section of ht OD. These sheets are highly reflective and line all inner surfaces of the OD to optimize light collection by PMTs in each section.

2.2.3 PMT

As shown in Figure 2.2, the PMTs are secured to the inner surface of the containment vessel, facing the center detecter. The LS is viewed by 2 types of PMTs, 1,325 fast 17-inch aperture Hamamatsu photomultiplier tubes (PMT) custom-designed for KamLAND,and 554 20-inch PMTs inherited from Kamiokande. Totally, the KamLAND ID has 1,879 PMTs. The total detector photo coverage is 34 % with 1,879 PMTs, and 22 % with only 17-inch PMTs.

The 17-inch PMTs were developed based on 20-inch PMTs, with the aim of considerable improvements in energy and time response. The big difference between 17-inch and 20-inch PMT is dynode shape. The 17-inch PMTs have the "line-focus" type dynode and the effective region is limited by masking the outer fringe of the photocathode plane to obtain better timing and energy resolution than 20-inch PMTs. In contrast, 20-inch PMTs have the "venetian-blind" type dynode which is suitable for large diameter photo-cathode. Figure 2.3 shows a schematic view of 17-inch and 20-inch PMTs.

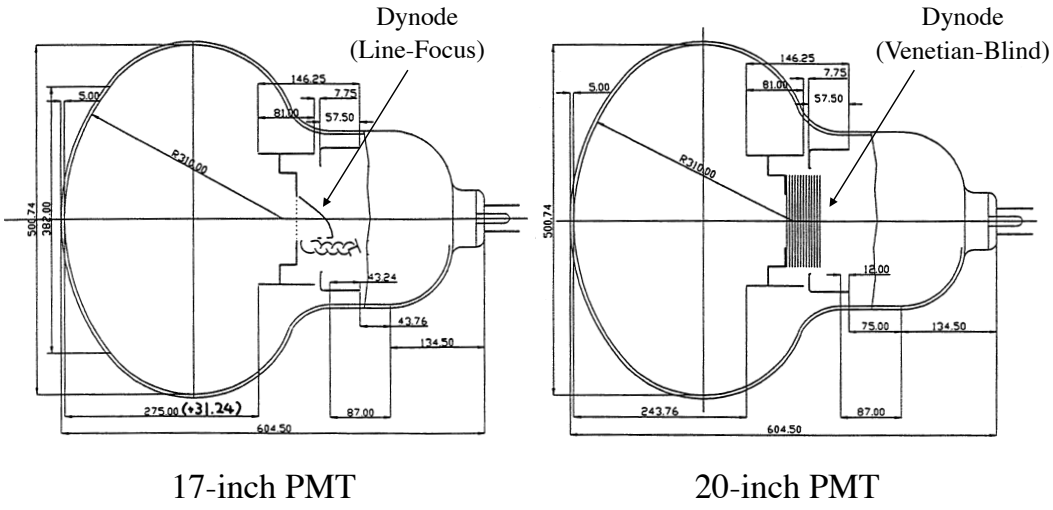

Figure 2.3: Schematic view of the 17-inch and 20-inch PMTs

The 17-inch PMT significantly improve transit-time-spread (TTS) from ∼5.5 nesc (FWHM) to ∼3 nsec. And the peack-to-valley (P/V) ratio is increase from ∼1.5 to ∼3, and it was measured using 1 photo-electron pulse hight distribution. This value is defined by the minimum hight where the noise level and the 1 photo-electron level cross. The 17-inch and 20-inch PMT's TTS and P/V measurement results are shown in Figure 2.4.

A magnetic field affects the electron trajectory and consequently the PMT gain. The Earth's magnetic field (∼50 mGauss) is no exception. Variation of the 1 p.e. pulse hight in magnetic fields below 50m Gauss is less than 20 % . For proper

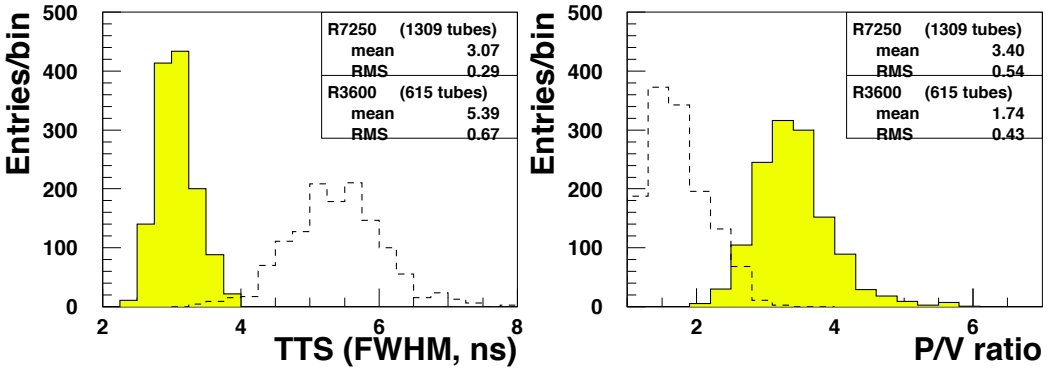

Figure 2.4: Performance difference between 17-inch PMT (shaded histogram) and 20-inch PMT. TTS means transit-time-spread, and P/V ratio is peack-to-valley ratio in the pulse height spectrum for 1 p.e. signals and dark current. Performance of 17-inch PMTs are better than that of the 20-inch PMTs.

operation of PMTs, a set of compensation coils encompassing the entire detector are used to reduce the terrestrial magnetic field.

The correlation of quantum efficiency with the wavelength of light is shown in Figure 2.5. It depends mainly on the material of the photo-cathode, bialkali, although individual differences exist because of variation in the thickness of the material.

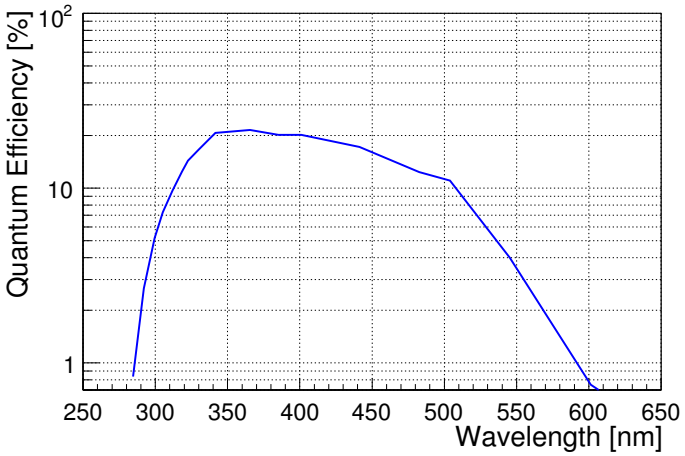

Figure 2.5: Quantum efficiency of PMT which measure by Hamamatsu company

2.2.4 Electronics and Data Acquisition

The system to record PMT data consists of three major components: the KamFEE (KamLAND Front-End Electronics, 200 boards), the trigger system, and the DAQ (Data AcQuision) system. The main purpose of these components are that the KamFEE system acquires and digitizes PMT waveforms, the trigger system decides whether to record the data, and the DAQ system records the data. These three components communicate with each other as shown in Figure 2.6. The DAQ system sends various commands to the trigger system, such as run start and stop. The DAQ

system also separately sends both the trigger system and the KamFEE system run conditions which determine the behavior of those components during a run. The Trigger board, a main part of the trigger system, has an internal 40 MHz clock signal, which is distributed to all the KamFEE boards to keep them synchronized with trigger board. On each clock tick, each KamFEE board sends the trigger board the number of PMTs connected to it that had a positive signal in the last 25 ns, Nsum. If the trigger board decides to record the data permanently, it generates a trigger record, and depending on which set of conditions are met, sends a waveform digitization command to the KamFEE boards. The DAQ system asynchronously reads out the trigger record and the waveform data. The details of the each components are given as follows.

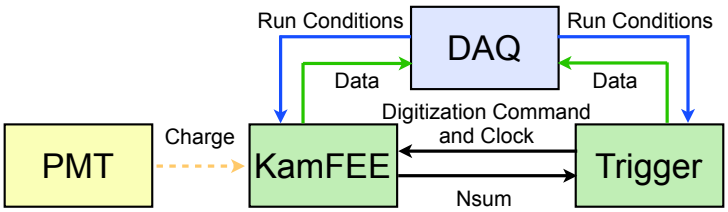

Figure 2.6: Schematic diagram of the communication among the electronics and the DAQ system.

Front-End Electronics (FEE)

A schematic diagram of the KamFEE is shown in Figure 2.7. This is based on the Analog Transient Waveform Digitizer (ATWD), which has an array of condenser and maintains waveform information in an analog format. The ATWD allows the fast sampling of the PMT pulses as a function of time with 128 10-bit samples in 1.49 nsec steps. When the discriminator is triggered, the record work stop and the waveform, is saved for 175 nsec. If the global trigger is issued, this waveform is digitized within 25 μsec. In order to reduce the dead time during the analog-digital conversion, the ATWD has two types of channel, A and B, for each PMT channel. For each ATWD, there are three gains to give enough dynamic range to collect events which have various energy.

- High gain channel
  collect 20 times amplified waveform in order to detect the single photo-electron signals.

- Middle gain channel
  collect 4 times amplified waveforms in case the high gain channel saturates.

- Low gain channel
  collect 0.5 times amplified waveforms, the large signal generated by muons with more than 1,000 p.e. per channel.

The KamFEE boards sum 12 PMT channels using a Field Programmable Gate Array (FPGA), and are separated for 17-inch PMTs, 20-inch-PMTs, and PMTs in

the outer detector. The data of the number of PMTs that exceed their discriminator threshold (Nsum), which is tuned 1/3 p.e. pulse hight (0.5 mV), is send to the trigger circuitry. Each discriminator generates a 125 nsec puls.

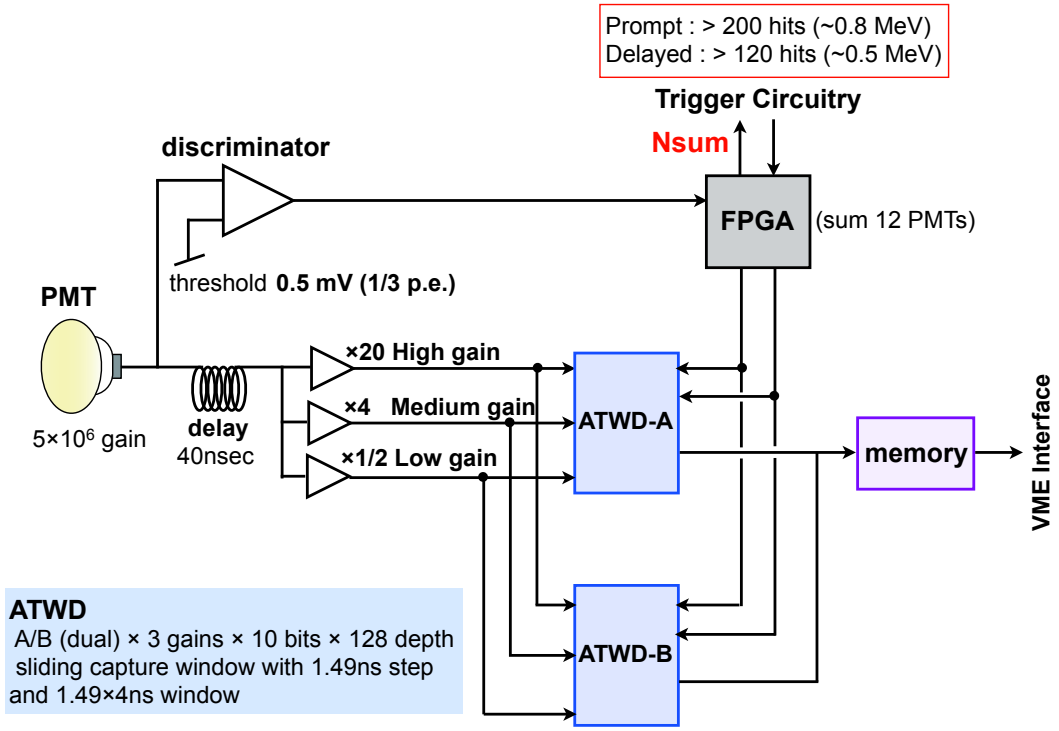

Figure 2.7: Schematic diagram of the KamLAND Front-End Electronics board.

Trigger System

The trigger system sums the hit information (Nsum) from the KamFEE boards, and communicates with the DAQ system. The trigger keeps track of the absolute event time through a 40MHz clock on the trigger board and all event information is obtained in multiples of 25 ns. The number of clock ticks since the start of a run is referred to as the timestamp. The trigger board decides whether the data should be recorded as digitized waveforms of hit PMTs.

The conditions on which this decision is made are referred to as the "trigger type". There are 3 types of triggers related to the ID. The most important trigger in normal physics data taking is the "prompt trigger". In the early period of KamLAND, it was issued when the Nsum excesses 200. It corresponds to more than 200 ID 17-inchPMT hits, and about 0.7 MeV. Following every prompt trigger, the "delayed trigger" is enabled for 1 msec, which was issued when Nsum excesses 120 (0.3 MeV) at the start of KamLAND. The delayed trigger is mainly used for the study of low energy background such as ^{214}Po, ^{212}Po and ^{85}Kr. The "prescale trigger" is issued to the ID KamFEE boards for the fraction of every second. It is used for high-rate data acquisition, such as source calibrations and low-threshold bacgrounds. Figure2.8 shows the history of the trigger conditions from the start of KamLAND, 2002. During 1st and 2nd purification, each trigger conditions was optimized to correct data for background studies. The prescale trigger was set at

the start of 1st purification to analyze low energy events such as solar neutrino. After 2nd purification, each trigger thresholds have been set lower levels than before because of low data rate below 1MeV due to background reduction. The prompt and delayed trigger threshold have been 70, and the prescale trigger threshold has been 40.

The ID history trigger is based on the total ID Nsum being above the ID history trigger threshold 120, and is issued every 25 nsec while above threshold up to a maximum of 200 nsec. The maximum of Nsum in the ID history trigger for an event is called "NsumMax". This trigger does not recode waveforms of hit PMTs, only contains information of number of hits, so the data taking with a very low threshold is possible.

For the OD, the top, upper , lower and bottom OD sections are triggered when their individual Nsum exceed 6, 5, 6 and 7, respectively. The important trigger for physics run is the "OD-to-ID trigger", which is issued when any of OD segment detects certain number of photons. It is useful to study OD-correlated event such as fast neutrons.

The prompt trigger efficiency for $\bar{\nu}_e$ analysis is estimated from the delayed trigger events and defined as follows,

$$\varepsilon_{\text{prompt trigger}}(E_{\text{vis}}) = \frac{\text{number of prompt trigger events with NsumMax} \geq N_{th}(\text{prompt})}{\text{number of delayed trigger event}(N_{th}(\text{delayed}))}, \tag{2.1}$$

where N_{th}(prompt) and N_{th}(delayed) are trigger threshold for each event. On the other hand, the delayed trigger efficiency for $\bar{\nu}_e$ analysis is estimated from the low threshold prescale trigger events and defined as follows,

$$\varepsilon_{\text{delayed trigger}}(E_{\text{vis}}) = \frac{\text{number of prompt delayed events with NsumMax} \geq N_{th}(\text{delayed})}{\text{number of prescale trigger event}(N_{th}(\text{prescale}))}, \tag{2.2}$$

where N_{th}(prescale) is the prescale trigger threshold. The efficiency curve within 6.0 m fiducial radius is shown in Figure 2.9. As shown in 2.8, three types of the trigger conditions are optimized for data taking status. The prompt trigger before and after purification are estimated to be 100% at 0.92 MeV in the visible energy scale. It corresponds to 1.10, 0.90 and 1.00 MeV in e^+, e^- and *gamma* energy scale, respectively. For the delayed trigger, 99% and 100% at 0.47 MeV in the visible energy scale for before and after purification. This energy corresponds to 0.54, 0.47 and 0.56 MeV in e^+, e^- and *gamma* energy scale.

Data Acquisition System

The main tusks of the DAQ system are to set run conditions for the trigger system and the KamFEE system, to readout the digitized waveform signals from these systems, to record them on the data storage disk asynchronously, and to provide the user interface for run control and configuration. Therefore signals from multiple events are mixed into one unified data. Then an event builder reads this asynchronous data, sorts it, groups the hits and trigger information into events, and stores the time-ordered data to disk. The digitized waveform data are then converted to time and charge information for each hit PMT.

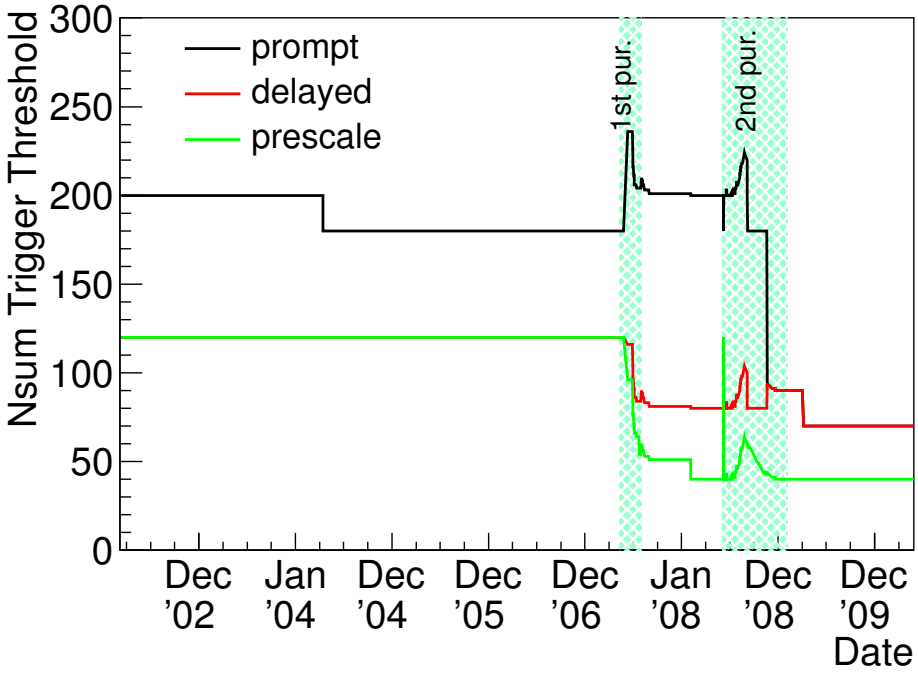

Figure 2.8: Time variation of trigger condition. The black, red and green lines correspond to the prompt trigger, the delayed trigger and the prescale trigger conditions, respectively. These trigger conditions are optimized to correct data for background studies.

2.3 Purification System

In 2002, the KamLAND detector was constructed with purified 1000 ton liquid scintillator using the 1st purification system. The specific targets for achievement in the purification were set with the aim of $\bar{\nu}_e$ detection, whose rate was expected to be $\sim$1 event/day. In order to reduce the background rate to a target revel (< 0.1 event/day), concentration of ^{232}U, ^{238}Th, and ^{40}K had to remove to $< 10^{-14}$ g/g, $< 10^{-14}$ g/g, and $< 10^{-15}$ g/g, respectively. However, further background reduction at low energy was essential to active low energy solar neutrino observation such as ^{7}Be, CNO and pep neutrinos. The 2nd purification and the high-purity nitrogen generator were newly constructed in Fall 2006, and the KamLAND liquid scintillator was purified in the period from March 2007 to August 2007, and from June 2008 to February 2009.

2.3.1 The 1st Purification System

Figure 2.10 shows a schematic view of the 1st purification system. During the KamLAND construction, the liquid scintillator and the buffer oil were purified independently. The system consists of two main parts such as the water-water extraction tower and the nitrogen purge tower. In the water-water extraction tower, the metal elements such as ^{232}U, ^{238}Th, and ^{40}K were removed by purified water. These are

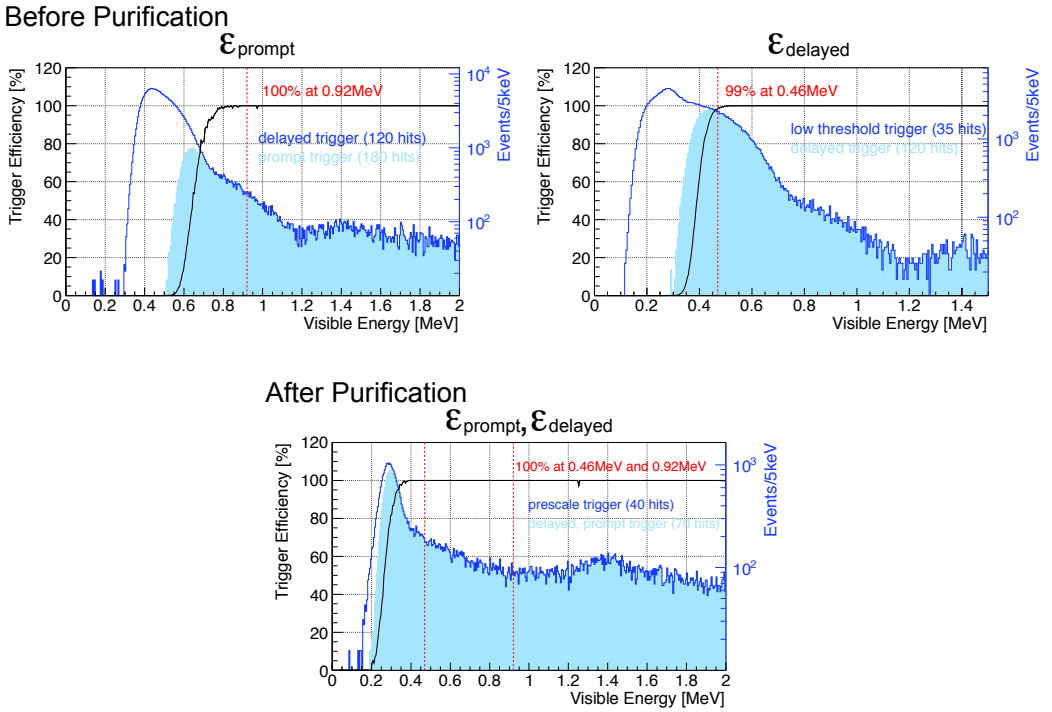

Figure 2.9: Trigger efficiency within 6.0 m radius fiducial volume (black line). The prompt and delayed trigger conditions for before and after purification are shown. The blue line histogram correspond to the energy spectrum for the denominator in Eq.2.1 and 2.2. The sly blue shaded histogram correspond to the energy spectrum for the numerator in them.

better partitioned to the polarized water molecules than the non-polarized liquid scintillator and buffer oil molecules. It can be performed at normal temperature and pressure without any chemical operations. After passing the water-water extraction tower, LS is sent to the nitrogen purge tower. The purge tower takes some roles before filling to the KamLAND detector. The small amount of dissolved water in the LS is purged out prevent from degrading the light yield and transparency of the LS. And also oxygen, which causes a decrease in light yield by quenching, was removed for LS. The radioactive noble gas elements such as ^{222}Rn, ^{85}Kr and ^{39}Ar are purged out to reduce the background for $\bar{\nu}_e$ detection.

Table 2.4 shows the measurement results of the radioactivities in each components of LS and purified LS. The raw LS components before purification were measured by ICP-MS. The purified levels of the final mixed LS after purification as measured in-situ by KamLAND are also given in the table. The 1st purification reduced the radioactivity of the LS by ∼5 orders of magnitude.

2.3.2 The 2nd Purification System

As discussed in Section 2.3.1, the 1st purification achieved the target background levels for $\bar{\nu}_e$ detection. Solar neutrino observation, however, required extremely low background levels, so dramatic reduction in low energy backgrounds such as ^{85}Kr and ^{210}Pb were needed. ^{210}Pb feeds the decay chain responsible for the production

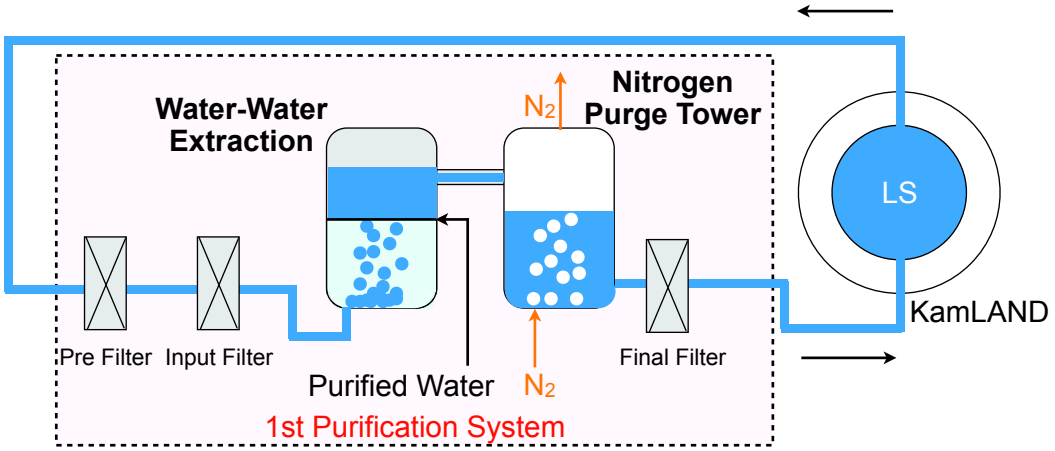

Figure 2.10: Schematic view of 1st purification system

Table 2.4: Radioactivity measurement results of before and after 1st purification. The raw LS components were measured by ICP-MS, and the final mixture after purification were measured in-situ by KamLAND. [21]

	Material	^{238}U [g/g]	^{232}Th [g/g]	^{40}K [g/g]
before	Isoparaffin	3×10^{-13}	$\leq 6 \times 10^{-12}$	-
	Decane	$\leq 10^{-13}$	$\leq 6 \times 10^{-12}$	$\leq 1.2 \times 10^{-12}$
	Pseudecumene	$\leq 10^{-13}$	-	-
	PPO	1.2×10^{-13}	$\leq 5 \times 10^{-11}$	$\leq 5.3 \times 10^{-11}$
after	LS	$(3.4 \pm 0.4) \times 10^{-18}$	$(5.7 \pm 0.8) \times 10^{-17}$	$\leq 2.7 \times 10^{-16}$
target level	LS	$< 10^{-14}$	$< 10^{-14}$	$< 10^{-15}$

of α-particles from ^{210}Po, which is one of the most major backgrounds for the geo-neutrino observation. The purification campaign have been conducted totally over nine months from 2007 to 2009. The total amount of of processed LS was over 5,000 m^3, and consisted three full volume exchanges of the LS.

Figure 2.11 shows the schematic view of 2nd purification system. The distillation procedure with 2nd purification system is as follows;

1. The LS drawn from the top of the KamLAND is sent to the buffer tank. The flow rate is controlled about 1.5 m^3/h, corresponding to 1.17 t/h

2. The LS is distilled to remove radioactive metal elements such as ^{210}Pb and ^{40}K. Each components of the LS is distilled in its own distillation tower whose pressure and temperature are well controlled.

3. The distilled each component is filled in the mixing tank. The density of the LS is adjusted by the flow of distilled product with the accuracy of 10^{-3} g/cm^3.

4. The adjusted LS is sent to the the nitrogen purge tower. The aim of the nitrogen purge tower is to remove the radioactive noble gas elements such as

^{222}Rn, ^{85}Kr and ^{39}Ar. The flow rate of nitrogen is 30 m^3/hour which is 20 times higher than that of the LS, and the whole system is depressurize down to 40 kPa.

5. The completed LS is sent to the KamLAND detector after checking the quality. It is needed to evaluate the various quality of the LS before filling to the KamLAND.

   - Transparency and light yield
   - ^{222}Rn and ^{85}Kr concentration
   - PPO concentration

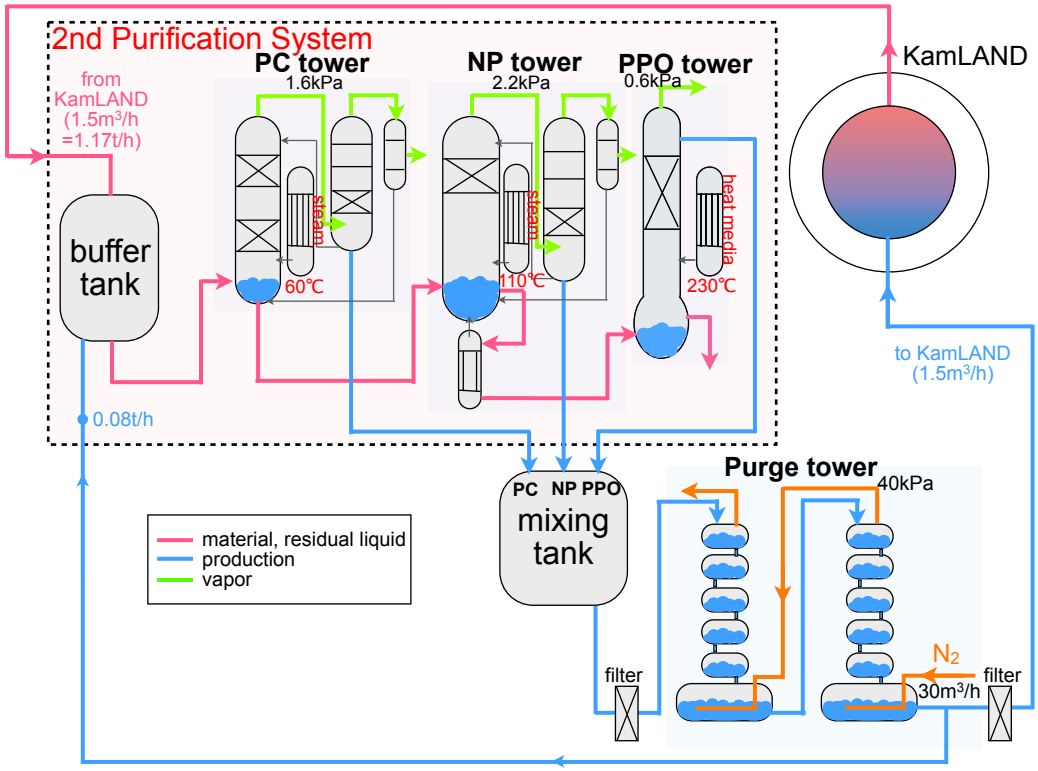

Figure 2.11: Schematic view of 2nd purification system

2.4 Calibration Equipment

KamLAND data quality is checked using the source calibration system which has known energy and well-controlled position. The neutron quickly thermalized via elastic interaction with protons ins the LS, and any scintillation emitted by the recoil nuclei in the process contributed negligible to the brightness of the prompt signal. The delayed coincidence method provides the extremely powerful background suppression.

Table 2.5: KamLAND calibration sources with their primary decay type and its corresponding real energy.

source	particle type	energy [MeV]	half-life
^{203}Hg	γ	0.2792	46.612 d
^{137}Cs	γ	0.6616	30.07 y
^{65}Zn	γ	1.1116	244.3 d
^{68}Ge	γ	0.511×2	270.8 d
^{60}Co	γ	1.1732, 1.3325	5.271 y
^{241}Am^{9}Be	γ, n	4.4, n$<$ 10	432 y
^{210}Po^{13}C	γ, n	6.13, n$<$ 7.5	22 y

2.5 Anti-Neutrino Detection Method

Electron antineutrinos are detected at KamLAND via the inverse β-decay reaction,

$$\bar{\nu}_e + p \rightarrow e^+ + n \tag{2.3}$$

A $\bar{\nu}_e$ annihilates with a proton (i.e. hydrogen atom) in the liquid scintillator, producing a positron and a neutron. The positron is ejected from the interaction vertex, and quickly slows down as it deposits its energy in the LS by ionizing molecules. Then, the positron annihilates with a nearby electron, producing two 511 keV γ's. This signal appears as "prompt signal". The neutron quickly thermalized via elastic interactions with protons in the LS, and any scintillation emitted by the recoil nuclei in the process contributes negligible to the brightness of the prompt signal.

The neutron is eventually captured by a proton via the interaction, which is written as follows,

$$n + p \rightarrow d + \gamma \tag{2.4}$$

where d is a deuteron and the 2.2 MeV γ carries away the mass difference between the initial and final states with mean capture time 207.5 $\pm$ 2.8 μsec. This signal becomes "delayed signal". Whereas these two successive signals have both timing or space correlation, the background does not have them. The delayed coincidence method provides the extremely powerful background suppression.

The energy conservation before and after the inverse β-decay is the center-of-mass frame is given as,

$$E_{cm}^{the} = \frac{(M_n + m_e)^2 - M_p^2}{2(M_n + m_e)} = 1.803[\text{MeV}] \tag{2.5}$$

where E_{cm}^{the} is the anti-neutrino energy, M_p is the proton mass (938.272 MeV), $p_{\bar{\nu}_e}$ is the anti-neutrino momentum, M_n is the neutron mass (939.565 MeV) and m_e is the electron mass (0.5110 MeV). In the laboratory frame,

$$E_{lab}^{the} = E_{cm}^{the} \frac{E_{cm}}{M_p} \tag{2.6}$$

$$E_{cm} = M_n + m_e. \tag{2.7}$$

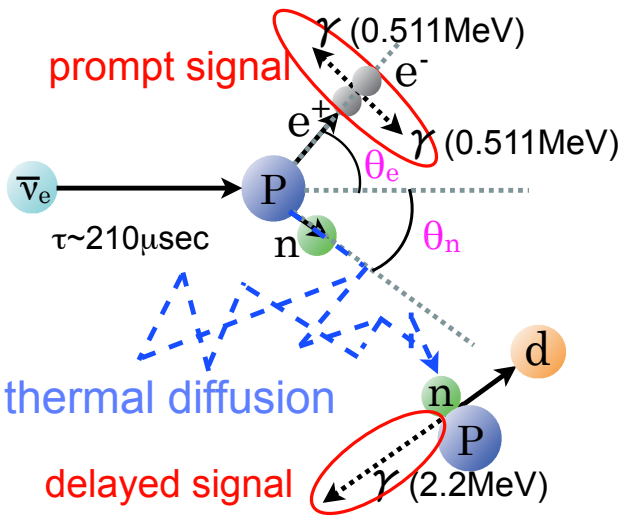

Figure 2.12: Inverte beta decay reaction.

There fore the energy threshold of the inverse β-decay reaction is written as,

$$E_{lab}^{the} = \frac{(M_n + m_e)^2 - {M_p}^2}{2M_p} = 1.806 \text{ [MeV]} \tag{2.8}$$

The prompt energy of the reaction is written as follows,

$$E_{prompt} = T_{e^+} + 2m_e \tag{2.9}$$

where T_{e^+} is electron kinetic energy. Here the energy conservation is thought,

$$E_{\bar{\nu}_e} + M_p = T_{e^+} + m_e + M_n + T_n \tag{2.10}$$

where T_n is neutron kinetic energy. From Eq. (2.9) and Eq. (2.10), E_{prompt} is written as

$$\begin{aligned} E_{prompt} &= (E_{\bar{\nu}_e} + M_p - m_e - M_n - T_n) + 2m_e \\ &= E_{\bar{\nu}_e} - T_n - 0.782 \text{ [MeV]} \end{aligned} \tag{2.11}$$

The thermalization of the neutron T_n is also the prompt event. It is quenched and can be ignored.

In the inverse β-decay, the positron's kinetic energy (T_{e^+}) and scattering angle (θ_e) are written as a function of the anti-neutrino energy. By the low of conservation of energy, the neutron's kinetic energy (T_n) and scattering angle (θ_n) can be calculated. Then, in the reactor anti-neutrino energy region, T_n is about 10 keV as shown in Figure 2.13.

2.5.1 Cross Section of Inverse Beta Decay

The matrix element ($\mathcal{M}$) of the inverse β-decay is written as follows,

$$\mathcal{M} = \frac{G_F \cos\theta_C}{\sqrt{2}} \left[\bar{u}_n \left(\gamma_\mu f - \gamma_\mu \gamma_5 g - \frac{i f_2}{2M} \sigma_{\mu\nu} q^\nu \right) u_p \right] \times [\bar{v}_{\bar{\nu}} \gamma^\mu (1 - \gamma_5) v_e, \tag{2.12}$$

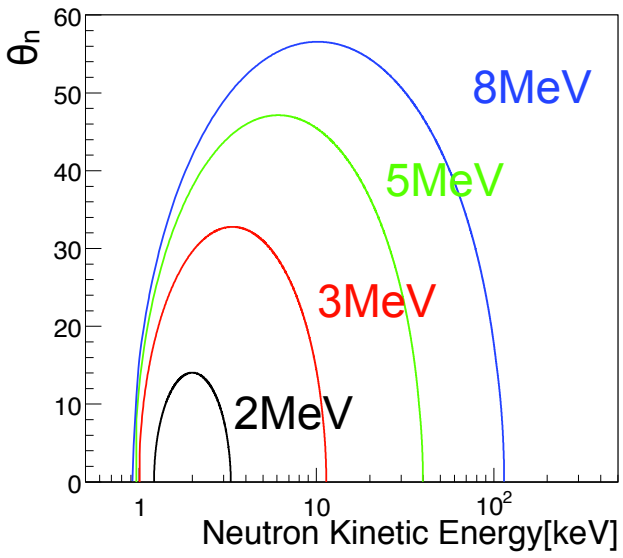

Figure 2.13: The correlation between the neutron kinetic energy and θ_n as a function of the anti-neutrino energy in the inverse β-decay. In the reactor anti-neutrino energy region, the mean energy is about 2.5 MeV, the neutron kinetic energy T_n is about 10 keV.

where,

$$\begin{aligned} f &= 1.0 \quad \text{(vector coupling constant)} \\ g &= 1.26 \quad \text{(axial} - \text{vector coupling constant)} \\ f_2 &= \mu_p - \mu_n - 1.0 = 2.793 + 1.913 - 1.0 = 3.706 \\ \cos\theta_{\rm C} &= 0.974 \end{aligned}$$

In the limit where the nucleon mass is taken to be infinite, i.e., zeroth order in $1/M$ (M is the average nucleon mass), the positron energy is [22] [23]

$$E_e^{(0)} = E_{\bar{\nu}_e} - \Delta, \tag{2.13}$$

where $\Delta = M_n - M_p$. At each order in $1/M$, the positron momentum $p_e = \sqrt{{E_e}^2 - {m_e}^2}$ and the veracity $v_e = p_e/E_e$. The differential cross section of the inverse β-decay at this order is,

$$\left(\frac{d\sigma(E_{\bar{\nu}_e})}{d\cos\theta_{\rm e}}\right)^{(0)} = \frac{\sigma_0}{2}\left[(f^2+3g^2) + (f^2-g^2)v_e^{(0)}\cos\theta_{\rm e}\right] E_e^{(0)} p_e^{(0)}. \tag{2.14}$$

The normalization constant σ_0, including the energy-independent inner radiative correction, is

$$\sigma_0 = \frac{G_F^2 \cos^2\theta_{\rm c}}{\pi}(1 + \delta_{inner}^{rad}), \tag{2.15}$$

where $\delta^{rad}_{inner} \backsimeq 0.024$. This gives the standard result for the total cross section,

$$\sigma^{(0)}_{tot} = \sigma_0(f^2 + 3g^2)E^{(0)}_e p^{(0)}_e \tag{2.16}$$

$$= 0.0952 \left(\frac{E^{(0)}_e p^{(0)}_e}{1\mathrm{MeV}^2} \right) \times 10^{-42}\mathrm{cm}^2. \tag{2.17}$$

The energy-independent inner radiative corrections affect the neutron beta decay rate in the same way, and hence the total cross section can also be written

$$\sigma^{(0)}_{tot} = \frac{2\pi/m^5_e}{f^R_{p.s.}\tau_n} E^{(0)}_e p^{(0)}_e, \tag{2.18}$$

where τ_n is the measured neutron lifetime and $f^R_{p.s.} = 1.7152$ is the phase space factor, including the Coulomb, weak magnetism, recoil, and outer radiative corrections.

At the 1st order in $1/M$, the positron energy depends on the scattering angle. It is

$$E^{(1)}_e = E^{(0)}_e \left[1 - \frac{E_{\bar{\nu}_e}}{M}(1 - v^{(0)}_e \mathrm{cos}\theta_\mathrm{e}) \right] - \frac{y^2}{M}, \tag{2.19}$$

where $y^2 = (\Delta^2 - m^2_e)/2$. The differential cross section at the 1st order is

$$\left(\frac{d\sigma(E_{\bar{\nu}_e})}{d\mathrm{cos}\theta_\mathrm{e}} \right)^{(1)} = \frac{\sigma_0}{2} \left[(f^2 + 3g^2) + (f^2 - g^2)v^{(1)}_e \mathrm{cos}\theta_\mathrm{e} \right] E^{(1)}_e p^{(1)}_e - \frac{\sigma_0}{2} \left[\frac{\Gamma}{M} \right] E^{(0)}_e p^{(0)}_e \tag{2.20}$$

where

$$p^{(i)}_e = \sqrt{(E^{(i)}_e)^2 - m^2_e} \quad (i = 0, 1) \tag{2.21}$$

$$v^{(i)}_e = p^{(i)}_e / E^{(i)}_e \quad (i = 0, 1) \tag{2.22}$$

$$\begin{aligned} \Gamma = {} & 2(f + f_2)g \left[(2E^{(0)}_e + \Delta)(1 - v^{(0)}_e \cos\theta_e - \frac{m^2_e}{E^{(0))}_e} \right] \\ & + (f^2 + g^2) \left[\Delta(1 + v^{(0)}_e \cos\theta_e) + \frac{m^2_e}{E^{(0)}_e} \right] \\ & + (f^2 + 3g^2) \left[(E^{(0)}_e + \Delta) \left(1 - \frac{1}{v^{(0)}_e} \cos\theta_e - \Delta \right) \right] \\ & + (f^2 - g^2) \left[(E^{(0)}_e + \Delta) \left(1 - \frac{1}{v^{(0)}_e} \cos\theta_e - \Delta \right) \right] v^{(0)}_e \cos\theta_e \end{aligned} \tag{2.23}$$

The total cross section of the inverse β-decay reaction considered to the order of $O(1/M)$ is given by

$$\sigma(E_{\bar{\nu}_e}) = \left[\int^1_{-1} \left(\frac{d\sigma(E_{\bar{\nu}_e})}{d\ \cos\theta} \right)^{(1)} d\ \cos\theta \right] \cdot (1 + \delta^{rad}_{outer}), \tag{2.24}$$

where δ^{rad}_{outer} is the energy-dependent outer radiative correction. The total cross section as a function of neutrino energy is shown in Figure 2.14.

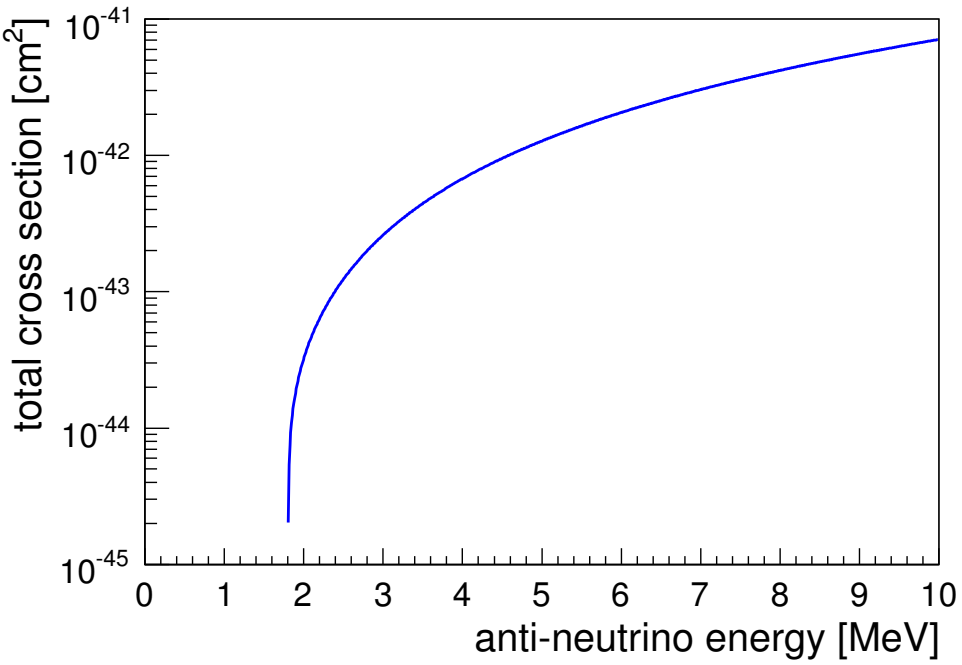

Figure 2.14: Total cross section of the inverse β-decay reaction, $\bar{\nu}_e + p \rightarrow e^+ + n$, as a function of $\bar{\nu}_e$ energy.

Chapter 3

Event Reconstruction and Detector Calibration

The KamLAND detector views the light produced in the ID by scintillation and Cherenkov radiation from ionization particles and muons using 1,879 PMTs. The energies and positions of 'point-like' events or 'track-like' event must be calculated from these PMT signals. The 'point-like' event makes the light emission at the point, and most of events at the low energy region are classified into the this point-like events. On the other hand the 'track-like' event makes the light emission on the line. These events are dominated by the cosmic-ray muons (∼0.3 Hz at KamLAND). The reconstructed events also include non-physics events, such as electrical noise, so it is necessary to identify physics events from the raw data. The procedure of event reconstruction is as follows :

1. waveform analysis (Section3.1)
   The waveforms are converted to time and charge information.

2. time and charge calibration of PMTs (Section3.2)
   Each PMT has a particular time and charge information. The transit time of each PMT are calibrated with a pulse dye-laser. The 1 p.e. distribution of each PMT are using for charge calibration run by run. To improve the energy and vertex resolution, known bad and unstable PMT channels have to be eliminated.

3. identification of events
   The reconstructed events are classified into two types, point-like or track-like events. The most muons go through the liquid scintillator, and these are selected by high energy event selection criteria. There are muons which only through the inner buffer and emit Cherenkov light. The number of these muons are about 1/20 of the scintillation light events, and these are tagged by OD hits. The 'track-like' events are reconstructed by 4-(a).

   The other are 'point-like' events. These events have energy and vertex information, and are reconstructed by 4-(b) and (c).

4. event reconstruction (Section3.3)

   (a) 'track-like' : muon track reconstruction

(b) 'point like' : vertex reconstruction

(c) 'point-like' : energy reconstruction

5. reconstruction quality check
   Finally, the reconstruction quality is evaluated from the time and charge information recorded by the PMTs. If the reconstructed events have not good quality, these are categorized as non-physics events.

The event reconstruction algorithm and quality check for anti-neutrino analysis are described in this chapter.

3.1 Waveform Analysis

In the waveform analysis, PMT hit information is extracted from recorded waveform data. Each PMT has particular offsets which are affected by individual analogue buffers. To evaluate these offset, a waveform's "pedestal" is recorded at the beginning of each run. In the waveform analysis, firstly the pedestal is subtracted from the event waveform. The waveform is then smoothed using an algorithm which calculates an average first derivative and special care is taken at the edge of the sample ("leading edge") to avoid a high frequency noise. The leading edge of the first peak in the waveform defines the first photon arrival at the PMT.

The waveforms receded by the KamFEEs are converted to time and charge information for each PMT. The total sampling time for each channel is 190 nsec, which is divided into 128 samples. The time difference between the samples is 1.49 nsec, which is almost comparable to the transit time spread (TTS) of the 17-inch PMTs. The charge is receded in 10 bit of the ADC channel for each sample, so its accuracy is enough to see the single photo electron peak.

3.1.1 Time Bin Width Calibration

Clock test is use for the calibration of the time bin width. The calibration is performed for each channel at the beginning of each run. The time interval of the clock pulse in 25 nsec. A typical number of sampling is $\sim$17 per on clock pulse. The time information for each channel is corrected by this calibration.

3.2 Time and Charge Calibration

3.2.1 TQ Correction

Each PMT and electronics channel exhibits slight differences is gain, cable length, quantum efficiency, noise etc. This indicate that each PMT has a different correlation between time and charge, which are evaluated channel by channel using a dye-laser pulse calibrations at various light intensities. Figure 3.2 shows the schematic view of the dye-laser calibration system. The dye-laser pulse which has $\sim$1.2 nesc width is sent to the center if the detector via a quartz optical fiber, and illuminates the PMTs. The wavelength of the dye-laser pulse is 500 nm, and absorption wavelength is less than 400 nsec. There is no affection of the absorption in the scintillator. This intensity can be changed by neutral density filters.

Figure 3.1 shows the timing response of one PMT as a function of charge. The fitting function $T(Q)$ is as follows,

$$T(Q) = P_0 + P_1 \times (\log_{10} Q) + P_2 \times (\log_{10} Q)^2, \tag{3.1}$$

where P_0, P_1 and P_2 are fitting parameters. These figging parameters are calibrated comparing photon arrival time of the other PMTs. The selection criteria for timing calibration is as follows:

- event selection
  fiducial volume (R $<$ 6.0m) and number of hit PMT $\leq$ 240
- PMT selection
  distance between focused event and PMT ($<$ 20 cm)

Figure 3.3 shows the timing difference distribution, which focused on PMT cable No.1 and ATWD Ach. To check the accuracy of timing calibration quality, a maximum-bin is searched on the distribution. If the maximum-bin is out of $\pm$5.0 nsec range, the deviation is added on the day-laser calibration data. Figure 3.4 shows the result of timing calibration.

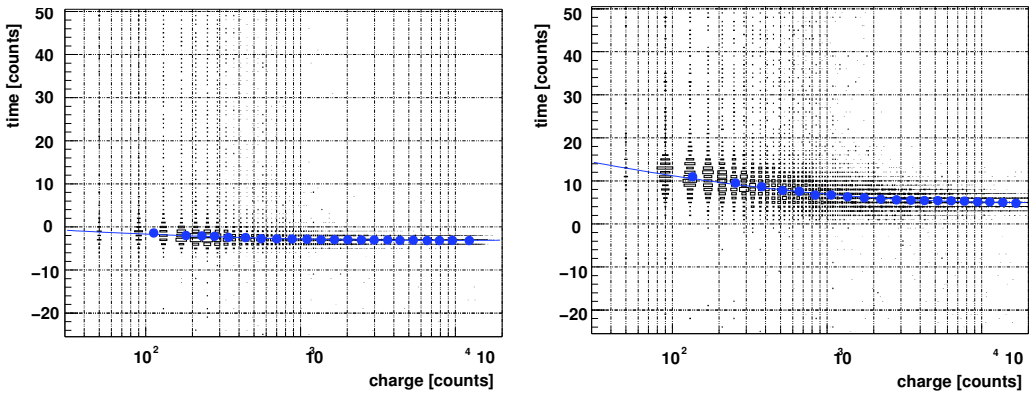

Figure 3.1: Correction between the time and charge in the day-laser timing calibration data. The left figure shows a typical 17-inch PMT, and the right figure shows a typical 20-inch PMT.

additional timing calibration with ^{60}Co source run

As shown above, the timing correction quality has been checked the photon arrival time distribution of the other PMTs. Number of PMTs that are beyond the assuming range, $\pm$5 nsec, increased after 2nd purification. This campaign succeeded in reducing the low energy background, on the other hand, it caused and decrease in light yield and charge. The cause of this timing calibration quality change is not clear, but the liquid scintillator condition was changed by the purification campaign.

Because it can be estimated that events arrive on each PMT at the same timing, ^{60}Co calibration data at the center of the detector is useful for the timing calibration. Figure 3.5 shows the timing distribution of PMT hits using ^{60}Co source run at the center of the detector. The mean value is used for the additional timing correction. The ^{60}Co calibration run has been taken regularly at intervals of 2 weeks. Small peculiar drift of the timing is relatively corrected using the calibration run.

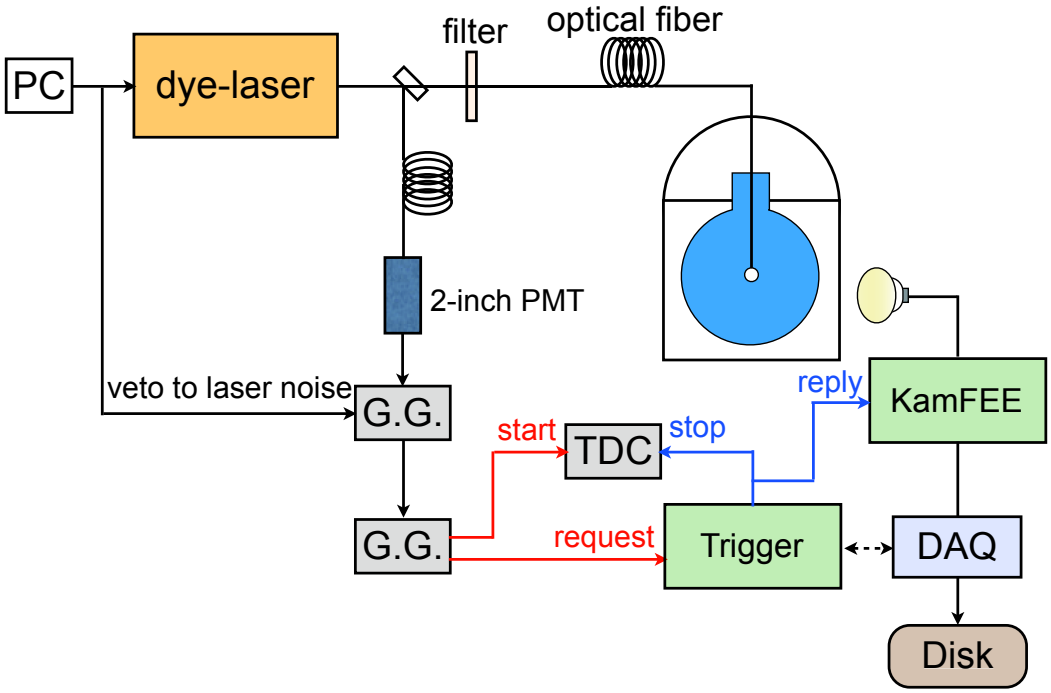

Figure 3.2: Schematic view of the dye-laser calibration system.

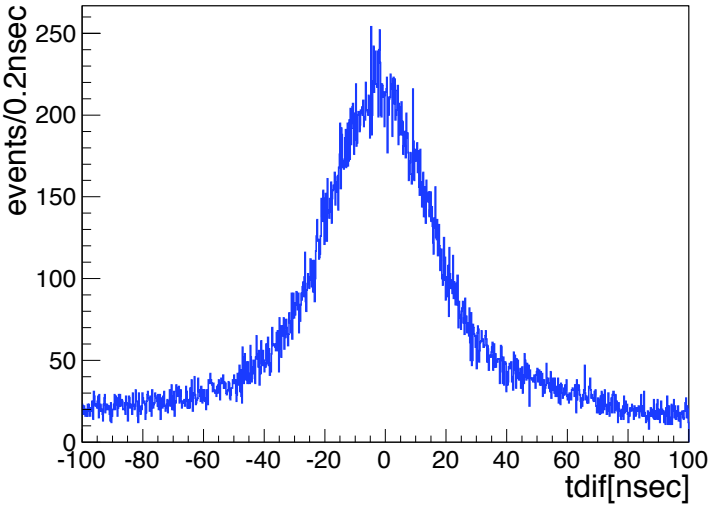

Figure 3.3: Timing difference distribution for timing calibration. It is focused on PMT cable No.0, ATWD Ach.

3.2.2 Gain Calibration

The single photo-electron (p.e.) charge is defined by area of a 1 p.e. pulse in a waveform. Small change of each PMT gain is corrected within normal run using well-defined 1 p.e. charge distribution run by run. The signal selection conditions for 17-inch PMT are as follows:

- muon and noise event veto
- 2 msec veto after muon

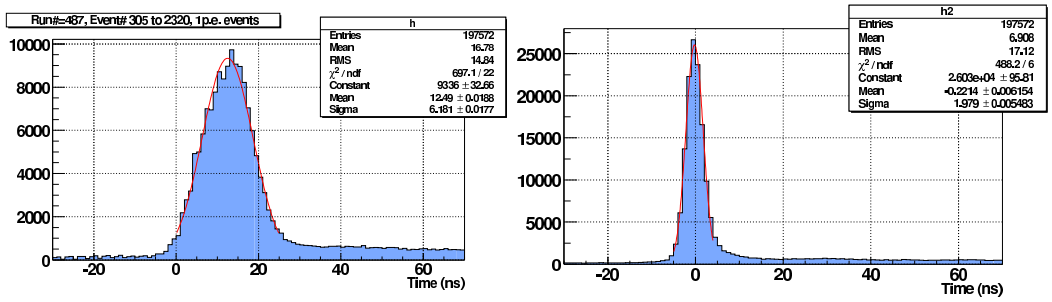

Figure 3.4: Timing distributions before (left) and after(right) TQ correction. The histograms show hit time distribution of all 17-inch PMT hits for 1 p.e. events using detector center calibration run.

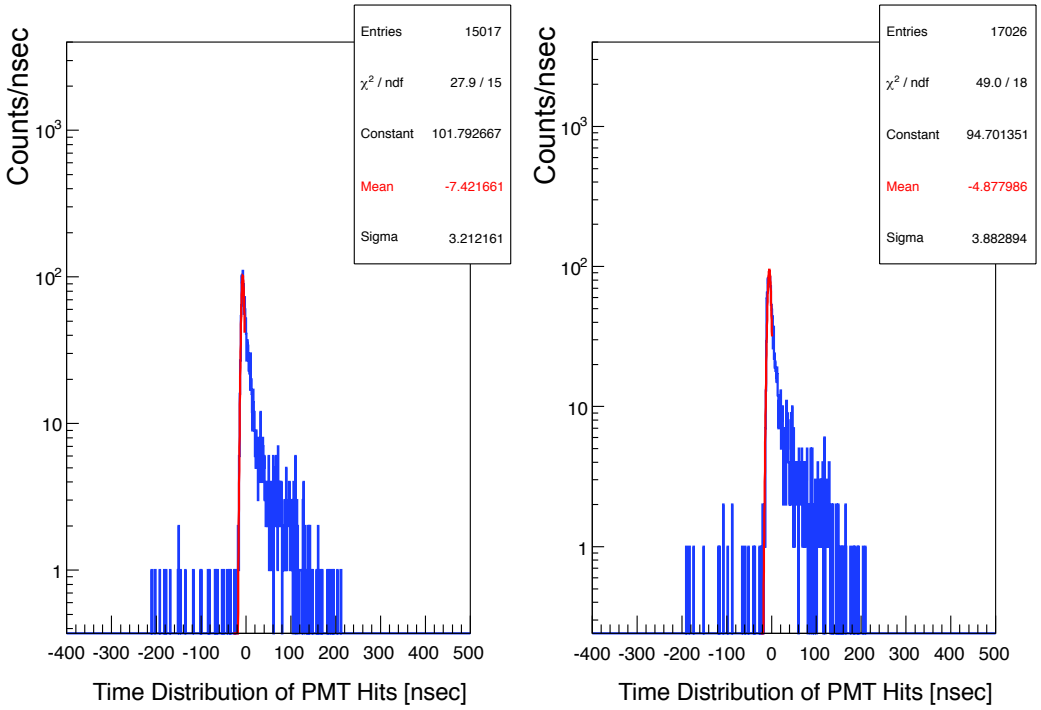

Figure 3.5: Timing distribution of PMT hits using ^{60}Co calibration run at the center of the detector. Cable No.0 is selected, and ATWD Ach is left, and ATWD Bch is right. The blue line shows the data, and the red line shows the fitting result. The mean value is used for ^{60}Co timing correction.

- 100 μsec veto for avoiding missing waveform events
- Nsum (the number of hit 17-inch PMT) cut for rejecting low occupancy events
  before purification : $120 \leq \text{Nsum} \leq 180$
  after purification : $120 \leq \text{Nsum} \leq 230$
- distance between PMT and reconstructed vertex > 6.0 m
- 1 peak in waveform

Figure 3.6 shows the 1 p.e. distribution of typical 17-inch and 20-inch PMTs. The distribution of 17-inch PMT has a clear peak, on the other hand, that of the 20-inch PMT can not make a peak due to the difference of the dynode type. It is better to use only 17-inch PMT 1 p.e. peak to gain calibration. As shown in Figure 3.6 left, the 17-inch 1 p.e. peak is obtained by Gaussian fitting. The gain calibration for 20-inch PMTs is perfumed using the charge ratio at a high photon levels (i.e. muon events) between adjust 17-inch PMTs and each 20-inch PMT. The charge ratio is defined as follows:

$$\text{ChargeRatio} = \frac{\text{Charge of target } 20-\text{inch PMT}}{\text{Average charge of 8 neighbor } 17-\text{inch PMTs}} \tag{3.2}$$

A comparison between the charge of one 20-inch PMT and average charge of 0 neighbor 17-inch PMTs is shown in Figure 3.7 left. By using this relation, the charge ratio is defined and calculated as Figure 3.7 right.

Figure 3.8 represents the time variation of the mean 1 p.e. charge for 17-inch and 20-inch PMTs. There are some gaps which are caused by some hardware activities or other operations. The gradual raise is also corrected by this gain correction.

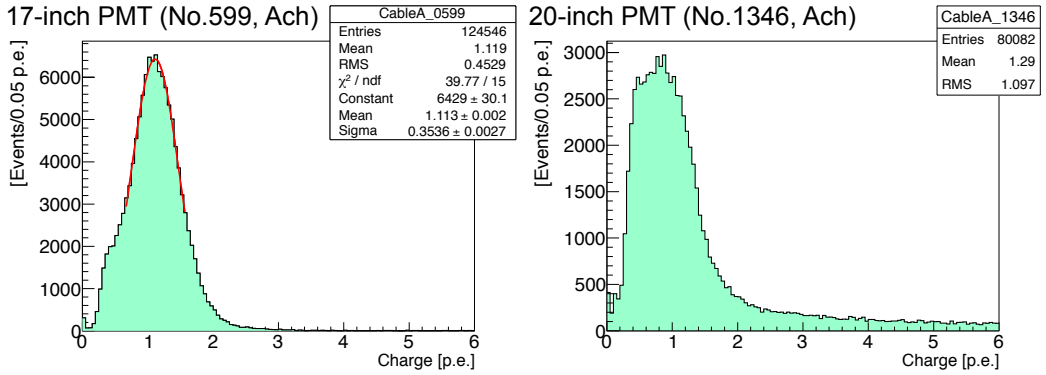

Figure 3.6: 1p.e. distribution of typical 17-inch (left) and 20-inch (right) PMT. The distribution of 17-inch PMT has a clear peak, but that of the 20-inch PMT can not make a peak due to the difference of the dynode type.

3.2.3 Bad Channel Selection

There are 1,868 PMTs in the inner detector and 241 PMTs in the outer detector. These PMTs include unstable channels, which have too many hits, no hit or strange charge. These abnormal signals are caused by the broken PMTs or the unstable high voltage supply for each PMTs or the miss connection of signal cables. These unstable channels are called "bad channels", which are masked in event reconstruction processes to prevent systematic biases. The bad channels are searched channel by channel and run by run, and the selection criteria for inner detector PMT is as follows:

- PMT hit rate $<$ 1,000 hits
  search bin width : 10,000 events
  target : low response channels due to electronics failures

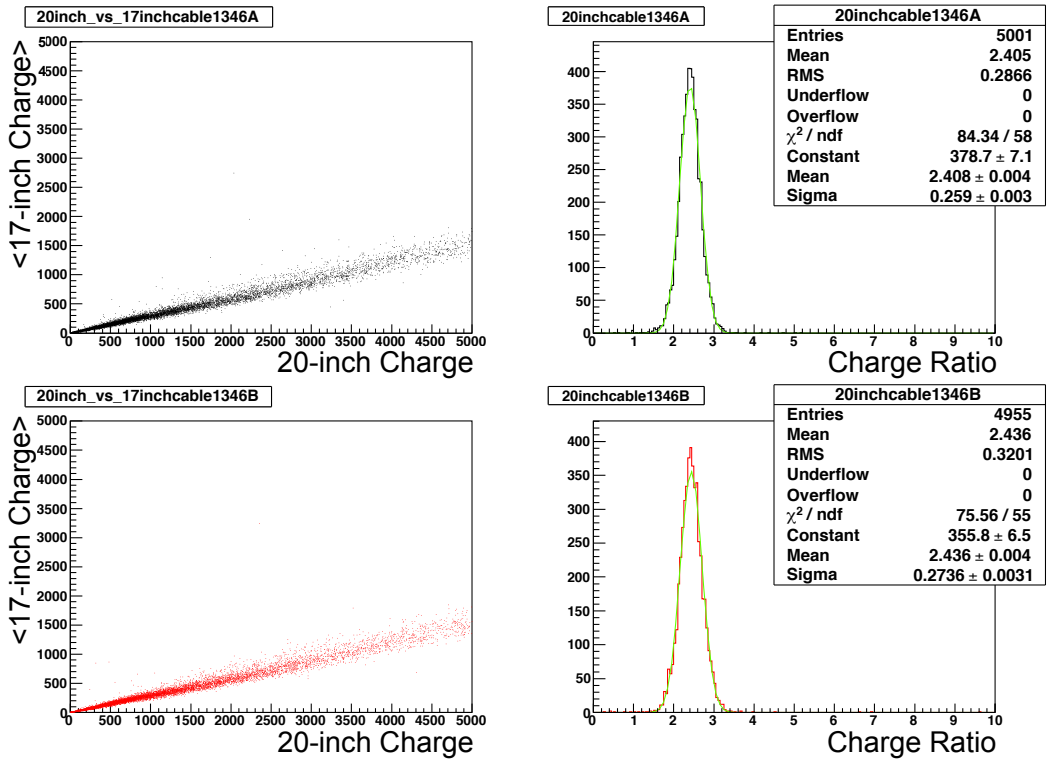

Figure 3.7: Gain calibration for 20-inch PMT. 20-inch gain table is calculated based on 8 neighbor 17-inch PMT channels. The top left figure shows the charge distribution of one 20-inch PMT A channel (No.1346, same as Figure 3.6) and average charge of 8 neighbor 17-inch PMT channels. The top right figure shows charge ratio between average charge of 8 neighbor 17-inch PMTs and the charge of target 20-inch PMT A channel. The bottom two figures are for B channel.

- PMT no-hit rate > 1,000 no-hits
  search bin width : 10,000 events
  target : no response channels due to high voltage problem

- Hit rate in high charge muon event
  search bin width : 100 high-charge-muons
  target : excessively low gain channels

- Difference of hit rate between A and B channel
  search bin width : 100,000 events
  target : bad channel in which ping-pong scheme of the FEE failed

- Charge difference in high charge muon event

$$\frac{1}{N_i}\sum_{j=1}^{N_i}\frac{(Q_i-Q_j)^2}{Q_j} > 400 \text{ p.e.} \qquad (Q_j > 0,\ j : \text{neighbor PMT}) \qquad (3.3)$$

  target : channels with a large gain difference by a comparison of the gain between neighbor channels

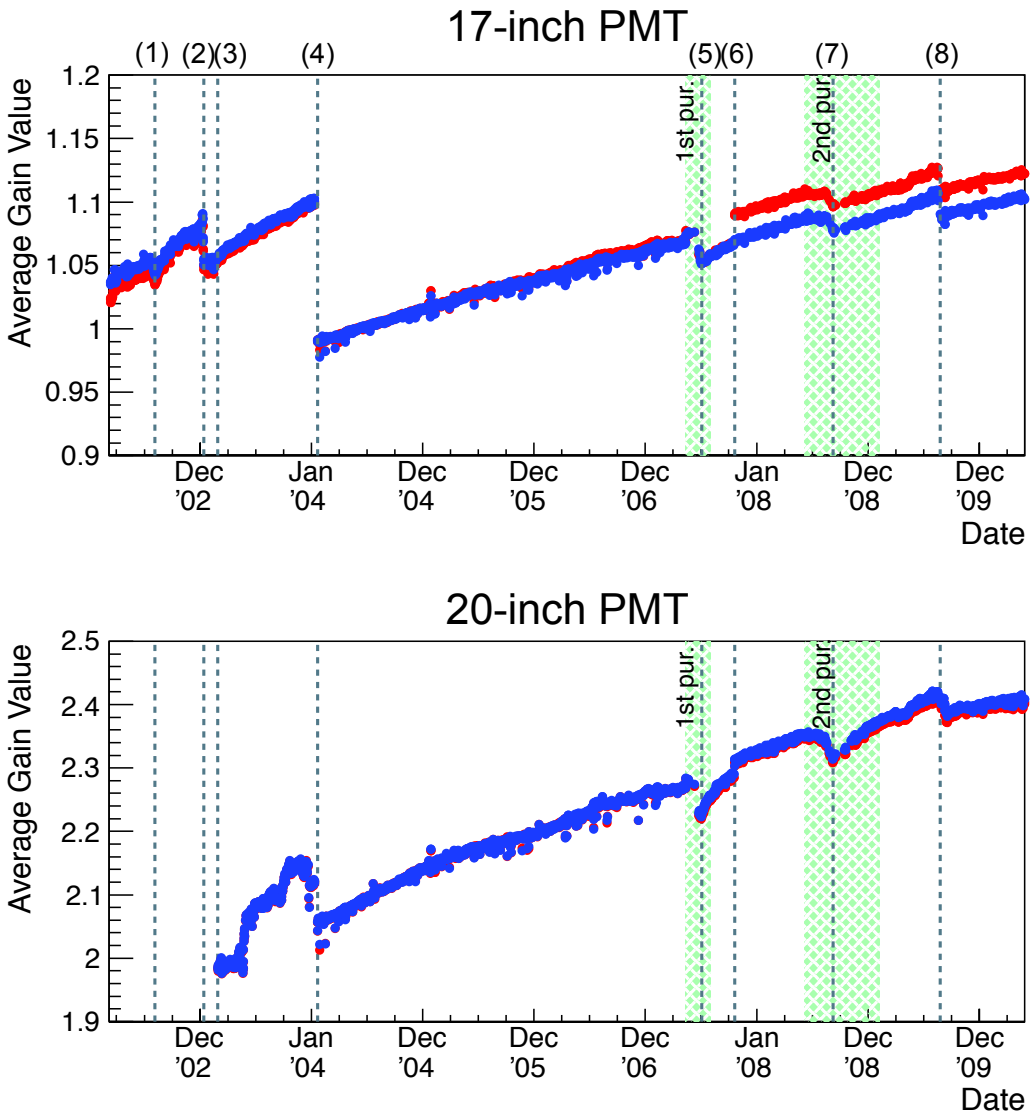

Figure 3.8: Time variation of gain correction of 17-inch PMTs (top) and 20-inch PMTs (bottom). The vertical axis shows the mean 1 p.e. charge for each PMT. The red points show ATWD A-ch and the black points show ATWD B-ch. The 1 p.e. charge increase gradually over data taking period for 17-inch and 20-inch PMTs. However some hardware or software activities affect the 1.p.e. charge, such as the following;
(1) HV test for 20-inch PMTs (Aug. 4, 2002)
(2) Electronics (FEE) upgrade (Jan. 13, 2003)
(3) Start of using 20-inch PMT (Feb. 25, 2003)
(4) HV replacement (Jan. 21, 2004)
(5) End of high dark rate period during 1st purification (Sep. 7, 2008)
(6) Electronics (FEE) upgrade (Oct. 20, 2008)
(7) Turning on all crate (Sep. 7, 2008)
(8) New electronics (MoGURA) installation (Aug. 25, 2009)

- Too low ADC counts for 1 p.e. ($< \bar{Q}_{adc} \times 1/4$) or too high ($> \bar{Q}_{adc} \times 4$)
  target : very low gain or very high gain channels
  ($\bar{Q}_{adc}$ is mean of ADC counts corresponding to 1 p.e. of all 17-inch channels.)

For outer detector PMT selection, only 1st criteria is applied.

Figure 3.9 shows the time variation of bad channels. There are many bad channels in the outer detector, and currently about 50 % of OD channels are badly masked. Mainly these OD bad channels are caused by dead PMTs via a water leak.

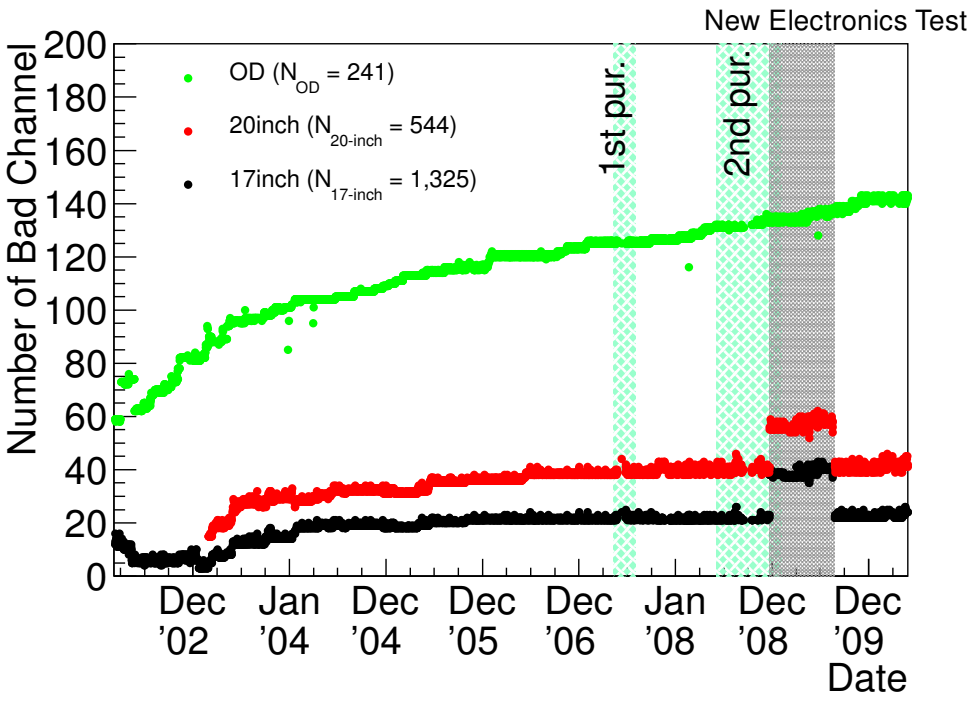

Figure 3.9: Time variation of number of bad channels. The green points show outer detector 20-inch PMTs, the blue and red points shows inner detector 17-inch and 20-inch PMTs. The total number of each PMT is shown in the graph legend. The green shaded areas represent the 1st and 2nd purification campaign periods, which did not affect number of bad channels. The black shaded area shows the test period for dead time free electronics.

3.3 Event Reconstruction

3.3.1 Muon Track Reconstruction

The 2,700 w.e. overburden reduced the cosmic ray flux by a factor of roughly 10^{-5} with respected to the surface flux. The cosmic ray muons which go through the inner detector are observed on constant frequency, 0.34 Hz. These muons sometimes interact with nuclei in the detector and produce radioactive isotopes that can mimic the coincidence neutrino signal. The algorithms to reconstruct these muon tracks are developed, and can efficiently remove the backgrounds for anti-neutrino detection.

In this section, muon selection criteria, tracking algorithm and its performance are described.

Muon Selection Criteria

Selection criteria for muon events is as follows:

- $Q_{\mathrm{ID17inch}} \geq$ 10,000 p.e. ($\sim$30 MeV): 0.31 $\sim$ 0.32 Hz
- $Q_{\mathrm{ID17inch}} \geq$ 500 p.e. and $N_{\mathrm{200OD}} \geq 5$ hits : 0.027 $\sim$ 0.028 Hz
  The muons which go through only the buffer oil region emit only Cherenkov photons. This 'Cherenkov muon' is selected by the OD tagging using the PMT hit information.
  Q_{ID17inch} [p.e.] : total charge sum of the 17-inch PMTs in the inner detector
  N_{200OD} : number of PMT hits in the outer detector within a 200 nsec time window

In order to remove accidental OD hits and improve OD efficiency for muons, a 200 ns timing cut is applied.

The selected events are shown in Figure 3.10. The muon rate is estimated to be about 0.34 Hz from the time difference between muon to muon. The charge spectrum gives clear information for classification of the type of muon using the charge sum. These two peaks correspond to 'through going muons' (Cherenkov light + scintillation light) and 'clipping muons' (Cherenkov light). The through going muons are further categorized into the following two types :

- Showering muons (ΔQ $> 10^6$ p.e.)
  These are energetic muons which often produce radiative isotopes and noise events.
- Non-showering muons (ΔQ $< 10^6$ p.e.)
  These are less energetic muons.
  ΔQ : residual charge, which is defined later.

Figure 3.11 shows the charge distribution of muon events.

The muon rate has been very stable from the start of KamLAND data taking, as shown in Figure 3.12. Figure 3.13 shows the time variation of the mean charge of the 17-inch PMTs for Cherenkov muons and Scintillation muons. This mean charge for Cherenkov muons is calibrated to correct in order to respond to change. While the muon charge for Cherenkov muons has been slowly increasing, that for Scintillation muons changed suddenly caused by the purification of the liquid scintillator, and by electronics updates, which can result in different effective thresholds.

Algorithm of Muon Track Reconstruction

The muon track is reconstructed using the timing information of PMT hits. The muons going through the detector produce a large amounts of light by scintillation in the LS and Cherenkov radiation in both of the LS and the buffer oil. The Cherenkov light is emitted at a constant angle, θ, with respect to the muon track, related to the index of refraction, as show in Figure 3.14 left. The later reemission photons are ignored. On the other hand, the scintillation photons are emitted to all directions.

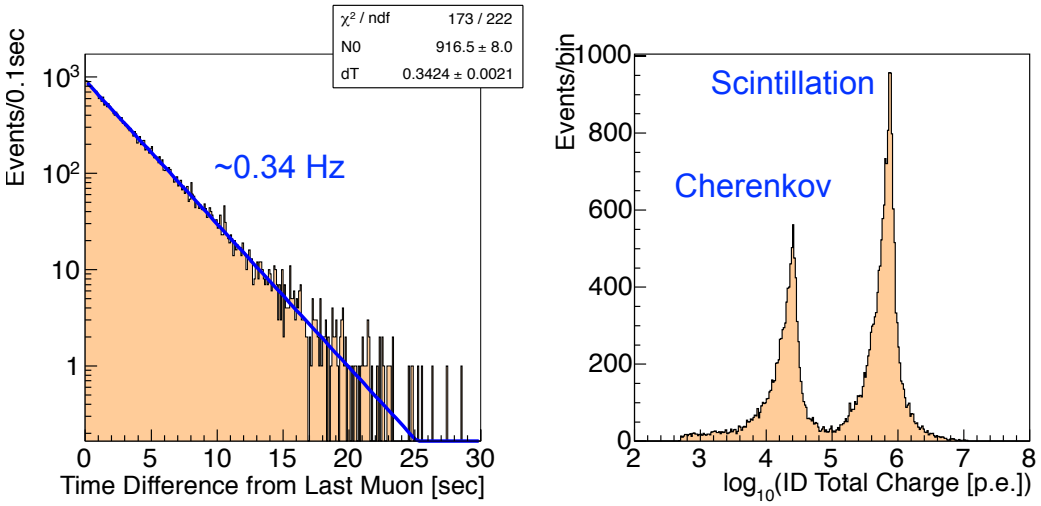

Figure 3.10: Time difference between muon to muon (left), and the charge distribution of muons (right). The muon rate is estimated to be about 0.34 Hz in KamLAND. The charge distribution has two clear peaks, 'through going muons' (Cherenkov light + scintillation light) and 'clipping muons' (Cherenkov light).

With notation of Figure 3.14 right, the observed time t of the earliest light arriving the PMT is expected as a function of l,

$$\begin{aligned} t &= t_0 + \frac{l}{c} + \frac{z-l}{\cos\theta} \times \frac{n}{c} \\ &= t_0 + \frac{l}{c} + \sqrt{(z-l)^2 + \rho^2} \times \frac{n}{c}, \end{aligned} \tag{3.4}$$

where t_0 is the time when a muon entered to the detector and n is the index of refraction. The velocity of the muon is approximated to be the speed of light. From Eq.(3.4), the minimum of t can be easely calculated with the equation $dt/dl = 0$ at the minimum we find :

$$\cos\theta = \frac{1}{n} \tag{3.5}$$

This angle is same as the Cherenkov angle when the velocity of the muon is same as the speed of light, and indicates the angle from which the earliest photons come. It allows the simplification of the optical system using only earliest photons. The muon track in reconstructed as the most likely track to have produced the PMT hit times. The index of refraction of the liquid scintillator and buffer oil is measured to be 1.44 $\sim$ 1.47 in the various wavelength of the scintillation light. In order to consider the difference of the pass length in the scintillator and buffer oil for each track, that parameter is tuned within the measured value in the reconstruction algorithm.

In the case that a muon spots in the detector or multiple muons go through the detector at the same time, this reconstruction algorithm is not appropriate. A muon which has too small charge sum for the reconstructed track length is classified as a 'miss-reconstructed muon'. This miss-reconstructed muons are classified with 'through going muon' and 'showering muon', and these rate is 0.2 % and 1.5 % for all muons, respectively.

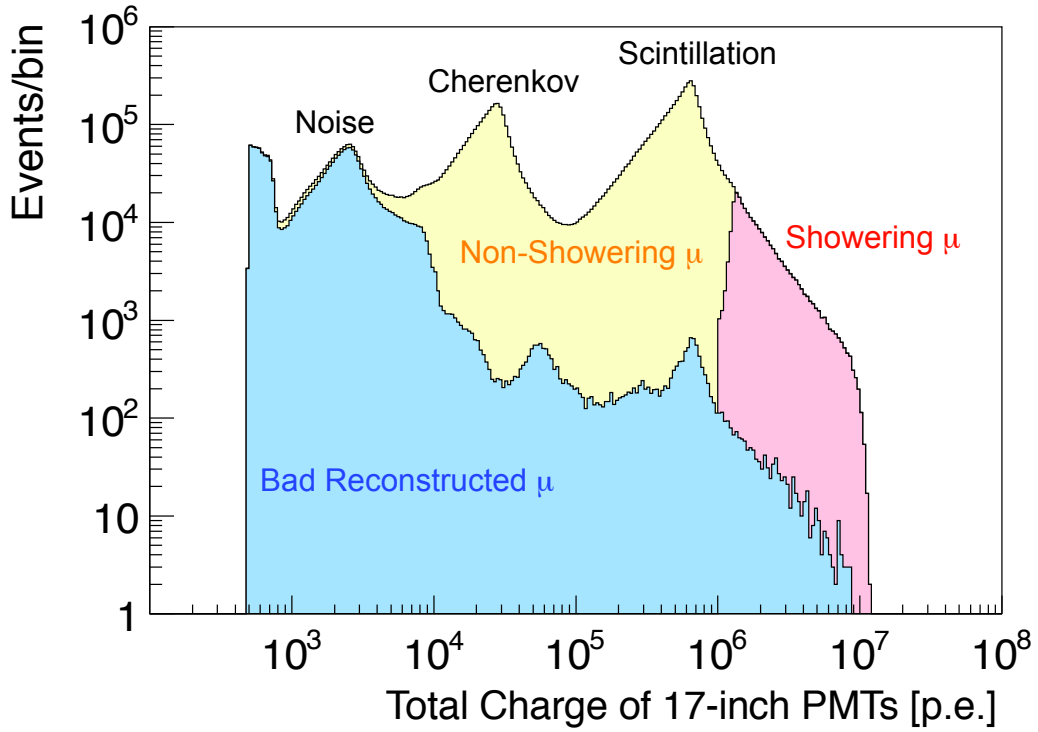

Figure 3.11: Charge distribution of muon events. There are three clear peaks in the yellow histogram. The highest peak corresponds to scintillation and Cherenkov light made by muons which go through the liquid scintillator. The another peak is made by muons which pass only through the buffer oil and hence emit only Cheremkov light. The lowest peak corresponds to noise events. The blue histogram is made by badly reconstructed muons (Badness > 100), and the pink histogram shows energetic muons which produce spallation products (ΔQ $> 10^6$ p.e.)

Tracking Performance

Figure 3.15 shows the correlation between the total charge in the detector and the shortest distance between the reconstructed muon track and the center of KamLAND (impact parameter). The boundary at 650 cm between the liquid scintillator and buffer oil regions is evident.

The distribution of normalized charge divided by reconstructed muon track length (dQ/dX) in the each region is shown in Figure 3.16. The definition is as follows :

$$\left(\frac{dQ}{dX}\right)_{Cherenkov} = \frac{Q_{ID}}{L_{BO}} \tag{3.6}$$

$$\left(\frac{dQ}{dX}\right)_{Scintillation} = \frac{Q_{ID} - L_{BO}\langle\frac{dQ}{dX}\rangle_{Cherenkov}}{L_{ID}} \tag{3.7}$$

where Q_{ID} is the total charge of the 17-inch PMTs, L_{ID} and L_{BO} are the reconstructed track lengths in the inner detector (liquid scintillator and buffer oil) and in the buffer oil only, and $(dQ/dX)_{Scintillation}$ includes the Cherenkov light created in the liquid scintillator. The ideal light emission per unit length is approximated by

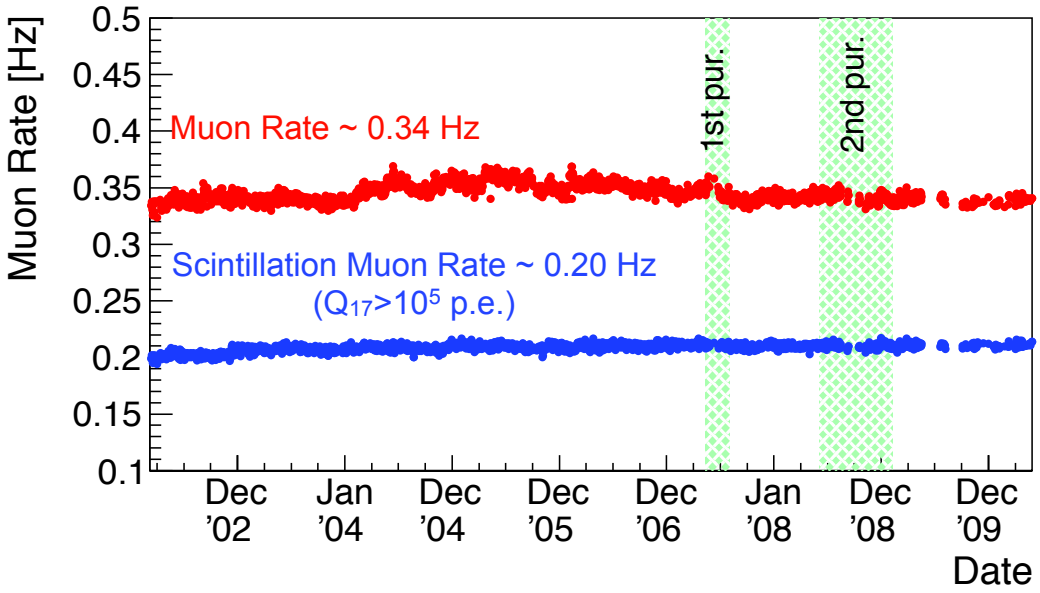

Figure 3.12: The time variation of muon rate. The red points shows the muon rate which is estimated using the time difference between muon to muon. The blue points shows the rate of the scintillation muons whose total charge is higher than 10^5 p.e. These muon rate base been stable from the start of KamLAND data taking, at about 0.34 Hz and 0.020 Hz, respectively.

the mean of a Gaussian fit with a lower edge,

$$\left\langle \frac{dQ}{dX} \right\rangle_{Cherenkov} = 31.45 \text{ p.e./cm} \tag{3.8}$$

$$\left\langle \frac{dQ}{dX} \right\rangle_{Scintillation} = 629.4 \text{ p.e./cm} \tag{3.9}$$

$\langle dQ/dX \rangle_{Scintillation}$ is about 20 times higher than $\langle dQ/dX \rangle_{Cherenkov}$.

The correlations between the total charge of the 17-inch PMTs and the muon track length in the liquid scintillator and buffer oil are as shown in Figure 3.17. Badly reconstructed muon events (Badness $>$ 100) are not plotted in this figure. A linear trend, corresponding to minimum ionizing muons, is apparent in both distributions. The slope of each line is the total charge per unit length in the respective material. The high energy muons, which correspond to the muons in Figure 3.17 generating light yields above the baseline linear trend, are likely to involve secondly particles. This process is called as appellation products, and the residual charge (ΔQ) is used to tag these muons. The definition of ΔQ is as follows :

$$\Delta Q = Q_{ID} - L_{ID} \left\langle \frac{dQ}{dX} \right\rangle_{Cherenkov} - L_{Scintillation} \left\langle \frac{dQ}{dX} \right\rangle_{Scintillation} \tag{3.10}$$

A muon whose ΔQ is higher than 10^6 p.e. is classified as showering muon, and this value corresponds to $\sim$3 MeV. 2 sec. whole volume veto after such muons is applied. A muon whose ΔQ is less than 10^6 p.e. is regard as non-showering muon. For these non-showering muons, 2 msec whole volume veto and 2 sec cylindrical region of 3 m radius along the muon track veto is applied.

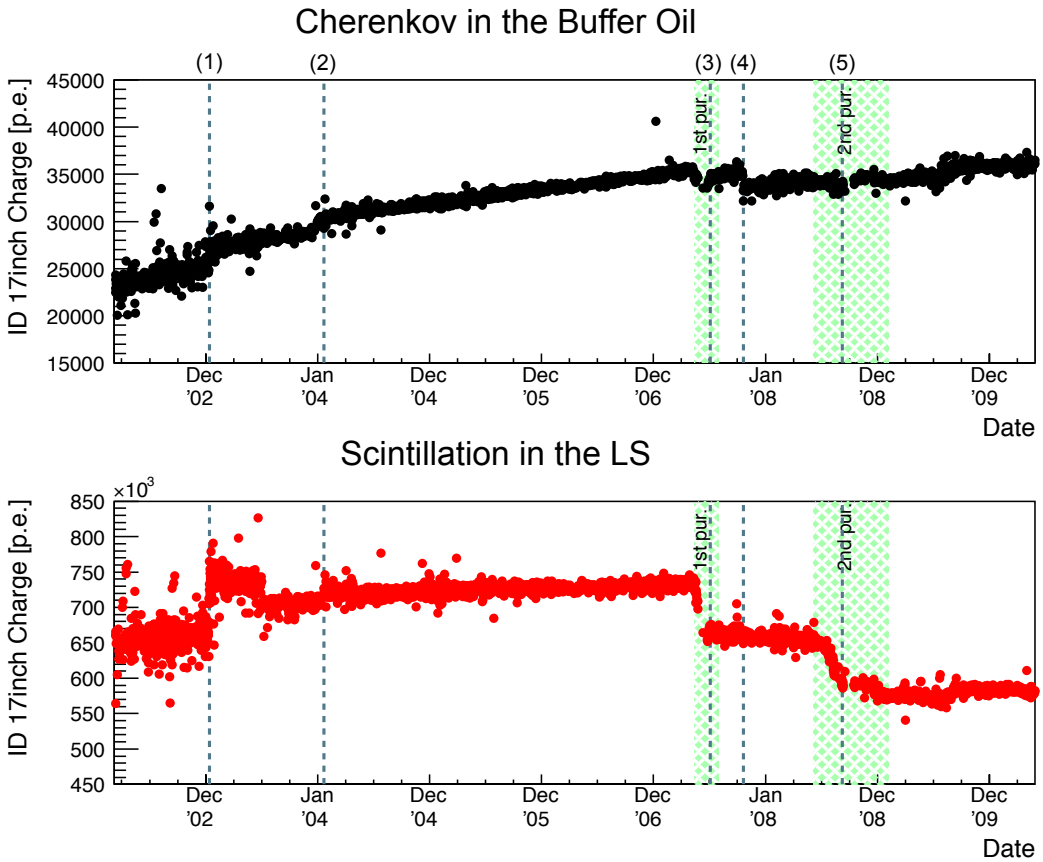

Figure 3.13: Time variation of the muon charge for muon events in the buffer oil (top) and the liquid scintillator (bottom) before muon gain correction. The 2 times purification affected the light emission in the liquid scintillator. There are sudden changes during purification and at the time of some electronics activities. The gray lines shows the activities :
(1) Electronics (FEE) upgrade (Jan. 13, 2003)
(2) HV replacement (Jan. 21, 2004)
(3) End of high dark rate period during 1st purification (Sep. 7, 2008)
(4) Electronics (FEE) upgrade (Oct. 20, 2008)
(5) Turning on all crate (Sep. 7, 2008)

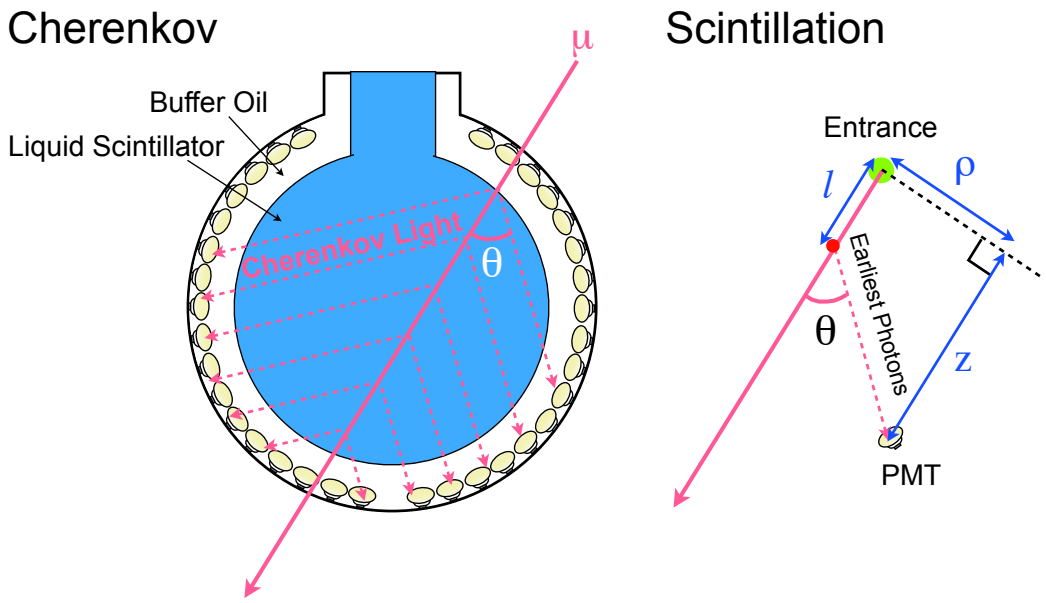

Figure 3.14: The schematic of muon track.

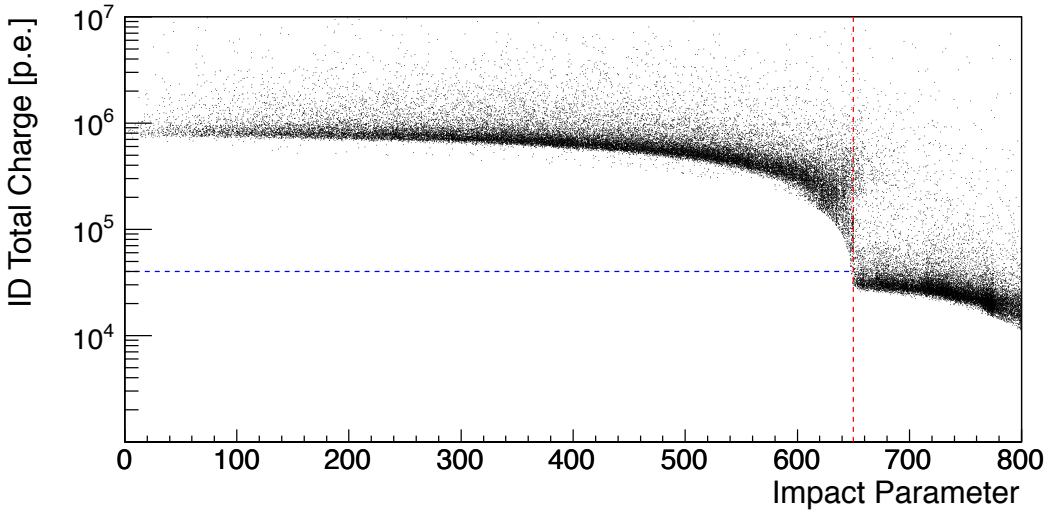

Figure 3.15: Correlation between total charge in the inner detector and the shortest distance from the muon track to the KamLAND detector center (Impact parameter). The vertical dashed red line represents to the boundary between the LS and BO at 650 cm. Events located to the left of this boundary and above the horizontal blue dashed line (total charge = 4×10^4 p.e.) are designated as LS muons.

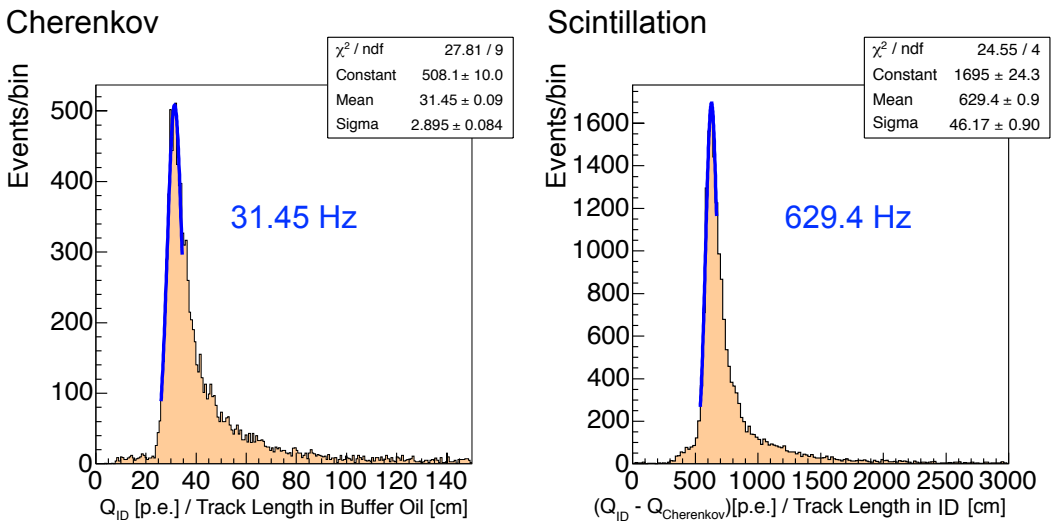

Figure 3.16: Normalized charge divided by reconstructed muon track length (dQ/dX). The left and right figures show dQ/dX for muons going through the buffer oil (clipping muon) and the liquid scintillator (through going muon), respectively. The ideal light emission per unit length is estimated to be 31.45 p.e./cm and 629.4 p.e./cm for each muons.

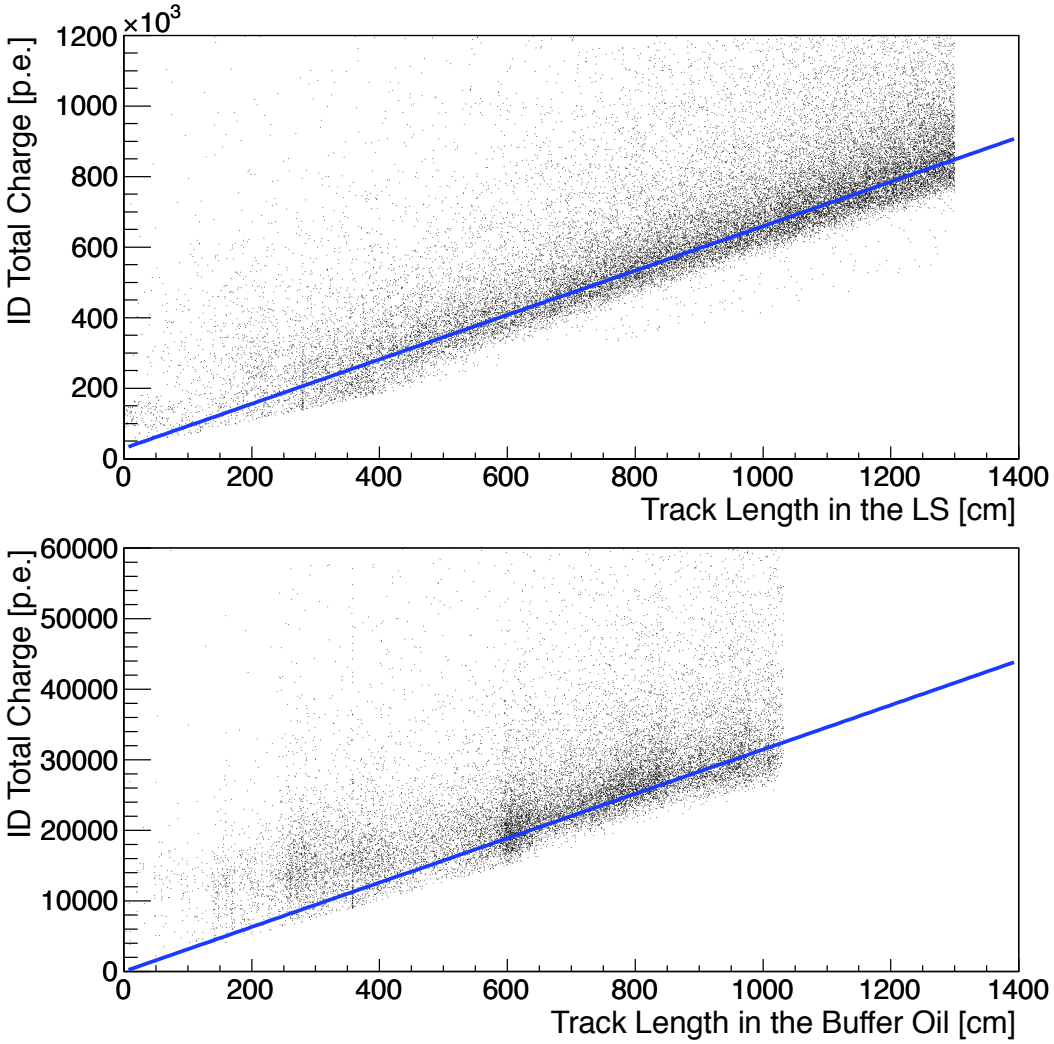

Figure 3.17: Correlation between total charge and the muon track length in the liquid scintillator (top) and the buffer oil (bottom). The blue lines show the fitted total charge per unit length in the respective material.

3.3.2 Vertex Reconstruction

The vertex is a fundamental parameter for 'point-like' events. The energy reconstruction (Section 3.3.3) and the event reconstruction quality are estimated by using this parameter.

Algorithm of Vertex Reconstruction

The vertex reconstruction is based on the PMT hit time distribution, which is called "pulse shape". The pules shape generally depends on the PMT type, distance from the source to PMT, the intensity of the signal, the origin of the signal (gamma, beta, neutrino, positron) and the distance traveled through the liquid scintillator. In the vertex reconstruction, the actual experimental pulse shapes obtained by the source calibration is used for producing the likelihood function. The maximum likelihood method is applied to determine the vertex position.

To connect the experimental observable PMT hit timings with the pulse shape used in the likelihood, the pulse shapes are parametrized with vertexes and hit time information. The four parameters are donated as x, y, z and τ of each PMTs. Here, τ represents the delay of the signal timings compared to the expectations calculated for some x, y, z, t:

$$\tau_i = t_i - t - TOF_i(i : \text{index of PMTs}), \tag{3.11}$$

where t_i is the observed timing in the i-th PMT and TOF_i (for Time Of Flight) is the distance form the point (x, y, z) to the i-th PMT divided by the speed of light in the liquid scintillator.

The pulse shapes at various points are collected form the available source calibration data, and these results are defined as the invariant pulse shapes. These invariant shapes also include the effect of the multiple hits and re-emission to the scintillation light. The likelihood function that takes into account only the signal timing and ignores charge and hit pattern information is the product of pulse shapes :

$$L = \prod_{i}^{N_{hits}} \psi\{\tau_i(x, y, z, t)\}, \tag{3.12}$$

As usual, the logarithm of the likelihood is more convenient for computations than its actual value :

$$\log(L) = \sum_{i}^{N_{hits}} \log(\psi\{\tau_i(x, y, z, t)\}), \tag{3.13}$$

where the multiplication is made only over the PMTs that are hit and have a signal, τ_i is the signal's delay according to the current values of $x, y, z.t$ under inspection, and ψ is a pulse shape evaluated at τ_i.

The maximum of the Eq. (3.13) is achieved at a point where 4-dimensional gradient turns into zero, i.e. partial derivatives with respect to x, y, z and t all

vanish :

$$\begin{aligned}
\frac{\partial(\log(L))}{\partial x} &= \sum_{i}^{N_{hits}} \frac{d(\log(L))}{d\tau_i}\frac{\partial \tau_i}{\partial x} = 0 \\
\frac{\partial(\log(L))}{\partial y} &= \sum_{i}^{N_{hits}} \frac{d(\log(L))}{d\tau_i}\frac{\partial \tau_i}{\partial y} = 0 \\
\frac{\partial(\log(L))}{\partial z} &= \sum_{i}^{N_{hits}} \frac{d(\log(L))}{d\tau_i}\frac{\partial \tau_i}{\partial z} = 0 \\
\frac{\partial(\log(L))}{\partial t} &= \sum_{i}^{N_{hits}} \frac{d(\log(L))}{d\tau_i}\frac{\partial \tau_i}{\partial t} = 0
\end{aligned} \tag{3.14}$$

The vertex fitter searches the solutions and gives the best vertex parameters, x, y, z and t.

Vertex Reconstruction Quality

The vertex reconstruction quality is regularly monitored by the source calibrations. The following is the check item for the vertex reconstruction.

1. Vertex Bias
   The vertex bias is verified with various calibration sources along z-axis. Figure 3.18 shows the vertex deviation between reconstructed z and expected positions of various sources. The deviations are estimated using before and after purification data, and that are less than 3.0 cm (before purification) and less than 5.0 cm (after purification). The results are same between 17-inch and 17- and 20-inch PMTs analysis. Figure 3.19 and 3.20 also represent the source dependent vertex deviation before and after purification. At the center of the detector, the vertex bias has been controlled within ±3.0 cm from the start of KamLAND data taking, as shown in Figure 3.19.

2. Vertex Resolution
   The vertex resolution is also estimated based on various calibration source results. Since the reconstructed vertex distribution is under the influence of a charge dispersion in the detector, the vertex distribution used for the vertex resolution estimation should be compared with the simulation results. Figure 3.22 shows the comparison between the radios distribution of the calibration data and simulation result obtained by GEANT4[24]. Obtained resolution is plotted in Figure 3.23 for only 17-inch and 17 + 20-inch PMT analysis before and after purification. The vertex resolution is estimated as follows :

   - before purification (17-inch) : 13.1 ± 2.1 cm / $\sqrt{\text{E}}$ [MeV]
   - before purification (17+20-inch) : 11.7 ± 2.2 cm / $\sqrt{\text{E}}$ [MeV]
   - after purification (17-inch) : 15.3 ± 2.5 cm / $\sqrt{\text{E}}$ [MeV]
   - after purification (17+20-inch) : 13.8 ± 2.3 cm / $\sqrt{\text{E}}$ [MeV]

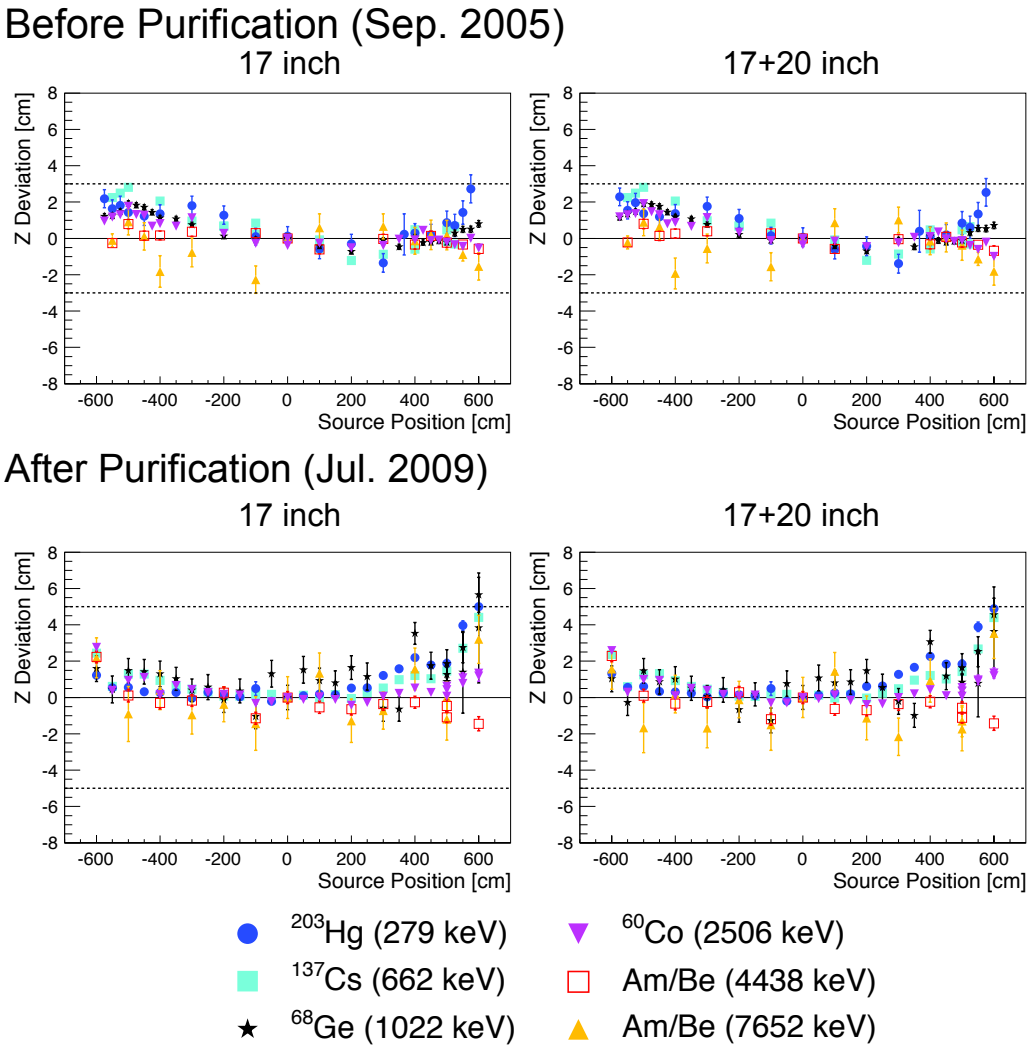

Figure 3.18: Vertex deviations between reconstructed z and expected position of various sources, ^{203}Hg (blue circle, 279 keV), ^{137}Cs (light blue triangle, 662 keV), ^{68}Ge (black star, 1022 keV), ^{60}Co (purple triangle, 2506 keV), Am/Be (red box, 4438 keV and orange triangle 7652 keV). The top two figures represent the vertex deviations before purification (September, 2005 calibration campaign), which estimated within ±3.0 cm using 17-inch (left) or 17 and 20-inch PMTs (right). The bottom two figures also represent the vertex deviations after purification (July, 2009 calibration campaign), which estimated within ±5.0 cm using 17-inch (left) or 17 and 20-inch PMTs (right). The deviations are less than 3.0 cm (before purification) or 5.0 cm (after purification) for 6.5m fiducial radius.

3. Miss Reconstruction Probability
   The miss reconstruction probability is evaluated from the distance distribution of calibration source events subtracted background events. ^{60}Co γ-rays (1173.2 + 1332.5 keV) are available to check the quality for anti-neutrino analysis energy range. The definition of the miss reconstruction probability is as follows

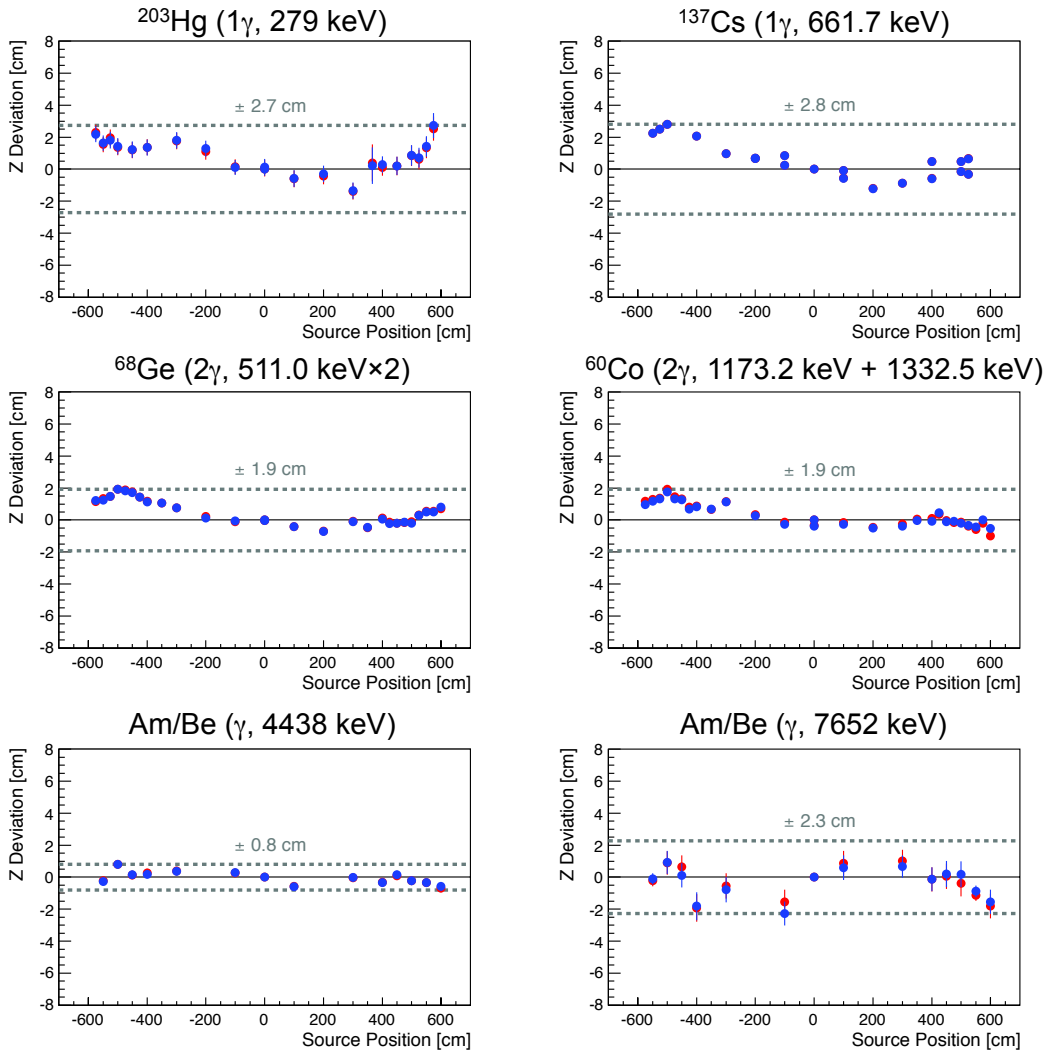

Figure 3.19: Vertex deviations between reconstructed z and expected position of various sources. The calibrations were preformed on September 2005, before purification. Blue points show only 17-inch PMTs analysis results and red points show 17- and 20-inch PMTs analysis results.

:

$$P = \frac{N(^{60}\mathrm{Co\ events\ with\ } \Delta \mathrm{R} > \mathrm{R_{cut}} - \mathrm{N(BG\ with\ } \Delta \mathrm{R} > \mathrm{R_{cut}})}{N(^{60}\mathrm{Co\ events}) - \mathrm{N(BG)}}, \qquad (3.15)$$

where R_{cut} is selected to be enough longer than the attenuation length of gamma rays. Figure 3.24 shows the distance distribution and the estimated miss reconstruction probability before and after purification. The miss reconstruction probability is suppressed within 0.2 % in each analysis.

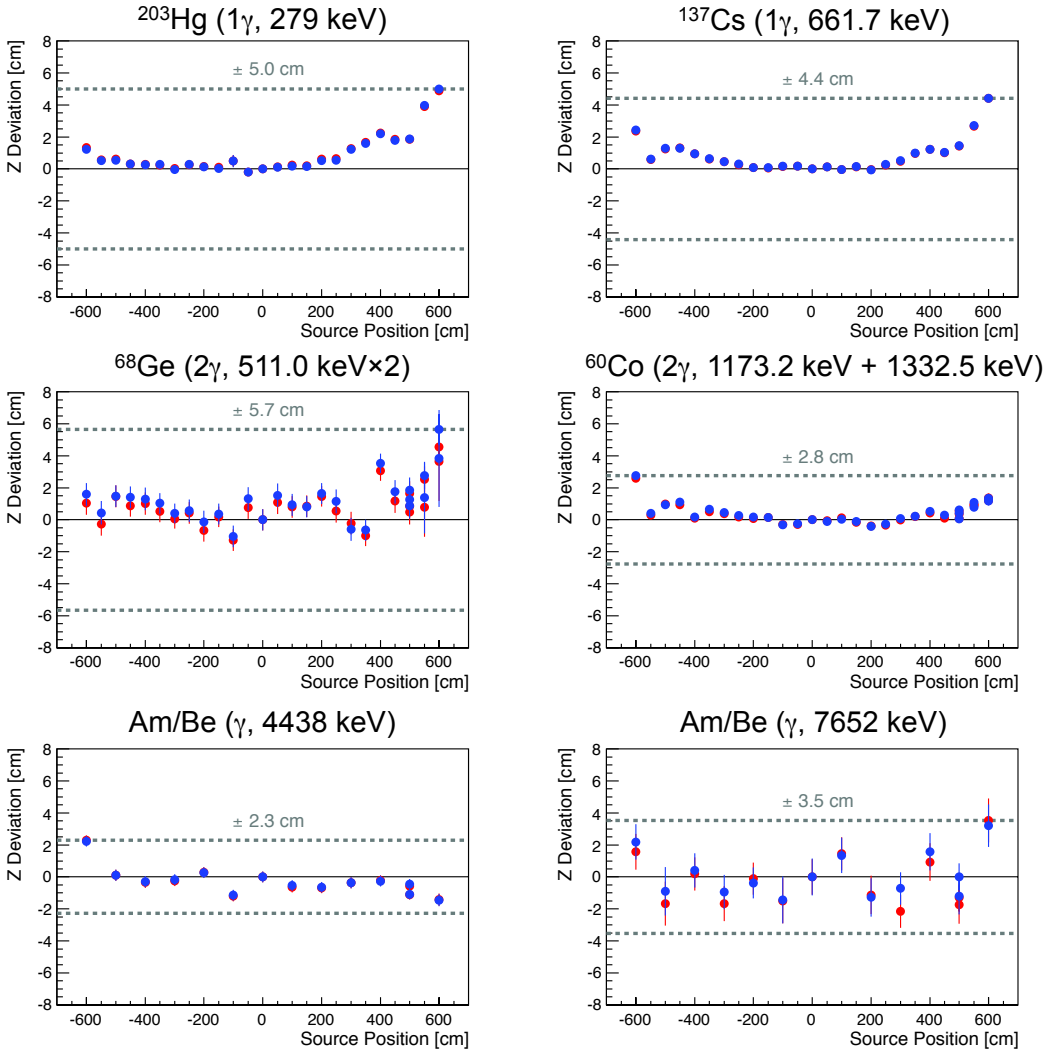

Figure 3.20: Vertex deviations between reconstructed z and expected position of various sources. The calibrations were preformed on July 2009, after purification. Blue points show only 17-inch PMTs analysis results and red points show 17- and 20-inch PMTs analysis results.

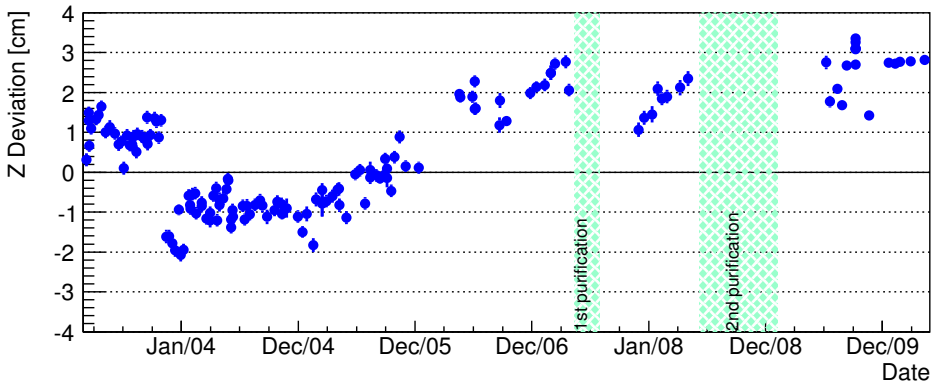

Figure 3.21: Time variation of vertex deviation between reconstructed z and detector center using ^{60}Co z=0 runs. All points represent 17-inch PMT analysis results. The vertex bias at the center of detector has been controlled within ±3.0 cm during all data taking period.

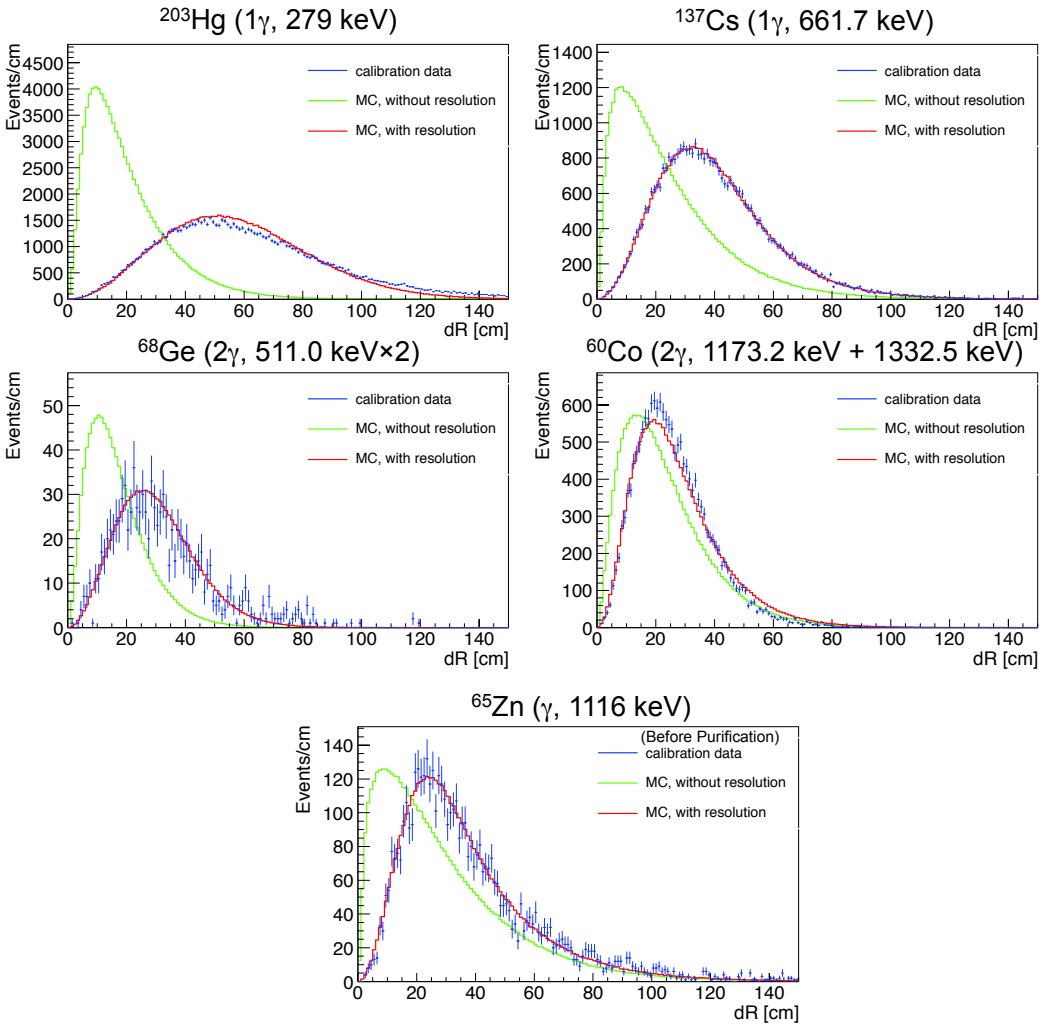

Figure 3.22: Radius distribution of each calibration source data and simulation result obtained by GEANT4[24]. The top four calibration source datas (^{203}Hg, ^{137}Cs, ^{68}Ge, ^{60}Co) were collected after purification, and the bottom one calibration data (^{65}Zn) was collected before purification. Blue points show the calibration data, green and red lines show the simulation results with and without vertex resolution effect, respectively. The red lines are represent the best fit vertex resolution searched by chi-square test.

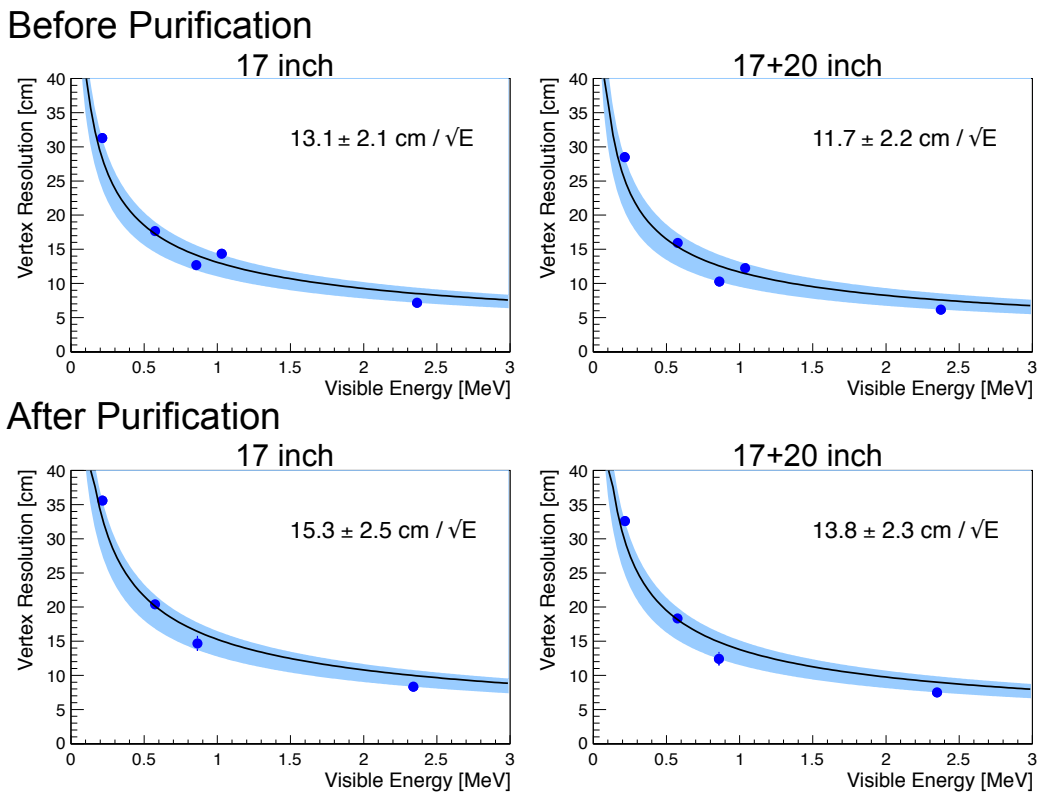

Figure 3.23: Vertex resolution for each calibration source as a function of visible energy. The upper and lower figures show the vertex resolution before and after purification. These estimations are based on 17-inch (left) or 17- and 20-inch PMTs (right) analysis, respectively. Blue points show the best fit vertex resolution obtained by comparison with the simulation results, as shown in Figure 3.22. The horizontal axis shows the visible energy estimated by energy spectrum fitting. Blue shaded area shows error region.

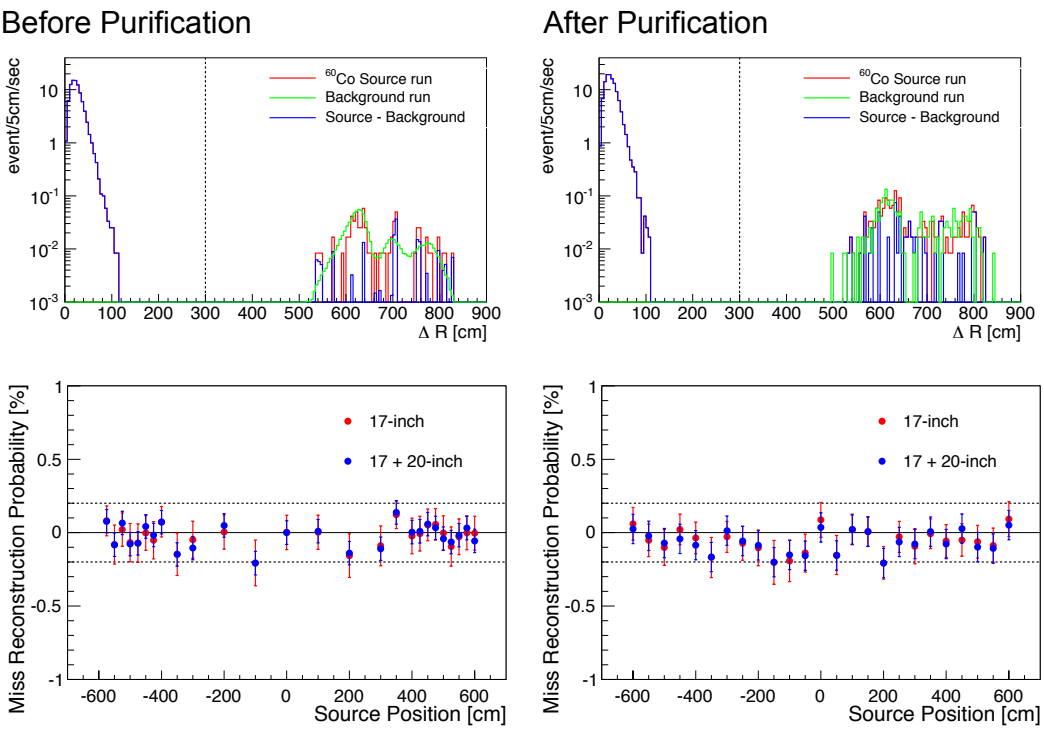

Figure 3.24: Miss reconstruction probability estimated with ^{60}Co events before (left) and after (right) purification. The top figures show the distance distribution of ^{60}Co events (red line), the background events (green line) and the background subtracted histogram (blue line). The bottom figures show the estimated miss reconstruction probability of 17-inch (red points) and 17+20-inch (blue points) PMTs analysis. The miss reconstruction probability has been suppressed within ±0.2 %.

3.3.3 Energy Reconstruction

The energy is determined as a measurement of hit and charge information of PMTs in the detector as visible energy, which corresponds to the scintillation light emission. The relation between the visible energy and deposited energy is expressed as the non-linear combination due to the dark hit charge, the detection efficiency of single photo-electron, the quenching effect of the liquid scintillator, and Cherenkov light effect. These non-linear sources generate uncertainties of energy scale.

Visible Energy Calculation

The observed energy is calculated using the detected charge information. The charge of each PMT is calibrated to reduce the time variation of the detector status.

- Gain calibration (Section 3.2.2)
  The single photo-electron (p.e.) charge is defined by area of a 1 p.e. pulse in a waveform. Small change of each PMT gain is corrected within normal run using well-defined 1 p.e. charge distribution run by run.

- Bad channel selection (Section 3.2.3)
  The bad channels are defined as the channel which has too many hots, no hits or strange charge. These channels are masked and removed before the energy estimation.

- Software discriminator threshold
  In order to reduce the contribution of the accidental dark hit which caused by the PMT noise, the software discrimination is applied at a 0.3 p.e. threshold for each PMT charge.

- Dark hit subtraction
  To reconstruct energies correctly, it is important to evaluate the dark hit contribution, which is estimated from hits in 50 nsec of off-time window. Figure 3.25 shows the timing distribution of PMT hits after the correction of the time of flight (TOF, T_0). The time variation of the dark hit charge is as shown in Figure**??**. The contribution of the dark hit charge is normally $10 \sim 15$ p.e., and it is related to the temperature in the buffer oil. There are high dark hit periods when the purification campaign.

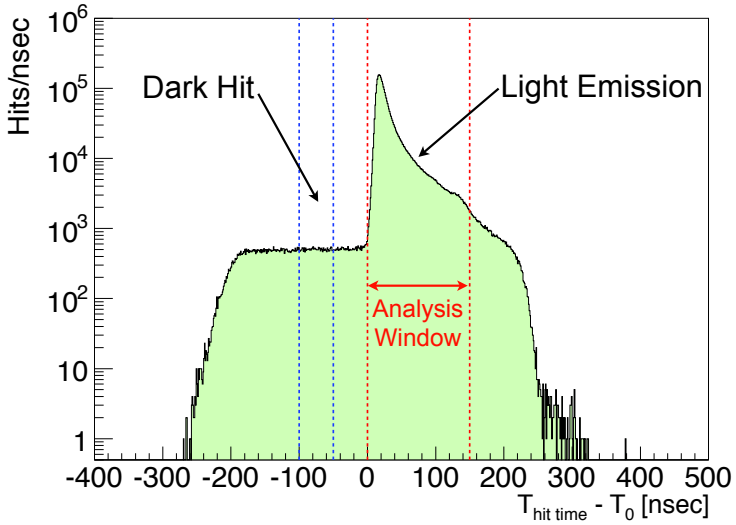

Figure 3.25: Timing distribution of PMTs hits after time of fright subtraction.

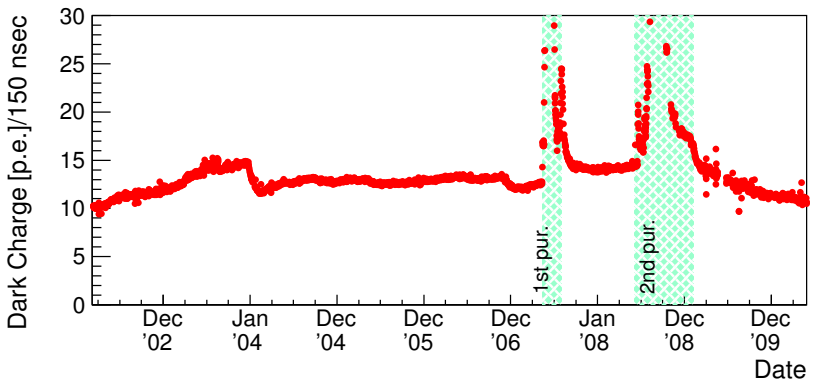

Figure 3.26: Time variation of dark charge.

Photon Yield Efficiency

- Shadow effect
  The charge of PMTs around the bottom and chimney regions are decreased due to the shadow effect by balloon and kevler ropes. This effect is corrected with the ^{60}Co source at the center of the detector. As shown is Figure 3.27, the small asymmetry of the polar angle distribution of charge is corrected after the shadow effect correction.

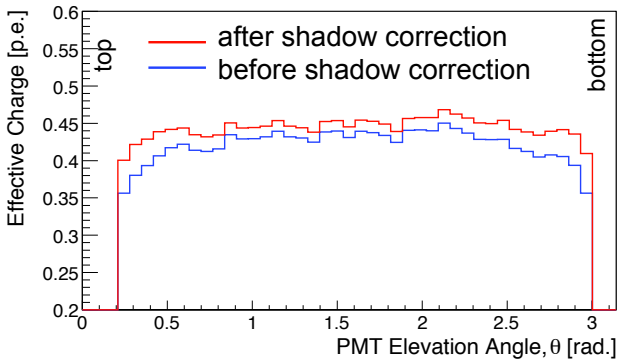

Figure 3.27: Correction of shadow effect from the balloon and kevlar ropes. After shadow correction, the small polar angle θ dependence is vanished.

- Attenuation length
  The attenuation length is one of the important parameter to estimate the light yield in the liquid scintillator. In KamLAND, the large fraction of scintillation light is absorbed by the liquid scintillator. These photon absorption excites the fluor and then it emits light again (re-emission light), which increases the light yield. Furthermore, the acrylic plate in the buffer oil reflects the scintillation or re-emission light and also change the effective attenuation length.

  Figure 3.28 shows the schematic view for the effective attenuation length estimation using the neutron spallation events. The photons are collected in the space perpendicular to the PMT surface in order to exclude the solid angle effect for the charge. The property of the liquid scintillator had an effect from the purification campaign, so the attenuation length is estimated at three separate terms. :

  - before 1st purification : Sep.16, 2006 - May. 12, 2007
  - before 1st purification : Sep.1, 2007 - Apr. 18, 2008
  - after 2nd purification : Mar.10, 2009 - May. 16, 2009

  Figure 3.29 shows the mean charge of neutron capture γ-rays including shadow effect as a function of the distance from PMT at the three periods. The attenuation length and the initial charge were decreased because of the purification campaign as summarized in this figure.

- Single photo-electron efficiency
  The inefficiency of 1 p.e. detection due to the 0.3 p.e. threshold causes the

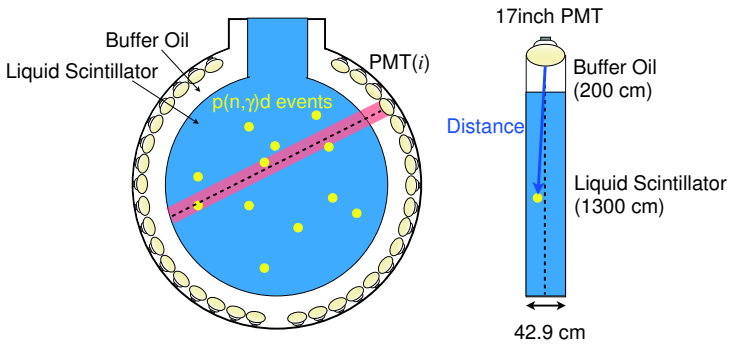

Figure 3.28: Schematic view for photon counting attenuation length estimation.

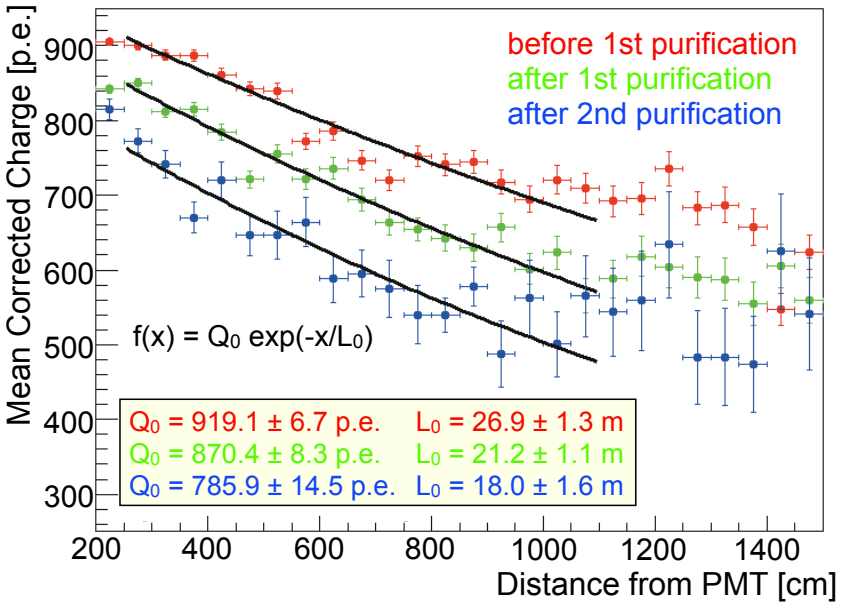

Figure 3.29: Effective attenuation length in the liquid scintillator using spallation neutron events. Red points, green points and blue points show before 1st purification, after 1st purification and after 2nd purification, respectively. The initial charge Q_0 and the attenuation length L_0 are obtained from exponential curve fitting.

non-linear bias for the visible energy. The mean number of photo-electrons μ in j-th PMT is calculated using the preliminary estimation of the expected charge for each PMT,

$$\mu \equiv \sum_i Q_i^{\text{observed}} \times \frac{Q_j^{\text{expected-no-threshold}}}{\sum_i Q_i^{\text{expected-no-threshold}}}. \tag{3.16}$$

Considering the 1 p,e, detection efficiency ε, probabilities of 0 p.e., 1 p.e. and

N p.e. (N $\geq$ 2) observation are written with Poisson statistics as follows,

$$\begin{aligned} P(0) &= e^{-\mu} + (1-\varepsilon)\mu e^{-mu} \\ &= e^{-\mu}[1 + (1-\varepsilon)\mu] \\ P(1) &= \varepsilon\mu e^{-\mu} \\ P(N) &= \frac{\mu^N}{N!}e^{-\mu}(N \geq 2). \end{aligned} \tag{3.17}$$

Then, the expected charge is calculated by adding up charges,

$$Q_i^{\text{expected}} = q(1) \cdot P(1) + \sum_{N\geq 2}[p(N) \cdot P(N)]. \tag{3.18}$$

Here, the normalization factor is omitted since it does not affect the energy non-linearity. If there is no threshold effect,

$$\sum_{N\geq 1}[q(N) \cdot P(N)] = \mu q_1 \equiv Q_i^{\text{expected}-\text{no}-\text{threshold}}, \tag{3.19}$$

where q_1 is the mean charge of 1 p.e. distribution without threshold effect. Then, considering that only 1 p.e. events are affected by the threshold effect, Eq. (3.20) is converted to

$$\begin{aligned} Q_i^{\text{expected}} &= \mu q_i - \mu e^{-\mu} q_1 + q(1)\varepsilon\mu e^{-\mu} \\ &= \mu q_1 \left[1 - e^{-\mu} + \frac{q(1)}{q_1}\varepsilon e^{-\mu}\right] \\ &= Q_i^{\text{expected}-\text{no}-\text{threshold}} \left[1 - e^{-\mu}(1 - \frac{q(1)}{q_1}\varepsilon)\right] \end{aligned} \tag{3.20}$$

Here, the $q(1)$ is determined from the following relation,

$$q_1 = q(1)\varepsilon + q_{loss}(1-\varepsilon), \tag{3.21}$$

where q_{loss} is the mean loss charge under threshold, which shold be less than 1/3 p.e.. From Eq. (3.20) and Eq. (3.21),

$$\begin{aligned} Q_i^{\text{expected}} &= Q_i^{\text{expected}-\text{no}-\text{threshold}}(1 - e^{-\mu\delta}) \\ \delta &\equiv \frac{q_{loss}}{q_1}(1-\varepsilon). \end{aligned} \tag{3.22}$$

The parameter δ is measured to be 0.03 using the calibration data. ^{60}Co (2 γ, 1.173 + 1.333 MeV) and ^{65}Zn (1 γ, 1.116 MeV) have similar γ-ray energy, so the effects of quenching and Cherenkov light work simiraly. Therefore, it is useful to separate the threshold effect, quenching, and Cherenkov light effects. These residual non-liniarity in energy determination can be caused by the single photoelectron threshold effect.

Combination of 20-inch PMTs

The signals from the 20-inch PMTs have been used from Feb. 2003. Since the 20-inch PMTs do not have high charge resolution, there are no 1 p.e. peak in the charge distribution. The charge dependence of the 20-inch PMT visible energy is also not the same as the 17-inch PMT. Therefore, the mean value of the visible energy from 20-inch PMTs (E_{20inch}) should be calibrated with that of 17-inch PMTs (E_{17inch}). They are combined to get better statistical accuracy as follows,

$$E_{visible} = (1-\alpha)\cdot E_{17inch} + \alpha \cdot E_{20inch}, \tag{3.23}$$

where α is the weighted factor giving the best energy resolution. This factor α is evaluated from the various calibration sources as shown in Figure 3.30, and it is optimized to 0.3. As shown in Figure , the deviation of the combined energy is compared with only 17-inch PMT energy, and its non-liniality is controlled within 0.6 %.

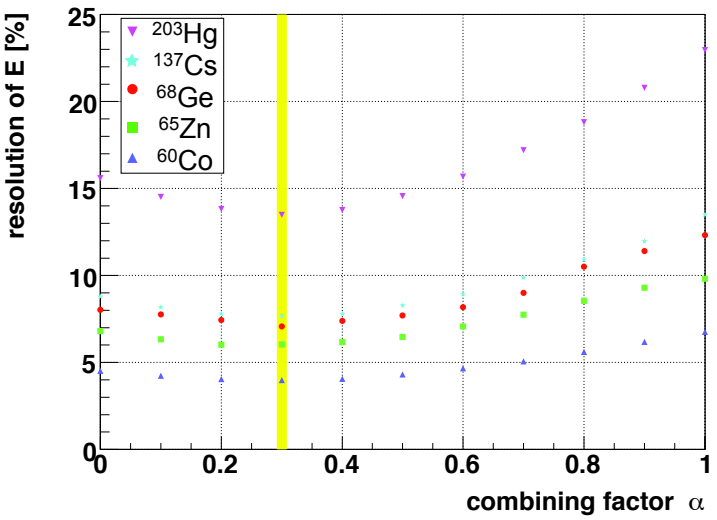

Figure 3.30: The combined energy resolution as a function of the combining factor, α The yellow line represents the best parameter, $\alpha = 0.3$.

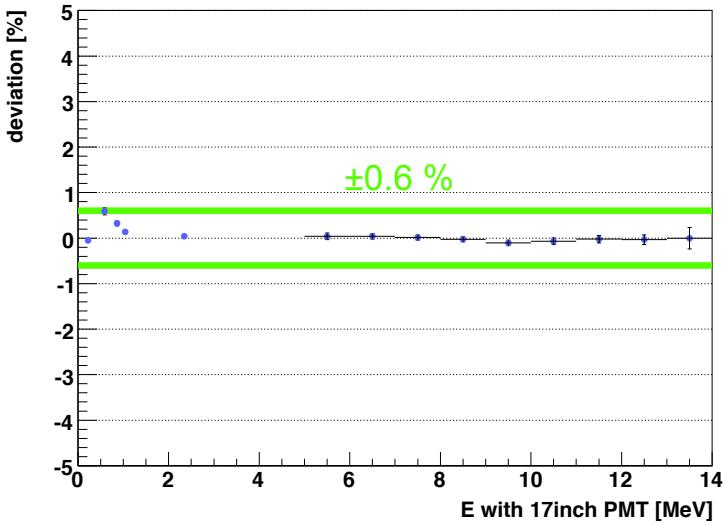

Figure 3.31: The combined energy linearity as a function of 17-inch PMT energy. The linearity of the combined energy is verified by the radioactive isotopes, ^{203}Hg, ^{137}Cs, ^{68}Ge, ^{65}Zn and ^{60}Co. The high energy region up to 14 MeV is confirmed by the spallation products such as ^{12}B. The uncertainty on the combined energy non-liniality is less than 0.6 %.

Algorithm of Energy Reconstruction

In KamLAND, the visible energy is reconstructed based of hit and charge information form PMTs. The hit-base estimation is used to reconstruct the lower energy events, below a few MeV, because it does not affected by the charge resolution and one photo threshold effect. On the other hand, the charge-base estimation has better resolution at higher energies, because the number of hits is saturated at the number of PMTs. Therefore, to achieve the high energy resolution extensively, the hit and charge information are combined on the energy reconstruction.

The energy estimator determines the visible energy using the maximum likelihood method. The maximum likelihood function consists of the probability density function of hit, charge and time distribution for each PMT as follows :

$$\begin{aligned} L &= \prod_{i}^{\text{no-hit}} P(\text{no}-\text{hit}|\mu_i) \prod_{i}^{\text{hit}} P(\text{hit}|\mu_i) P(q_i|\mu_i) \eta_i(t_i|\mu_i) \\ &= \prod_{i}^{\text{no-hit}} \kappa_{i,0}(\vec{R}_{\text{PMT}_i}, \vec{R}_{\text{source}}, E_{\text{vis}}) \prod_{i}^{\text{hit}} \left[\sum_{j=1}^{\infty} \kappa_{i,j}(\vec{R}_{\text{PMT}_i}, \vec{R}_{\text{source}}, E_{\text{vis}}) f_{i,j}(q_i) \right] \times \eta_i(t_i|\mu_i), \end{aligned} \tag{3.24}$$

where

$$\kappa_{i,j} = \begin{cases} \nu_i e^{-\mu_i} = [1 + (1-\varepsilon)\mu_i] e^{-\mu_i} & (j = 0, \text{ no-hit}) \\ \dfrac{\mu_i^j}{j!} e^{-\mu_i} & (j > 0, \text{ hit}) \end{cases} \tag{3.25}$$

$$\begin{aligned} \mu_i &= c E_{\text{vis}} \Omega_{\text{eff}_i}(\vec{R}_{\text{PMT}_i}, \vec{R}_{\text{source}}) + d_i \\ &\equiv b_i(\vec{R}_{\text{PMT}_i}, \vec{R}_{\text{source}}) E_{\text{vis}} + d_i. \end{aligned} \tag{3.26}$$

Here, i is the index for each PMT, μ_i is expected number of photons hitting i-th PMT including the corrections related to quantum efficiency of PMTs, shadowing effect coursed by balloon and ropes, and light attenuation effect. q_i is the observed charge in the i-th PMT. The probability density function of i-th PMT hit information, $P(\text{no}-\text{hit}|\mu_i)$ and $P(\text{hit}|\mu_i)$, is denoted by $\kappa_{i,j}$ provided by the Poisson distribution with μ_i as a parameter (Eq. (3.26)). j means actual number of photons. In calculating $P(\text{no}-\text{hit}|\mu_i)$, 1 p.e. threshold effect should be considered, and it is given as ν_i. In addition, ε is the detection efficiency of 1 p.e. threshold signal above the 0.3 p.e., which is estimated to be 0.964 determined from the 1 p.e. distribution. The expected number of photons μ_i is including some parameters as decried in Eq. (3.25). c is some constant proportionality coefficient between MeV of energy scale and dimensionless occupancy factor μ, Ω_{eff_i} is effective solid angle including quantum efficiency of PMT, attenuation and shadow effects, and d_i is probability of a dark hit of i-the PMT during 192 + 175 nsec time window, which corresponds to the waveform recording time and pre-window time before trigger. Moreover, $f_{i,j}(q_i)$ is charge probability density function for i-th PMT given the expected number of incident photons μ_i, and η_i means probability density function of hit time distribution for i-th PMT.

The probability density function of charge distribution is essentially derived from the calibration data and the expected number of photons for each PMT, μ_i is derived

Table 3.1: Superiority of each term in log-likelihood function at low and high energy.

term	low energy	high energy
no-hit	large, negative	small
hit	large, positive	small
charge	small	relatively large
time	significant correction	small

from the ratio of no-hits to hit. However, the calibration data can not cover whole photon range. Accordingly this charge probability density function $f_{i,j}$ is modeled by Poisson and Gaussian distribution as follows :

$$\begin{aligned}\sum_{j=1}^{\infty}\kappa_{i,j}\cdot f_{i,j} &= \sum_{j=1}^{\infty}\frac{\mu_i^j}{j!}e^{-\mu}\cdot\frac{1}{\sqrt{2\pi j\sigma^2}}e^{-\frac{(q_i-j)^2}{2j\sigma^2}} \\ &= \underbrace{(1-\nu_i e^{-\mu_i})}_{\text{hit term}}\underbrace{\sum_{j=1}^{\infty}\frac{1}{1-\nu_i e^{-\mu_i}}\frac{\mu_i^j}{j!}e^{-\mu_i}\frac{1}{\sqrt{2\pi j\sigma^2}}e^{-\frac{(q_i-j)^2}{2j\sigma^2}}}_{\text{charge term}} \\ &\equiv (1-\nu_i e^{-\mu_i})\cdot l_i\end{aligned} \tag{3.27}$$

where σ is the sigma of 1 p.e. distribution, which is evaluated to be 0.39 p.e.. This model well duplicates the source calibration data.

The log-likelihood method is used for finding the best reconstructed energy. The condition is :

$$\frac{\partial \log L}{\partial E} = 0. \tag{3.28}$$

The first derivative of log-likelihood function for each term can be calculated as follows :

$$\left.\frac{\partial \log L}{\partial E}\right|_{\text{no-hit}} = \sum_{i=1}^{\text{no-hit}} -\frac{b_i[\nu_i-(1-\varepsilon)]}{\nu_i} \tag{3.29}$$

$$\left.\frac{\partial \log L}{\partial E}\right|_{\text{hit}} = \sum_{i=1}^{\text{hit}} \frac{b_i[\nu_i-(1-\varepsilon)]}{\nu_i} \tag{3.30}$$

$$\left.\frac{\partial \log L}{\partial E}\right|_{\text{charge}} = \sum_{i=1}^{\text{hit}} b_i\cdot\frac{\partial}{\partial\mu_i}\log l_i \tag{3.31}$$

$$\left.\frac{\partial \log L}{\partial E}\right|_{\text{time}} = \sum_{i=1}^{\text{hit}} \frac{b_i d_i(\phi_i(t_i)\cdot\Delta T-1)}{(b_i\phi_i(t_i)\cdot\Delta T\cdot E_{\text{vis}}+d_i)\mu_i}, \tag{3.32}$$

where $\phi_i(t_i)$ is real pulse shape function for given vertex. The charge term can be only numerically calculated. In Table 3.1, the superiority of each term at low and high energy is summarized. Eq. (3.32) can work as a hit-based fitter at low energy, and charge-based fitter at high energy.

Energy Reconstruction Quality

The estimated visible energy is checked using calibration sources which have known energy of radioactive γ-ray and spallation products induced by cosmic ray muons. These checking sources are summarized in Table 3.2.

Table 3.2: Checking sources for visible energy reconstruction quality.

source	particle type	energy [MeV]
^{203}Hg	γ	0.2792
^{137}Cs	γ	0.6616
^{65}Zn	γ	1.1116
^{68}Ge	γ	0.511×2
^{60}Co	γ	1.1732, 1.3325
^{241}Am^{9}Be	γ, n	4.4, n$<$ 10
^{210}Po^{13}C	γ, n	6.13, n$<$ 7.5
np $\rightarrow$ dγ	γ	2.22457

- Source Calibration
  The source calibration are performed along the vertical axis periodically using various radioactive γ-ray sources. Figure 3.32 shows the energy distribution of each source at detector center before and after purification. These events are selected within 1.0 m from each source position. To estimate the energy deviation and energy resolution, the clear peaks on the energy distribution are fitted by Gauss function.

  The energy deviation and resolution are evaluated from that of each sources considering the uncertainty of position dependence and time variation.

  - Energy Deviation
    The z dependence of energy deviation for various sources are shown in Figure 3.33 (before purification, performed on September 2005) and Figure 3.34 (after purification, performed on July 2009), respectively. Figure 3.35 shows the time variation of energy deviation for each calibration source located at the center of detector. In this analysis, the time variation is less than 1.5 % for the data set.
  - Energy Resolution
    The z deviation of energy resolution for various sources are shown in Figure 3.36 (before purification, performed on September 2005) and Figure 3.37 (after purification, performed on July 2009), respectively. Figure 3.38 shows the time variation of energy resolution. The uncertainty of position dependence is slightly farther than that of time variation. In Figure 3.39, the energy resolution before and after purification are also shown. The estimated energy resolution for each periods are summarized in Table 3.3.

- Spallation Neutron Capture Events
  Gamma-ray generated by neutron capture interaction is also the calibration

Table 3.3: Energy resolution for each period. Since the light yield of liquid scintillator was decreased due to two times purification, the energy resolution after purification is worser than before.

Period	17-inch [% / $\sqrt{}$E[MeV]]	17+20-inch [% / $\sqrt{}$E[MeV]]
before purification	7.0 ± 0.1	6.1 ± 0.1
after purification	8.2 ± 0.1	7.0 ± 0.1

source which are uniformly distributed in the detector. It is useful to check the time variation and position dependence of reconstructed energy. Figure 3.40 shows the time variation of the spallation neutron capture events, and the deviation has been suppressed within 0.1 % for all of dataset. As shown in Figure 3.41 and 3.42, the radius and z dependence for before and after purification are estimated to be 0.3 % and 0.4 %, 0.7 % and 1.0 %, respectively. Therefore, the uncertainty for position dependence before and after purification are assigned as 0.7 % and 1.0 %.

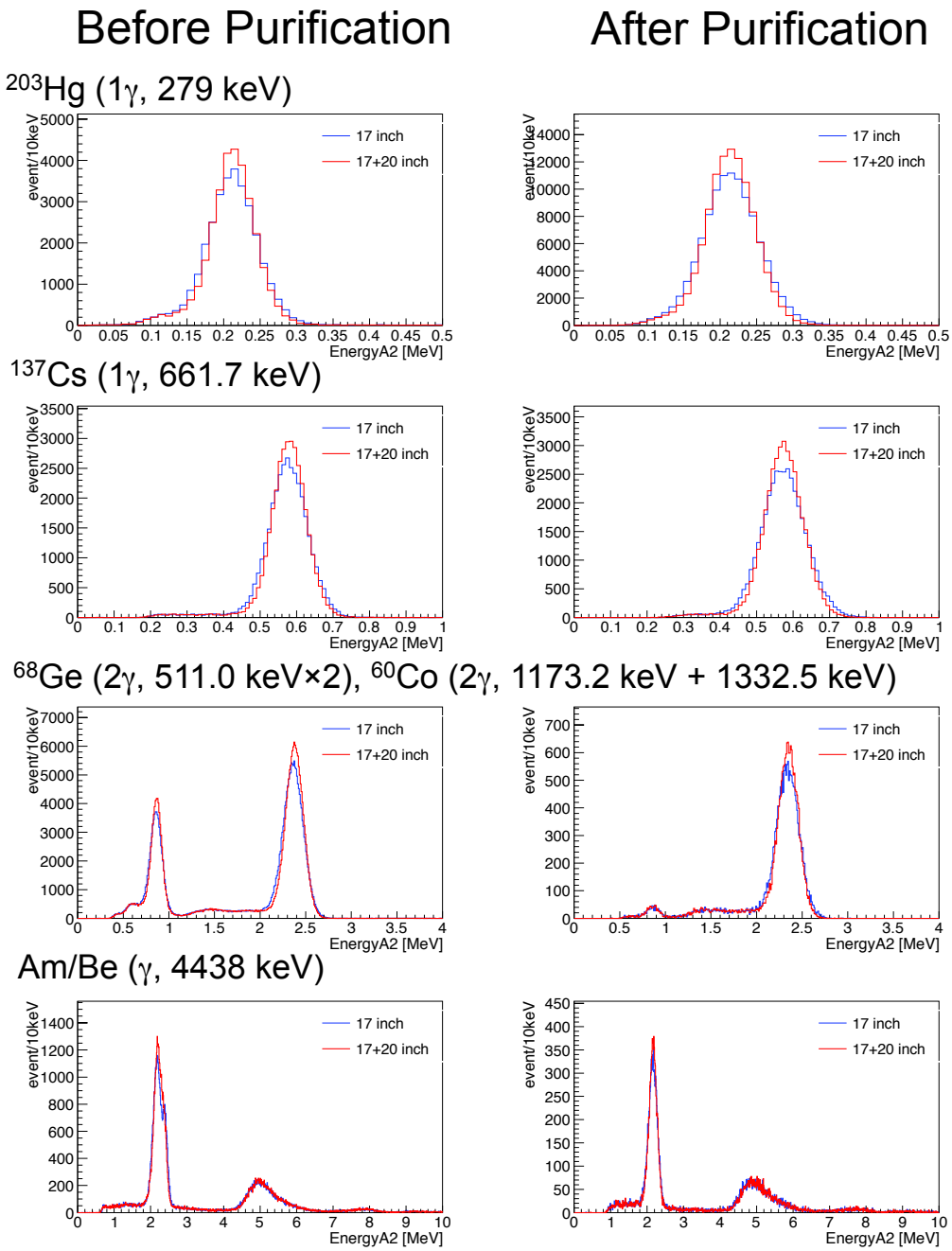

Figure 3.32: Visible energy for each source before (left) and after (light) purification. Blue line shows 17-inch PMT analysis and red line shows 17- and 20-inch PMT analysis. There are clear peaks on the energy distribution, and these are fitted to estimate energy deviation and energy resolution.

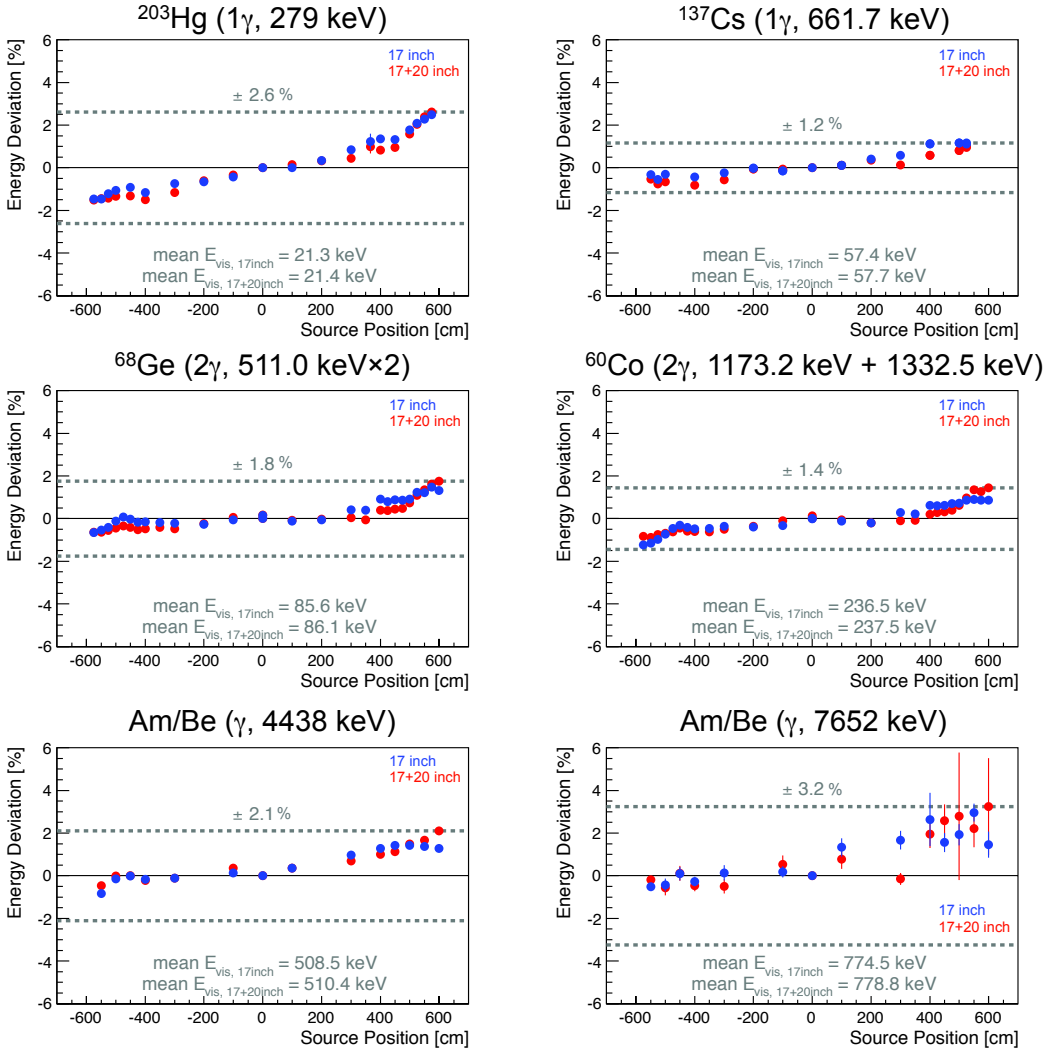

Figure 3.33: Z dependence of energy deviation for various sources. The calibrations were preformed on September 2005, before purification. Blue points show only 17-inch PMTs analysis results and red points show 17- and 20-inch PMTs analysis results.

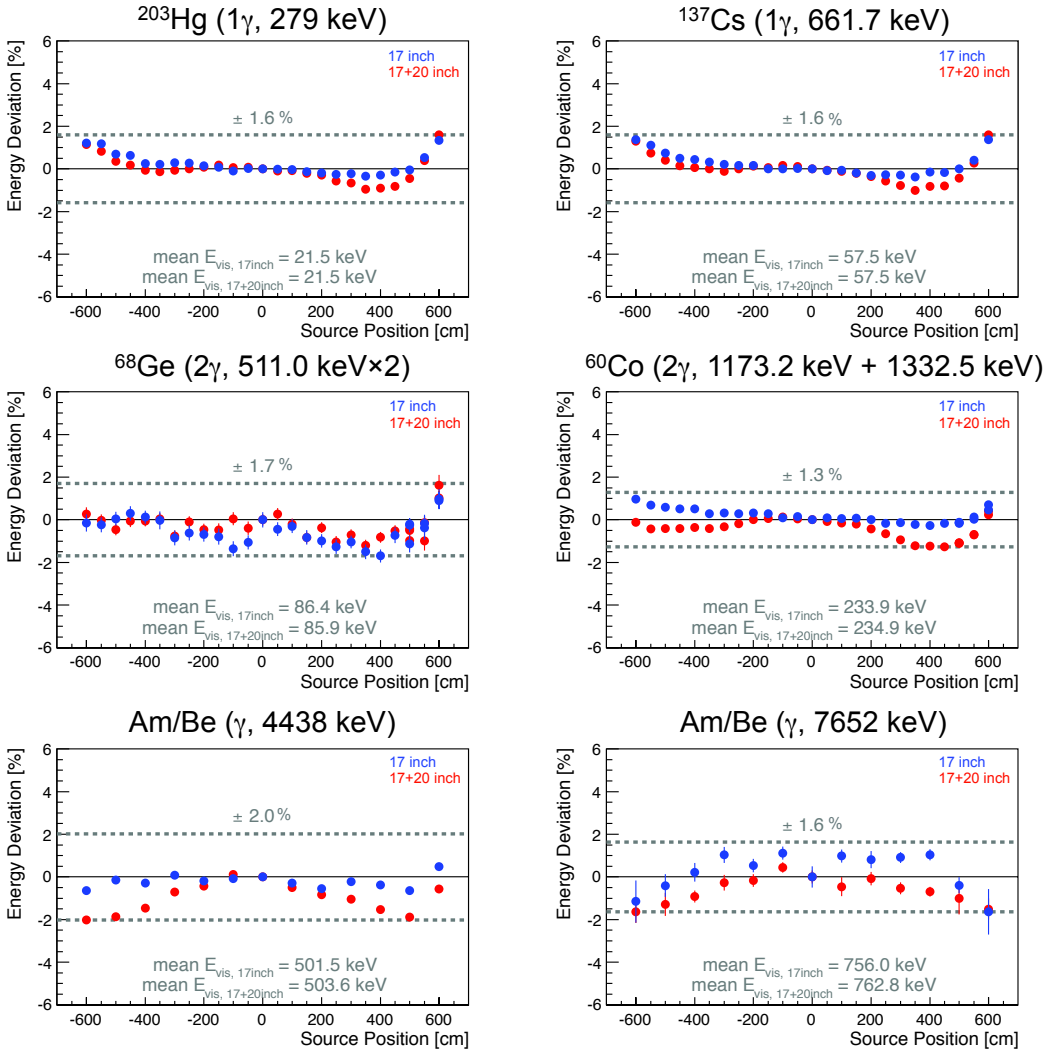

Figure 3.34: Z dependence of energy deviation for various sources after purification. The calibrations were preformed on July 2009, after purification. Blue points show only 17-inch PMTs analysis results and red points show 17- and 20-inch PMTs analysis results.

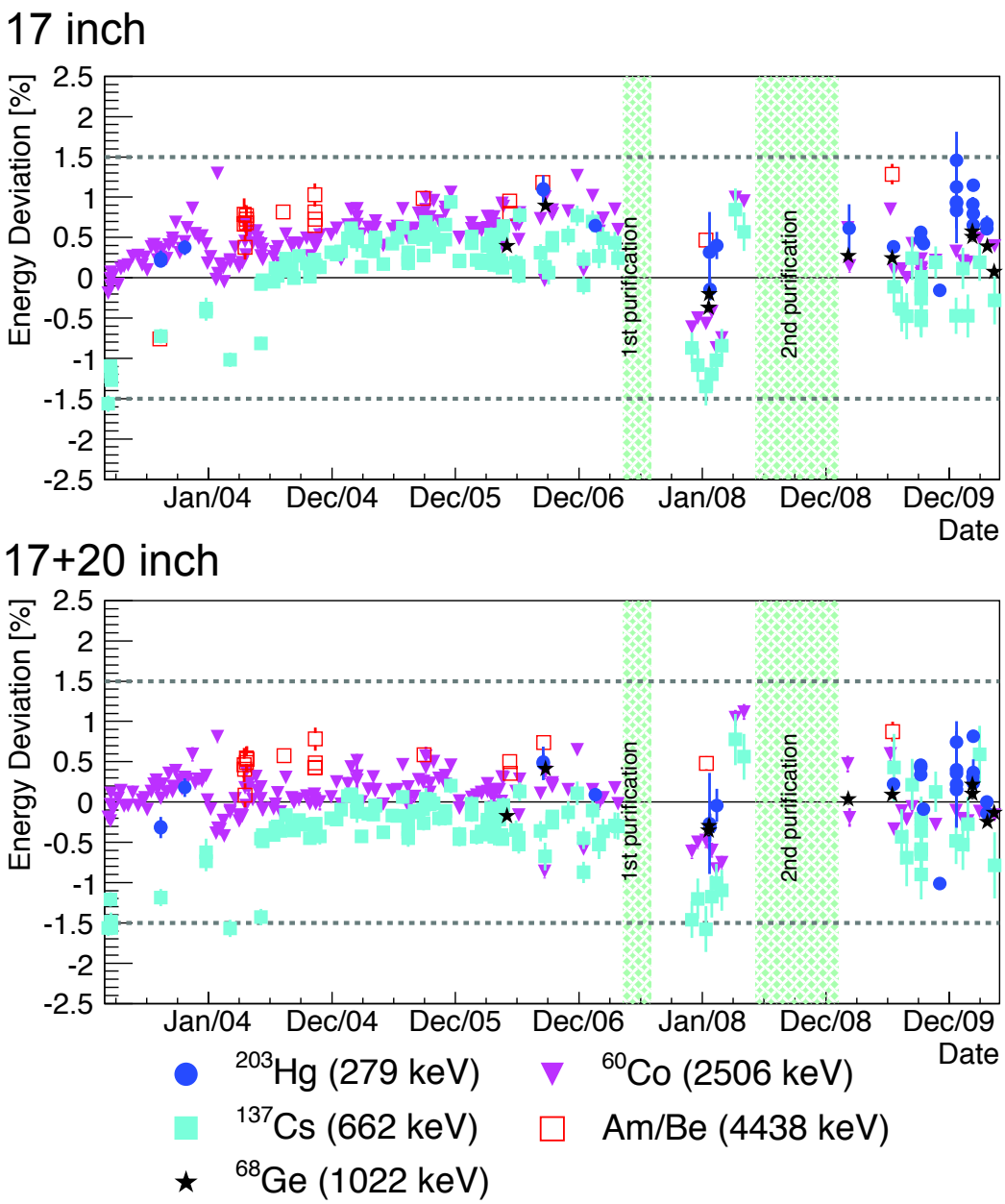

Figure 3.35: Time variation of energy deviation for each calibration source located at the center of detector. Top figure shows 17-inch PMTs analysis results and bottom figure shows 17- and 20-inch PMTs analysis results. Time variation is within 1.5 % for the all of data set.

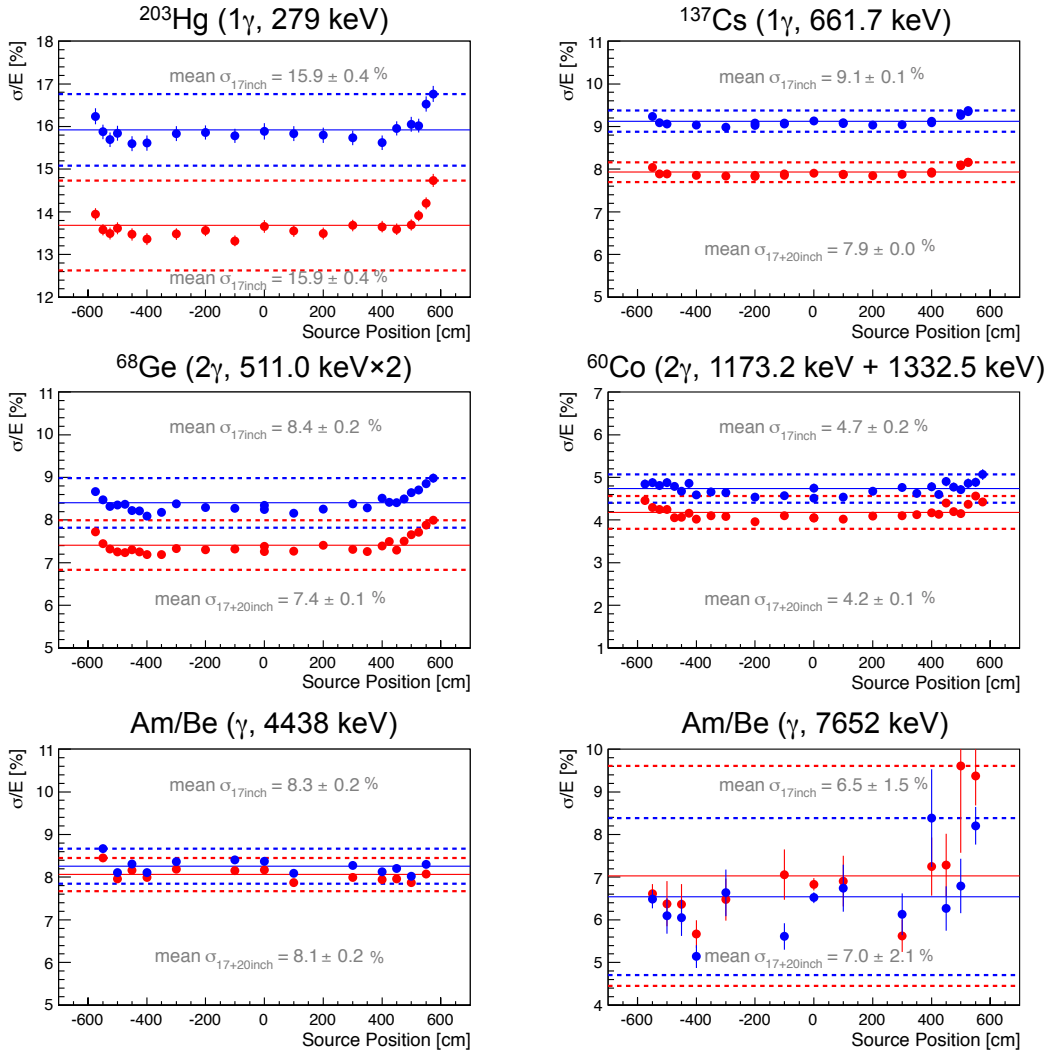

Figure 3.36: Z dependence of energy deviation for various sources. The calibrations were preformed on September 2005, before purification. Blue points show only 17-inch PMTs analysis results and red points show 17- and 20-inch PMTs analysis results.

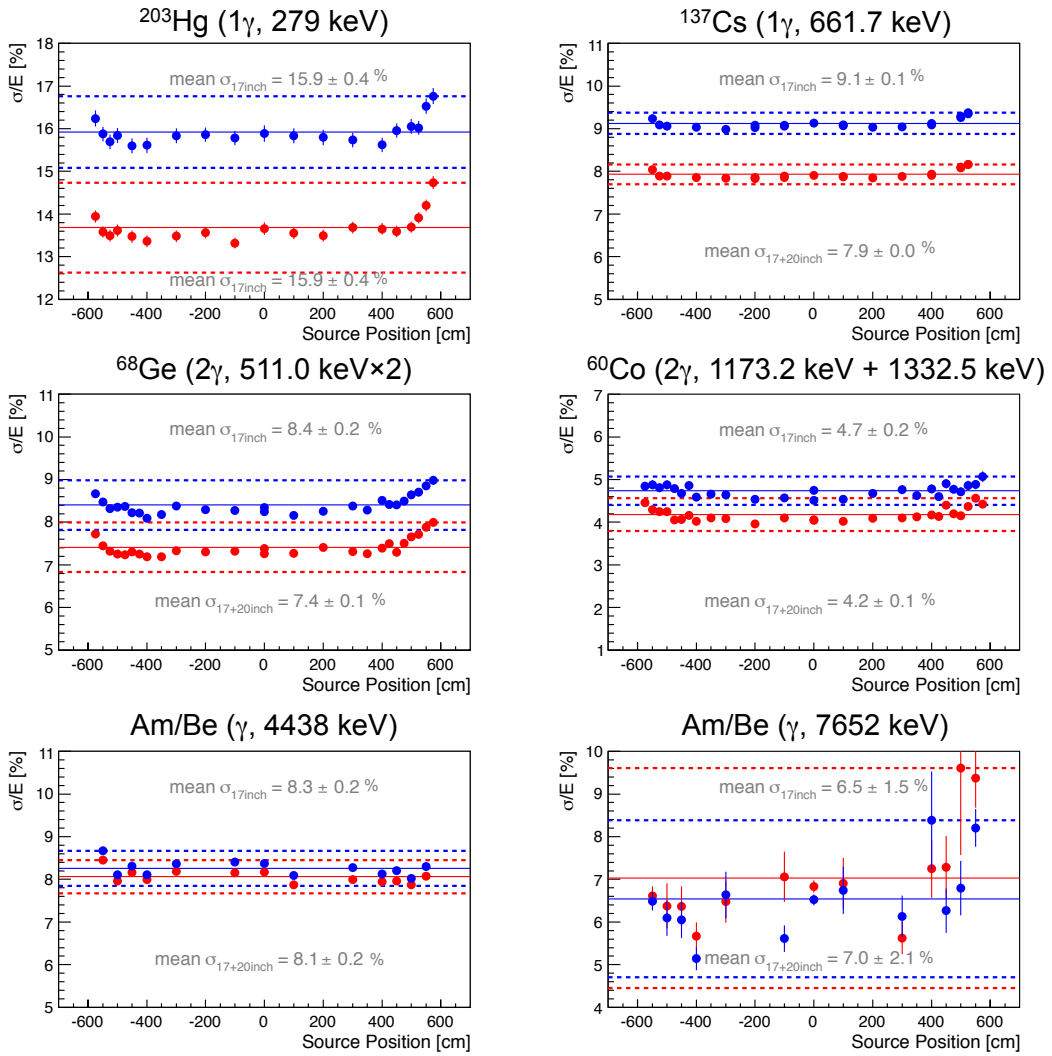

Figure 3.37: Z dependence of energy deviation for various sources after purification. The calibrations were preformed on July 2009, after purification. Blue points show only 17-inch PMTs analysis results and red points show 17- and 20-inch PMTs analysis results.

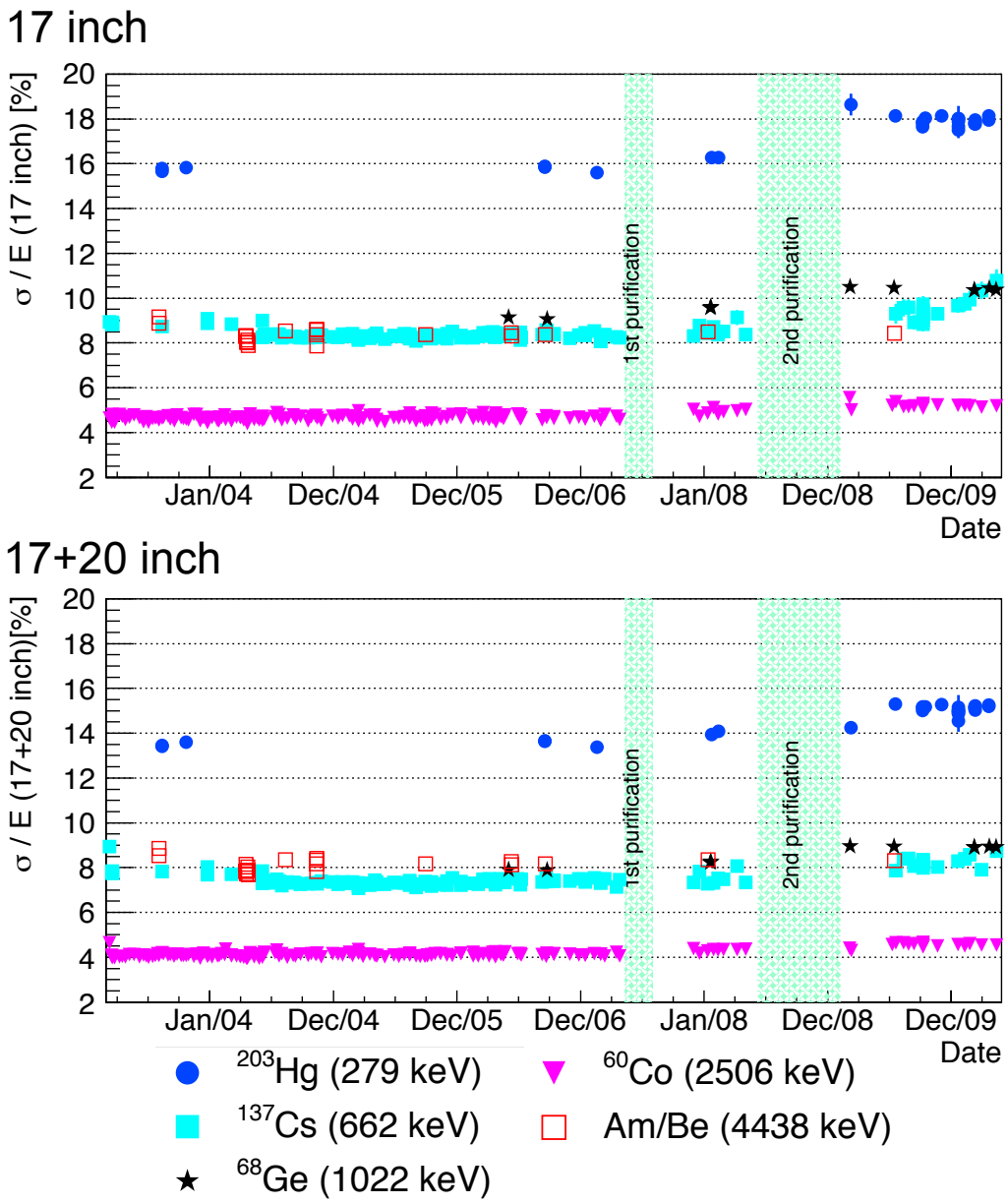

Figure 3.38: Time variation of energy resolution. Top figure shows 17-inch PMTs analysis results and bottom figure shows 17- and 20-inch PMTs analysis results. The energy resolution estimated by each sources have been stable from the start of data taking. There are small gaps around just after 2nd purification campaign due to the light yield decreasing.

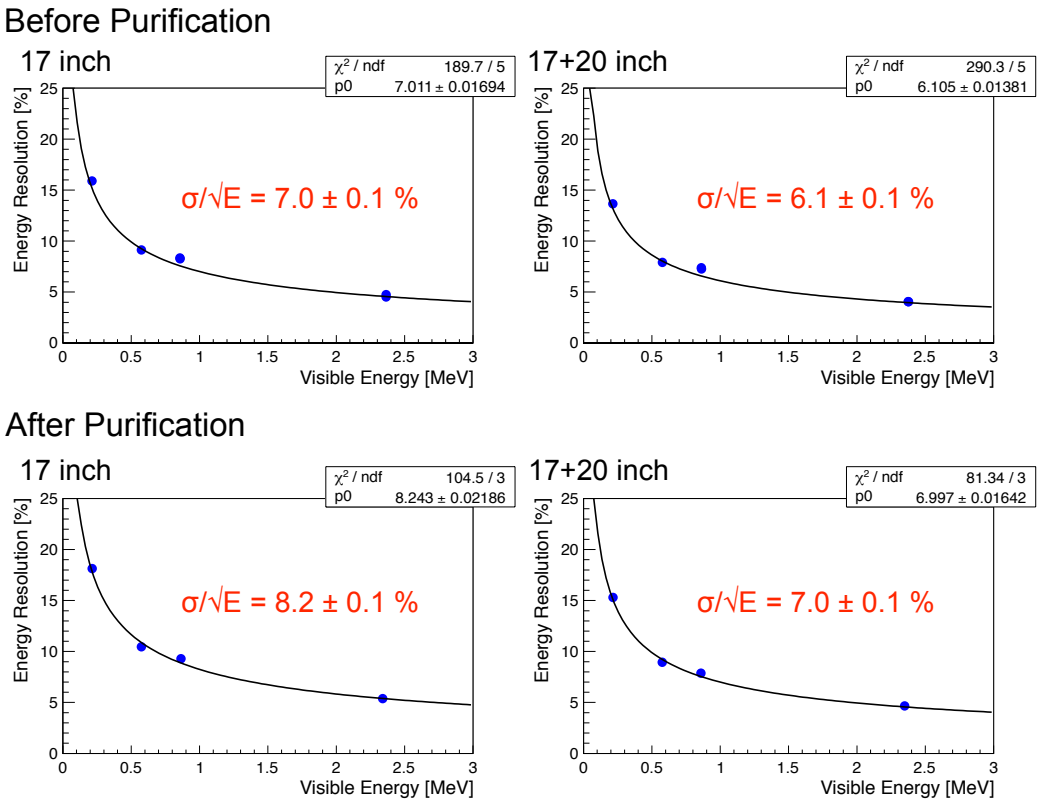

Figure 3.39: Energy dependent energy resolution for each calibration sources before (top) and after (bottom) purification. 17-inch (left) and 17- and 20-inch PMTs analysis are also shown.

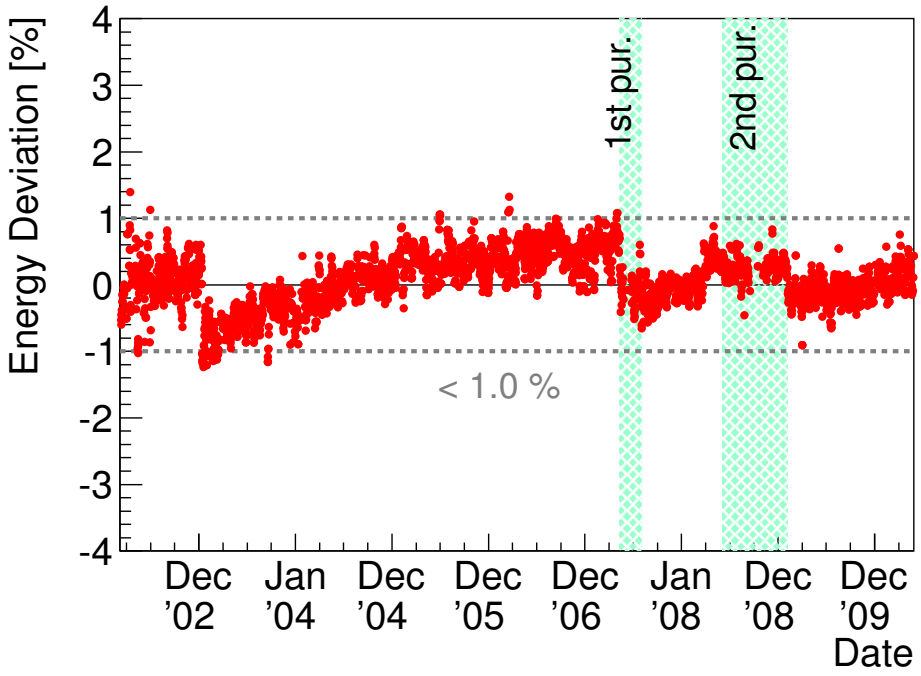

Figure 3.40: Time variation of γ-rays from spallation neutron capture on proton (real energy 2.22457 MeV). The vertical axis shows the deviation between the mean energy estimated by the energy spectrum fitting and the typical visible energy (2.211 MeV). The deviation has been suppressed within ± 1.0 % for all of dataset.

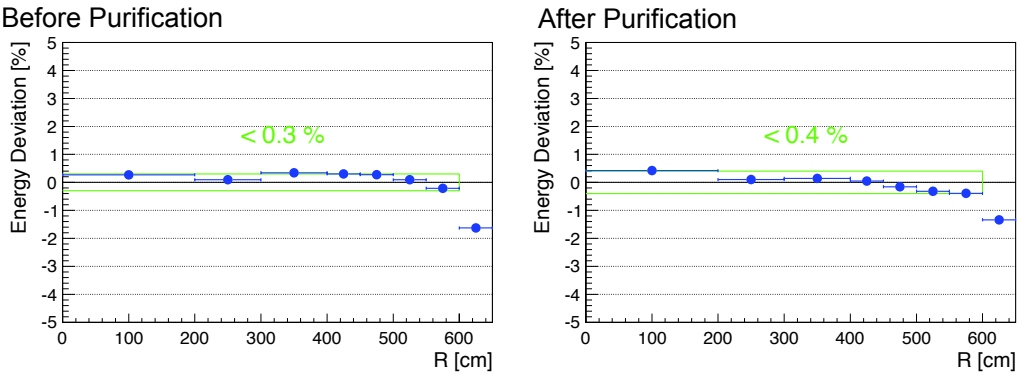

Figure 3.41: R dependence of γ-rays from spallation neutron capture on proton before (left) and after (right) purification. The events are selected with $\sqrt{X^2 + Y^2}$ > 200 cm. The deviation for before and after purification are estimated to be 0.3 % and 0.4 % in the 6.0 m fiducial radius, respectively.

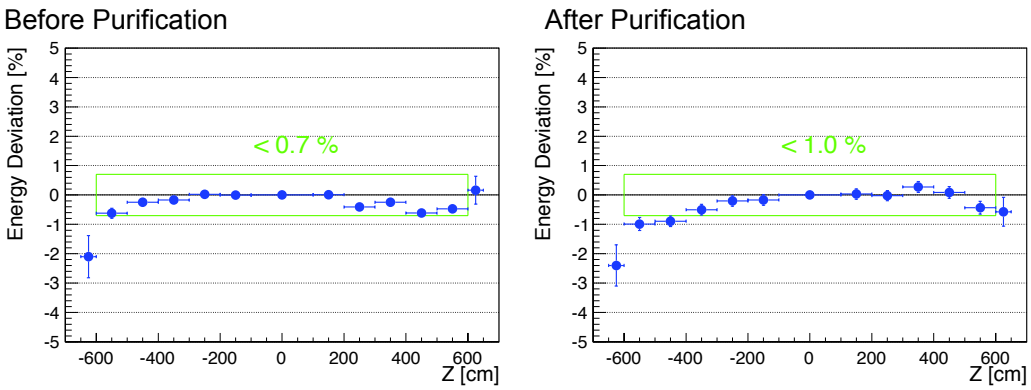

Figure 3.42: R dependence of γ-rays from spallation neutron capture on proton before (left) and after (right) purification. The events are selected with $\sqrt{X^2 + Y^2}$ < 200 cm. The deviation for before and after purification are estimated to be 0.7 % and 1.0 % in the 6.0 m fiducial radius, respectively.

3.4 Vertex and Energy Uncertainties Estimation Using Calibration Data

3.4.1 Fiducial Volume Uncertainty

Fiducial Volume Uncertainty Estimation

The fiducial volume for anti-neutrino analysis is sphere within a 6.0 m radius. For checking vertex and energy reconstruction quality and improving systematic error which comes from fiducial volume uncertainty, off-axis calibration were done in 2006 and 2007. From this off-axis calibration data within 5.5 m radius, the 6.0 m radius fiducial volume was established using 2.2 MeV γ from neutron capture and ^{12}B/^{12}N events generated by ID going muons which are distributed uniformly in the balloon. Furthermore, the fiducial volume uncertainty after purification is verified by extrapolating that for before purification.

The total volume of the liquid scintillator is 1171 $\pm$ 25 m^3 measured by flow meters during the liquid scintillator filling at the start of detector construction. The nominal fiducial volume within 6.0 m radius corresponds to 0.773 $\pm$ 0.016 of the total liquid scintillator volume. To estimate the fiducial volume uncertainty, this ratio is compared with the reconstructed number of neutron and ^{12}B/^{12}N events in the fiducial volume to that in the total volume.

- before purification
  The ^{12}B/^{12}N events counting gives the event ration as follows :

$$\frac{N_{5.5\mathrm{m}}}{N_{\mathrm{total}}}(\text{before purification}) = 0.768 \pm 0.002\ (\mathit{stat.}) \tag{3.33}$$

  On the other hand, the volume ratio ($V_{5.5\mathrm{m}}/V_{\mathrm{total}}$) is estimated to be 0.773 $\pm$ 0.016. The difference is calculated to be

$$\frac{N_{5.5\mathrm{m}}}{N_{\mathrm{total}}}(\text{before purification}) - \frac{V_{5.5\mathrm{m}}}{V_{\mathrm{total}}} = -0.3\% \pm 0.3\%(\mathit{stat.}). \tag{3.34}$$

  Then the systematic error is less the 0.6 % consider ion statistical uncertainly. From the analysis of the off-axis calibration, the fiducial volume biases are less than 3.0 cm, corresponding to 1.6 % precision for 5.5 m radius. Finally, 0.6 % systematic uncertainty by ^{12}B/^{12}N analysis and 1.6 % error from the off-axis analysis should be combined as follows :

$$\begin{aligned} &\text{fiducial volume error with 6.0 m radius (before purification)} \\ &= \sqrt{0.016^2 + 0.006^2} \\ &= 0.018 \end{aligned} \tag{3.35}$$

  1.8 % fiducial volume error is assigned at the anti-neutrino analysis within 6.0 m fiducial radius before purification.

- after purification
  Since there is no off-axis calibration data after purification, the difference between the ^{12}B/^{12}N event counting ratio in the 6.0 m radius before and after purification is useful.

1. count ^{12}B/^{12}N event in 6.0 m radius
   The ratio before and after purification are estimated as follows :

$$\frac{N_{6.0\mathrm{m}}}{N_{\mathrm{total}}}(\text{before purification}) = 0.794 \pm 0.002\ (stat.) \tag{3.36}$$

$$\frac{N_{6.0\mathrm{m}}}{N_{\mathrm{total}}}(\text{after purification}) = 0.795 \pm 0.003\ (stat.) \tag{3.37}$$

2. consider systematic uncertainties
   The systematic uncertainties related to purification should be considered when the difference between before and after purification is evaluated. The sources of the systematic uncertainties are
   - total liquid scintillator volume : < 1.4 %
     The total volume of liquid scintillator had been monitored during two times purification by flow mater. This uncertainty is suppressed mess than 1.4 %, corresponding to 16 m^3 amount of the liquid scintillator volume.
   - energy scale : 0.7 %
     The ^{12}B/^{12}N events are selected with the condition of the visible energy > 4.0 MeV. The energy scale difference between before and after purification may cause a bias for the event-counting.

   Totally, the systematic uncertainty related to purification is calculated as follows :

$$(syst.\ before\ after) = \sqrt{0.014^2 + 0.007^2} = 0.016\% \tag{3.38}$$

3. calculate the difference uncertainty including the systematic uncertainties

$$\begin{aligned}&\frac{N_{6.0\mathrm{m}}}{N_{\mathrm{total}}}(\text{after purification}) - \frac{N_{6.0\mathrm{m}}}{V_{\mathrm{total}}}(\text{before purification})\\ &= (0.795 - 0.794) \pm 0.002(stat.\ before) \pm 0.003(stat.\ after) \pm 0.013(syst.\ before\ after)\end{aligned} \tag{3.39}$$

   Then, the error is calculated as follows :

$$error = \sqrt{0.005^2(deviation) + 0.013^2(syst.\ before\ after)} \quad = 0.014 \tag{3.40}$$

   This error corresponds to 1.8 % (0.014 / 0.794) difference uncertainty. Here, the deviation is calculated conservatively as

$$(0.795 - 0.794) + \sqrt{0.002^2(stat.\ before) + 0.003(stat.\ after)} = 0.005. \tag{3.41}$$

4. calculate the fiducial volume uncertainty for after purification

   fiducial volume error with 6.0 m radius (after purification)

$$\begin{aligned}&= \sqrt{0.018^2(\text{before pur.}) + 0.018^2(\text{difference between before and after pur.})}\\ &= 0.025\end{aligned} \tag{3.42}$$

2.5 % fiducial volume error is assigned at the anti-neutrino analysis within 6.0 m fiducial radius after purification.

The fiducial volume uncertainty before and after purification are summarized in Table3.4.

Table 3.4: Fiducial volume uncertainty before and after purification.

Period	before purification	after purification
Uncertainty	1.8 %	2.5 %

Fiducial Volume Stability Check

Since $^{12}B/^{12}N$ events and 2.2 MeV γ from neutron capture are distributed uniformly in the detector, these are useful for checking the fiducial volume stability. Figure 3.43 shows R^3 distribution of 2.2 MeV neutron capture γ which are selected by the energy cut $1.8 < E < 2.6$ MeV and the off-timing background subtraction. The R^3 distribution of $^{12}B/^{12}N$ events is shown in Figure 3.44. It is made by the energy cut $E > 4.0$ MeV and the off-timing background subtraction. The counting $^{12}B/^{12}N$ event ratio is expected to be stable in the detector. Figure 3.45 shows the time variation of $^{12}B/^{12}N$ event ratio between all volume and 6.0 m radius region. These data points have been stable and kept around the expected ratio level calculated by actual measured volume.

The energy dependence of the fiducial volume uncertainty is investigated using $^{8}He/^{9}Li$ delayed coincidence events which prompt events are beta and the delayed events are 2.2 MeV γ-rays from neutron capture on proton. Figure 3.46 shows a vertex difference between the prompt and delayed events for each data-set. The bias around fiducial volume, 6.0 m radius is within $\pm$3.0 cm, which correspond to 1.5 % volume error at 6.0 m fiducial radius. This uncertainty is already included in the fiducial volume uncertainty estimation before purification.

Figure 3.47 shows the analysis for the balloon edge estimation to verify the vertex reconstruction stability. The R distributions are made by the energy cut (^{40}K : $1.2 < E < 1.6$ MeV, ^{208}Tl : $2.4 < E < 3.0$ MeV) for each $\cos\theta$, and then the balloon edge is estimated from fitting results. The time variation of the fitted balloon edge is less than 1.0 cm which corresponds to 0.5 %, and its contribution to the fiducial volume uncertainty can be negligible. Figure represents the stability of balloon edge.

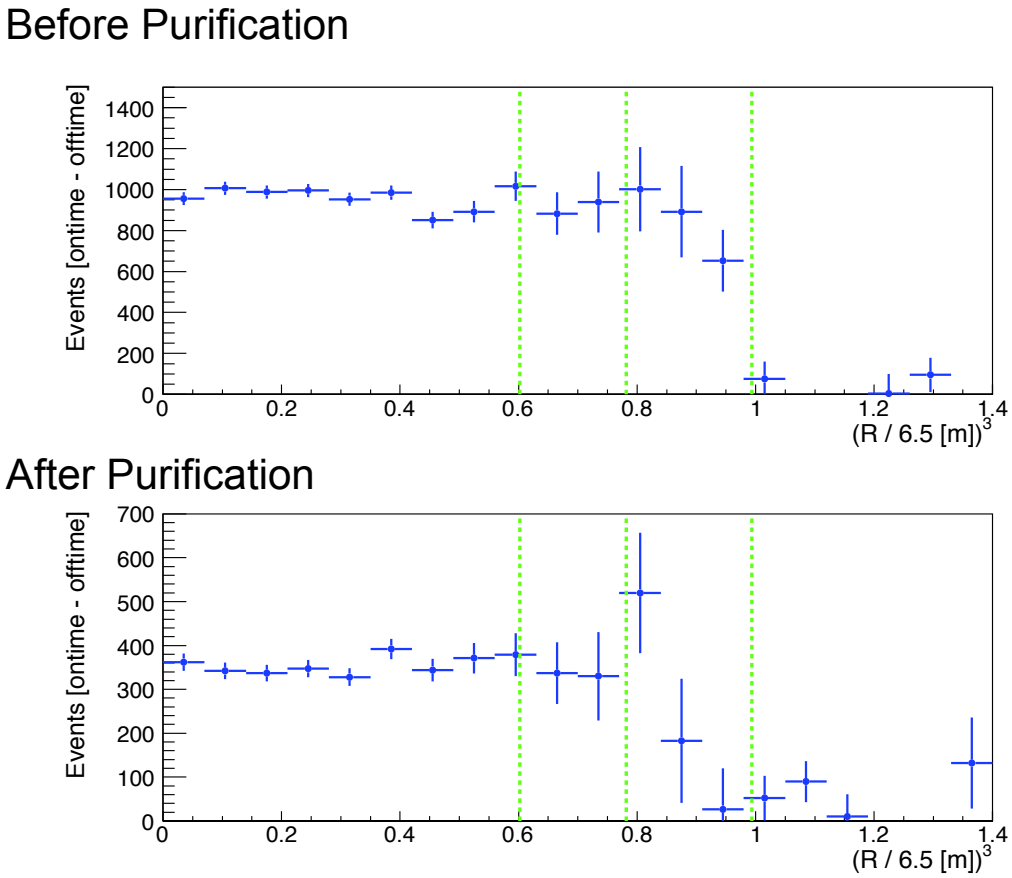

Figure 3.43: R^3 distribution of spallation neutrons before (top) and after (bottom) purification. 2.2 MeV γ-rays by neutron capture on proton are selected. Green lines shows 5.5 m radius, 6.0 m radius and the balloon edge of 6.5 m radius, respectively. The events are selected by $1.8 < E < 2.6$ MeV and off-timing background subtraction.

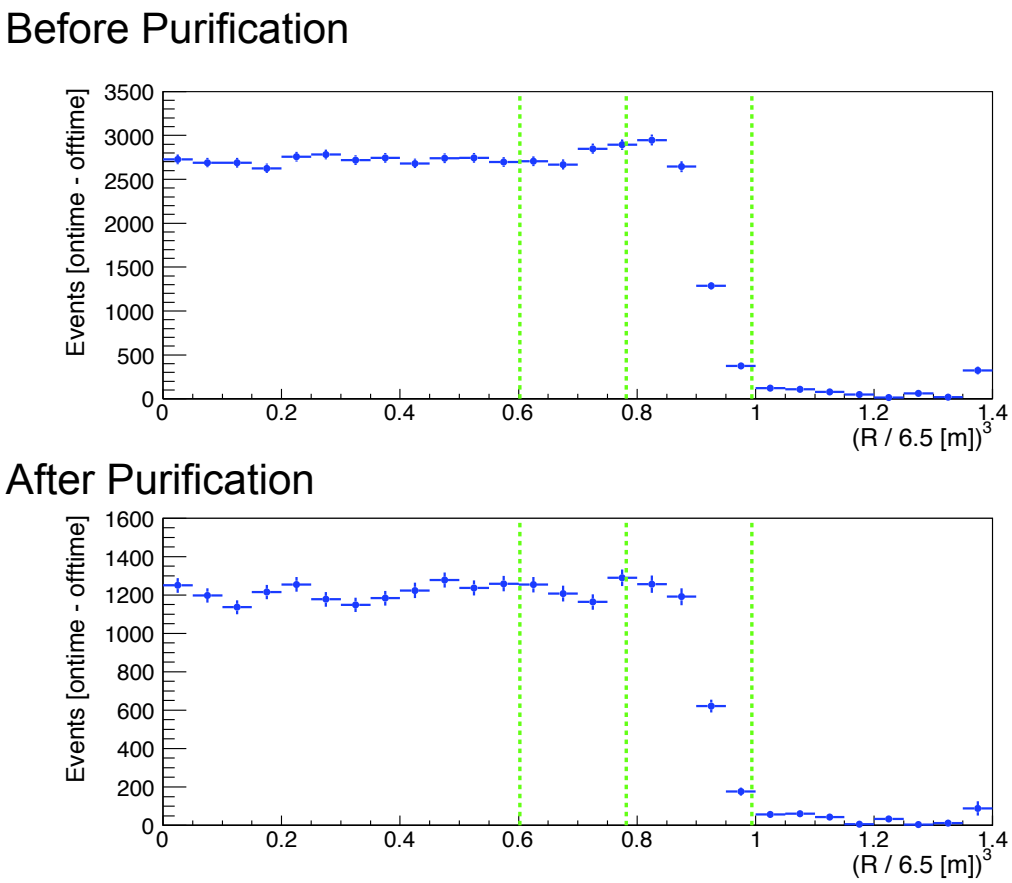

Figure 3.44: R^3 distribution of ^{12}B events before (top) and after (bottom) purification. Green lines show 5.5 m radius, 6.0 m radius and the balloon edge of 6.5 m radius, respectively. The events are selected by E > 4.0 MeV and off-timing background subtraction.

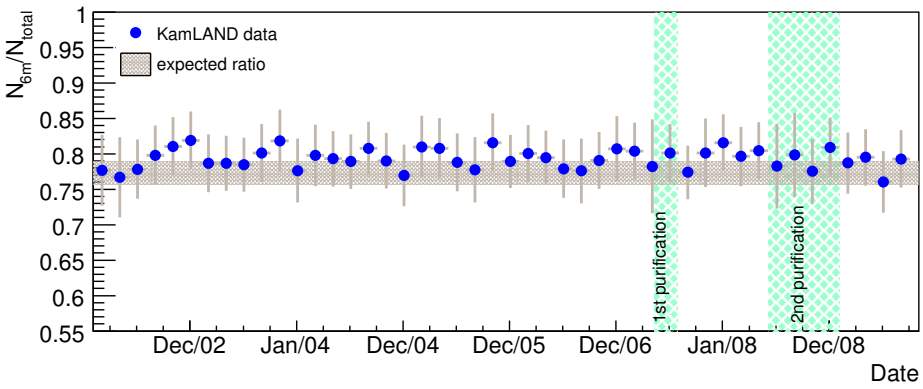

Figure 3.45: $^{12}B/^{12}N$ event ratio time variation for checking the fiducial volume uncertainty. Gray shaded area shows the expected ratio which calculated by measured liquid scintillator volume, 0.773 ± 0.016. The ratio has been stable from the start of data taking, and kept around the expected level.

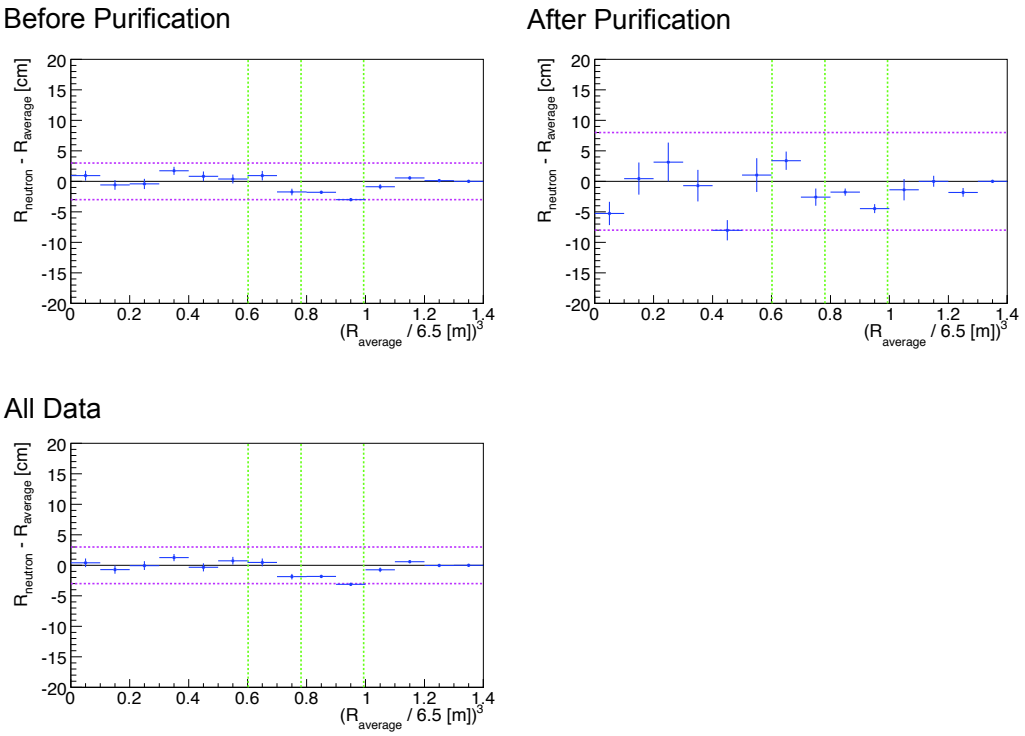

Figure 3.46: Energy dependence vertex bias using ^{8}He/^{9}Li delayed coincidence events before purification (left), after purification (middle) and all period (right). Green line shows 5.5 m, 6.0 m and 6.6 m radius, respectively. The vertical axis shows $R_{neutron}$ - $R_{average}$, which $R_{average}$ is the mean of prompt and delayed events. The magenta lines show ±3.0 cm (before purification and all data) and ±8.0 cm (after purification). In after purification analysis, the uncertainty is slightly larger than others, and the vertex bias around fiducial volume 6.0 m is within ±3.0 cm. They correspond to 1.5 % volume error at 6.0 m fiducial radios.

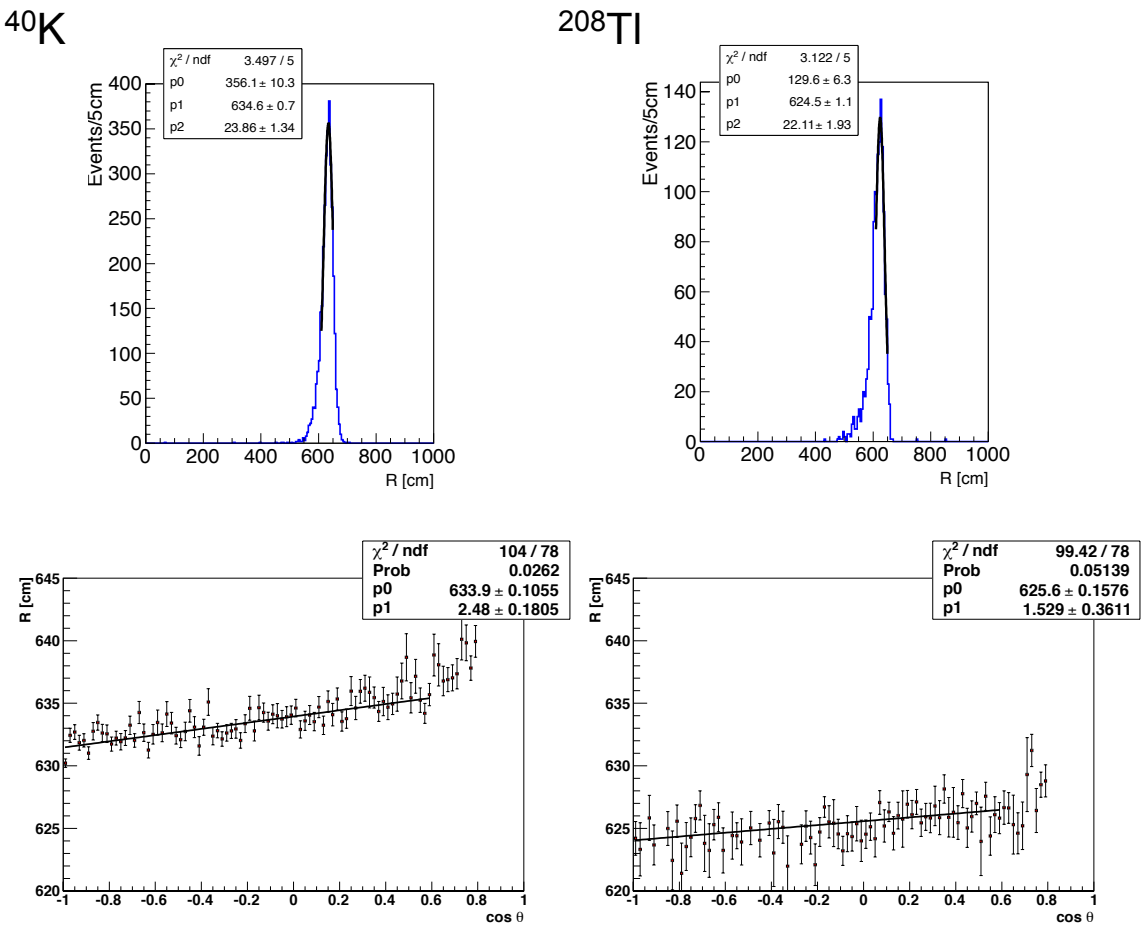

Figure 3.47: Balloon edge estimation using various radioactivities, ^{40}K (left) and ^{208}Tl (right). Top figures show the R distribution selected $0 < \cos\theta < 0.01$. Bottom figures show balloon edge distribution as a function of $\cos\theta$ which are estimated by fitting the R distribution.

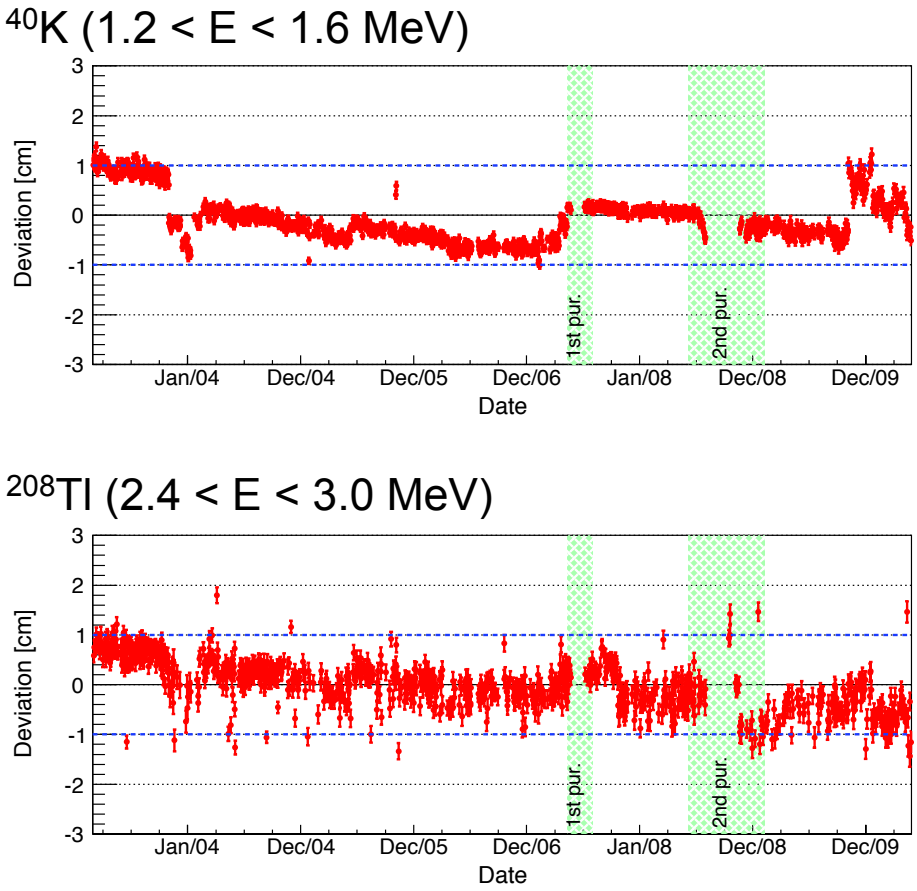

Figure 3.48: Time variation of balloon edge deviation for ^{40}K (top) and ^{208}Tl (bottom) event. These deviation are kept within ± 1.0 cm stably as shown in blue lines. It corresponds to 0.5 % for the fiducial volume, and can be negligible.

3.4.2 Uncertainties of Energy Scale

The events in the detector are reconstructed using PMT information, and calibrated by source calibration data. About the visible energy, it has still deviations caused by some factors. The sources of this uncertainty of the energy scale are as follows :

- Position dependence
  The uncertainty from the position dependence is estimated with the neutron capture γ and various source calibrations as shown p.70 $\sim$. As shown in Figure 3.41 and 3.42, The radius and z dependence from the neutron capture γ for before and after purification are 0.3 % and 0.4 %, 0.7 % and 1.0 %. Therefore, 0.7 % (before purification) and 1.0 % (after purification) systematic uncertainties are assigned.

- Time variation
  The time variation uncertainty of source calibration is 1.5 % (Figure 3.35), and that of spallation neutron γ is 1.0 % (Figure 3.40), respectively. Therefore, 1.5 % systematic uncertainty is assigned.

- Non-linearlty for the 20-inch PMTs
  As shown in Figure 3.31, the uncertainty come from the linearity between the combined energy (17+20-inch PMTs) and the energy with only 17-inch PMTs is assigned to 0.6 %.

- Contribution of Cherenkov light
  In the liquid scintillator, the Cherenkov photons are emitted from the charged particle in addition to scintillation light. The number of Cherenkov photons depends on its energy. The direct contribution of Cherenkov light can be ignored because the dominant wavelength is below the absorption waveform of the liquid scintillator. However, the liquid scintillator reemits absorbed Cherenkov photons. These reemission photons contribution to the reconstructed energy should be considered, and it rise to the energy non-linearity, and tuned by altering the contribution of the questing effect.

- Quenching effect
  The number of scintillation photons is proportional to the deposited energy in the first order, but there is an non-negligible dependence on the ionization density called "quenching effect", causing the energy non-linearity for each particle. In the heavy particle such as α-particle, the quenching effect becomes very large because of its high ionization density. In order to estimate the contribution of the quenching effect, the most popular way is using Birk's formula [25],
  $$\frac{dL}{dx} = L_0 \frac{dE/dx}{1 + k_B(dE/dx)}, \tag{3.43}$$
  where k_B is Birk's constant, L is the luminescence, L_0 is the luminescence at low specific ionization density and dL/dx is the emitted light intensity per unit length.

- Dark hit subtraction
  As shown in Figure 3.25, the mean dark charge is calculated for each PMT run

by run. The uncertainty from the dark hit subtraction gets more significant as lower energy.

Summary of Energy Non-Liniality

The contribution from quenching effect, Cherenkov light and the dark hit subtraction effect are determined using the following sources :

- 6+2 γ-ray sources
  - 6 source calibration sources : ^{203}Hg, ^{137}Cs, ^{68}Ge, ^{60}Co
  - spallation neutron capture on proton and ^{12}C
- 2 positron sources : ^{11}C, ^{10}C
- 1 electron source : ^{12}B

In the case of multiple γs, such as the two γs of ^{68}Ge (0.511 MeV $\times$ 2) and γs of ^{60}Co (1.173 + 1.333 MeV) are treated as mean of them (0.511 MeV and 1.253 MeV, respectively), because the quenching effect depends on the energy of each γ-rays, not total energy of them. In the γ-ray case, MC simulation using GEANT4[24] is employed to calculate dE/dx of electrons produced in Compton scattering and photoelectron absorption. The non-linearity of energy scale is corrected using the following equation with four parameters, such as k_B, $C_{\rm sic}$, $C_{\rm che}$ and $E_{\rm dark}$. These parameters are determined by the χ^2 minimization.

$$E_{\rm vis} = C_{\rm che}E_{\rm che}(k_B) + C_{\rm sci}E_{\rm sci}(k_B) + E_{\rm dark}/n_\gamma, \tag{3.44}$$

where k_B is Birk's constant, $C_{\rm sic}$ is the scintillation intensity, $C_{\rm che}$ is the Cherenkov intensity, and $E_{\rm dark}$ is energy of dark charge. The constant parameter, n_γ, is the number of γ-rays of each sources.

Part II

Low Energy Anti-Neutrino

Chapter 4

Low Energy Anti-neutrino Sources

KamLAND was designed to detect electron anti-neutrinos, especially which come from distant reactors. Furthermore, the experiment presented the first experimental study of geo-neutrinos in 2005. In this chapter, this two important anti-neutrino sources which have a few MeV energy are presented: nuclear reactors emitting $\bar{\nu}_e$ from β-decays following nuclear fission, and radioactive decays inside the Earth emitting $\bar{\nu}_e$ from some β-decays in the ^{238}U and ^{232}Th decay chains.

Figure 4.1 shows expected energy spectrums of reactor $\bar{\nu}_e$ and geo $\bar{\nu}_e$, and summarizes the relationship between them. The reactor $\bar{\nu}_e$ measurement has many statistics, and its fluxes are calculated precisely based on detailed operational data provided for all Japanese commercial reactors. On the other hand, the most serious background for geo $\bar{\nu}_e$ measurement is reactor $\bar{\nu}_e$.

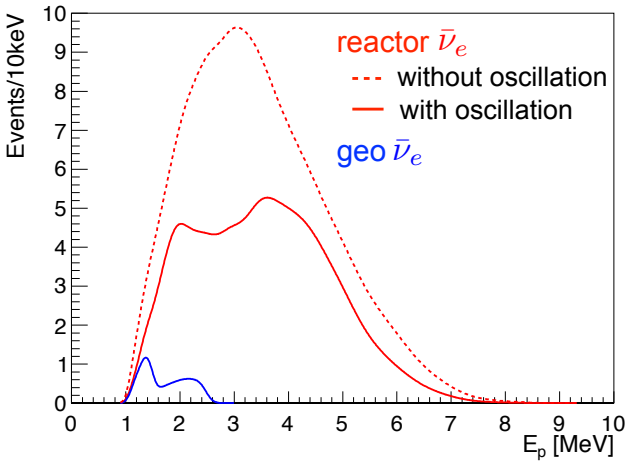

Figure 4.1: Expected energy spectrums of reactor $\bar{\nu}_e$ (red) and geo $\bar{\nu}_e$ (blue).

4.1 Anti-Neutrinos from Reactors

4.1.1 Anti-Neutrino Flux from Reactors

The anti-neutrino flux at KamLAND is dominated by 56 Japanese nuclear power reactors. The flux-weighted average baseline to these reactors is ∼180 km. In Figure 4.2 and Figure 4.3, the distribution of reactors are shown in Japan and in the world [26] [27]. The information of these reactors are listed in Table 4.1 and Table 4.2. The position of Japanese reactors were precisely obtained from Tokyo Electric Power Company (TEPCO). The uncertainty of the distance was studied based on the comparison with coordinated of the reactors taken from an ordinary topographical map, and discrepancies were found to be within 70 m. The difference of the number of expected reactor $\bar{\nu}_e$ caused by this discrepancies is less than 0.1 %.

Reactors are classified by type of neutron moderator. Commonly used neutron moderators include water (light water, 75 % of world's reactors), solid graphite (20 %) and heavy water (5 %). Additionally, the light water reactors are mostly crucified into Boiling Water Reactor (BWR) and Pressurized Water Reactor (PWR). In the case of the light water reactors, the reactor core consists of fuel rods containing enriched ^{235}U and control rods, and is filled with water. In the reactor core, Uranium is depleted and Plutonium is bred according to time evolution. This effect is called as "burn-up effect". The total fission rate of each isotope in the reactor core can be calculated from the thermal power and the burn-up data of the each reactor, provided for all Japanese commercial reactors by a consortium of Japanese electric power companies. By using a simple and practical modeling of the reactor core for calculating the fuel composition, developed by TEPCO, the fission date for each isotope at each reactor in Japan is calculated [28]. The uncertainty for $\bar{\nu}_e$ flux is estimated to be 1.0 % compared with detailed simulation by TEPCO. The absolute thermal power, used to normalize the fission rates, is measured to within 2 % for each reactor. This uncertainty is determined by uncertainty of feed-water flowmeters, which are calibrated within 2 %, and conservatively assumed to be correlated across all reactors, though some potentially uncorrelated components have been put forward in **??**.

The data points are typically provided at weekly frequency during regular operations when the relative instability is of the order of 10^{-3}. When the operating parameters vary more quickly, the data are provided at higher frequency, with a period between 10 min and 1 h. Figure 4.4 shows the time variation of $\bar{\nu}_e$ flux from reactors in Japan and Korea for this analysis data set. In July 2007, Kashiwazaki-Kariwa nuclear station, which has largest thermal power in Japan, was stopped due to an earthquake. Because of this power reduction, not under control of the experiment, Shika nuclear station contribution got larger than before. The detailed reactor operation data are also used for accurate tracking of the flux-weighted average reactor baseline and spectrum shape change over the course of the experiment. The relative fission yields, averaged over the entire live time period, for isotopes (^{235}U : ^{238}U : ^{239}Pu : ^{241}Pu) are (0.571 : 0.078 : 0.295 : 0.056), respectively.

The contribution of Korean reactors, based on reported electric power generation, is estimated to be (3.4 ± 0.32) %. This 0.32 % uncertainty comes from the 10 % contribution, which is the conversion uncertainty from electric power to thermal power. The contribution form Japanese research reacts and the remainder of the

global nuclear power industry, estimated using reactor specifications from the International Nuclear Safety Center [27], is (0.96 ± 0.48) %. Its uncertainty is assigned as a half of it.

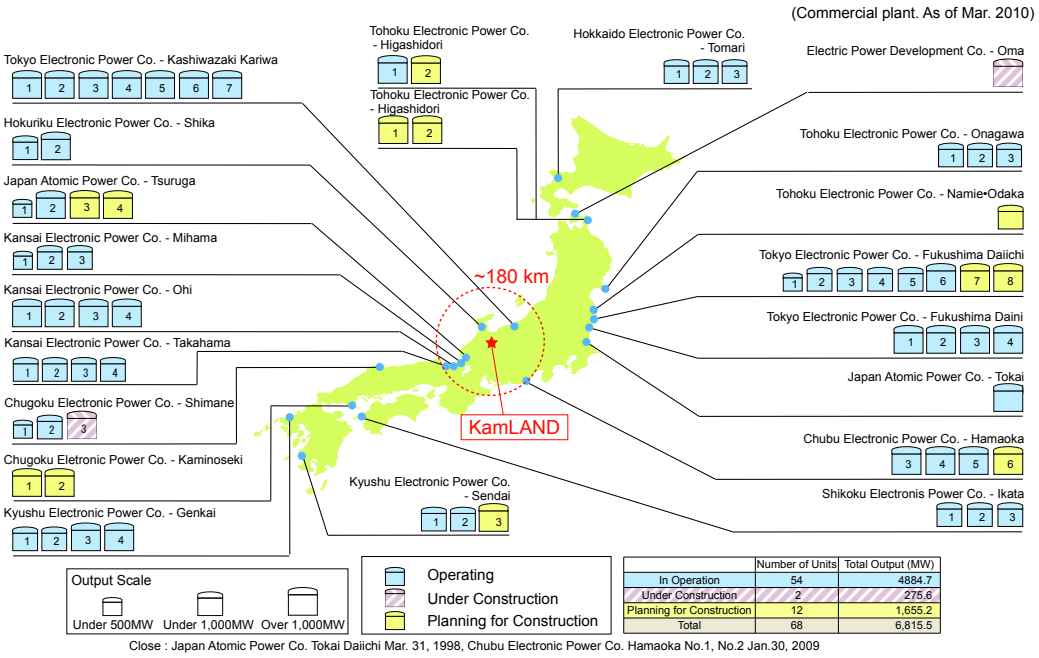

Figure 4.2: Status of operation and development for Japanese reactors (Mar. 2010) [26]. There are 56 Japanese nuclear power reactors.

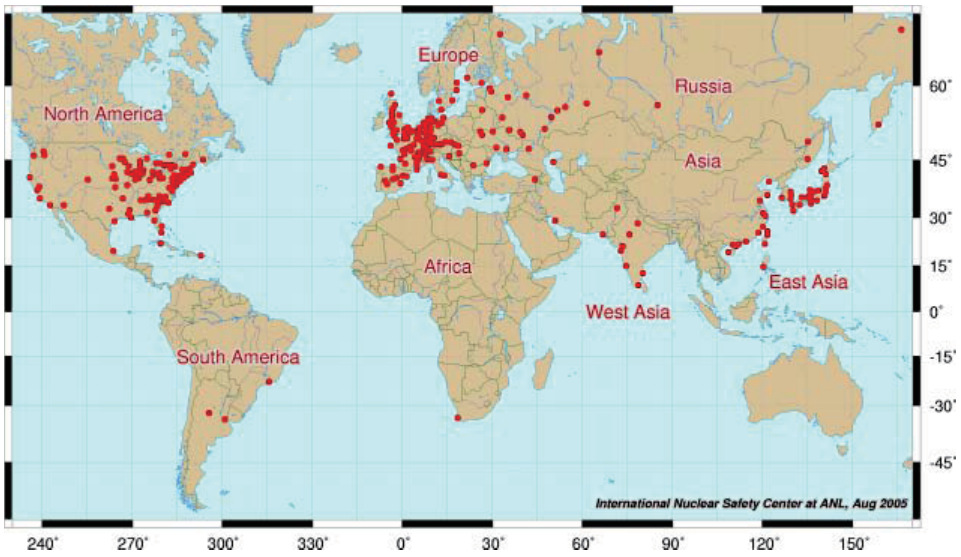

Figure 4.3: Locations of world nuclear reactors [27].

Table 4.1: Japa and Korean Reactors (1)

Company	Reactor	Distance [km]	Type	Thermal Power [MW]	Electrical Power [MW]
Chubu	Hamaoka-1 [1]	213.7234	BWR	1593	540
	Hamaoka-2 [2]	213.7989	BWR	2436	840
	Hamaoka-3	214.0054	BWR	3293	1100
	Hamaoka-4	214.1454	BWR	3293	1137
	Hamaoka-5	214.5230	BWR	3926	1380
Chugoku	Shimane-1	401.0722	BWR	1380	460
	Shimane-2	401.2178	BWR	2436	820
Genden	Tokai2	295.3710	BWR	3293	1100
	Tsuruga-1	138.4669	BWR	1064	357
	Tsuruga-2	138.4837	PWR	3423	1160
Hokkaido	Tomari-1	783.0410	PWR	1650	579
	Tomari-2	782.9227	PWR	1650	579
	Tomari-3	782.7350	PWR	2660	912
Hokuriku	Shika-1	87.6750	BWR	1593	540
	Shika-2	87.7190	BWR	3926	1358
Japan Nuclear Cycle	Fugen	138.5051	ATR	557	165
	Monju	141.5101	FBR	714	280
Kansai	Mihama-1	145.7192	PWR	1031	340
	Mihama-2	145.7683	PWR	1456	500
	Mihama-3	145.8325	PWR	2440	826
	Ohi-1	178.7497	PWR	3423	1175
	Ohi-2	178.8259	PWR	3423	1175
	Ohi-3	179.0409	PWR	3423	1180
	Ohi-4	179.1589	PWR	3423	1180
	Takahama-1	191.2394	PWR	2440	826
	Takahama-2	191.2706	PWR	2440	826
	Takahama-3	191.6824	PWR	2660	870
	Takahama-4	191.7137	PWR	2660	870
Kyusyu	Genkai-1	754.4024	PWR	1650	559
	Genkai-2	754.5135	PWR	1650	559
	Genkai-3	754.6288	PWR	3423	1180
	Genkai-4	754.7399	PWR	3423	1180
	Sendai-1	830.3809	PWR	2660	890
	Sendai-2	830.3023	PWR	2660	890
Shikoku	Ikata-1	560.7897	PWR	1650	566
	Ikata-2	560.8451	PWR	1650	566
	Ikata-3	560.7029	PWR	2660	890

Table 4.2: Japa and Korean Reactors (2)

Company	Reactor	Distance [km]	Type	Thermal Power [MW]	Electrical Power [MW]
Tohoku	Onagawa-1	430.4803	BWR	1593	524
	Onagawa-2	430.6040	BWR	2436	825
	Onagawa-3	430.5102	BWR	2436	825
	Higashidori-1	635.8910	BWR	3293	1100
Tokyo	Fukushima1-1	349.4254	BWR	1380	460
	Fukushima1-2	349.3744	BWR	2381	784
	Fukushima1-3	349.3377	BWR	2381	784
	Fukushima1-4	349.3011	BWR	2381	784
	Fukushima1-5	349.5532	BWR	2381	784
	Fukushima1-6	349.5902	BWR	3293	1100
	Fukushima2-1	345.3411	BWR	3293	1100
	Fukushima2-2	345.3976	BWR	3293	1100
	Fukushima2-3	345.4388	BWR	3293	1100
	Fukushima2-4	3454.717	BWR	3293	1100
	KashiwazakiKariwa-1	159.1046	BWR	3293	1100
	KashiwazakiKariwa-2	159.2254	BWR	3293	1100
	KashiwazakiKariwa-3	159.3356	BWR	3293	1100
	KashiwazakiKariwa-4	159.5382	BWR	3293	1100
	KashiwazakiKariwa-5	160.6191	BWR	3293	1100
	KashiwazakiKariwa-6	160.5195	BWR	3926	1356
	KashiwazakiKariwa-7	160.3986	BWR	3926	1356
KHNP (Korea)	Kori-1	734.5180	PWR	1727	587
	Kori-2	734.5180	PWR	1913	650
	Kori-3	734.5180	PWR	2796	950
	Kori-4	734.5180	PWR	2796	950
	Ulchin-1	711.8130	PWR	2796	950
	Ulchin-2	711.8130	PWR	2796	950
	Ulchin-3	711.8130	PWR	2943	1000
	Ulchin-4	711.8130	PWR	2943	1000
	Wolsong-1	708.5790	PWR	1995	678
	Wolsong-2	708.5790	PWR	2060	700
	Wolsong-3	708.5790	PWR	2060	700
	Wolsong-4	708.5790	PWR	2060	700
	Yonggwang-1	986.4090	PWR	2796	950
	Yonggwang-2	986.4090	PWR	2796	950
	Yonggwang-3	986.4090	PWR	2943	1000
	Yonggwang-4	986.4090	PWR	2943	1000
	Yonggwang-5	986.4090	PWR	2943	1000
	Yonggwang-6	986.4090	PWR	2943	1000
	Ulchin-5	711.8130	PWR	2943	1000
	Ulchin-6	711.8130	PWR	2943	1000

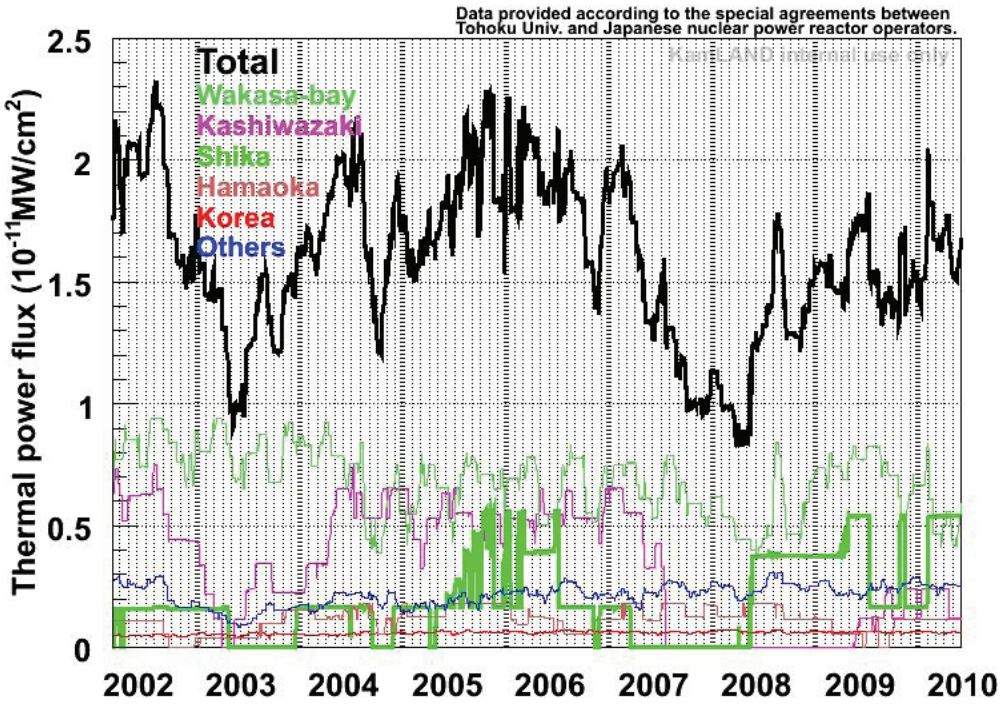

Figure 4.4: Time variation of $\bar{\nu}_e$ flux from reactors for this analysis data set. In July 2007, Kashiwazaki-Kariwa nuclear station (magenta line), which has largest thermal power in Japan, was stopped due to an earthquake. Because of this power reduction, Shika (green bold line) nuclear station contribution got larger than before.

4.1.2 Reactor Anti-Neutrino Energy Spectrum

Nuclear power reactors are rich anti-neutrino sources. The four main isotopes, ^{235}U, ^{238}U, ^{239}Pu and ^{241}Pu, contribute 99.9 % of total power generation.

- ^{235}U
  ^{235}U in the reactor core absorbs a thermal neutron and fissions. Then fission fragments are unstable and emit $\bar{\nu}_e$s via β decays,

$$^{235}\mathrm{U} \rightarrow \mathrm{A} + \mathrm{B} + 6.1\beta^- + 6.1\ \bar{\nu}_e + 202\ \mathrm{MeV} + 2.4\ \mathrm{n} \tag{4.1}$$

- ^{238}U
  ^{238}U fissions with a fast neutron,

$$^{238}\mathrm{U} + \mathrm{n}(> 1[\mathrm{MeV}]) \rightarrow \mathrm{C} + \mathrm{D} + 5 \sim 7\beta^- + 5 \sim 7\ \bar{\nu}_e + 202\ \mathrm{MeV} + \mathrm{xn}, \tag{4.2}$$

  or produces the ^{239}Pu via two β-decays after capturing a thermal neutron,

$$\begin{aligned} ^{238}\mathrm{U} + \mathrm{n} &\rightarrow ^{239}\ \mathrm{U} \\ &\rightarrow ^{239}\ \mathrm{Np} \\ &\rightarrow ^{239}\ \mathrm{Pu} \quad (T_{1/2} = 24,100\ \mathrm{year}) \end{aligned} \tag{4.3}$$

- ^{239}Pu
  ^{239}Pu fissions with a thermal neutron,

$$^{239}\mathrm{Pu} + \mathrm{n} \rightarrow \mathrm{E} + \mathrm{F} + 5.6\ \beta^- + 5.6\ \bar{\nu}_e + 210\ \mathrm{MeV} + 2.9\ \mathrm{n}, \tag{4.4}$$

  or produces the ^{241}Pu after capturing two thermal neutrons,

$$\begin{aligned} ^{239}\mathrm{Pu} + \mathrm{n} &\rightarrow ^{240}\ \mathrm{Pu} \\ ^{240}\mathrm{Pu} + \mathrm{n} &\rightarrow ^{241}\ \mathrm{Pu} \end{aligned} \tag{4.5}$$

- ^{241}Pu
  ^{241}Pu fissions with a thermal neutron,

$$^{241}\mathrm{Pu} + \mathrm{n} \rightarrow \mathrm{G} + \mathrm{H} + 6.4\ \beta^- + 6.4\ \bar{\nu}_e + 212\ \mathrm{MeV} + 2.9\ \mathrm{n} \tag{4.6}$$

The $\bar{\nu}_e$ energy spectrum from each sources are provided in [29] [30] [31]. Figure 4.5 shows the anti-neutrino spectra from each fissile nuclei. The spectra have been checked previous short baseline experiment within 1.4 % accuracy [32].

There are some long-lived beta decay nuclei produced by fission of ^{235}U, ^{238}U, ^{239}Pu and ^{241}Pu as listed in Table 4.3. ^{97}Zn, ^{132}I and ^{93}Y attain equilibrium within tendays and do not affect on KamLAND reactor anti-neutrino measurement seriously. The neutrino flux of other three nuclei, ^{106}Ru, ^{144}Ce and ^{90}Sr changes according to their lifetime. The decay chains of these nuclei are,

$$^{106}\mathrm{Ru} \xrightarrow[\mathrm{Q}_\beta=0.0394\ \mathrm{MeV}]{\mathrm{T}_{1/2}=373.6\ \mathrm{days}} {}^{106}\mathrm{Rh} \xrightarrow[\mathrm{Q}_\beta=3.541\ \mathrm{MeV}]{\mathrm{T}_{1/2}=29.8\ \mathrm{sec}} {}^{106}\mathrm{Pd}$$

$$^{144}\mathrm{Ce} \xrightarrow[\mathrm{Q}_\beta=0.3187\ \mathrm{MeV}]{\mathrm{T}_{1/2}=284.9\ \mathrm{days}} {}^{144}\mathrm{Pr} \xrightarrow[\mathrm{Q}_\beta=2.9975\ \mathrm{MeV}]{\mathrm{T}_{1/2}=12.3\ \mathrm{sec}} {}^{144}\mathrm{Nd}$$

$$^{90}\mathrm{Sr} \xrightarrow[\mathrm{Q}_\beta=0.546\ \mathrm{MeV}]{\mathrm{T}_{1/2}=22.8\ \mathrm{days}} {}^{90}\mathrm{Y} \xrightarrow[\mathrm{Q}_\beta=2.282\ \mathrm{MeV}]{\mathrm{T}_{1/2}=64.1\ \mathrm{sec}} {}^{90}\mathrm{Zr}$$

Table 4.3: Long-lived nuclei produced by fission of ^{235}U, ^{238}U, ^{239}Pu and ^{241}Pu.

.

Fission Fragment	Half Life	E_{max} [MeV]	Yield [%] ^{235}U	^{238}U	^{239}Pu	^{241}Pu
^{97}Zn	16.9 hr.	1.922	5.95	5.50	5.30	4.89
^{132}I	2.295 hr.	2.104	4.30	5.16	5.40	4.14
^{93}Y	10.18 hr.	2.890	6.40	4.97	3.89	3.51
^{106}Ru	373 day	(^{106}Rh) 3.541	0.40	2.55	4.31	6.18
^{144}Ce	285 day	(^{144}Pr) 2.996	5.48	4.50	3.74	4.39
^{90}Sr	28.8 yr.	(^{90}Y) 2.279	5.82	2.10	1.57	3.12

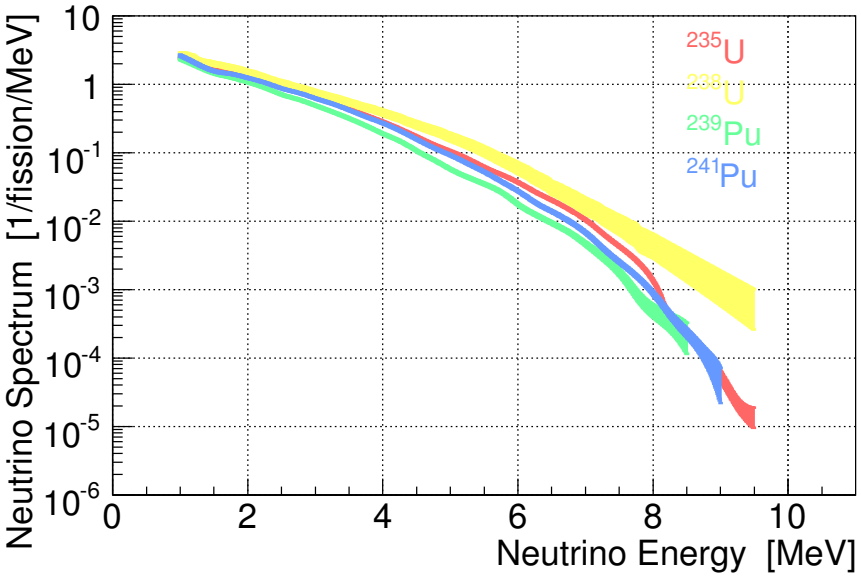

Figure 4.5: Energy spectrum of $\bar{\nu}_e$ flux from nuclear fissions, ^{235}U, ^{238}U, ^{239}Pu and ^{241}Pu [29] [30] [31]. Overall spectrum is checked within 1.4 % accuracy [32].

4.1.3 Expected Events from Reactors at KamLAND

The expected number of neutrino events and the energy spectrum from reactors at KamLAND are calculated by fluxes from all reactors, fission rate of nuclei and neutrino oscillation probability. The $\bar{\nu}_e$ flux $f(E_{\bar{\nu}_e}, t)$ is written as follows :

$$f(E_{\bar{\nu}_e}, t) = \sum_{i}^{\text{reactor}} \sum_{j}^{\text{nuclei}} \left(\frac{R_i^j(t)}{4\pi L_i^2} \cdot F^j(E_{\bar{\nu}_e}) \cdot P(E_{\bar{\nu}_e}, L_i) \right), \tag{4.7}$$

where

$$\begin{aligned} i &: \text{reactor number} \\ j &: \text{fission nuclei} = (^{235}\text{U}, ^{238}\text{U}, ^{239}\text{Pu and } ^{241}\text{Pu}) \\ R_i^j(t) &: \text{fission rate at time } t \\ L_i &: \text{distance from } i\text{-th reactor} \\ F^j(E_{\bar{\nu}_e}) &: E_{\bar{\nu}_e} \text{ energy spectrum from fission nuclei } j \\ P(E_{\bar{\nu}_e}, L_i) &: \text{neutrino oscillation probability} \end{aligned}$$

Then, the neutrino energy spectrum $n(E_{\bar{\nu}_e})$ is written as follows :

$$n(E_{\bar{\nu}_e}) = \int N_p \cdot f(E_{\bar{\nu}_e}, t) \cdot \sigma(E_{\bar{\nu}_e}) \cdot \varepsilon_d(E_{\bar{\nu}_e}) dt, \tag{4.8}$$

where $\sigma(E_{\bar{\nu}_e})$ is cross section of inverse beta decay reaction (Section 2.5.1), N_p is the number of target proton in 6.0 m fiducial radius (Section 5.8) and $\varepsilon_d(E_{\bar{\nu}_e})$ is detection efficiency (Section 5.7). The detection efficiency includes prompt and delayed space correlation, time correlation, vertex distribution, energies, and depends on the prompt positron energy E_e. The number of expected events N_{expected} can be calculated as an integration of the neutrino energy spectrum,

$$N_{\text{expected}} = \int n(E_{\bar{\nu}_e}) dE_{\bar{\nu}_e} \tag{4.9}$$

The anti-neutrino energy $E_{\bar{\nu}_e}$ can be written as a function of the prompt positron energy E_e. Considering that the positron angular distribution is almost isotopic, it is sufficiently accurate to use $\cos\theta = 0$. Thus, the relation between E_e and $E_{\bar{\nu}_e}$ is written as follows :

$$E_{\bar{\nu}_e} \simeq E_e + \Delta + \frac{1}{M}[E_e(E_e + \Delta) + y^2], \tag{4.10}$$

where $\Delta = M_{\text{n}}$ - M_{p} and $y^2 = (\Delta^2$ - $m_e^2)$ / 2. Therefore, Eq. (4.8) and Eq. (4.10) are written as a function of the prompt positron energy E_e,

$$\begin{aligned} N_{\text{expected}} &= \int n(E_e) dE_{\bar{\nu}_e} \\ n(E_e) &= \int N_p \cdot f(E_{\bar{\nu}_e}, t) \cdot \sigma(E_{\bar{\nu}_e}) \cdot \frac{dE_{\bar{\nu}_e}}{dE_e} \cdot \varepsilon_d(E_e) dt \\ \frac{dE_{\bar{\nu}_e}}{dE_e} &= 1 + \frac{2E_e + \Delta}{M} \end{aligned} \tag{4.11}$$

To take account of time variation of the fission rate during each run, the time integral is approximated by the sum of livetime. The energy resolution σ effect is included using convolution integral written as follows :

$$n^{'}(E_e^{'}) = \int n(E_e) \cdot \frac{1}{\sqrt{2\pi}\sigma} \cdot \exp^{-\frac{(E_e - E_e^{'})^2}{2\sigma^2}} dE_e \tag{4.12}$$

4.1.4 Reactor Related Uncertainties

The reactor related systematic uncertainties are summarized in Table 4.4. The uncertainty of the distance between KamLAND and reactors, the thermal power for Japanese, Korean and other reactors, the chemical composition, and long-lived nuclei are described in Section 4.1.1.

The uncertainty of time-lag effect is needed to assign to the $\bar{\nu}_e$ flux, since the fission rate becomes in equilibrium within one day above $\sim$ 2 MeV in neutrino energy. Thus, this uncertainty is estimated from the difference between the total $\bar{\nu}_e$ yield and that with shifting the run time by one day. Finally, this uncertainty is assigned as 0.01 %.

The neutrino energy spectra and uncertainties of four fissile nuclei are given in Ref. [29] [30] [31] and over all spectrum has been checked by ILL experiment [32] within 1.4 % accuracy. The spectrum uncertainty is assigned to the systematic uncertainty of $\bar{\nu}_e$ detection. In no-oscillation case, this error is 2.39 %.

Table 4.4: Summary of reactor related systematic uncertainties.

period	Before Purification		After Purification	
analysis threshold	0.9 MeV	2.6 MeV	0.9 MeV	2.6 MeV
distance	<0.1 %			
thermal power				
Japanese reactors	2.0 %		2.0 %	
Korean reactors	0.32 %		0.42 %	0.43 %
other reactors	0.48 %		0.63 %	
chemical composition	< 1.0 %			
anti-neutrino spectra	2.39 %	2.65 %	2.39 %	2.64 %
time lag	0.01 %			
long-lived nuclei	0.31 %	0.02 %	0.35 %	0.02 %
total	3.34 %	3.52 %	3.38 %	3.54 %

4.2 Anti-Neutrinos from Radioactive Decays in the Earth

4.2.1 Geo-Neutrino

The detection of $\bar{\nu}_e$ produced by natural radioactivity in the Earth could yield important geophysical information. Radioactive isotopes are abundant in the present Earth are crucified into three groups; isotopes in ^{238}U, ^{232}Th and ^{40}K decay series. All other isotopes contributions to radiogenic energy generation are negligible compared with ^{238}U, ^{232}Th and ^{40}K decay series.

Radiogenic heat is produced by decays of isotopes, in which processes electron-type (anti-) neutrinos are emitted.

$$^{238}\mathrm{U} \rightarrow^{206} \mathrm{Pb} + 8\ ^{4}\mathrm{He} + 6\ e^{-} + 6\ \bar{\nu}_e + 51.7\ [\mathrm{MeV}] \tag{4.13}$$

$$^{232}\mathrm{Th} \rightarrow^{208} \mathrm{Pb} + 6\ ^{4}\mathrm{He} + 4\ e^{-} + 4\ \bar{\nu}_e + 42.7\ [\mathrm{MeV}] \tag{4.14}$$

$$^{40}\mathrm{K} \xrightarrow{89.28\%} {}^{40}\mathrm{Ca} + e^{-} + \bar{\nu}_e + 1.311\ [\mathrm{MeV}] \tag{4.15}$$

$$^{40}\mathrm{K} + e^{-} \xrightarrow{10.72\%} {}^{40}\mathrm{Ar} + \nu_e + 1.505\ [\mathrm{MeV}] \tag{4.16}$$

From these reaction, geo-neutrino luminosity tells us the shout of radiogenic heart generation directly. Since the energy spectrum of beda decay is given by a well-established formula, that of geo-neutrino can be written with maximum electron energy $E_{\max}$,

$$dN(E_e) = \frac{G_F^2 |M|^2}{2\pi^3 \hbar^7 c^5} F(Z, E_e)(E_{\max} - E_e)\sqrt{E_e^2 - m_e^2 c^4} E_e\ dE_e \tag{4.17}$$

$$E_{\bar{\nu}_e} = E_{\max} - E_e, \tag{4.18}$$

where $F(Z, E_e)$ is the Fermi Function , corresponding to the effect of electron field of nuclei

$$F(Z, E_e) = 2(1+\gamma)(2\sqrt{W^2-1}R)^{2(\gamma-1)} e^{xy} \frac{|\Gamma(\gamma + iy)^2|}{|\Gamma(2\gamma+1)^2|} \tag{4.19}$$

$$\gamma = \sqrt{1-(\alpha Z)^2} \qquad W = \frac{E_e}{mc^2} \qquad y = \alpha Z \frac{W}{\sqrt{W^2-1}}$$

$$R = 0.426 \alpha A^{1/3} \qquad \alpha = \frac{e^2}{\hbar c} = 1/137.035989$$

Considering radioactive equilibrium, the energy spectrum of the anti-neutrinos are calculated by summing up the normalized spectra of every beta-decay of every isotope as follows :

$$\frac{dN}{dE_\nu} = \sum_{\text{isotope}} \sum_{\text{branch}} R_{\text{isotope}} R_{\text{branch}} \left(\frac{1}{N} \frac{dN}{dE_\nu} \right)_{\text{isotope, branch}} \tag{4.20}$$

$$R_{\text{isotope}} = \begin{cases} 1 & \text{(decay series head)} \\ \sum_{\text{parent}} \sum_{\text{branch}} R_{\text{parent}} R_{\text{branch}} & \text{(daughter isotopes)} \end{cases} \tag{4.21}$$

where R_{isotope} is the production ratio of an isotope, R_{parent} is the production rate of a parent isotope and R_{branch} is the branching ratio of beta decay. The anti-neutrino energy spectra from ^{238}U, ^{232}Th and ^{40}K can be calculated as shown in Figure 4.6.

In this calculation, 82 beta decays in the U series and 70 beta decays in the Th series are included.

Radiogenic heat generation is calculated by subtracting neutrino energy from the decay Q value, and given as follows :

$$Q_{\rm heat} = Q - Q_\nu = Q - \int_0^{E_{\rm max}} E_\nu \frac{dN}{dE_\nu} dE_\nu, \tag{4.22}$$

where $N(E_\nu)$ is the neutrino spectrum given by Eq. (4.17). The radiogenic heat generation is calculated as summarized in Table 4.5. Properties of ^{238}U, ^{232}Th and ^{40}K, and a luminosity of their anti-neutrinos are listed in Table 4.6. From these calculations, the relation between neutrino luminosity and radiogenic heat generation is expressed be :

$$\text{Uranium} : \frac{L_{\bar{\nu}_e}}{[\text{sec}]} = 7.84 \times 10^{11} \cdot \frac{Q_{\rm heat}}{[\text{W}]} = 7.41 \times 10^7 \cdot \frac{M}{[\text{kg}]} \tag{4.23}$$

$$\text{Thorium} : \frac{L_{\bar{\nu}_e}}{[\text{sec}]} = 6.18 \times 10^{11} \cdot \frac{Q_{\rm heat}}{[\text{W}]} = 1.62 \times 10^7 \cdot \frac{M}{[\text{kg}]} \tag{4.24}$$

$$\text{Potassium} : \frac{L_{\bar{\nu}_e}}{[\text{sec}]} = 7.98 \times 10^{12} \cdot \frac{Q_{\rm heat}}{[\text{W}]} = 2.70 \times 10^4 \cdot \frac{M}{[\text{kg}]} \tag{4.25}$$

Table 4.5: Radiogenic heat generation per decay for ^{238}U-series, ^{232}Th-series and ^{40}K.

	^{238}U-series	^{232}Th-series	^{40}K	
			β^- (89.28 %)	EC (10.72 %)
Q [MeV/decay]	51.7	42.7	1.311	1.505
Q_ν [MeV/decay]	3.96	2.23	0.724	0.044
$Q_{\rm heat}$ [MeV/decay]	47.7	40.4	0.587	1.461

Table 4.6: Radiogenic heat generation and neutrino luminosity.

- Isotope -	^{238}U	^{232}Th	^{40}K
Natural Abundance [%]	99.27	100	0.01167
$N_{\rm atom}$ / mass [1/kg]	2.530×10^{24}	2.596×10^{24}	1.506×10^{25}
Lifetime [sec]	2.034×10^{17}	6.397×10^{17}	5.814×10^{16}
$N_{\rm decay}$ / mass [1/sec/kg]	1.244×10^{7}	4.058×10^{6}	2.590×10^{8}
$N_{\bar{\nu}_e}/N_{\rm decay}$	6	4	0.8927
$L_{\bar{\nu}_e}$/ mass [1/sec/kg]	7.464×10^{7}	1.623×10^{7}	2.312×10^{8}
$Q_{\rm heat}$/ mass [W/kg]	9.515×10^{-5}	2.628×10^{-5}	2.824×10^{-5}

- Natural Element -	Uranium	Thorium	Potassium
$L_{\bar{\nu}_e}$/ mass [1/sec/kg]	7.410×10^{7}	1.623×10^{7}	2.698×10^{8}
$Q_{\rm heat}$/ mass [W/kg]	9.446×10^{-5}	2.628×10^{-5}	3.380×10^{-5}

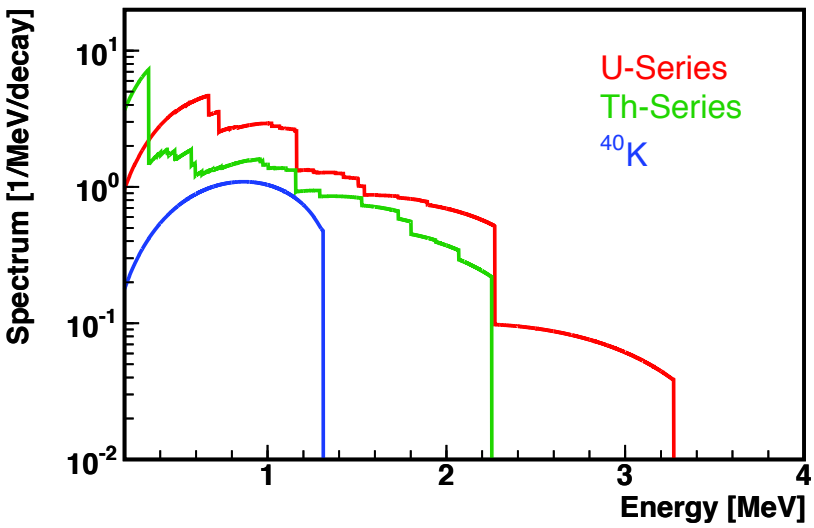

Figure 4.6: $\bar{\nu}_e$ energy spectra of U-series, Th-series and ^{40}K[33].

4.2.2 Structural Models of the Earth

Preliminary Earth Reference Model

Models of the Earth's structure has been constructed mostly using seismic data. Figure 4.7 shows the seismic wave velocity and density profiles as a function of radius given in the Preliminary Earth Reference Model (PREM, in 1981) [34]. As shown in this figure, Earth generally consists of the following major concentric regions : crust (approximate radial thickness = 6 $\sim$ 30 km), upper and lower mantle (2900 km), outer core (2300 km), inner core (1200 km).

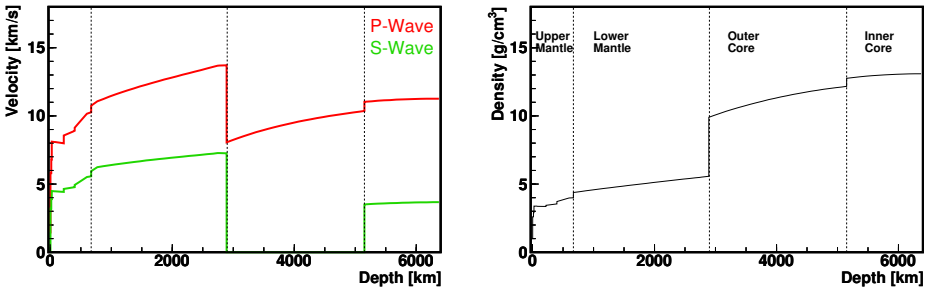

Figure 4.7: Seismic wave velocities (left) and density (right) profiles as a function of depth given in the Preliminary Reference Earth Model [34]. The Earth's global layer structure, crust, upper mantle, lower mantle, outer core and inner core is clearly demonstrated.

Crustal Models

Seismological analysis is also useful to determine the local crustal structure. Seismic wave measurements were compiled to make 2° × 2° grid crustal thickness map (CRUST 2.0 [35]), describing the thickness and density of soft sediment, hard sediment, upper crust, middle cruet and lower crust. Figure 4.8 shows the crustal thickness map given by CRUST 2.0 data set, based on 560 seismic refection measurements published between 1948 and 1995. For the crustal model around Japanese Islands, D.Zhao *et al.* analyzed more than 1,300 arrival times of 562 shallow earthquakes [36]. By applying an inversion method, they obtained a precise map of the Conrad and Moho discontinuity depth beneath the Japan Islands.

Earth Structural Model

From the seismological analysis, Earth's structure is now well understood. Figure 4.10 shows the Earth structural model revealed by seismological analysis.

- Crust
  There are two distinctive types of crusts, such as oceanic crust and continental crust. The oceanic crust is relatively young ($\sim$80 million years old) since it is constantly renewed at the mid-ocean ridges and recycled back into the inner Earth at subduction zones. And the continental crust is $\sim$2 billion years old on average, thicker than the oceanic crust, and further subdivided into upper, middle, and lower crusts. Sediment consisting of eroded continental crust

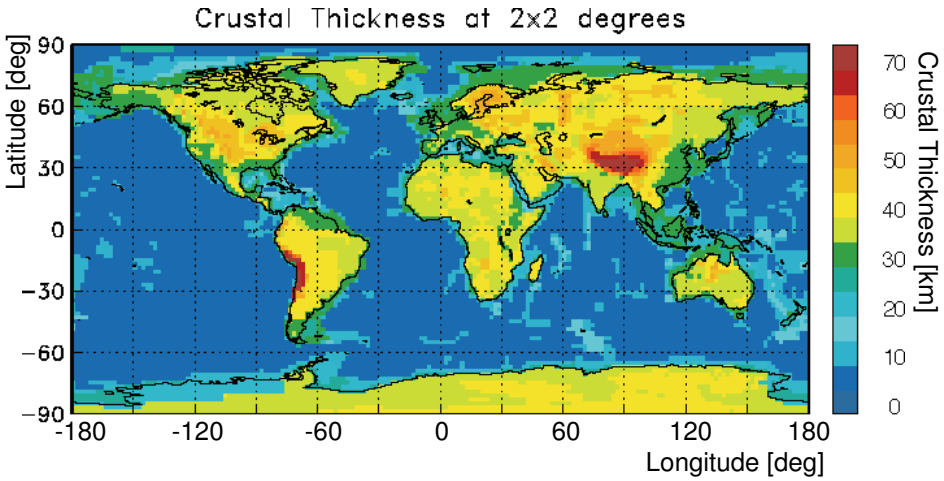

Figure 4.8: Crustal thickness map given by CRUST 2.0 data set [35].

and volcanic and biological materials covers surface of both the continental and oceanic crusts. The composition of the sediment covering the continental crust is assumed to be the same as that of the continental crust.

- Mantle
  The mantle is sub-divided into two layers, the upper mantle and the lower mantle. Seismological analysis shows seismic speed non-uniformity in the upper mantle and the lower mantle, and this non-uniformity suggests the global mantle convection. Currently there are two contradictory arguments for the mantle convection [37].

  – Two-layer Model
    Geochemists support the two-layer model in which the upper layer of mantle, depleted in incompatible elements, is separated from the primitive lower mantle by a boundary at a depth of 660 km.

  – Whole-mantle Model
    Seismologists support the whole-mantle model of circulation which exchange between subduction crust and upwelling plumes. In this story, the mantle circulation changed from two-layer to on-layer about 2.7 billion years ago.

  The word 'plume' means a large convection in the mantle. As shown in Figure 4.10, two up-going streams (the super plumes) beneath South Pacific Ocean and Africa, and one down-going stream (the cold plume) beneath Asia are clearly seen. The plume tectonics explains the direction of plate movement unlike the plate tectonics.

- Core
  The core has an internal structure which consists of a liquid outer core and a solid inner core. The core is commonly believed to be very high density Fe-Ni alloy, and that of mass amounts to about 32.5 % of the mass of Earth.

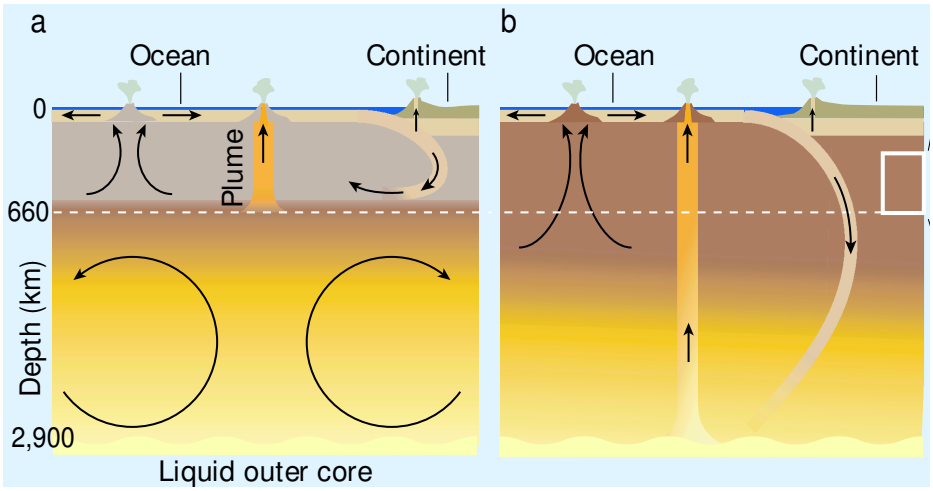

Figure 4.9: Two models of mantle convection, the tow-layer model (left) and the whole-mantle model [37].

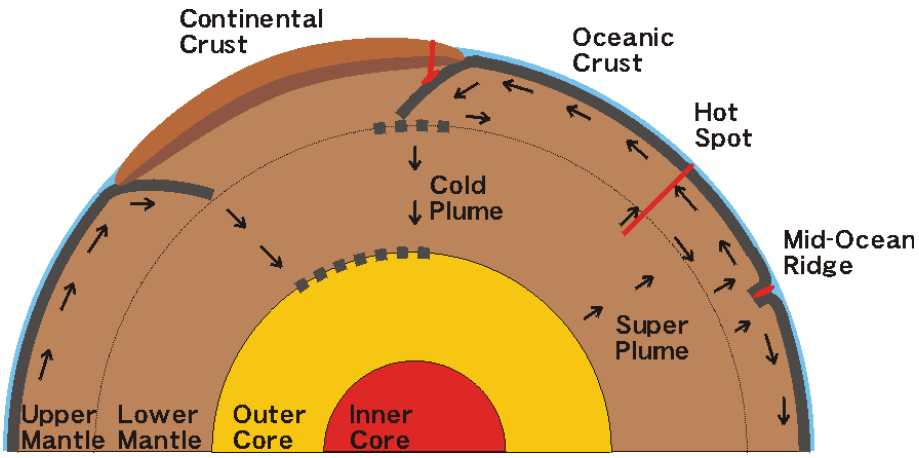

Figure 4.10: Earth structural model revealed by seismological analysis. The solid part of the Earth consists of several layers, such as crust, mantle, liquid outer core and solid inner core.

4.2.3 Geochemical Model of the Earth

The chemical properties of the Earth has been studied with various methods, such as direct sampling of crusts obtained from bore-holes and analysis of "Xenoliths", rock fragments brought up from the mantle to the surface in lava flows without melting, and so on. However the chemical properties of the Earth are rather less understood compared with the physical properties. One of motivation of geo-neutrino measurement is understanding the chemical composition of the bulk Earth.

Bulk Silicate Earth Model

The bulk chemical composition of the Earth is studied based on analysis of CI carbonaceous chondrite meteorite composition, which is thought to be close to Earth's ingredients because of its inclusion of volatile elements and compositional similarities to the solar photosphere. The bulk composition of the silicate Earth (i.e. mantle + crust) is derived from it by considering escape of volatile elements and separation of the core. A model of bulk silicate Earth composition was constructed with taking account of lithological and geological measurement on the surface [38]. This model is known as the Bulk Silicate Earth (BSE) model, and one of the fundamental bases of geochemistry. It provides a starting point to construct a geochemical model of the Earth. Different authors proposed a range of BSE models based on different constraints, such as carbonaceous chondrites and enstatite chondrites. In Table 4.7, the abundance of U, Th and K provided by several BSE models are summarized.

Table 4.7: U, Th and K abundances provided by several BSE models.

Authors of difference BSE models	U [ppb]	Th [ppb]	K [ppb]	Th/U	K/U
Taylor & McLennan (1985) [39]	18	65	180	3.6	1.0×10^4
Hart & Zindler (1986) [40]	21	79	264	3.8	1.3×10^4
Hofmann & Criss (1988) [41]	20	80	254	4.0	1.3×10^4
McDonough & Sun (1995) [38]	20.3 ± 4.1	79.5 ± 11.9	240 ± 48	3.9	1.2×10^4
Javoy *et al.* (1999) [42]	20	69	270	3.5	1.4×10^4
Palme & O$'$Neil (2003) [43]	21.8 ± 3.3	83.9 ± 12.5	261 ± 39	3.8	1.2×10^4
Lyubetskya & Korenaga (2007) [44]	17.3 ± 3.0	62.6 ± 10.7	190	3.6	1.1×10^4

Earth Geochemical Model

- Crust
  As described in Section 4.2.2, the crust is categorized into two types, such as oceanic crust and continental crust by the seismological analysis. There is a difference between the chemical composition of these types of crust.
  - Continental Crust
    The continental crust constitutes only 0.4% of the total Earth mass, but about half of Uranium and Thorium are believed to be contained in the continental crust. Since Uranium and Thorium are Large Ion Lithophile elements, these are highly incompatible with the mantle and the core.

There are some different approaches to estimate the chemical composition of the continental crust, and they usually lead to different result as summarized in Table 4.8. Tectonic models (relies on plate tectonics models), geological models (uses geological map and chemical analysis of representative rock) and seismic models (uses observed seismic profiles) are generally used for this study.

Table 4.8: Uranium and Thorium concentration in the continental crust.

	Source	Concentration [ppm]			
		Upper	Middle	Lower	Bulk
Taylor & McLennan (1985, 1995) [39] [45]	U	2.8	-	0.53	1.1
	Th	10.7	-	2.0	4.2
Wedepohl (1995) [46]	U	2.5	1.93		1.7
	Th	10.3	6.6		8.5
Rudnick & Fountain (1995) [47]	U	(2.8)	1.6	0.2	1.4
	Th	(10.7)	6.1	1.2	5.6
Rudnick & Gao (2003) [48]	U	2.7	1.4	0.2	1.3
	Th	10.5	6.5	1.2	5.6

  - Oceanic Crust
    The oceanic crust covers approximately the half of the Earth surface, and relatively homogeneous in thickness (thin, ∼7km) and in chemical composition as compared with the continental crust. Most of the oceanic crust is formed at mid-ocean ridges, some of them are formed at intra-plate volcanoes, back-arc basins such as the Sea of Japan, and oceanic plateaus. There are basaltic layers under sediment layer, and those Uranium and Thorium concentrations are estimated to be ∼0.10 ppm and ∼0.22 ppm, respectively [39].

- Mantle
  The mantle is important part of the Earth, and constitutes 83% of total volume, and 67% of total mass. From study of seismological analysis, the mantle is divided into two layers, the upper mantle and the lower mantle.

  It is hard to measure directly the chemical composition in the mantle, especially lower mantle. Currently, the chemical composition in the lower mantle is studied based on seismology, cosmo-chemistry, and laboratory experiments of ultra-high pressure and temperature lithology. For the upper mantle, things are slightly in better in understanding, because some mantle samples are available on the surface as ultramafic massifs, such as "Xenoliths". However, it is not clear whether mantle samples represent the unbiased mantle composition, because special tectonic settings are responsible to bring the sample to the surface. Here, for the reference Earth model discussed in Section 4.2.5, the chemical composition of the mantle is determined by subtraction that of the crust from the expected composition of the Earth, and assumed uniform distribution in the whole mantle.

- Core
  The core corresponds to the center part of the Earth, and that volume and mass are 16.0% and 32.5% of the Earth, respectively. The core is studied with seismic waves, terrestrial magnetism and Earth's orbital behavior. Analysis of meteorites, especially CI carbonaceous chondrite and iron meteorites, helps understand the chemical composition of Earth ' s core. The core is believed to be very high density Fe-Ni alloy, and refractory lithophile elements such as Uranium and Thorium are commonly believed to be absent from the core. Furthermore, laboratory composition experiments show that only low-atomic-weight elements such as H, C, N. O. Mg, Si and S can be contained in such a high density alloy [49] [50]. On the other hand, the possibility of the existence of potassium in the core is pointed out from high-pressure and high-temperature experimental data [51].

4.2.4 Earth's Heat

There are some possibilities of Earth's heat sources (1) radiogenic heat from U, Th and K decay, (2) release of gravitational energy through accretion or metallic core separation, and (3) latent heat from the growth of inner core. It is important to understand the Earth's heat to establish the geophysical activity.

Heat Flow From Surface

The total heat flow is an important constraint for thermal models of the Earth. Based on our knowledge of the absolute abundances of radioactive isotopes such as ^{238}U and ^{232}Th in the Earth, we can evaluate the Earth energy budget and determine whether the Earth is heating up, in thermal equilibrium, or cooling down.

The total heat flow of the Earth's interior is estimated to be 44.2 $\pm$ 1.0 TW by summing the heat from measurements made in bore-holes and calculations based on empirical estimators derived from the observation for unsurveyed areas and areas with hydrothermal effects [52]. It means that the heat flow measurements from many ocean floor areas are known to be biased too low due to the ocean water circulation removing the measurable heat. A more controversial approach, using only the heat flow measurements made in bore-holes without the estimators that corrects for the hydrothermal circulation effects, yields 31 $\pm$ 1 TW [53]. Recently the new measurement result 47 $\pm$ 2 TW is reported based on $\sim$40,000 measurements results in deep bore-holes (55% more than used in previous estimation), and the heat loss through the sea floor is estimated by a half-space cooling approximation [54]. The total heat flows estimated by several authors are summarized in Table 4.9. Furthermore, the expected sources of global heat flow are summarized in Table 4.10 [55].

Radiogenic Heat

Based on chondritic abundances of Uranium and Thorium, and cosmochemical consideration of the volatility of K, the current model of the bulk silicate Earth (BSE) [38] gives heat generation of 8 TW by ^{238}U decay chain, 8 TW by ^{232}Th decay chain, and 4 TW by ^{40}K [60]. A total of 20 TW radiogenic heat generates in the Earth's interior. In this model, radiogenic heat constitutes nearly half of the total rate of

Table 4.9: Total heat flow from Earth's interior.

	Total Heat Flow [TW]
Willians & von Herzan (1974) [56]	43
Davies (1980) [57]	41
Sclater (1980) [58]	42
Pollack *et al.* (1993) [52]	44 ± 1
Hofmeister *et al.* (2005) [53]	31 ± 1
Jaupart *et al.* (2007) [59]	46 ± 3
Davies and Davies (2010) [54]	47 ± 2

Table 4.10: Expected sources of the global heat flow [55].

Energy supply contribution	[TW]
- Potential energy contributions -	
Conducted from core	8.6
Mantle differentiation	0.6
Thermal contraction	2.1
Earthquake induced gravitational energy	2
Radiated seismic energy	0.3
Tidal fraction	$1 \sim 2$
Total non-radiogenic	$\mathbf{15 \sim 16}$
- Radiogenic -	
Present radiogenic; BSE	19 ∼31
Present radiogenic; Continental crust	5.8 ∼8
Delayed radiogenic (between production and arrival at surface)	5
Total radiogenic	$\mathbf{24 \sim 26}$
- Secular cooling -	$\mathbf{0 \sim 14}$
Total input	$\mathbf{39 \sim 66}$

heat emission from the Earth's interior. Clearly, quantitative information about the radiogenic, heat-producing elements is essential for establishing the energy budget, which in turn is key to understanding the Earth's formation and evolution.

The fraction of heat produced in the Earth by radioactive decay is usually referred to as "Urey ratio", corresponding to the proportion of radiogenic heat to the total heat flow of the Earth. The "convective Urey ratio" as defined assumes whole mantle convection; that is, the entire mantle convects as a single layer (or one could say that the physical interpretation of the Urey ratio is straightforward for whole mantle convection). Most geochemical models and, in particular, the BSE model used above set the convective Urey ratio to about 0.3, allowing for a substantial fraction of the heat to be of primordial origin, whereas geophysicists prefer some models assuming higher convective Urey ratios that range up to ∼1.0 [61]. For example, a fully radiogenic model assuming Urey ratio of 1 is constructed by uniformly introducing U and Th in the mantle (homogeneous hypothesis) and, alternatively,

by locating all U and Th at the mantle-core interface ("sunken layer" hypothesis). The latter case is an attempt to test the compatibility of the fully radiogenic model with the geo-neutrino flux, by distributing the sources as far from the detectors as possible.

4.2.5 Reference Earth Model

A reference Earth model for geo-neutrino flux estimation was constructed based on structural and geochemical Earth models by Enomoto *et al.* [**?**]. For constructing the model, there are some assumptions in the U and Th concentrations.

- Core : fixed to zeto
- Crust and sediment : assigned some petrographic analysis results
- Mantle : assumed to be uniform and obtained by subtracting the crustal composition from the BSE composition

Based on the structural model, the solid Earth is decided into ten parts: continental sediment, oceanic sediment, upper continental crust, middle continental cruet, lower continental crust, oceanic crust, upper mantle, lower mantle, outer core, and inner core. The chemical composition of each part is assigned as summarized in Table 4.11. It's distribution is assumed to be uniform.

Table 4.11: Reference Earth model.

Reservoir		U [ppm]	Th [ppm]	Reference
Sediment	Continental	2.8	10.7	-
	Oceanic	1.68	6.91	Plank *et al.* (1998) [62]
Continental crust	Upper	2.7	10.5	Rudnick & Gao (2003) [48]
	Middle	1.4	6.5	
	Bottom	0.2	1.2	
Oceanic crust		0.10	0.22	Taylor *et al.* (1985) [39]
Mantle	Upper	0.012	0.048	-
	Lower	0.012	0.048	-
Core	Outer	0	0	McDonough (1999) [49]
	Inner	0	0	McDonough (1999) [49]
Bulk silicate (BSE model)		0.02	0.08	McDonough (1995) [38]

Geo-Neutrino Flux

The differential geo-neutrino flux at a position $\vec{r}$ is determined from the isotopic abundances $a_i(\vec{r'})$ at the location of the sources, $\vec{r'}$,

$$\frac{d\Phi(E_\nu, \vec{r})}{dE_\nu} = \sum_i^{\text{isotopes}} A_i \frac{dn_i(E_\nu)}{dE_\nu} \int_\oplus d^3\vec{r'} \frac{a_i(\vec{r'})\rho(\vec{r'})P(E_\nu, |\vec{r} - \vec{r'}|)}{4\pi|\vec{r} - \vec{r'}|^2}, \tag{4.26}$$

where the integration extends oner the Earth's volume, A_i is the decay rate per unit mass, $dn_i(E_\nu)/dE_\nu$ is the energy spectrum of $\bar{\nu}_e$'s for each mode of decay, $a_i(\vec{r'})$ is in units of isotope mass per unit rock mass, $\rho(\vec{r'})$ is the rock density, and $P(E_\nu, |\vec{r} - \vec{r'}|)$ is the $\bar{\nu}_e$ survival probability due to the phenomenon of oscillation after traveling a distance $|\vec{r} - \vec{r'}|$. For the present purpose, the $\bar{\nu}_e$ survival probability is well approximated by the two-flavor oscillation formula,

$$P(E_\nu, L) \simeq 1 - \sin^2 2\theta_{12} \sin^2 \left(\frac{1.27 \Delta m^2_{21}[\mathrm{eV}^2] L[\mathrm{m}]}{E_\nu[\mathrm{MeV}]} \right), \tag{4.27}$$

where $L = |\vec{r} - \vec{r'}|$. The neutrino oscillation parameters Δm^2_{21} and $\sin^2 \theta_{12}$ are determined with substantial accuracy by a combined statical analysis of different data sets, including the one from KamLAND using $\bar{\nu}_e$ produced at nuclear reactors and those from solar neutrino experiments, under the assumption of CPT invariance. Corrections from the "matter effect" are founded to affect at 1% on Eq.(4.27), and negligible for the present accuracy of geo-neutrino measurement. In practice, given the energy spectrum of the geo-neutrinos, the size of the Earth and the oscillation parameters measured, the second sine function in Eq.(4.27) is averaged out in the integral over the volume of the Earth, giving $P(E_\nu, L) \simeq 1 - 0.5 \sin^2 2\theta_{12}$ with very good accuracy.

The calculated geo-neutrino flux at KamLAND from each reservoir is summarized in Table 4.12. As a unit of the geo-neutrino flux, [1/cm^2/sec] and [TNU] are often used. TNU is Terrestrial Neutrino Unit and defined as the number of events per 10^{32} targets per year. The relation between [TNU] and [1/cm^2/sec] is given as,

$$\text{Uranium} : 1\text{TNU} = 7.674 \times 10^4 [1/\mathrm{cm}^2/\mathrm{sec}] \tag{4.28}$$

$$\text{Thorium} : 1\text{TNU} = 2.477 \times 10^5 [1/\mathrm{cm}^2/\mathrm{sec}] \tag{4.29}$$

Figure 4.11 shows the calculated geo-neutrino flux as a function of distance from KamLAND.

Table 4.12: Geo-neutrino flux at KamLAND [63].

Reservoir		U geo-neutrino		Th geo-neutrino	
		$\times 10^5$[1/cm^2/sec]	[TNU]	$\times 10^5$[1/cm^2/sec]	[TNU]
Sediment	Continental	0.61	0.80	0.51	0.20
	Oceanic	0.14	0.18	0.12	0.05
Continental crust	Upper	11.5	15.01	9.57	3.86
	Middle	4.31	5.61	3.57	1.44
	Bottom	0.53	5.61	0.69	0.28
Oceanic crust		0.09	0.12	0.04	0.02
Mantle	Upper	2.20	2.87	1.91	0.77
	Lower	4.03	5.25	3.51	1.42
Core	Outer	0	0	0	0
	Inner	0	0	0	0
Bulk silicate (BSE model)		23.4	30.52	19.9	8.04

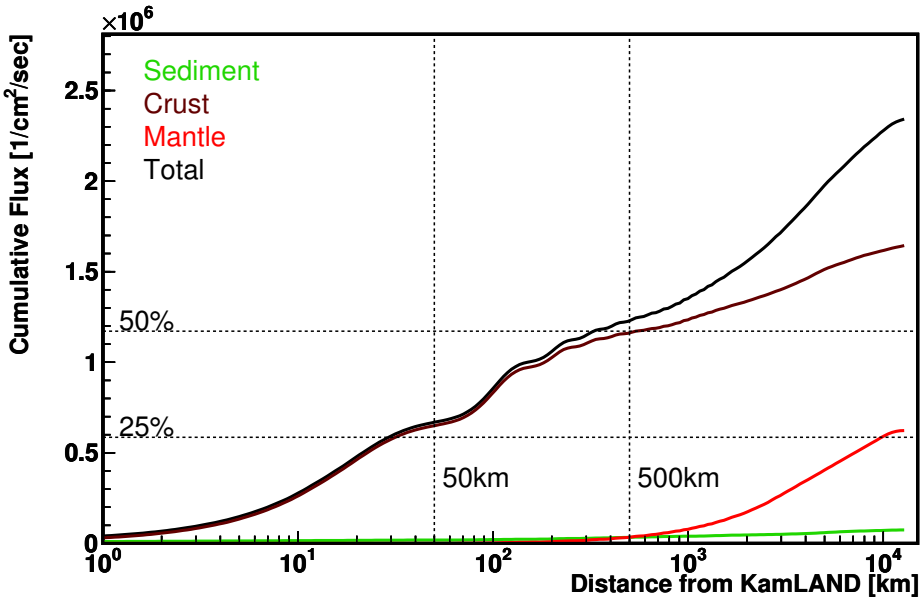

Figure 4.11: Geo-neutrino flux within a given distance from KamLAND [63]. The continental crust contributions to be $\sim$ three fourths of total flux. One fourth of total flux comes from the region within 50 km in radios from KamLAND and half of total flux comes from the region within 500 km in radius.

Chapter 5

Event Selection

Event selection procedure for low energy anti-neutrinos such as reactor and geo neutrino is described in this chapter. The various selection criteria are applied for the data set to improve the quality of anti-neutrino samples. This analysis is based on the data set corrected between March 2002 to May 2010. The data set includes low-background period, which was corrected after purification campaign. The anti-neutrino detection signature, prompt-delayed event-pairs produced by inverse β-decay and their subsequent neutron captures, is selected by applying a set of cats, described in Section 5.3. Furthermore, to improve the selection efficiency for anti-neutrino candidate, the likelihood selection is also applied, as described in Section 5.7. Finally, the detector-related and reactor-related uncertainties are summarized in Section 5.8.

5.1 Dataset Summary

Table 5.1 shows the summary of dataset for this analysis. As shown in Figure 5.1, the dataset is categorized into two periods, designed as DS-1 and DS-2. DS-1 is collected before purification, and its livetime is estimated to be 1485.7 days. On the other hand, DS-2 includes the high-quality data collected after purification. DC-2 accounts for 35.29 % of total livetume.

Table 5.1: Summary of dataset

	DS-1	DS-2
LS status	before purification	after purification
date	March 9, 2002 - May 24, 2007	July 7, 2007 - May 18, 2010
livetime [days]	1485.7	810.3

5.2 Run Selection

Not all of collected data are appropriate for physical data due to some fails of readout electronics circuit or external troubles such as power fail. To reject those

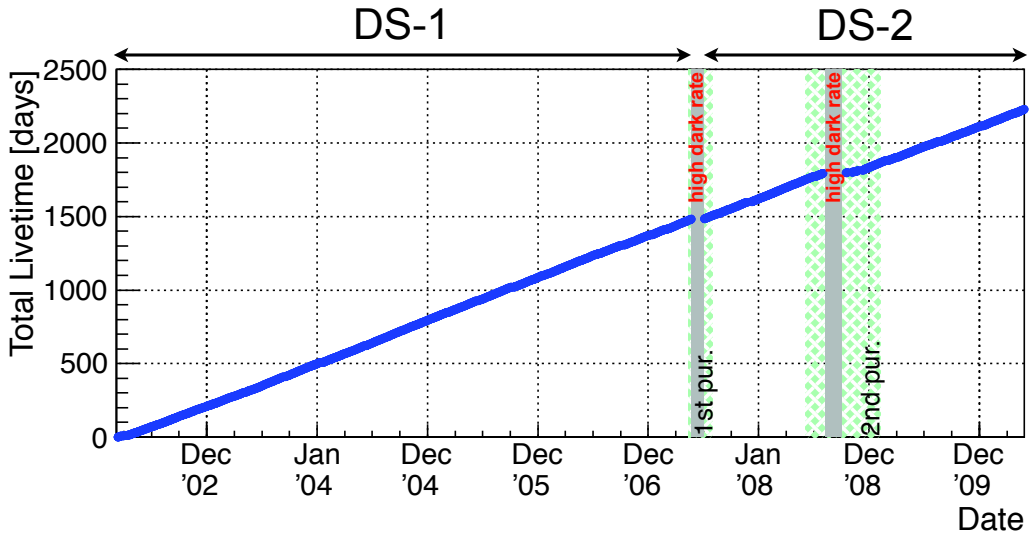

Figure 5.1: Total livetime for the analysis. Green shaded periods show the 1st and 2nd purification, and gray shaded areas show the high dark rate period because of the purification activity, which are not included in the dataset. The dataset is categorized into two periods, designed as DS-1 and DS-2. DS-1 is collected before purification, and DS-2 includes the high-quality data collected after purification.

data, quality of collected data is examined in prior to physics analysis. The check parameters are as follows :

- Number of bad channel
  If the data flow from ATWD of each front end electronics boards has some abnormalities, the channel is ruled unfit to use for physics analysis. The number of the bad channel is checked run by run, and if there are many bad channels, it should be crucified as bad run.

- Trigger rate, muon rate, and event rate
  If data taking is smooth, these rates are confirmed to be stable in the detector. These are monitored for stability with respect to recent good runs.

- Run time
  The short run whose run time is less than is crucified as bad run.

In one run, there is a possibility that the data taking quality sometimes becomes not good. To reject such a bad period, this run is crucified as "half-bad run", and data is analyzed except for the bad period. If only 20-inch PMTs have some failures, the run is called "20-inch bad run". These runs are excluded in the analysis to avoid a worsening of the energy resolution.

5.3 Physics Event Selection

KamLAND real data includes unphysical events such as noise events, flasher events and ringing events. These are rejected before physics analysis. Figure 5.2 shows the 17-inch PMT's charge distribution including unphysical events. In high energy region, over 10^4 p.e., almost all events are muons. On the other hand, there are many events at or below 2,000 p.e., and theses are eliminated by the 2 msec veto after muon.

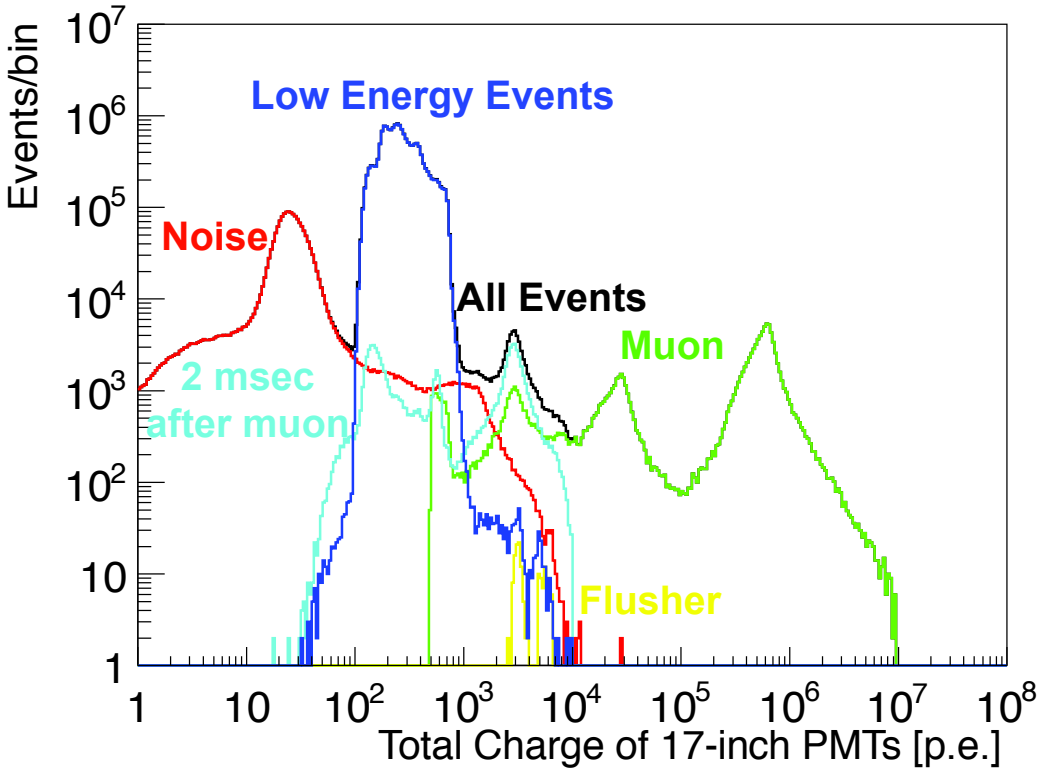

Figure 5.2: Total charge of 17-inch PMTs distribution for various type of events.

5.3.1 Noise Event

Non-physical events are characterized by their abnormal PMTs hit time distribution. A noise event is defined as an event which has no timing cluster of PMT hit. To select the noise event, a parameter "N_{100}" is useful, which represents the number of PMT hits with 100 nsec time window. The 100 nsec time window is adjusted to contain the maximum number of hits within the time window. Figure 5.3 shows the distribution between the number of PMT hits within 100 nsec (N_{100}) and the number of PMT hits of the inner detector in an event ($Nhit_{ID}$). The noise events are clearly separated, and the selection criteria is

$$N_{100} \leq \frac{Nhit_{\mathrm{ID}} + 50}{2}, \tag{5.1}$$

which shown with a green line in the figure.

The inefficiency of the noise even cut is estimated using ^{68}Ge calibration data. ^{68}Ge releases annihilation γ-rays (2×0.511 MeV) which energy corresponds to the minimum energy of the prompt energy of the inverse beta decay. The same cut is applied to the calibration data, and the inefficiency of the noise events before and after purification are estimated 3×10^{-4}% and < 0.02%, respectively.

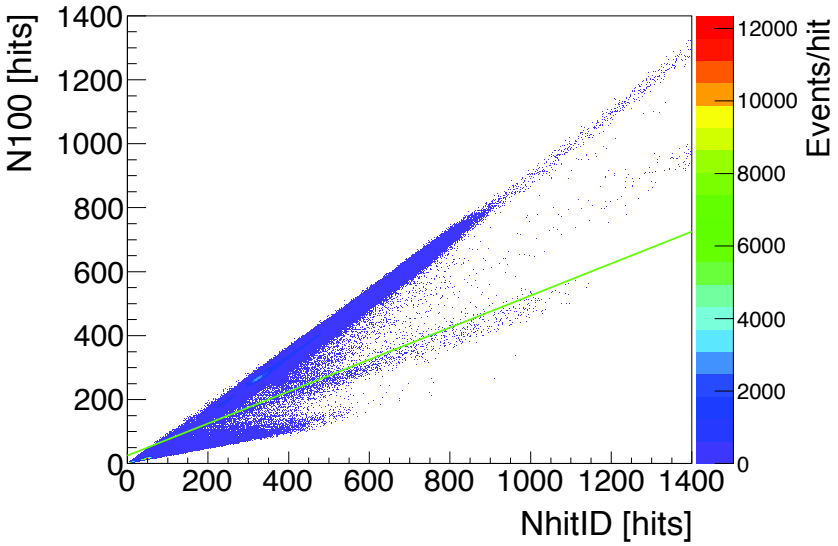

Figure 5.3: Noise event selection criteria. The horizontal axis shows the number of PMT hits in an event, and the vertical axis shows the number of PMT hits within 100 nsec in an event. The green line shows cut off range of the noise region.

5.3.2 Flasher Event

A flasher event is caused by light emission from the PMT due to discharge in its dynode. The surrounding PMTs detect the light from the discharge, generating an event. The flasher signal mimics the high energy events up to ~20 MeV, however, they are easely selected using the maximum of the PMT charge. The selection criteria of the flasher events is as follows :

- Total charge of 17-inch and 20-inch PMTs in the Inner detector (Q_{ID}) $\geq$ 2,500 p.e.
- Maximum single-PMT charge / $Q_{ID} \geq 0.6$
- Mean charge of the neighbor PMTs surrounding the flasher PMT $\geq$ 20 p.e.
- Not a noise event or muon event

As shown in Figure 5.4, the flusher events are clear separated from normal events.

The event rate of flusher event is about 2.9×10^{-3} Hz (before purification), and 1.2×10^{-3} Hz (after purification). These correspond to about 8×10^{-3}% and 9×10^{-3}% of total low energy events. The inefficiency of the flasher cut is estimated to be less than 8×10^{-3}% (before purification), and 9×10^{-3}% (after purification), respectively.

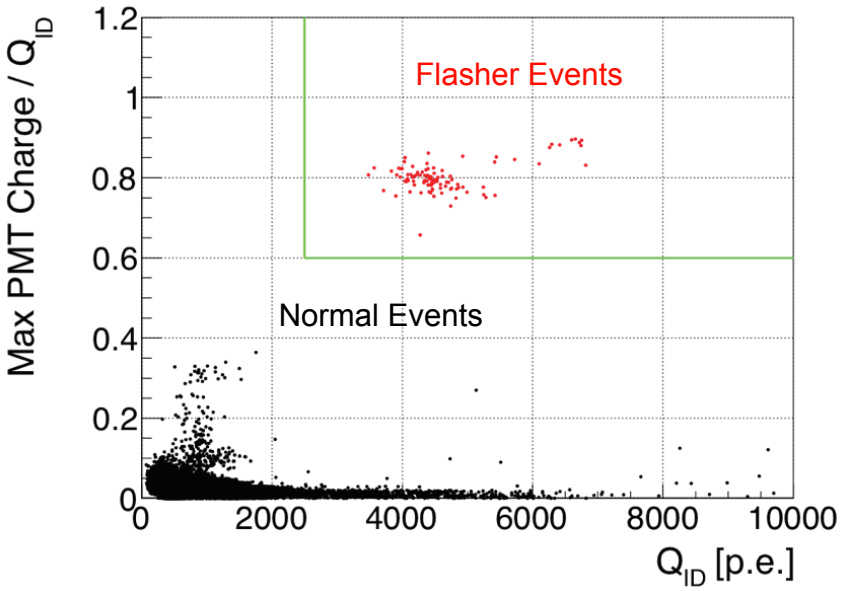

Figure 5.4: Flasher event selection criteria. The 'max PMT charge' means the maximum of the PMT charge of the inner detector in an event. The horizontal axis shows the total charge sum, and the vertical axis shows the ratio between the maximum PMT charge and the total charge. Green lines show the cut-off condition for the flasher events.

5.3.3 Ringing Event

After the KamFEE upgrade on Jun. 2003, fake muon signals start to appear in the data. These events are caused ringing in KamFEE baseline and are called "ringing event". Figure 5.5 shows the Δ T_{muon} distribution. The ringing events can be effectively rejected by $\Delta T_{muon} < 1\mu$sec cut, as shown in the figure. This events do not affect on the anti-neutrino analysis.

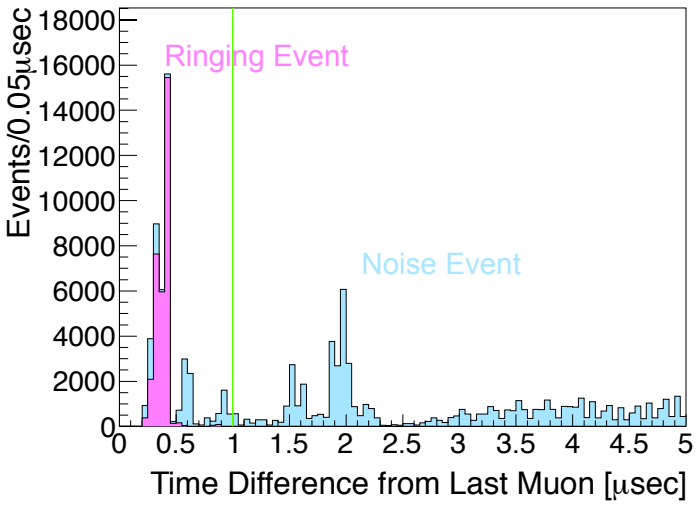

Figure 5.5: Time difference distribution from last muon. Ringing events are selected with $N_{hit} > 600$, and these can be effectively suppressed by the time correlation cut, $\Delta T_{muon} < 1$ μsec. The muon events are rejected in the both distribution.

5.4 Anti-Neutrino Selection

The selection criteria for anti-neutrino events are summarized in Table 5.2. The anti-neutrino delayed coincidence events are characterized by spatially correlated timely correlated two signals. To reject the muon and its related background, spallation cut and some kind of veto are applied. The details of each selection and its efficiencies are described in this section.

Table 5.2: Selection criteria for anti-neutrino events.

Parameters	Criteria
Prompt Energy	$0.9 < E_p < 8.5$ MeV
Delayed Energy	$1.8 < E_d < 2.6$ MeV
	$4.4 < E_d < 5.6$ MeV
Space Correlation	$\Delta R < 2.0$ m
Time Correlation	$0.5 < \Delta T < 1000$ μsec
Fiducial Volume	$R < 6.0$ m

5.4.1 Energy Cut

The prompt energy threshold 0.9 MeV corresponds to the energy threshold of inverse-beta decay. The delayed energy windows are optimized to effectively select mainly two types of signals.

- $1.8 < E_d < 2.6$: neutron capture on proton (99.48 %)
  This reaction emits 2.22 MeV γ-ray.

- $4.4 < E_d < 5.6$: neutron capture on ^{12}C (0.512 %)
  This reaction emits 4.90 MeV γ-ray.

The ratio of neutron capture on other nucleus such as ^{13}C is less than 1.0×10^{3} %, and negligible.

The selection efficiency on the delayed energy depends on the energy resolution.

$$\begin{aligned}&\text{(Efficiency of delayed delayed energy cut (1.8-2.6 MeV))}\\ &= \frac{1}{\sqrt{2\pi\sigma^2}}\int_{1.8\text{MeV}}^{2.6\text{MeV}} \exp\left(-\frac{(x-2.211)^2}{2\sigma^2}\right)dx \qquad (5.2)\\ &\text{(Efficiency of delayed delayed energy cut (4.4-5.6 MeV))}\\ &= \frac{1}{\sqrt{2\pi\sigma^2}}\int_{4.4\text{MeV}}^{5.6\text{MeV}} \exp\left(-\frac{(x-5.061)^2}{2\sigma^2}\right)dx \qquad (5.3)\end{aligned}$$

where σ is estimated energy resolution. The energy resolution for 17-inch and 17+20-inch PMTs (also shown in 3.3) and calculated efficiencies are summarized in Table 5.3. The effect of the resolution uncertainties is negligible.

Table 5.3: Delayed energy selection efficiency.

Period		17-inch	17+20-inch
before purification	σ [% / $\sqrt{\text{E[MeV]}}$]	7.0 ± 0.1	6.1 ± 0.1
	efficiency (1.8-2.6 MeV)	99.99 %	100 %
	efficiency (4.4-5.8 MeV)	100 %	100 %
after purification	σ [% / $\sqrt{\text{E[MeV]}}$]	8.2 ± 0.1	7.0 ± 0.1
	efficiency (1.8-2.6 MeV)	99.89 %	99.99 %
	efficiency (4.4-5.8 MeV)	99.99 %	100 %

5.4.2 Space Correlation

The distance and interval of prompt and delayed signals are essentially determined by the neutron thermal diffusion and capture process. The distance is also affected by the vertex resolution. The space correlation is evaluated using the MC, which includes the physics process and the effect of the vertex resolution in the detector. AmBe source calibration datas, which have prompt 4.4 MeV γ-rays and delayed 2.2 MeV neutron capture γ-rays, are useful for checking the space correlation efficiency. Figure 5.6 shows the result of AmBe calibration source located at the center of the detector. The neutron capture time is fitted to ∼208 μsec and the efficiency of ΔR $<$ 2.0 m cut is 99.84 %.

5.4.3 Time Correlation

The time correlation cut threshold 0.5 μ sec is applied to avoid the noise effect which comes from the electronics. The selection efficiency for the time correlation can be estimate directly using KamLAND data, the spallation neutron events. The time difference from the muon to the spallation neutron capture events are shown in Figure 5.7. In order to avoid the busy electronics condition due to the multiple neutrons, high charge muons are cut for this analysis. The mean capture time (τ) before and after purification are estimated to be 209.0 ± 2.7 μsec and 209.5 ± 3.9 μsec, respectively. Therefore, the efficiency of the time correlation is calculated using the fitting results as follows :

$$\begin{aligned}(\text{Efficiency of time correlation}) &= \frac{1}{\tau}\int_{0.5\mu\text{sec}}^{1000\mu\text{sec}} \exp\left(-\frac{t}{\tau}\right) dt \\ &= 98.93 \pm 0.05\%(\text{before purification}) \\ &= 98.92 \pm 0.06\%(\text{after purification})\end{aligned}$$

5.4.4 Spallation Cut and Veto

Interactions between cosmic muons and nuclei in the liquid scintillator produce not only neutrons, but also a variety of unstable isotopes. Most of them have short lifetime, and produce signals which can mimic anti-neutrino events.

- Low Energy Muon (Q $<$ 40,000 p.e.) : 2 msec whole volume veto

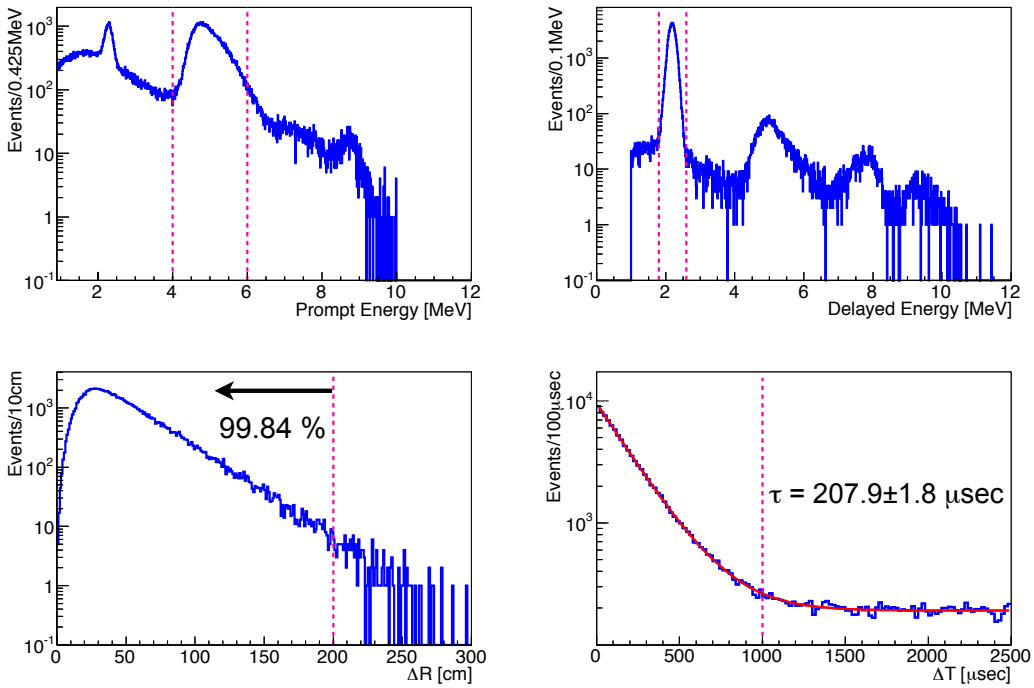

Figure 5.6: Delayed coincidence calibration using AmBe calibration source located at the center of the detector. The selection cuts for undisplayed parameters are applied, and each cut conditions are shown as pink lines. (Top-left) Prompt energy spectrum. Two peaks correspond to the neutron capture on proton (2.2 MeV) and the γ-ray emission from the first excited state of ^{12}C. (Top-right) Delayed energy spectrum. The accidental coincidence events of 4.4 MeV γ-ray overlap with the γ emission from the neutron capture on ^{12}C. (Bottom-left) Space correlation between the source position and the delayed neutron. The efficiency for the 2.0 m cut is estimated by counting the number of event, 99.84 %. (Bottom-right) Time correlation between the prompt and delayed event. The capture time is estimated with exponential feeing, $\sim$207.9 μsec.

- High Energy Muon (Q $>$ 40,000 p.e.)

  - Showering Muon (ΔQ $>$ 10^6 p.e.) : 2 sec whole volume veto
  - Bad Reconstructed Muon (badness $\geq$ 100) : 2 sec whole volume veto
  - Well Reconstructed Non-Showering Muon (badness $<$ 100 and ΔQ $<$ 10^6 p.e.) :
    2 msec whole volume veto and 2 sec cylindrical volume veto for the 3-m radius around the muon track.

Q is the total charge of 17-inch PMTs, ΔQ is the residual charge and badness is the parameter for muon reconstructed quality. The spallation products are described in Section 6.3.

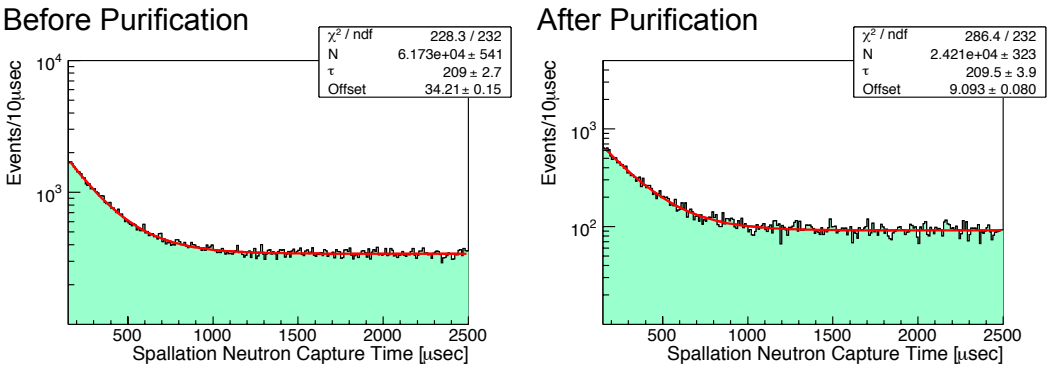

Figure 5.7: Time correlation between muons and spallation neutron capture events before (left) and after (right) purification. To avoid the unknown effe t from the multiple neutron events, the selection is $350 < \mathrm{NsumMax} < 550$ and $\Delta Q < 0$ p.e.. The mean capture time estimated by fitting are 209.0 ± 2.7 μsec and 209.5 ± 3.9 μsec, respectively.

5.4.5 Multiple Coincidence Cut

Multiple neutrons are emitted by the spontaneous fission of ^{238}U in the detector or neutral current interaction of the atmospheric neutrinos. Since these events are mis-identification as the delayed event signal of anti-neutrino events, the multiple coincidence cut is applied.

5.5 Live Time Calculation

The live time is defined as the active time period of the detector for neutrino observation, and calculated run by run from the following items.

- Run Time
  Time of the data taking period, defined as
  (time of the last event in the run) - (time of the first event in the run)

- Dead time
  Time of no data taking period or abnormal data taking period.

- Veto time
  Time of veto period for the background rejection such as muon events.

Deadtime

The deadtime is classified to five types :

- Bad run
  The definition of bad run is summarized in Section . The data quality is worse to use for the physics analysis. This run is vetoed for whole period.

- Half bad run
  A part of run satisfy the conditions of bad run. Typically, a trouble on HV supply in some crate leads to occur the bad period.

- Trigger disable period
  Since the trigger module is busy, the disable flag is recorded in the data.

- Trigger dead period
  The trigger dead period is caused by the broken data packet by network problem. That is tagged by the large time intervals (>100msec) between each history events.

- Missing muons
  The multiple noise events are usually coming within 150 μsec after muons because of the ringing on FEE baseline. If there is no muons within 150 μsec before a cluster of noise events, there is a possibility that a muon was missed because of an unknown deadtime. Mussing muons are tagged by multiple noise events preceded by no muons within 1 msec, and this period is conservatively taken to be deadtime. Another method, that the missing muon is tagged by missing waveform, i.e. Nhit (number of reconstructed waveform) < NsumMax.

The uncertainty of deadtime finding is estimated from 1 PPS trigger events. This trigger is the forced acquisition trigger at every second synchronizing with GPS module except the supernova trigger. Ideally the following relationship should be satisfied :

(Number of 1 PPS trigger) = (run time) - (veto time) - (supper nova trigger period). (5.4)

Then, the unknown deadtime ratio is defined as

$$R = \left| 1 - \frac{\text{Number of 1 PPS trigger} \times \text{1sec}}{\text{run time - veto time - supernova trigger period}} \right|. \quad (5.5)$$

Figure 5.9 shows the ratio of unknown deadtime. The average unknown deadtime ratio before and after purification is estimated to be ∼0.02 % and ∼0.01 %, respectively.

Live Time Calculation

The live time is calculated form the run time, the dead time, and the veto time information run by run. To check the overlap of each veto in time and volume, the MC generated events which have uniform timing and vertex distribution are used. The live time definition is as follows :

$$\frac{\text{live time}}{\text{run time}} = \frac{\text{number of events after applying all cuts}}{\text{numberofevents}} \quad (5.6)$$

The uncertainty of the live time calculation is dominated by the statistics of the generated events. About 10^7 events are generated and analyzed for a typical one day run, and the vetoed events are about 1 % of the total generated events for good runs. The uncertainty of the live time is derived from the unknown effect of the dead time period, which corresponds to 0.02 % and 0.01 % for before and after purification. Figure 5.9 shows the ratio between live time and run time for good runs and half bad runs.

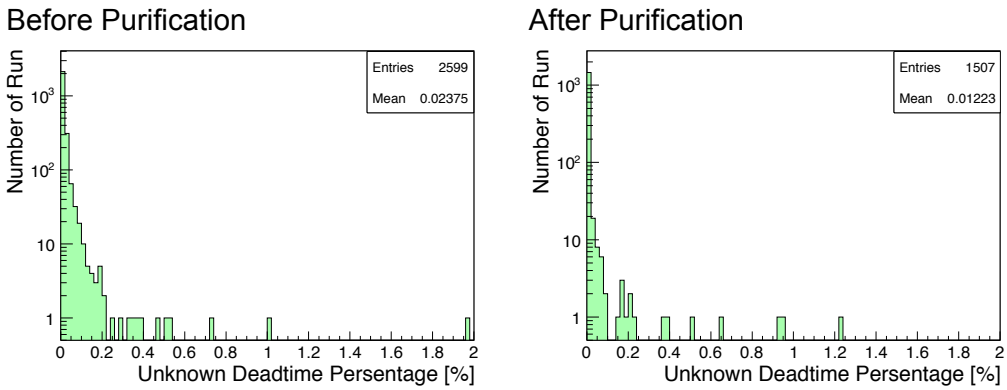

Figure 5.8: Unknown deadtime ratio before (top) and after (bottom) purification. The average unknown deadtime ratio is estimated to be ∼0.02 % and ∼0.01 %, respectively.

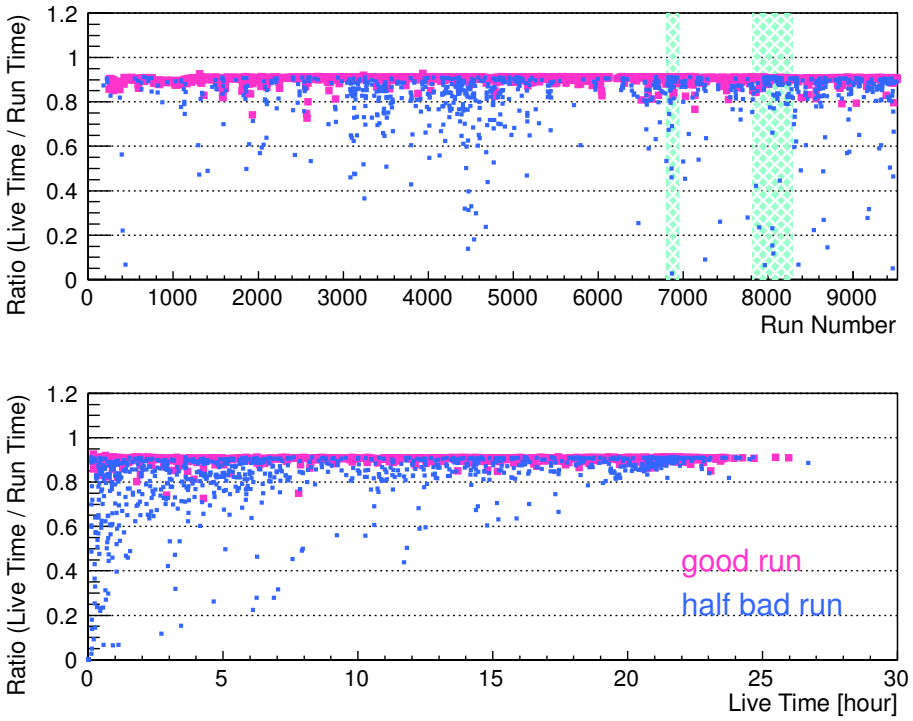

Figure 5.9: Ratio between live time and run time for each run. The pink points shows good runs, and blue points shows half-bad runs. The small ratio indicated that the run has noisy period. The average ratio for all runs is estimated to be 88.5 %.

5.6 Likelihood Selection

As described in Section , the candidates for the anti-neutrino delayed coincidence (DC) pairs are selected by performing the cuts of the energy, space correlation, time correlation and fiducial volume. In order to increase the ratio of signal to accidental background, a second-level cut is applied using a likelihood selection method. This analysis procedure is as follows :

1. select anti-neutrino DC pairs (1st-level cut, Section)
2. construct probability density function (PDF) for anti neutrino DC pairs ($f_{\bar{\nu}_e}$) and accidental DC pairs (f_{acci})
   The anti neutrino events $f_{\bar{\nu}_e}$ is constructed from GEANT4 simulation. On the other hand, the accidental events f_{acci} is evaluated directly from the data of accidental backgrounds.
3. select prompt energy dependent likelihood ratio ($L_{ratio}(E_{\text{prompt}})$) to get maximum figure of merit (FOM)
4. apply second-level cut for anti-neutrino DC pairs using selected L_{ratio}

5.6.1 Classification of Selection

The background rate fluctuates due to the liquid scintillator condition, especially whose impurely level of radioactive isotopes. Figure 5.10 shows the time variation of accidental DC event rate. These events are selected with same conditions of 1st-level cut, and plotted by each energy region. To address the changes in the accidental background rate, the dataset is classified 5 periods as summarized in Table 5.4. Especially LH-2 is prepared for the data corrected during purification or just after purification, whose background conditions are changeable due to the purification activities. The probability density functions for accidental DC pairs are verified for each periods.

Table 5.4: Dataset classification for likelihood selection.

Period	Date	Run	Livetime (Occupancy)
LH-0	March 9, 2002 - October 31, 2003	220 - 2985	461.5 d (20.1 %)
LH-1	November 1, 2003 - May 12, 2007	2986 - 6801	1056.2 d (46.0 %)
LH-2	May 12, 2007 - August 5, 2007	6802 - 6953	172.2 d (7.5 %)
	July 7, 2008 - April 7, 2009	7872 - 8501	
LH-3	August 6, 2007 - July 7, 2008	6954 - 7871	270.9 d (11.8 %)
LH-4	April 7, 2008 - May 18, 2010	8502 - 9519	335.2 d (14.6 %)

5.6.2 Probability Density Function for Signal and Background

The probability density function for accidental DC pairs f_{acci} is evaluated directly from the data of accidental backgrounds. The selection criteria for the accidental

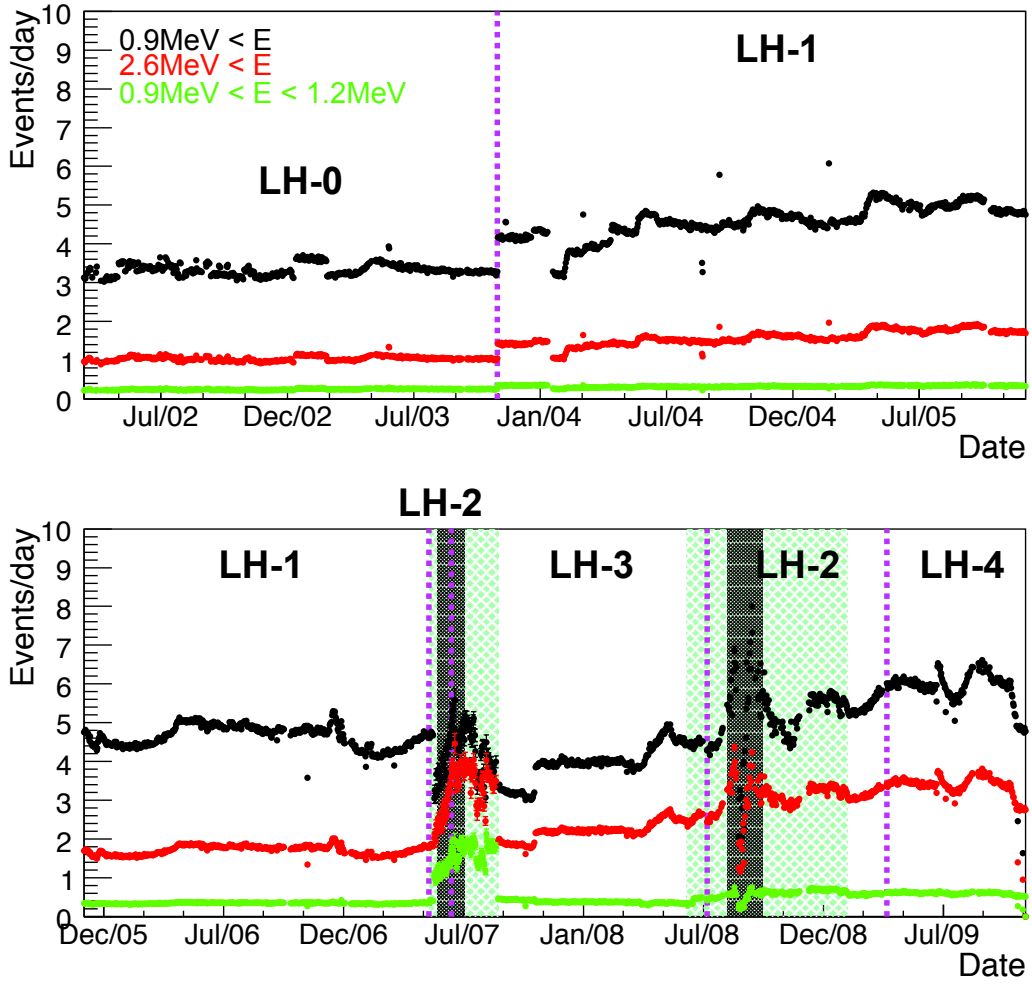

Figure 5.10: Time variation of accidental background rate for likelihood selection classification. The dataset is classified 5 periods defined as LH-0 to LH-4. Black, red and green points shows the accidental background rate for 0.9MeV $<$ E, 2.6 MeV $<$ E, and 0.9 $<$ E $<$ 1.2 MeV energy ranges, respectively. Green shaded areas correspond to the purification periods, and gray shaded areas show high dark rate periods because of purification activity.

backgrounds are summarized in Table 5.5. To investigate the contribution from the accidental backgrounds, the same 1st-level cut conditions on prompt / delayed energy and vertex correlation are applied for the accidental DC pairs selection. However, the time correlation cut is applied for an off-timing window, 10 msec $<$ ΔT $<$ 10 sec.

The probability density function for anti-neutrino DC pairs $f_{\bar{\nu}_e}$ is evaluated from GEANT4 simulation [24]. The prompt events are created from uniformly distributed events with proper charge dispersion, vertex resolution and energy resolution. The delayed neutron events are aerated from position generated vertices with neutron diffusion, 2.2 MeV γ charge dispersion, vertex resolution and energy resolution. The

time correlation between prompt and delayed events is independently simulated from the measured capture time.

The probability density functions for accidental DC pairs and anti-neutrino DC pairs are defined as $f_{acci}(E_{\rm p}\ ;\ E_{\rm d},\ \Delta R,\ \Delta T,\ R_{\rm p},\ R_{\rm d})$, and $f_{\bar{\nu}_e}(E_{\rm p}\ ;\ E_{\rm d},\ \Delta R,\ \Delta T,\ R_{\rm p},\ R_{\rm d})$, respectively. The accidental events and anti-neutrino events are divided into 1,200 bins ($= 76 \times 3 \times 16 \times 5 \times 5 \times 1$) defined as follows :

- $E_{\rm p}$ (76 bins) : 0.9 $\sim$ 8.5 MeV, every 0.1 MeV bin

- $E_{\rm d}$ (3 bins) :
  a. 2.0 $\sim$ 2.4 MeV
  b. 1.9 $\sim$ 2.0 MeV and 2.4 $\sim$ 2.5 MeV
  c. 1.8 $\sim$ 1.9 MeV and 2.5 $\sim$ 2.6 MeV

- ΔR (16 bins) :
  a. 0 $\sim$ 500 cm
  b. 50 $\sim$ 200 cm every 10 cm bin

- $R_{\rm p}$, $R_{\rm d}$ (5 bins, 5 bins) :
  a. 0 $\sim$ 500 cm
  b. 500 $\sim$ 600 cm every 25 cm bin

- ΔT (1 bin) :
  (accidental) non-binned but a uniform distribution from 0.5 μsec to 1000 μsec
  (anti-neutieno) non-binned but exponential distribution $e^{-t/211.1\mu{\rm sec}}$ from 0.5 μsec to 1000 μsec

Accidental events which have delayed energy between 4.4 MeV and 5.8 MeV are estimated independently.

Table 5.5: Accidental background selection for f_{acci}

Parameters	Criteria
Prompt Energy	0.9 MeV $<$ $E_{\rm p}$
Delayed Energy	1.8 $<$ $E_{\rm d}$ $<$ 2.6 MeV
Space Correlation	ΔR $<$ 2.0 m
Time Correlation	10 msec $<$ ΔT $<$ 20 sec
Fiducial Volume	R $<$ 6.0 m
Muon Veto	
·all μ	2 msec whole volume veto (prompt, delayed)
·showering μ, bad reconstructed μ	2 sec whole volume veto (delayed)
·non-showering μ	2 sec 3 m cylinder volume veto along μ track (delayed)

5.6.3 Definition of Likelihood Selection

To optimize the selection conditions using the likelihood method, the prompt energy dependent likelihood ratio ($L_{ratio}(E_{\rm p})$) is constructed as a selection parameter.

$L_{ratio}(E_{\rm p})$ is defined as follows :

$$L_{ratio}(E_{\rm p}) = \frac{f_{\bar{\nu}_e}}{f_{\bar{\nu}_e} + f_{acci}}. \tag{5.7}$$

For each 0.1 MeV interval in prompt energy, $L_{cut}(E_{\rm p})$ is selected for getting the best figure of merit (FOM) defined as follows :

$$FOM(E_{\rm p}) = \frac{S(L_{ratio})}{\sqrt{S(L_{ratio}) + B_{acci}(L_{ratio})}}, \tag{5.8}$$

where

$$\begin{aligned} S(L_{ratio}) &\equiv \int_{L_{ratio}}^{1} (\text{number of signal events with } L) dL \\ B_{acci}(L_{ratio}) &\equiv \int_{L_{ratio}}^{1} (\text{number of accidental events with } L) dL. \end{aligned} \tag{5.9}$$

S is the number of anti-neutrino events expected from the unoscillated reactor and geo anti-neutrino. B_{acci} is the number of observed accidental background which selected with the same cut conditions for anti-neutrino candidates. Since the f_{acci} is constructed based on the events selected with off-timing window, ΔT_{acci}(10msec $\sim$ 20sec, the number of selected accidental background should be scaled by the time window ratio. It means

$$\text{scaling factor} = \frac{\Delta T_{\bar{\nu}_e}(0.5\mu\text{sec} \sim 1000\mu\text{sec})}{\Delta T_{acci}(10\text{msec} \sim 20\text{sec})} = 5.0 \times 10^{-2}. \tag{5.10}$$

Figure 5.11 shows the prompt energy distribution of input anti-neutrino signal for LH-0 period. This input signal is arranged for each period. Figure 5.12 and 5.13 represent the procedure for getting $L_{cut}(E_{\rm p})$ for each 0.1 MeV $E_{\rm p}$ bin. Top figures show the signal and accidental distribution as a function of L_{ratio}. As shown by Eq. (5.9), $S(L_{ratio})$ and $B_{acci}(L_{ratio})$ are the results of integration from L_{ratio} to 1. The center figures show signal and background distribution. Finally, from these distribution, the maximum figure of merit at each $E_{\rm p}$ is evaluated as shown in the bottom figures. The green lines represent the L_{cut} for each $E_{\rm p}$. Figure 5.14 shows the estimated maximum figure of merit distribution for 17-inch and 17+20-inch PMTs cases. The $L_{cut}(E_{\rm p})$ which has the maximum figure of merit distributes as shown in Figure 5.15. This parameter is used for secant-level event selection.

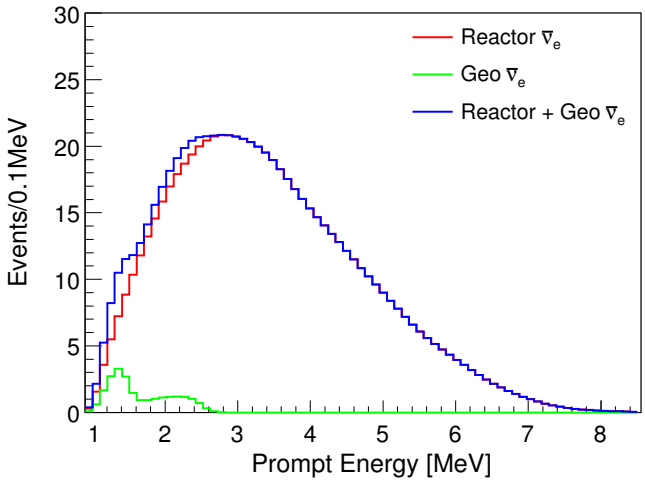

Figure 5.11: Energy distribution of input anti-neutrino signal for likelihood selection and LH-0 period. The green line shows the reactor anti-neutrino and the blue line shows the geo anti-neutrino, respectively. The red line shows the sum of the green and the blue histogram. These spectrum represent no-oscillation case, and cut with 6.0 m fiducial volume.

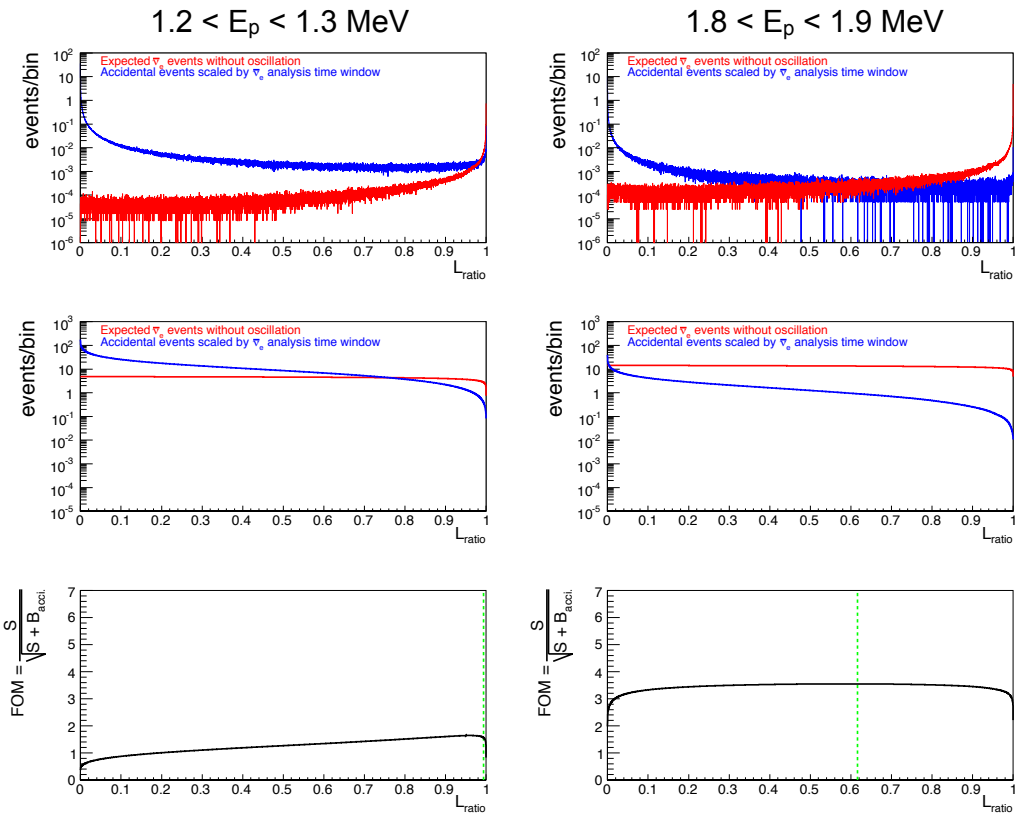

Figure 5.12: Procedure for $L_{cut}(E_{\mathrm{p}})$ estimation of 2.5 to 2.6 MeV and 3.5 to 3.6 MeV cases. Top figures show the signal and accidental distribution as a function of L_{ratio}, center figures show signal and background distribution constructed by integrating the top figures, and bottom figures are show figure of merit distribution. Finally, estimated $L_{cut}(E_{\mathrm{p}})$ are represented as green lines.

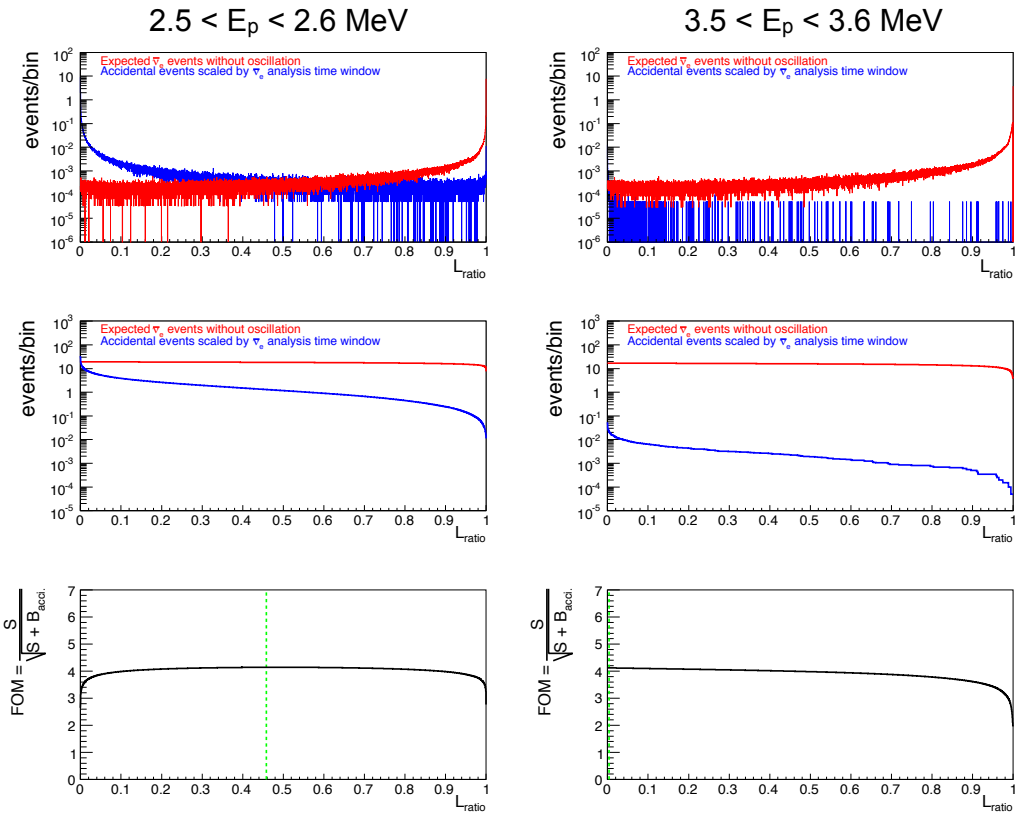

Figure 5.13: Procedure for $L_{cut}(E_{\mathrm{p}})$ estimation of 2.5 to 2.6 MeV and 3.5 to 3.6 MeV cases.

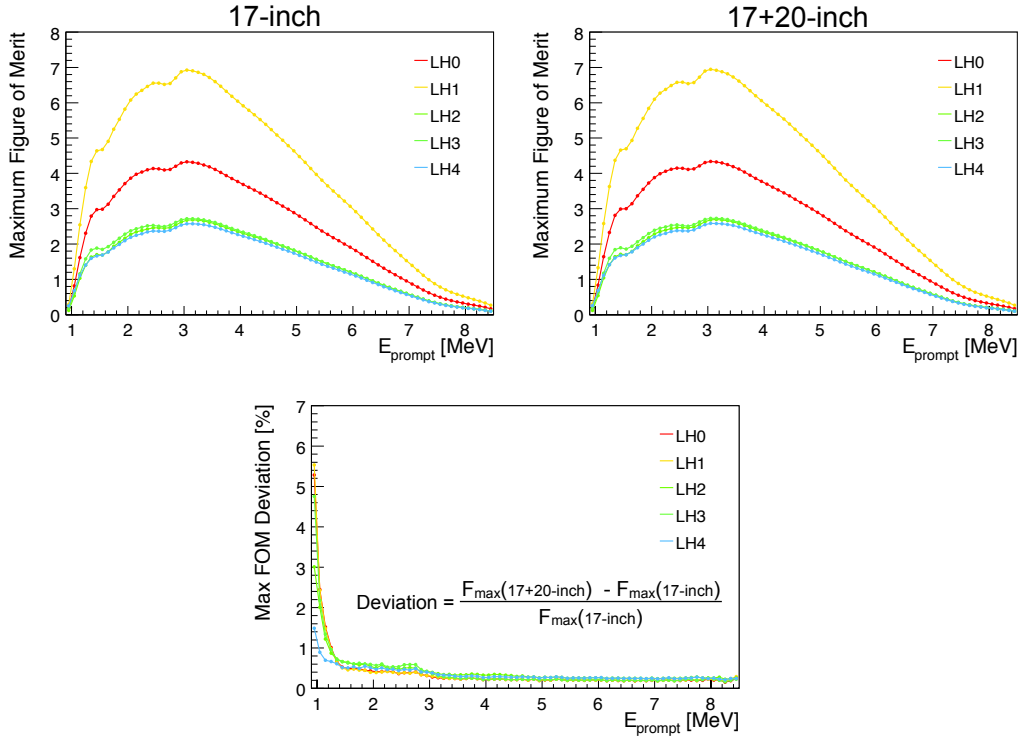

Figure 5.14: Maximum figure of merit as a function of E_{p} for each LH period. Top figures show 17-inch and 17+20-inch analysis case, respectively. Bottom figure shows the deviation between the maximum FOM for 17-inch and 17+20-inch cases. As the prompt energy becomes smaller, the deviation becomes larger.

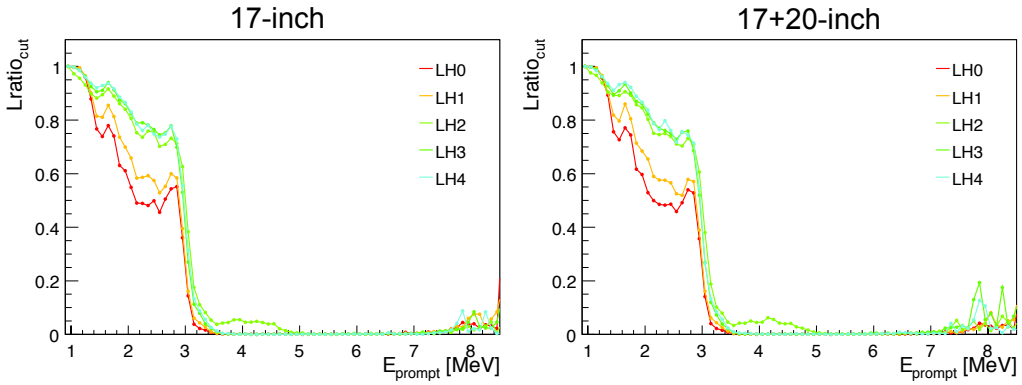

Figure 5.15: L_{cut} distribution as a function of E_{p} for each LH period. 17-inch and 17+20-inch PMT analysis cases are shown. The L_{cut} which his the maximum figure of merit is used for the event selection.

5.6.4 Efficiency Estimation

The prompt energy dependent detected efficiency $\varepsilon(E_{\rm p})$ is evaluated for each LH period using the MC. 1.0×10^7 anti-neutrino events are simulated uniformly in the 7.5 m radios for each $E_{\rm p}$ bin, and the likelihood selection cut is applied. $\varepsilon(E_{\rm p})$ is calculated from the number of anti-neutrino events after all selection cut are applied divided by the number of generated events in 6.0 m radius. $\varepsilon(E_{\rm p})$ definition is as follows :

$$\varepsilon(E_{\rm p}) = \frac{\text{number of survival events after all selection applied}}{\text{number of generated events in R} < 6\text{ m}}. \tag{5.11}$$

Time Variation of Efficiency

As discussed in Section 3.3.3, the liquid scintillator purification caused a decrease in the light yield. This change has a chance to affect vertex and energy resolution. Since the selection efficiency of anti-neutrino events is based on counting the number of remaining events, it can be affected by the quality of event reconstruction. To address the change in the detector, the time dependent selection efficiency which estimated by the source calibration data and the 2.2 MeV neutron capture γ events.

To reduce the energy scale gap between before and after purification, source calibration data and spallation capture events are analyzed minutely in z-axis, off-axis and time dependence run by run except for off-axis dependence after purification.

- During Purification
  - z-axis : neutron capture on proton ($\pm$ 5 days average)
  - off-axis : neutron capture on proton ($\pm$ 5 days average)
  - time variation : neutron capture on proton ($\pm$ 3 days average)
- After Purification
  - z-axis : ^{60}Co source calibration
  - off-axis : neutron capture on proton in two periods
  - time variation : neutron capture on proton ($\pm$ 3 days average)

From this analysis, the correction factor $F_{\rm z-axis}$, $F_{\rm off-axis}$ and $F_{\rm time}$ are evaluated to reconstruct visible energy stably. A correction factor F_ε, called "quenching factor", is defined for time-dependent selection efficiency as follows :

$$F_\varepsilon = F_{\rm z-axis} \times F_{\rm off-axis} \times F_{\rm time} \tag{5.12}$$

Figure 5.16 shows the time variation of the quenching factor. For dataset collected before purification, the quenching factor is set at 1.0 for 17-inch and 17+20-inch PMTs analysis in order to reflect estimated vertex and energy resolution before purification for calculation. The quenching factor after purification is evaluated in response to time-dependent fluctuation. Finally, time-dependent energy and vertex resolution for selection efficiency estimation are calculated as follows :

$$\text{Energy resolution} : \sigma_{\rm E} = \sigma_{\rm E}(\text{before purification}) \times \sqrt{E \times F_\varepsilon} \tag{5.13}$$

$$\text{Vertex resolution} : \sigma_{\rm Vertex} = \sigma_{\rm Vertex}(\text{before purification})/\sqrt{E/F_\varepsilon}, \tag{5.14}$$

where σ_{E}(before purification) [%/$\sqrt{\mathrm{E}}$] and σ_{Vertex}(before purification) [cm $\cdot$ $\sqrt{\mathrm{E}}$] are energy and vertex resolution estimated by calibration data analysis, and E is the energy of simulated events.

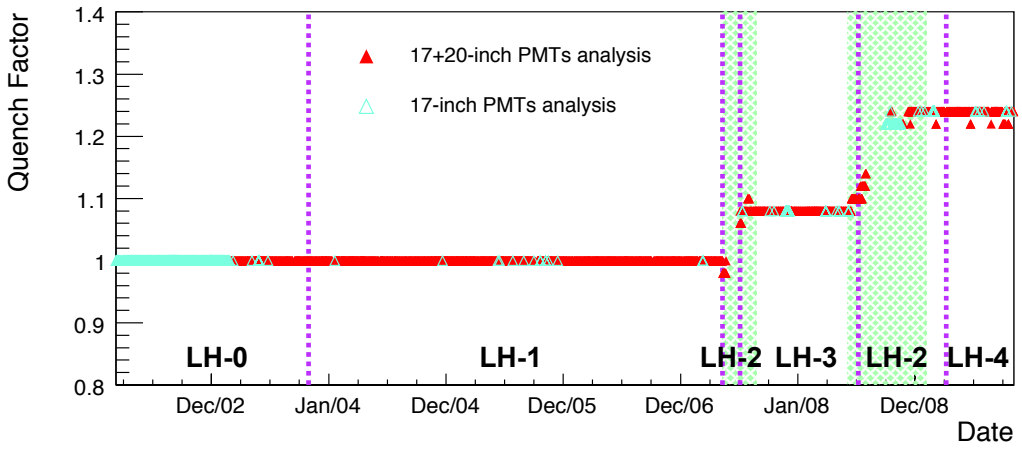

Figure 5.16: Quenching factor for time-dependent selection efficiency calculation. Red triangle and blue triangle show the quenching factor for 17-inch PMTs and 17+20-inch PMTs analysis. Green shaded areas show the purification periods. This quenching factor can lead to the change in the detector, such as the decreasing in the light yield.

- Comparison between 17-inch, 17+20-inch PMTs analysis, and without likelihood selection
  Figure 5.17 shows the selection efficiency after applying likelihood selection. Below 1.2 MeV, the efficiency is lower due to ^{210}Bi accidental events. The valley around 1.4 MeV corresponds to ^{40}K γ-ray accidental events from the balloon film and ropes. Moreover, ^{208}Tl γ-ray accidental events which come from the outside of the detector affect the efficiency around 2.6 MeV. Above 3.0 MeV, there are no radioactive isotopes which give accidental backgrounds. Therefore the difference between the selection efficiency with and without likelihood selection is very small in the high energy region.

- Comparison between five likelihood selection periods
  Figure 5.19 shows the selection efficiency for each likelihood selection periods. Above 3.0 MeV, the difference between the each period is very small. On the other hand, lower than 3.0 MeV, the selection efficiencies for LH-0 and LH1 are larger than that for LH-2, LH3, and LH-4. In July 2007, Kashiwazaki-Kariwa nuclear power station was stopped due to an earthquake. Since that station is most effective for KamLAND, the reactor anti-neutrino event rate clearly decreased after the earthquake. Therefore that difference at low energy region is caused by the decreasing in the anti-neutrino signals.

- Comparison between quenching factor F_ε
  Figure 5.19 shows the selection efficiency difference between each quenching factor. As quenching factor becomes larger, the deviation from $F_\varepsilon = 1.0$ becomes larger, especially in the low energy region. The deviation is performed within -1.1 % at the maximum.

5.6.5 Uncertainties of Likelihood Selection

- Binned Efficiency
  As shown Figure 5.11, the input signal spectrum is divided by 0.1 MeV bins. However, the actual signal is continuous. The uncertainty of binned signal is estimated from the difference between the number of input signal and the number of counting signal. Its uncertainty is 0.8 % for the geo neutrino analysis and less than 0.1 % for the reactor neutrino analysis.

- Uncertainty of time correlation cut
  The uncertainty of time correlation cut for the likelihood selection is estimated from the neutron capture time shown in Figure 5.7.

- Uncertainty of space correlation cut
  The uncertainty of space correlation cut for the likelihood selection is estimated from the difference between data and simulation using GEANT4. ^{68}Ge (2×0.511 MeV γ) and AmBe (2.2 MeV neutron capture on proton) calibration source datas are used for this estimation. The simulation events are constructed from 0 MeV e^+ and 2$\sim$6 MeV neutrons for same conditions of KamLAND, such as detector geometry, charge dispersion, neutron diffusion and vertex/energy resolution.

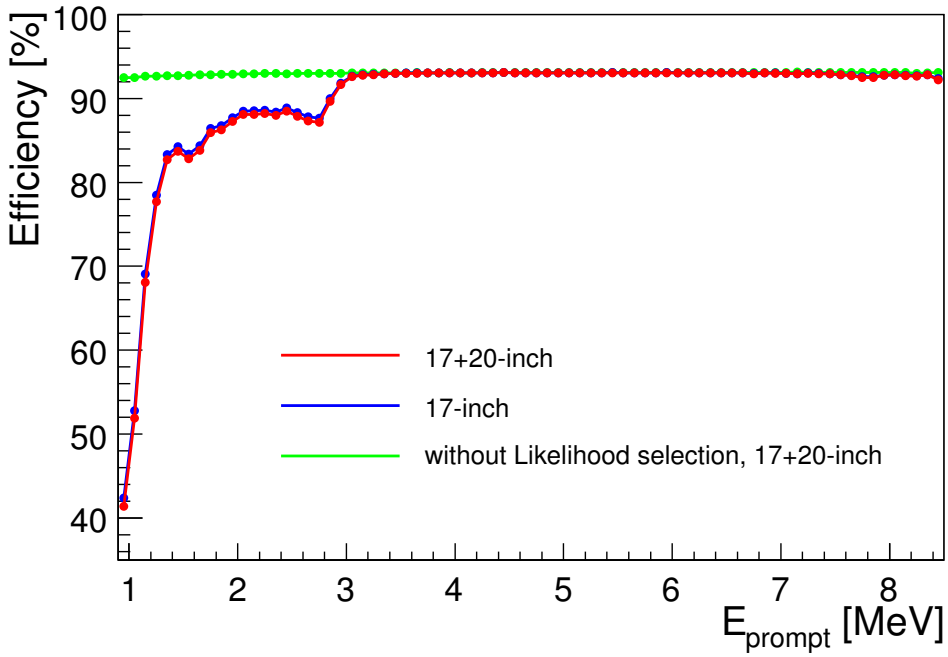

Figure 5.17: Selection efficiency after applying the likelihood selection as a function of the prompt energy. Read and blue points show the selection efficiency for 17+20-inch and 17-inch PMTs analysis. Green points shows the selection efficiency for 17+20-inch PMT analysis without the likelihood selection. Below 1.2 MeV, the selection efficiency decreases due to the ^{210}Bi accidental background. The valley around 1.4 MeV and 2.6 MeV correspond to the ^{40}K γ-ray and ^{208}Tl γ-ray accidental backgrounds. Above 3.0 MeV, the selection efficiency is stable because there are no radioactive sources which have high energy region, and almost same as without likelihood selection case.

- Uncertainty of delayed energy cut
  The uncertainty of delayed energy cut for the likelihood selection is also estimated from the simulation.

Figure 5.20 shows the uncertainty for the likelihood selection as a function of the prompt energy.

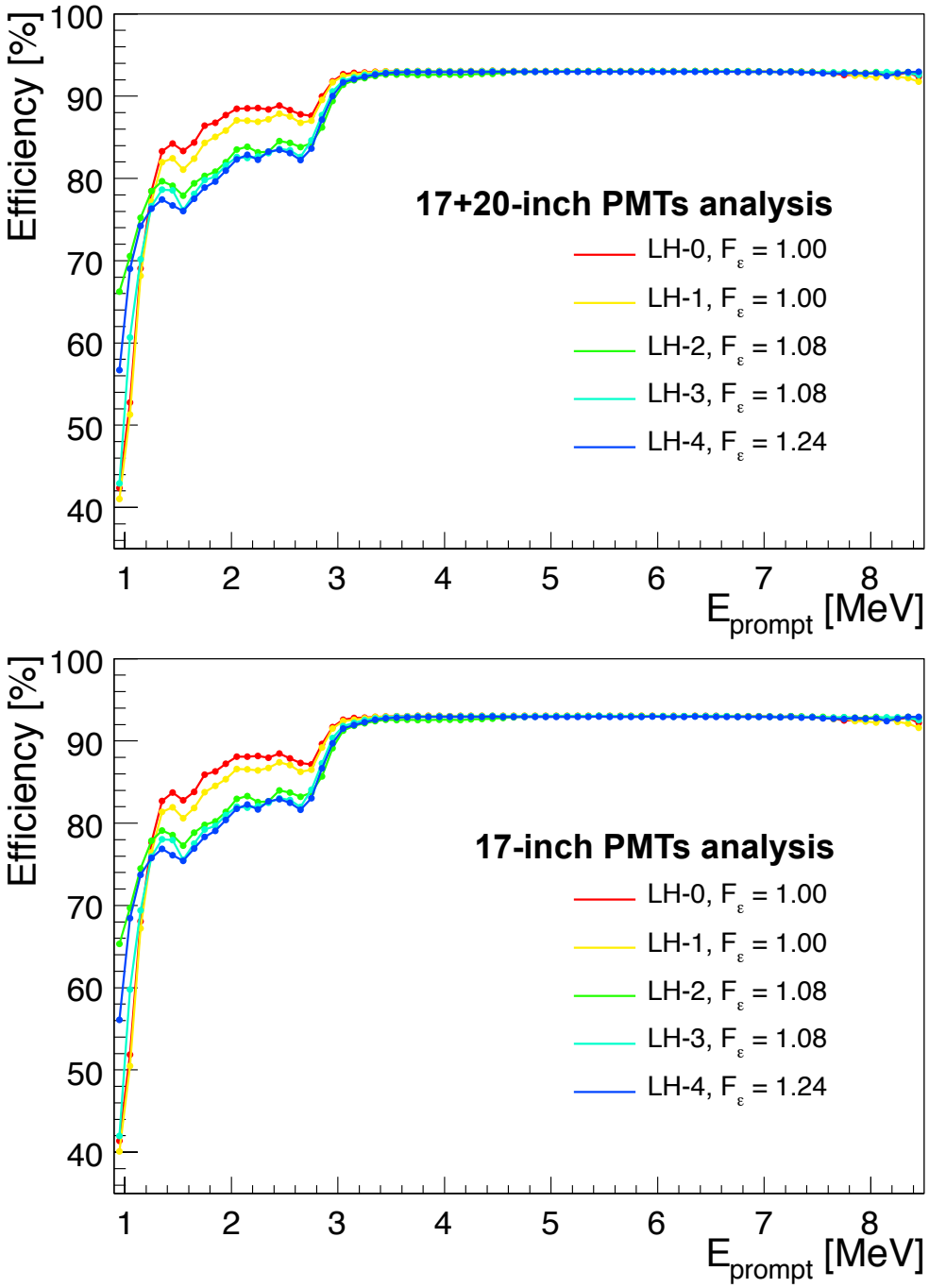

Figure 5.18: Selection efficiency for five likelihood selection periods in 17+20-inch (top) and 17-inch PMTs analysis. Below 3.0 MeV, the selection efficiency for LH-2, LH-3 and LH-4 are smaller than that for LH-0 and LH-1. In July 2007, the Kashiwazaki-Kariwa nuclear power station was stopped due to an earthquake, and the anti-neutrino event rate in the detector decreased. This difference is caused by the decreasing in the anti-neutrino signals.

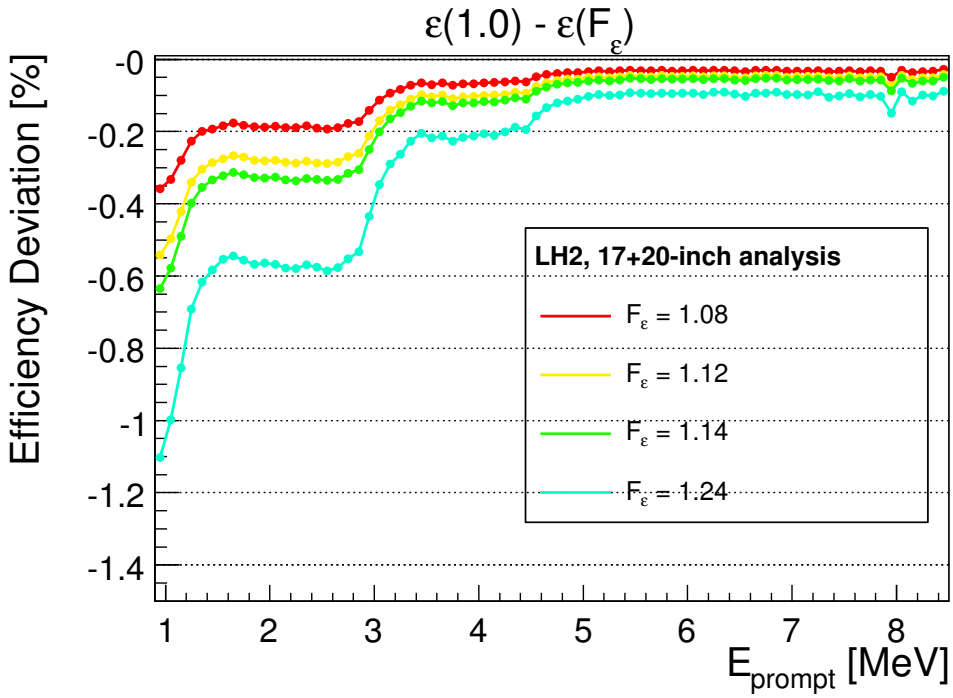

Figure 5.19: Deviation of the selection efficiency for each quenching factor F_ε. This figure shows at the case of LH-2 period. Vertical axis shows the selection efficiency deviation between $F_\varepsilon = 1.0$ case. This deviation is performed within -1.1 % at the maximum.

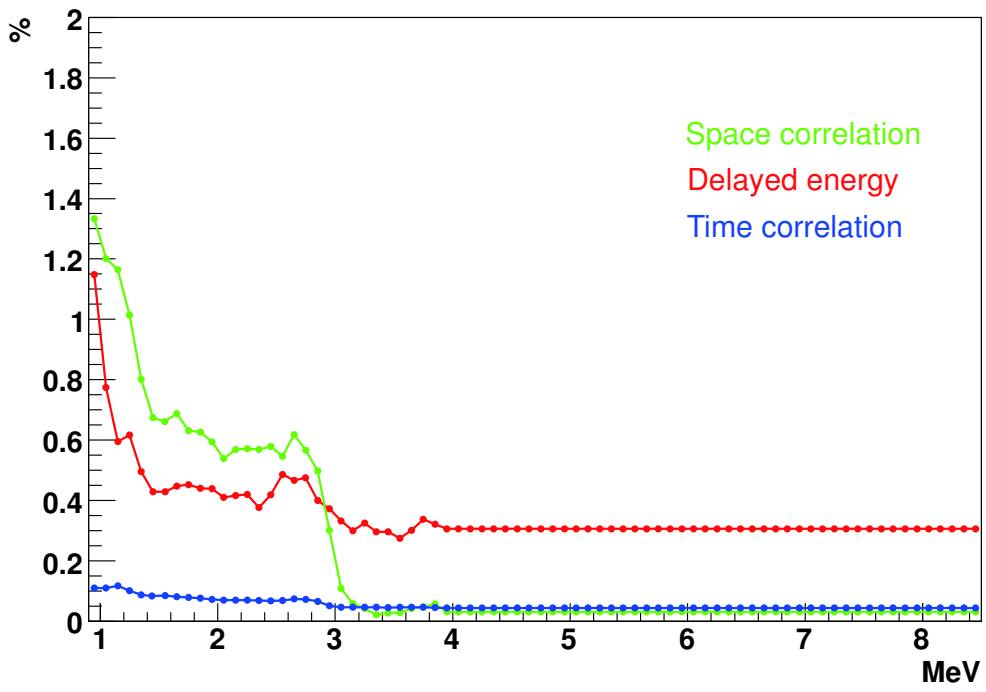

Figure 5.20: Uncertainties from likelihood selection for LH-0 period. Green, red and blue points show the uncertainties for space correlation, delayed energy and time correlation, respectively. These uncertainties have energy dependence only below ∼3 eV.

5.7 Anti-Neutrino Candidate

The selection criteria for the anti-neutrino are described in Section (1st-level cut) and (2nd-level cut, the likelihood selection). Finally, the event reduction procedure to select the final-sample of anti-neutrino events is shown.

5.7.1 Event Reduction

The anti-neutrino candidate are selected using the following reduction procedure. A reducing factor, F, is also estimated on each process.

1. Bad-run and Deadtime Reduction
   · Total runtime = 2481.09 days $\Longrightarrow$ Total livetime = 2296.01 days (1.46×10^{10} events)
   · $F \sim 0.925$

2. Noise and Flasher Cut
   · $1.46 \times 10^{10} \Longrightarrow 9.99 \times 10^{9}$ events
   · $F \sim 0.683$

3. Muon Event Cut
   · $9.99 \times 10^{9} \Longrightarrow 9.91 \times 10^{9}$ events
   · $F \sim 0.992$

4. 2 msec veto after muons
   · $9.91 \times 10^{9} \Longrightarrow 9.85 \times 10^{9}$ events
   · $F \sim 0.994$

5. Delayed Coincidence Selection
   · Selection Criteria
   - Prompt Energy : $0.9 < \mathrm{E_p}$ (only lower cut)
   - Delayed Energy : $1.8 < \mathrm{E_d} < 2.6$ MeV, $4.4 < \mathrm{E_d} < 5.6$ MeV
   - Space Correlation : $\Delta\mathrm{R} < 2.0$ m
   - Time Correlation : $0.5 < \Delta\mathrm{T} < 1000$ μsec

   · $9.85 \times 10^{9} \Longrightarrow 2.00 \times 10^{6}$ events
   · $F \sim 2.03 \times 10^{-4}$

6. 6.0 m Fiducial Volume Cut
   · $2.00 \times 10^{6} \Longrightarrow$ 31,462 events
   · $F \sim 0.016$

7. Spallation Cut
   · 31,462 $\Longrightarrow$ 25,784 events
   · $F \sim 0.820$

8. Upper Prompt Energy Cut ($E_\mathrm{p} < 8.5$ MeV)
   · 25,784 $\Longrightarrow$ 25,667 events
   · $F \sim 0.995$

9. Multiple Neutron Events Cut
   · 25,667 $\Longrightarrow$ 25,656 events
   · $F \sim 0.999$

10. Likelihood Selection
   · 25,656 $\Longrightarrow$ 2,249 events
   · $F \sim 0.088$

Above all procedures for the anti-neutrino event selection are shown in Figure 5.21. The 1st spectrum has huge high energy events such as the noise and the flusher events, muons, and muon related events. After applying the muon related cuts, the delayed coincidence selection effectively rejects the accidental backgrounds which do not have the correlation of the space and the time. The rejection factor of the delayed coincidence selection is estimated to be 2.03×10^{-4}. Furthermore, the fiducial volume cut can suppress the radioactive backgrounds which related to the balloon and the rope. The anti-neutrino candidate events after applying the 1st-level cut still has the accidental backgrounds caused by ^{208}Tl, ^{40}K and ^{210}Bi. However, since they have different vertex distribution and correlation, they can be strongly reduced by the likelihood selection. The number of the final candidates is estimated to be 2,249 events after applying all cuts.

5.7.2 Anti-Neutrino Candidate

Finally, 2,249 events remain above 0.9 MeV prompt energy threshold after applying all selections. To check these events profile, Figure 5.22, 5.23, 5.24, 5.25 and 5.26 are shown using various parameters. From these figures, the accidental backgrounds are efficiently rejected, especially above 3.0 MeV. The tight delayed energy cut is found to be useful for removing ^{208}Tl contribution for low energy region (E_{prompt} ¡ 1.4 MeV).

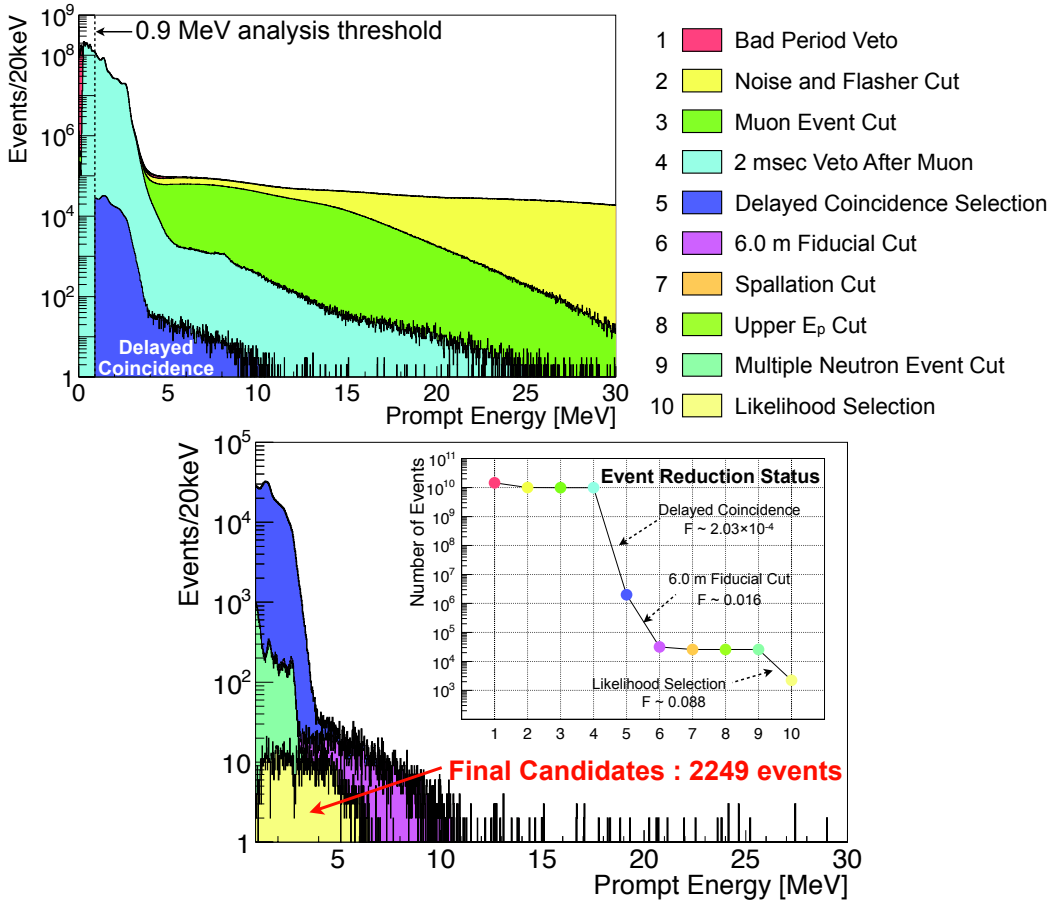

Figure 5.21: Transition of prompt energy distribution with the anti-neutrino selection. As shown at top-right legend, ten steps of the anti-neutrino selection are applied. These colors correspond to the prompt energy spectrum after applying the selection. In the bottom figure, the status of the number of survival events at each selection. The delayed coincidence selection clearly rejects the background events, and its reduction factor is estimated to be 2.03×10^{-4}. Finally, the accidental backgrounds are strongly rejected by the likelihood selection. The final number of the anti-neutrino candidates is estimated to be 2,249 events.

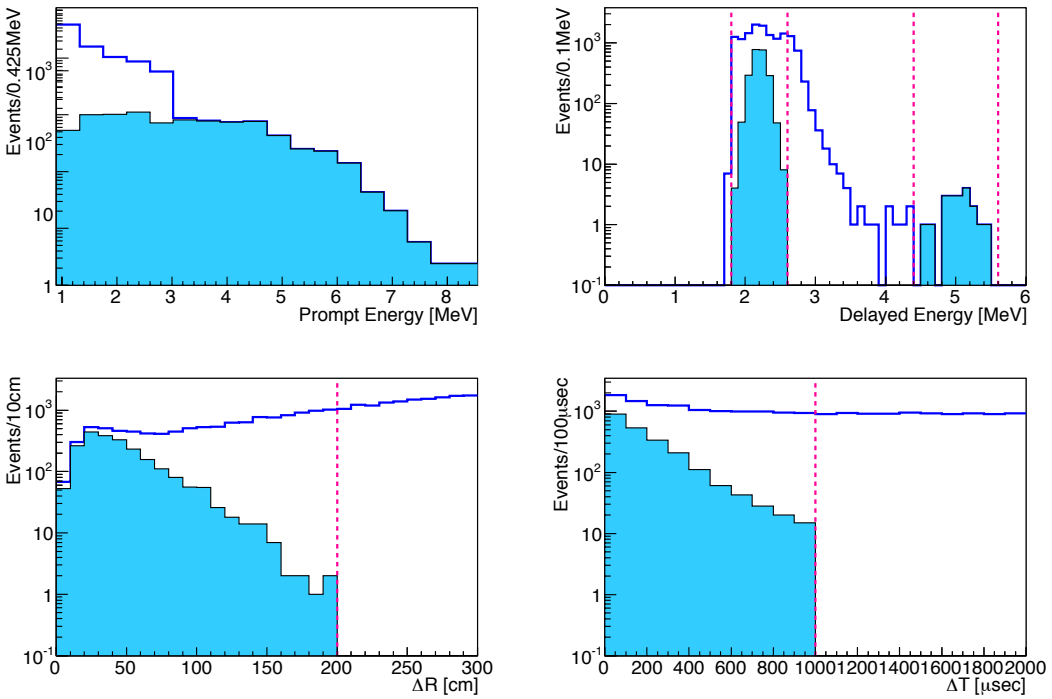

Figure 5.22: Profiles of anti-neutrino candidates. The blue line histogram shows the events before applying the likelihood selection, and the light-blue shaded histogram shows 2,249 final candidates after applying the likelihood selection. The pink lines show the selection criteria for each parameters.
(Top-Left) Prompt energy distribution
(Top-Right) Delayed energy distribution
(Bottom-Left) Vertex correlation between prompt and delayed events
(Bottom-Right) Time correlation between prompt and delayed events
The accidental coincidence events below prompt energy 3.0 MeV are clearly rejected by the likelihood selection.

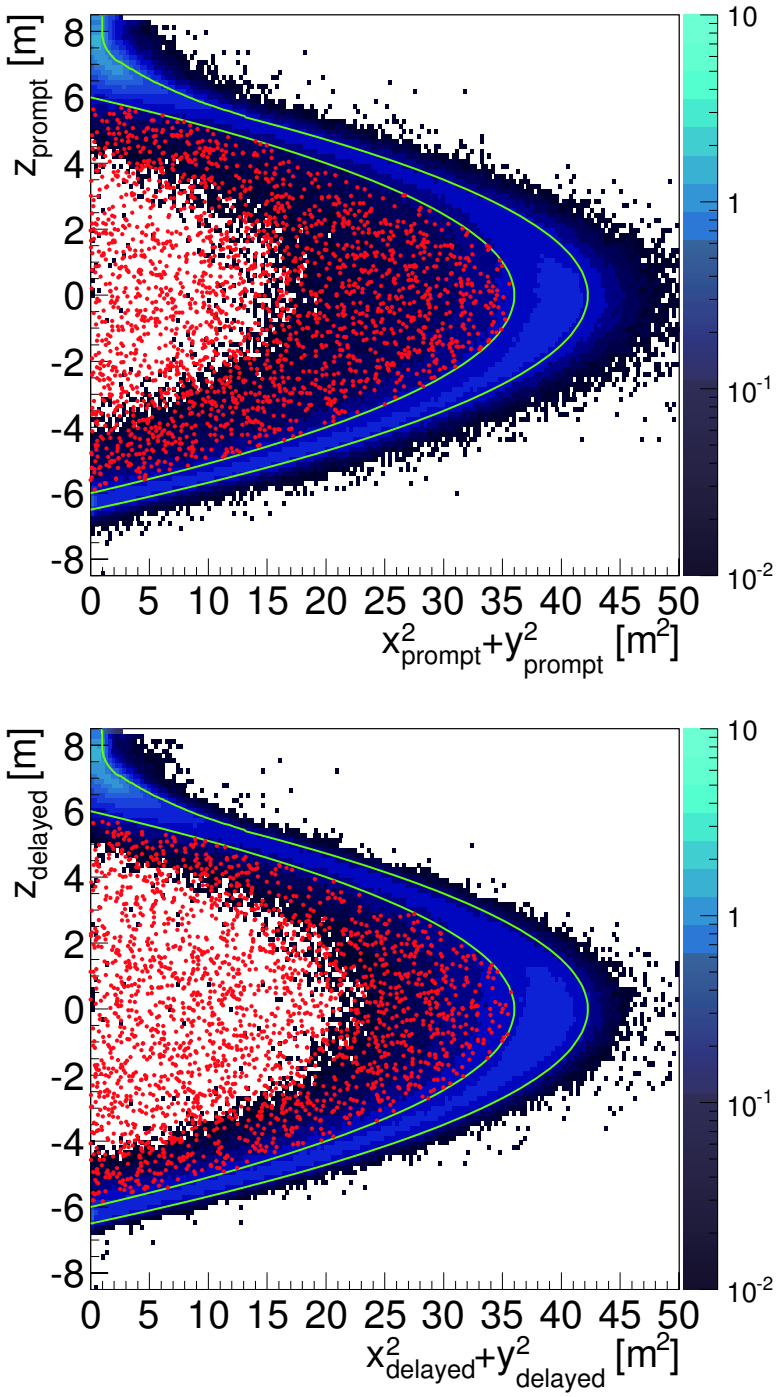

Figure 5.23: Vertex distribution of anti-neutrino candidates for prompt (top) and delayed (bottom) events. The histogram shows the events rejected by the likelihood selection, and the red points show the final sample of anti-neutrino candidates after applying the likelihood selection. The green lines show the KamLAND balloon and the 6.0 m fiducial radios.

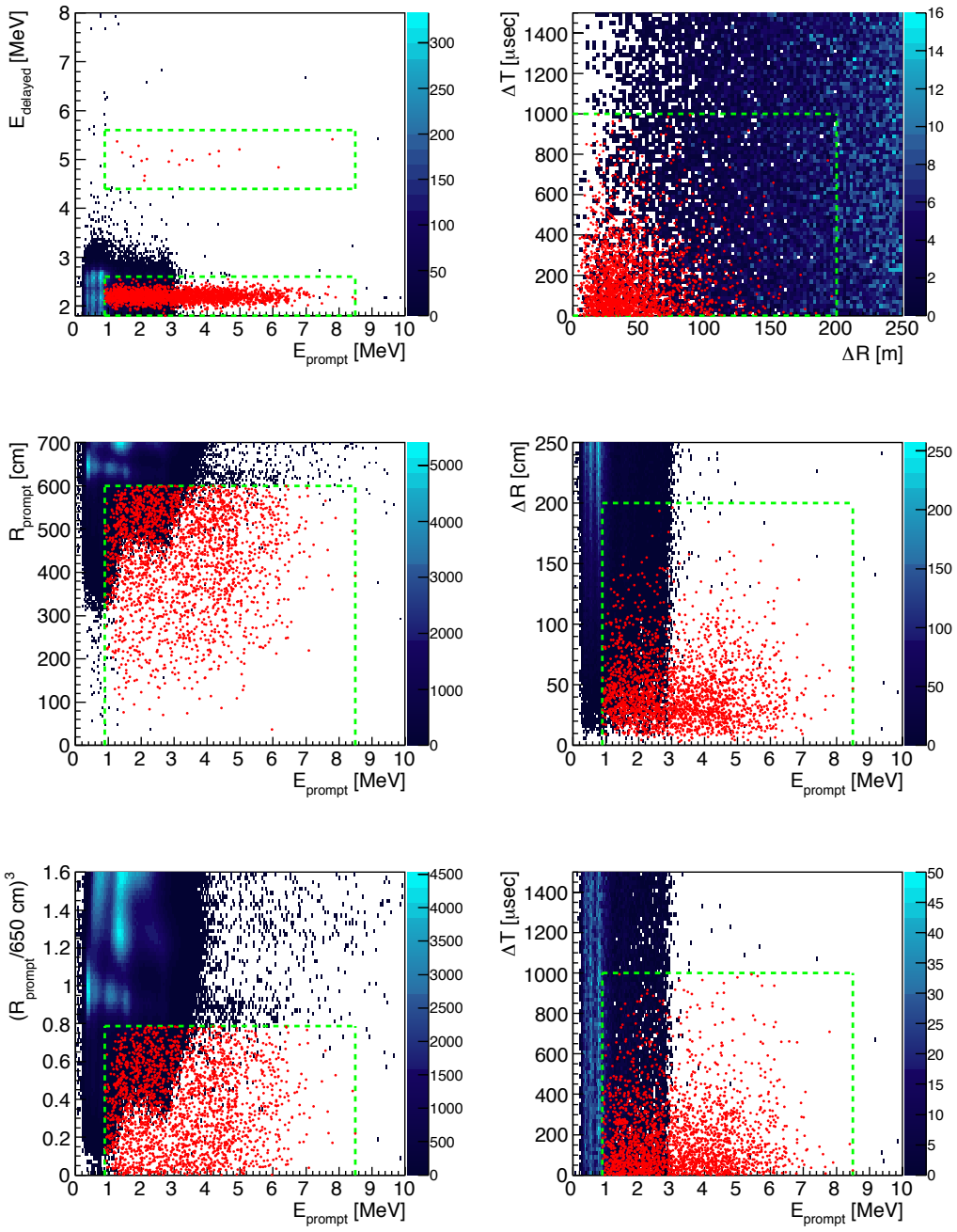

Figure 5.24: Various correlation of anti-neutrino candidates. The histogram shows the events rejected by the likelihood selection, and the red points show the final samples of anti-neutrino. The green lines show the selection criteria.
(Top-Left) E_{prompt} and $E_{delayed}$: Around E_{prompt} 0.9MeV, events are rejected by tight $E_{delayed}$ cut.
(Top-Right) ΔR and ΔT : The events which have large ΔR and Δ are rejected.
(Middle-Left) E_{prompt} and R_{prompt} : The events which have low E_{prompt} and large R_{prompt} are rejected.
(Middle-Right) E_{prompt} and ΔR
(Bottom-Left) E_{prompt} and $R^3{}_{prompt}$
(Bottom-Right) E_{prompt} and ΔT

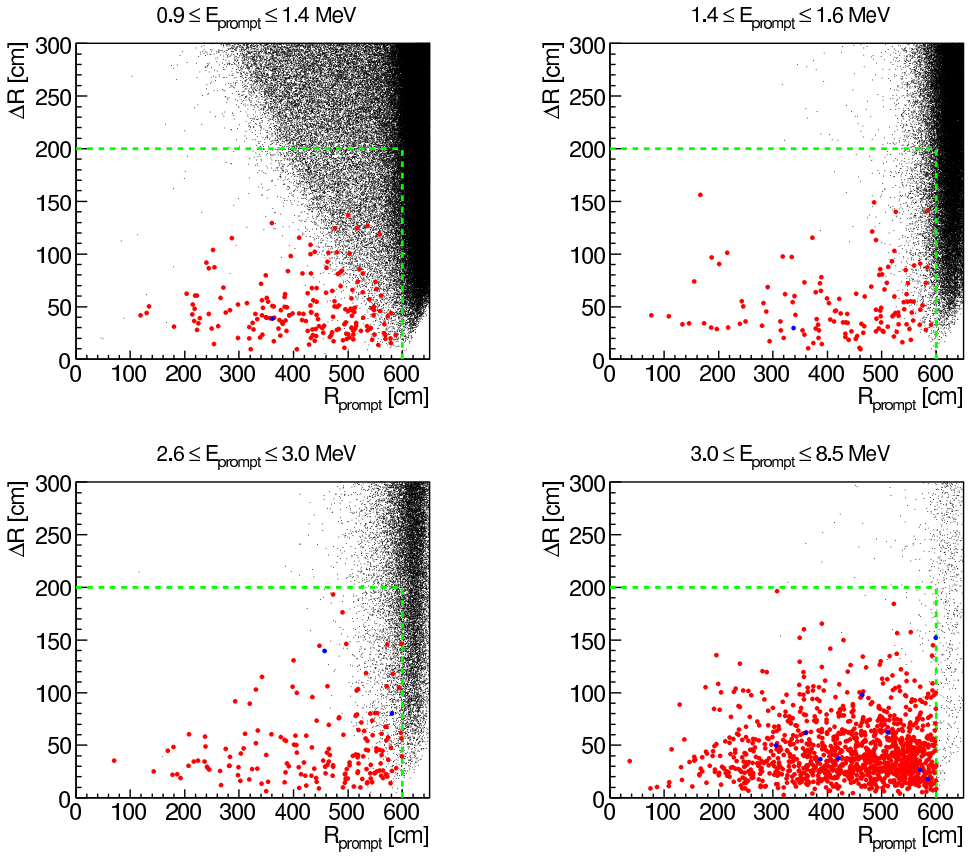

Figure 5.25: Correlation between R_{prompt} and ΔR of anti-neutrino candidates. The prompt energy is selected for each figure,
$0.9 \leq E_{prompt} \leq 1.4$ MeV (top-left), $1.4 \leq E_{prompt} \leq 1.6$ MeV (top-right), $2.6 \leq E_{prompt} \leq 3.0$ MeV (bottom-left) and $3.0 \leq E_{prompt} \leq 8.5$ MeV (bottom-right). The black points show the events rejected by the likelihood selection. The red points show the anti-neutrino candidates which have $1.8 \leq E_{delayed} \leq 2.6$ MeV γ (neutrino capture on proton), and the blue points show also the anti-neutrino candidates which have $4.4 \leq E_{delayed} \leq 5.8$ MeV γ (neutrino capture on ^{12}C). The green lines show the selection criteria.

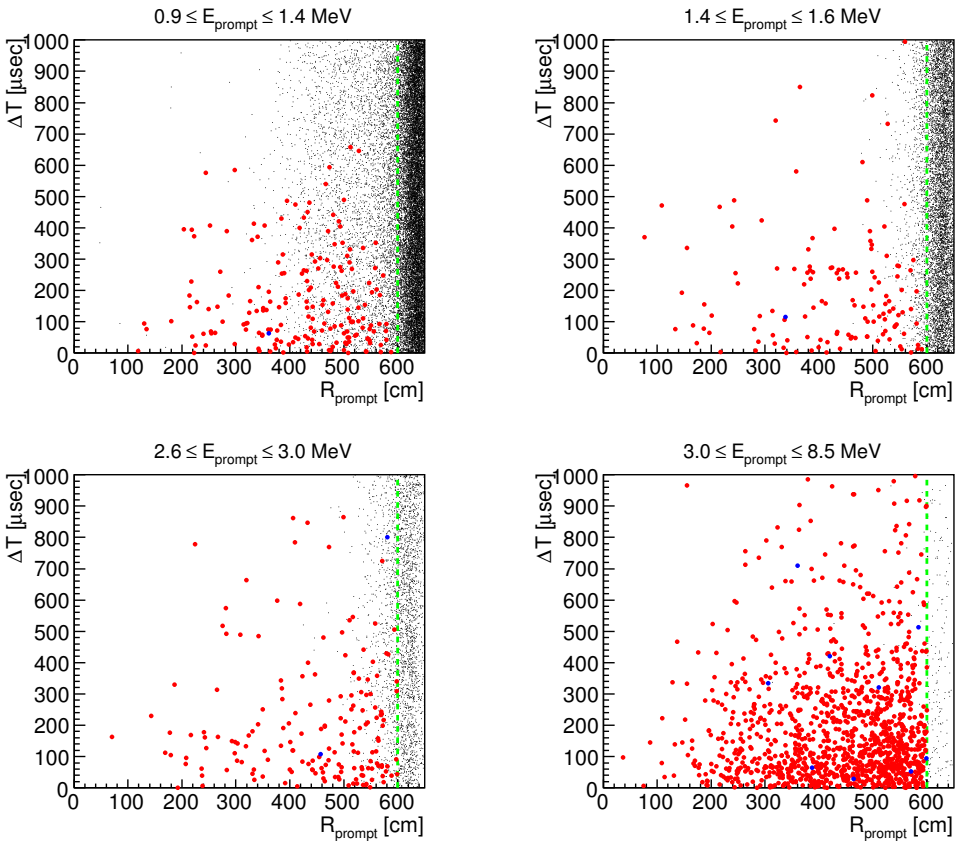

Figure 5.26: Correlation between R_{prompt} and ΔT of anti-neutrino candidates. The prompt energy is selected for each figure, $0.9 \leq E_{prompt} \leq 1.4$ MeV (top-left), $1.4 \leq E_{prompt} \leq 1.6$ MeV (top-right), $2.6 \leq E_{prompt} \leq 3.0$ MeV (bottom-left) and $3.0 \leq E_{prompt} \leq 8.5$ MeV (bottom-right). The black points show the events rejected by the likelihood selection. The red points show the anti-neutrino candidates which have $1.8 \leq E_{delayed} \leq 2.6$ MeV γ (neutrino capture on proton), and the blue points show also the anti-neutrino candidates which have $4.4 \leq E_{delayed} \leq 5.8$ MeV γ (neutrino capture on ^{12}C). The green lines show the selection criteria.

5.8 Detector Related Uncertainties

Number of Target Proton and Cross Section

As discussed in Section 2.5, the anti-neutrino events are detected via the inverse-β decay ($\bar{\nu}_e + p \rightarrow e^+ + n$). The number of target proton in 6.0 m radius fiducial volume is calculated using the chemical composition of the liquid scintillator and density measurement. Before the liquid scintillator purification, the uncertainty of target proton was only caused by an error of the liquid scintillator temperature. On the other hand, during the liquid scintillator purification, the density of filled liquid scintillator was precisely controlled to make a layered structure. The number of target protons should be calculated with considering the change of the density.

The various information such as density, temperature and flow rate is logged constantly.

OD Hit Event Cut

In order to remove accidental OD hit, the OD hit event cut, N_{200} OD ≥ 5, is applied for candidate selection. The parameter "N_{200} OD" is the number of hit PMTs in the outer detector within a 200 nsec time window. Using muon events, the definition of OD hit cut inefficiency is as follows :

$$\text{OD hit cut inefficiency} = \frac{\text{Number of ID hit events with 100,000 p.e.} < Q_{17} \text{ and } N_{200} \text{ OD} < \text{selection}}{\text{Number of ID hit events with 100,000 p.e.} < Q_{17}} \tag{5.15}$$

Figure 5.27 shows the OD hit cut inefficiency as a function of N_{200} OD, and Figure 5.28 shows the time variation of OD hit cut inefficiency for N_{200} OD ≥ 5. The Uncertainty of OD hit event cut is estimated to be 0.25 %.

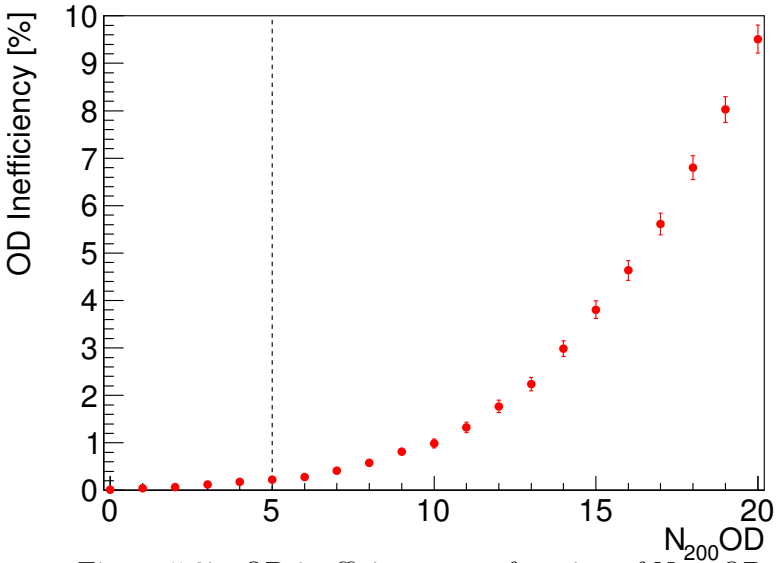

Figure 5.27: OD inefficiency as a function of N_{200} OD.

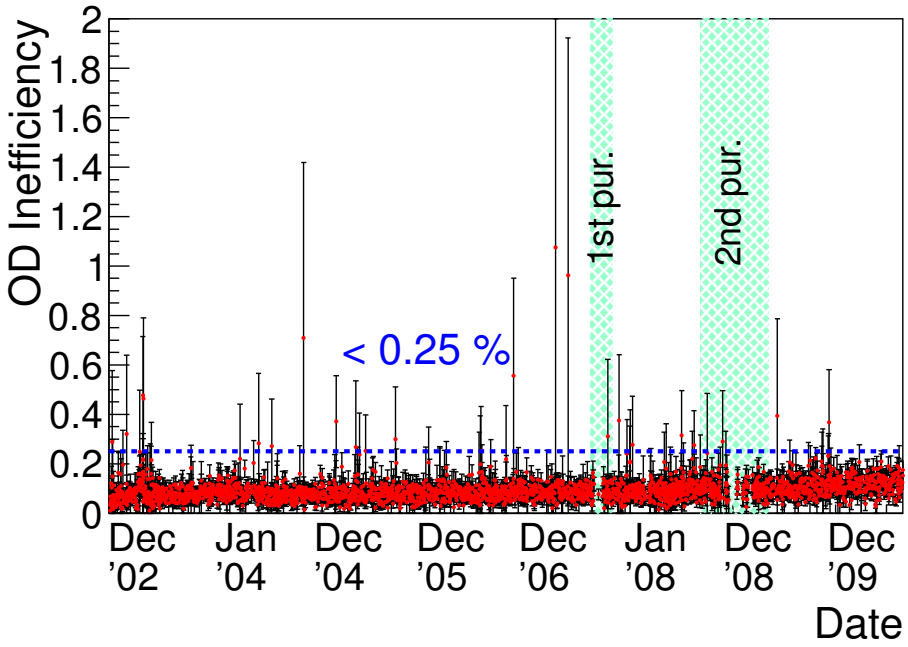

Figure 5.28: Time variation of OD inefficiency. The uncertainty of OD hit event cut is estimated to be 0.25 %.

Table 5.6: Summary of detector related systematic uncertainties.

	Before Purification		After Purification	
	reactor	geo	reactor	geo
- efficiency -				
likelihood selection	0.7 %	1.5 %	0.8 %	1.2 %
binned efficiency	< 0.1 %	0.8 %	< 0.1 %	0.8 %
trigger efficiency	0.002 %		0.001 %	
livetime calculation	0.02 %		0.01 %	
- event selection and reconstruction -				
flasher event cut	< 0.0008 %		< 0.0009 %	
noise event cut	0.0003 %		< 0.02 %	
OD hit event cut	0.25 %		0.25 %	
fiducial volume cut	1.8 %		2.5 %	
miss-recon. probability	0.2 %		0.2 %	
energy scale	1.1 %	1.6 %	1.3 %	2.0 %
- number of target and cross section -				
number of target proton	<0.1 %			
cross section	0.2 %			
total	2.25 %	2.97 %	2.96 %	3.53 %

Chapter 6

Background Estimation

The electron anti-neutrino detection signature, prompt-delayed event-pairs produced by inverse β-decay and their subsequent neutron captures, is selected by applying a set of cuts as described in Section 5.3. There are various background sources in the detector, such as radioactive impurities and spallation neutrons caused by cosmic muons. The background events can be classified into two types. The first is correlated events related to neutrons produced by muons to α-rays, spallation products with neutron emitters, short life nuclei, spontaneous fission of nuclei and other anti-neutrino sources. The second is uncorrelated events, such as accidental events. The backgrounds are categorized as follows :

- Accidental Background
  The cause of the accidental coincidence is mainly radioactive impurities. The events around the balloon surface come from outside of the detector become candidates for the accidental background. Fiducial volume cut is effective to reject this backgrounds.

- ^{9}Li/^{8}He
  ^{8}He and ^{9}Li are neutron emitters, which mean life time are 171.7 msec and 257.2 msec. There is time correlation between delayed coincidence events and muons.

- (α,n)
  The main (α,n) reaction is ^{13}C(α,n)^{16}O, and the α source is ^{210}Po. The purity of KamLAND liquid scintillator was improved, eliminating most of the ^{210}Pb that used to feed the decay chain responsible form the production of α-particles from ^{210}Po decay. This in turn dramatically reduced the (α, n) backgrounds.

- Fast Neutron
  The fast neutron events are detected as delayed coincidence events which tagged with a muon which passed only in the outer detector. The prompt signal is the proton which is recoiled by neutron. Since the outer detector has small inefficiency, the miss-tagging events become background for anti-neutrino. The contribution from a muon which passed only in the surrounding rock are considered separately.

- Atmospheric $\bar{\nu}_e$

The conservative background rates from the atmospheric neutrinos are estimated by the typical flux calculation model.

- Spontaneous Fission
  The small contribution from the spontaneous fission of ^{238}U should be considered. The details are described Section **??**.

The details of the anti-neutrino signals which comes from the reactor and the earth's interior are described in this section. The reactor $\bar{\nu}_e$ can be categorized as background for the geo $\bar{\nu}_e$ analysis. On the other hand, the geo $\bar{\nu}_e$ contribution is considered as the background in the reactor $\bar{\nu}_e$ analysis.

6.1 Backgrounds for Sigle Events

The background sources for the single events include the radioactive impurities in the liquid scintillator and the spallation products related to muons. The details of them are described as follows.

- Radioactive backgrounds
  Figure 6.1 and 6.2 show the energy spectrum for various fiducial volumes up to 14 MeV and up to 3 MeV before and after purification. The single events are selected by applying a 2 msec veto after muons and various bad-event cuts described. There are two peaks around 1.46 MeV and 2.62 MeV which correspond to the γ-ray from ^{40}K and ^{208}Tl, respectively. Most of the ^{40}K events come from the balloon and ropes, and its measured rate is about 0.86 Hz. The concentration of radioactivities in the balloon and ropes measured by ICP-MS are listed in Table 6.1. The majority of the ^{208}Tl backgrounds come from outside of the detector. The sounding rock contains a high concentration of ^{232}Th, which decays and produces ^{208}Tl as a doughtier isotope. The ^{208}Tl background rate is measured to be about 2.8 Hz. Figure 6.3 shows the vertex distribution for various energy windows. As shown in the figure for $1.0 < \mathrm{E} < 3.0$ MeV, the fiducial volume cut can effectively suppress the external gamma ray backgrounds.

  In the energy spectrum after 2nd purification, the radioactive background rates especially in the low energy region are extremely lower than that of before purification. The liquid scintillator is successfully purified by the purification campaign.

  The ^{40}K events contribute to the accidental background for the anti-neutrino analysis as fake prompt events. The ^{208}Tl events contribute to the accidental background as both fake prompt and fake delayed events.

- Spallation products
  The high energy region is dominated by the long-life spallation products induced by cosmic ray muons and external γ-rays from (α, n) and (n, γ) events produced in the outside of the detector, mainly in the surrounding rock. The number of spallation products are listed in Table 6.2.

Table 6.1: Concentration of radioactivities in the balloon and ropes measured by ICP-MS.

Radioactivities	Balloon		Rope	
	Concentration [ppb]	Activity [Bq]	Concentration [ppb]	Activity [Bq]
^{238}U	0.018	0.02	0.08	0.1
^{232}Th	0.014	0.006	0.8	0.33
^{40}K	0.27	7.2	1.2	31

Table 6.2: Summary of spallation products in KamLAND

Isotopes	Life Time	Q Value [MeV]	Decay Mode	Production Rate [events/day/kton]	
				Hagner et al. [64]	Measurements
^{12}B	29.1 ms	13.4	β^-	-	58.7 ± 2.5
^{12}N	15.9 ms	17.3	β^+	-	2.1 ± 0.4
^{8}Li	1.21 s	16.0	$\beta^-\alpha$	5	27.3 ± 0.8
^{8}B	1.11 s	18.0	$\beta^+\alpha$	8	<4.7
^{9}C	182.5 ms	16.5	β^+	5.5	7.4 ± 2.9
^{8}He/^{9}Li	171.7/257.2 ms	10.7/13.6	$\beta^-\gamma n$	2.4	2.7 ± 0.8
^{11}C	29.4 ms	1.98	β^+	1039	1093 ± 176
^{10}C	27.8 s	3.65	$\beta^+\gamma$	139	21.6 ± 2.7
^{11}Be	19.9 s	11.5	β^-	<2.4	<2.2
^{6}He	1.16 s	3.51	β^-	19	-
^{7}Be	76.9 day	0.478	ECγ	231	-

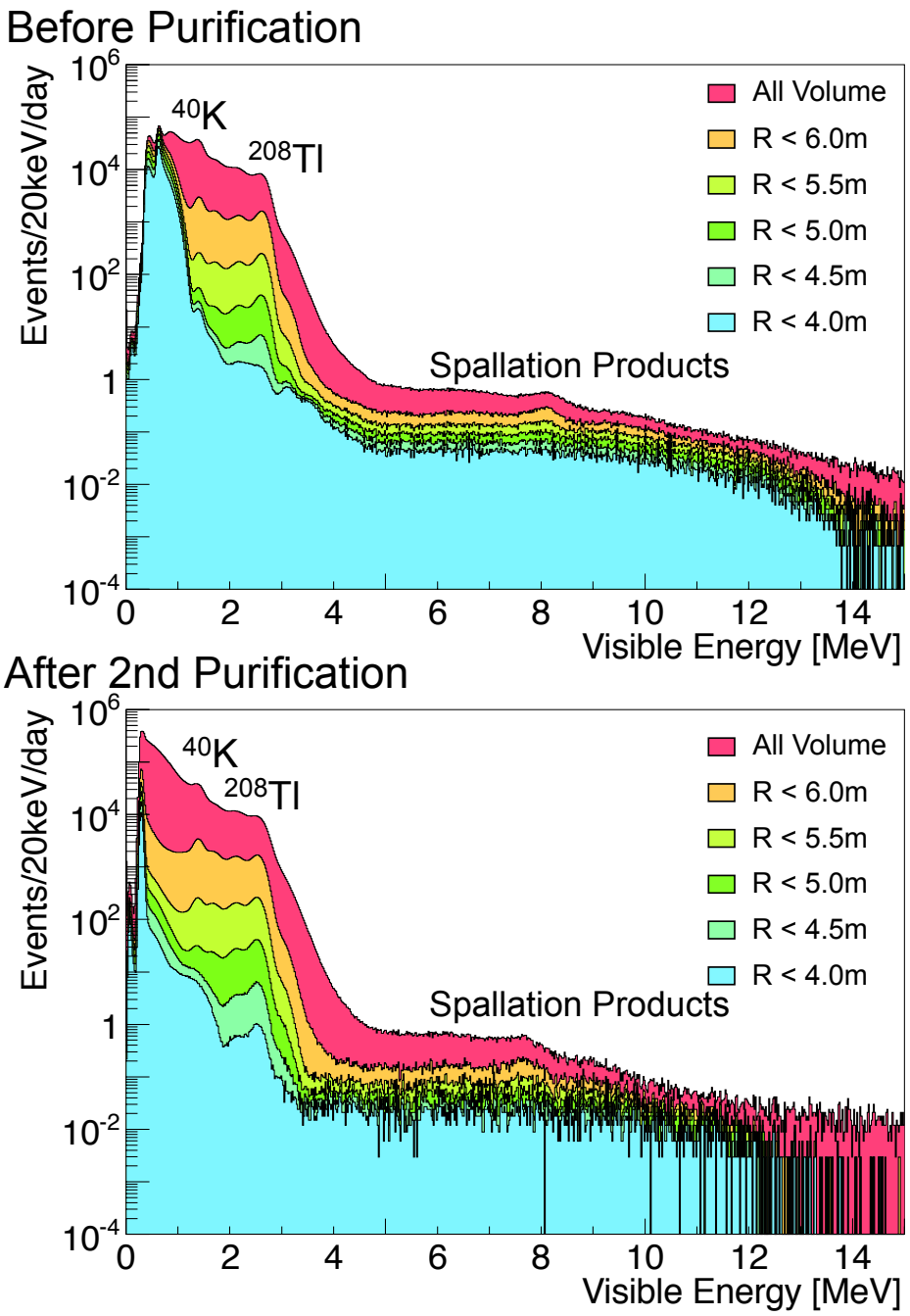

Figure 6.1: Single energy spectrum for various fiducial volumes up to 14 MeV before (top) and after (bottom) purification. The events are applied a 2 msec veto after muons and various bad-event cuts. The fiducial volume cut significantly suppresses external radiations, such as ^{40}K and ^{208}Tl. After purification, the background rates especially low energy region are clearly lower than that of before purification.

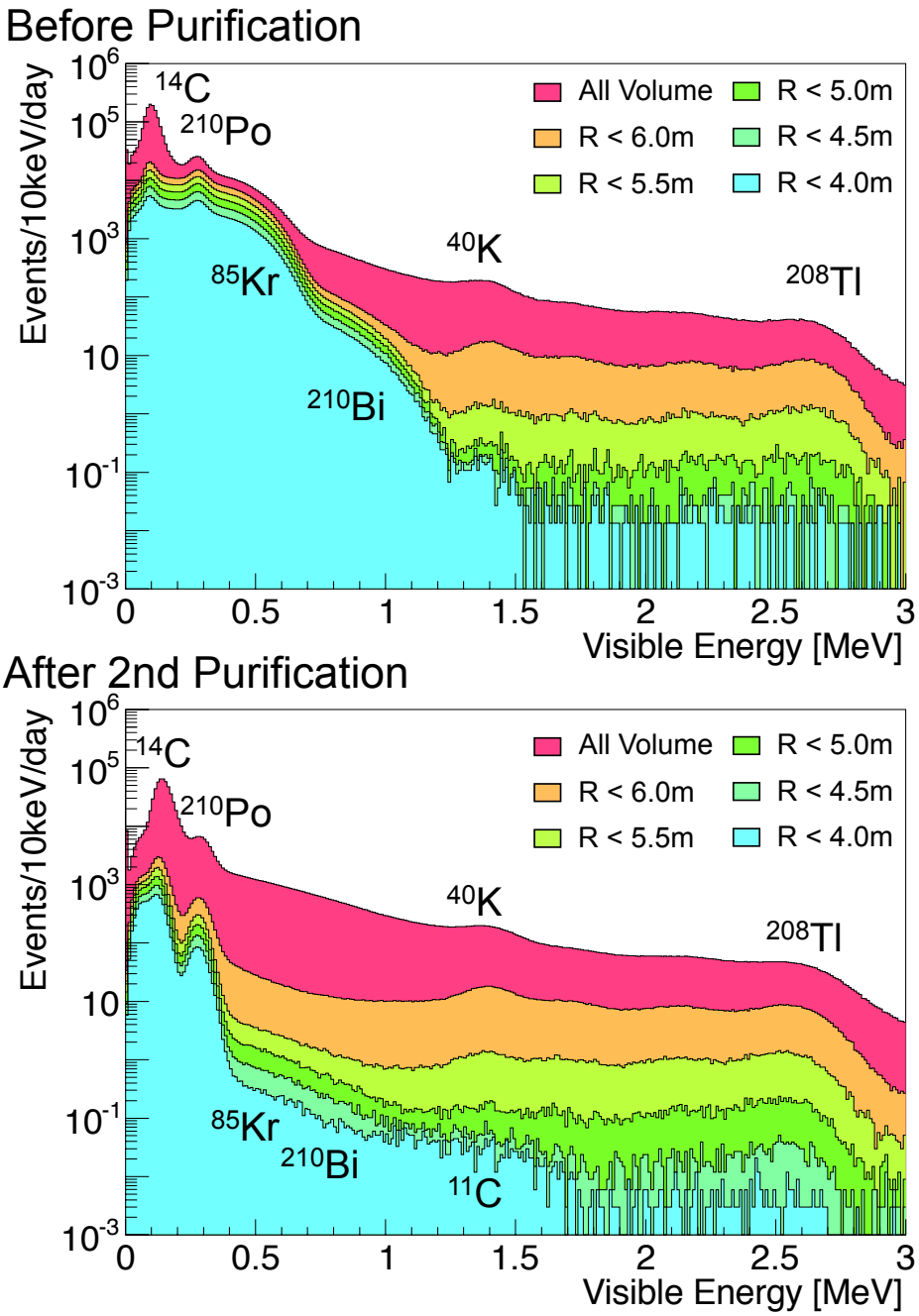

Figure 6.2: Single energy spectrum for various fiducial volume up to 3 MeV before (top) and after (bottom) purification. The 2 msec veto after muons is applied. In the top figure, two β spectra correspond to ^{85}Kr and ^{210}Bi which are clearly seen below 1.0 MeV. The peak around 0.2 MeV corresponds to ^{210}Po α decay and peak around 0.1 MeV corresponds to ^{14}C β decay and trigger efficiency. In the bottom figure, the radioactive backgrounds especially below 1.0 MeV are significantly reduced by the purification.

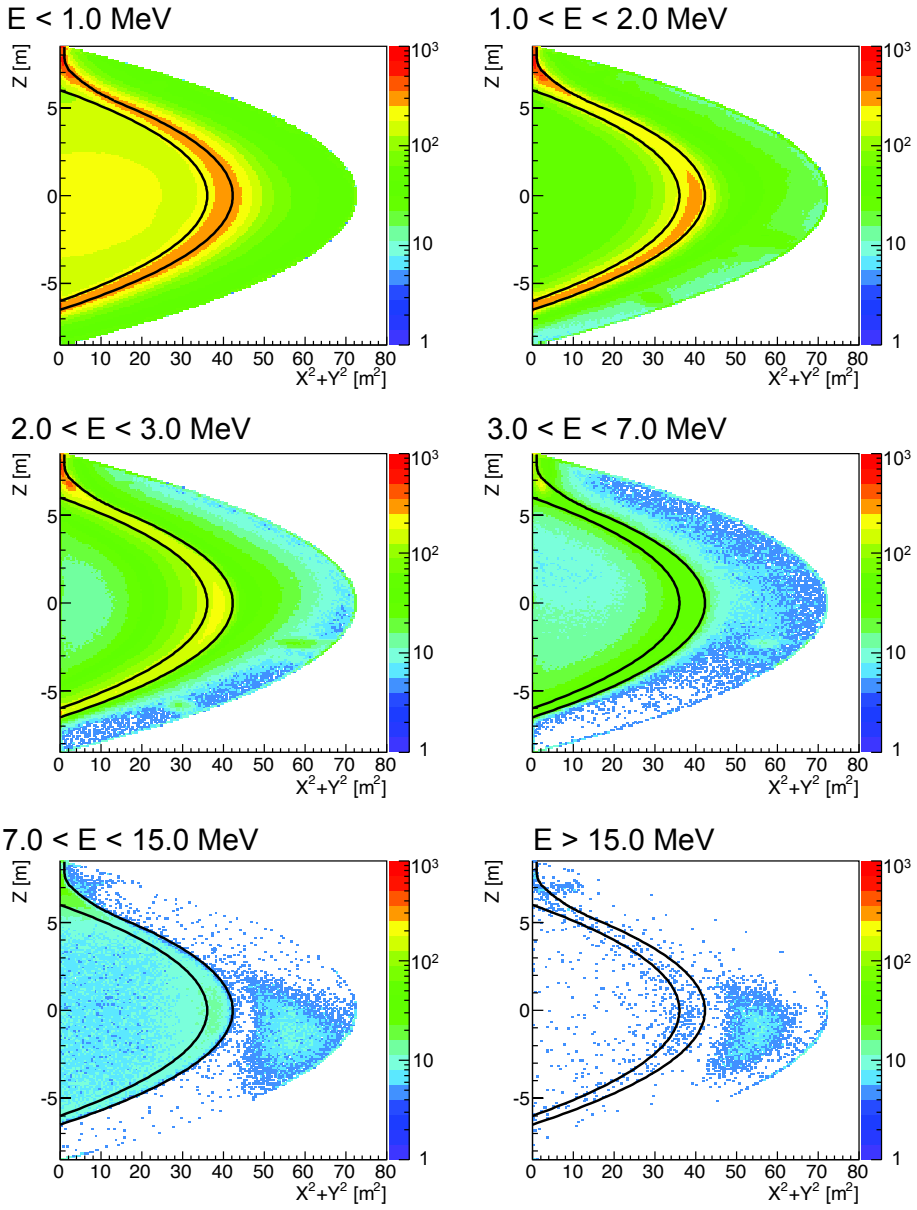

Figure 6.3: Vertex distribution for various energy window in the whole volume. The two black lines show the 6.0 m fiducial radius and 6.5 m balloon edge radius. The external radiation from ^{40}K and ^{208}Tl decays appear in the energy dance 1.0 < E < 3.0 MeV.

6.2 Radioactive Impurities

6.2.1 ^{238}U-Series

The concentration of ^{238}U is estimated from the ^{214}Bi-^{214}Po delayed coincidence method.

$$^{214}\text{Bi} \xrightarrow[Q_\beta=3.272\ \text{MeV},99.989\ \%]{T_{1/2}=19.9\ \text{min}} {}^{214}\text{Po} \xrightarrow[Q_\alpha=7.687\ \text{MeV}]{T_{1/2}=164.3\ \mu\text{sec}} {}^{210}\text{Pb}.$$

The selection criteria for ^{214}Bi-^{214}Po delayed coincidence is summarized in Table 6.3. In order to avoid the ^{212}Bi-^{212}Po coincidence (^{212}Po $T_{1/2}$ = 0.299 μsec), the lower time window cut, $\Delta T \geq 5$ μsec is applied.

Table 6.3: Summary of ^{214}Bi-^{214}Po event selection.

Type	Selection
Prompt Energy (E_p)	$0.35 < E_p < 3.5$ MeV
Delayed Energy (E_d)	$0.35 < E_d < 0.8$ MeV
Space Correlation (ΔR)	$\Delta R < 120$ cm
Time Correlation (ΔT)	$5 < \Delta T < 1200$ μsec
Off Time Window	$1205 < \Delta T < 2400$ μsec
Fiducial Cut	$R_d < 400$ cm

6.2.2 ^{232}Th-Series

The concentration of ^{232}Th is estimated from the ^{212}Bi-^{212}Po delayed coincidence method.

$$^{212}\text{Bi} \xrightarrow[Q_\beta=2.254\ \text{MeV},64.06\ \%]{T_{1/2}=60.55\ \text{min}} {}^{212}\text{Po} \xrightarrow[Q_\alpha=78.784\ \text{MeV}]{T_{1/2}=299\ \text{nsec}} {}^{208}\text{Pb}.$$

The selection criteria for ^{212}Bi-^{212}Po delayed coincidence is summarized in Table 6.4. In the time correlation cut, since there is dead time within 300 nsec of a previous event, the lower cut ($\Delta T > 0.4$ μsec)is applied.

Table 6.4: Summary of ^{212}Bi-^{212}Po event selection.

Type	Selection
Prompt Energy (E_p)	$0.35 < E_p < 2.5$ MeV
Delayed Energy (E_d)	$0.5 < E_d < 1.0$ MeV
Space Correlation (ΔR)	$\Delta R < 100$ cm
Time Correlation (ΔT)	$0.4 < \Delta T < 2.5$ μsec
Off Time Window	$2.9 < \Delta T < 5.0\mu$sec
Fiducial Cut	$R_d < 400$ cm

6.2.3 Low Energy Backgrounds below 1.0 MeV

In the low energy region, backgrounds are dominated by the radioactive noble gases, such as ^{85}Kr, ^{222}Rn (daughter nuclei : ^{210}Bi and ^{210}Po) and ^{39}Ar.

- ^{85}Kr

$$^{85}\mathrm{Kr} \xrightarrow[\mathrm{Q}_\beta=0.687\ \mathrm{MeV}]{\mathrm{T}_{1/2}=10.76\ \mathrm{year}} {}^{85}\mathrm{Rb}$$

- ^{222}Rn

$$^{210}\mathrm{Pb} \xrightarrow[\mathrm{Q}_\beta=0.0635\ \mathrm{MeV}]{\mathrm{T}_{1/2}=22.3\ \mathrm{year}} {}^{210}\mathrm{Bi}$$
$$\xrightarrow[\mathrm{Q}_\beta=1.162\ \mathrm{MeV}]{\mathrm{T}_{1/2}=5.013\ \mathrm{day}} {}^{210}\mathrm{Po}$$
$$\xrightarrow[\mathrm{Q}_\alpha=5.047\ \mathrm{MeV}]{\mathrm{T}_{1/2}=138.4\ \mathrm{day}} {}^{206}\mathrm{Pb}$$

- ^{39}Ar

$$^{39}\mathrm{Ar} \xrightarrow[\mathrm{Q}_\beta=0.565\ \mathrm{MeV}]{\mathrm{T}_{1/2}=269\ \mathrm{year}} {}^{39}\mathrm{K}$$

Figure 6.4 shows the single spectrum fitting by the beta spectrum of ^{85}Kr ^{210}Bi and ^{210}Po. The special low-threshold run is used for before purification analysis, and the prescale trigger data is used for after 1st and 2nd purification analysis. The beta spectrum are taken from Ref. [65] and converted to the visible energy spectrum in KamLAND. The decay rate is estimated by fitting for this single energy spectrum. The time variation of these backgrounds are shown in Figure 6.5. The low energy background rates are clearly decreased by the liquid scintillator purification. These measured rate of each background are summarized in Table 6.5.

Table 6.5: Summary of the measured radioactivity of ^{210}Bi, ^{210}Po and ^{85}Kr

Isotope	Radius	Measurement [mBq/m^3]		
		before pur. (Jan. 11, 2006)	after 1st pur. (Jan. 23, 2008)	after 2nd pur. (May 17, 2009)
^{210}Bi	4.0 m	37.2 ± 3.6	9.5 ± 0.3	0.43 ± 0.17
^{210}Po	5.5 m	44.3 ± 1.5	12.1 ± 0.1	3.0 ± 0.1
^{85}Kr	5.5 m	580.5 ± 3.6	169.6 ± 0.3	0.11 ± 0.13

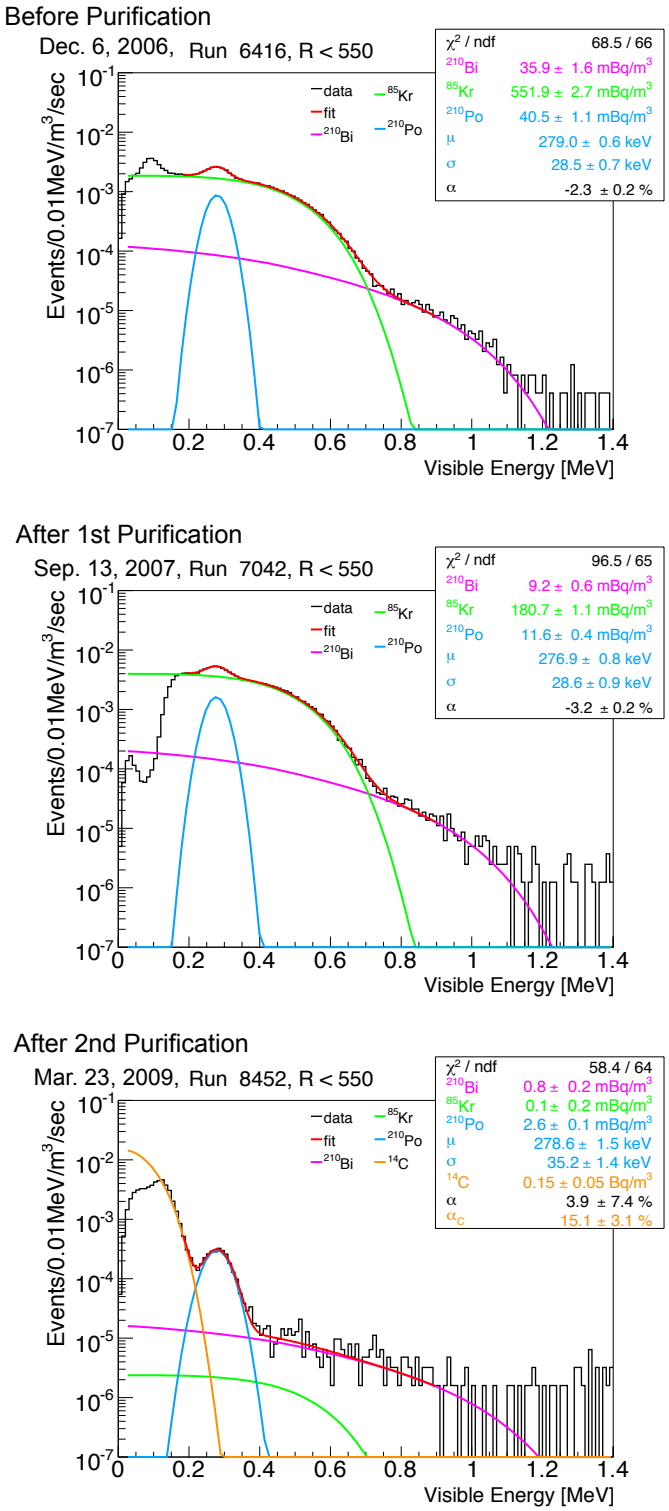

Figure 6.4: Single spectrum fitted with beta spectra (^{210}Bi : magenta, ^{85}Kr : green and ^{14}C : orange) and a gaussian (^{210}Po : blue) for before purification (top), after 1st purification (middle) and after 2nd purification (bottom). The events are selected within 5.5 m radius. For before purification analysis, the low-threshold data is used, and for after 1st and 2nd purification analysis, the prescale threshold datas are used. Since the threshold is not enough to correct the ^{14}C events, the ^{14}C spectrum is added only after 2nd purification. α is the energy scale parameter to response the visible energy uncertainty. ^{210}Bi, ^{85}Kr, ^{14}C and ^{210}Po are free fit parameters, and α is a constrained fit parameter.

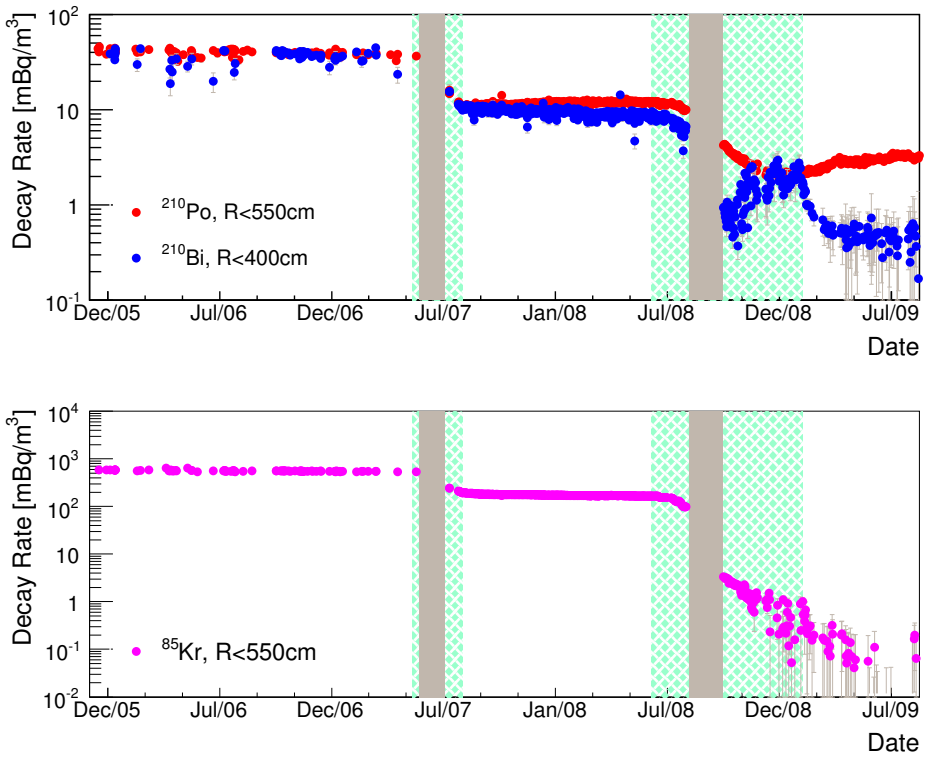

Figure 6.5: Time variation of low energy background events (^{210}Bi : blue, ^{210}Po : red, and ^{85}Kr : magenta). These events are selected with a fiducial volume cut, R $<$ 550 cm for ^{210}Po and ^{85}Kr, R $<$ 400 cm for ^{210}Bi. The green shaded areas show 1st and 2nd purification campaign periods, and the gray shaded areas show the high dark rate periods which are vetoed for anti-neutrino analysis. These background events are clearly rejected by two times purification. Final rejection factors are estimated to be about 10^{-2}, 10^{-2} and 10^{-4} for ^{210}Bi, ^{210}Po and ^{85}Kr, respectively.

^{210}Po and ^{85}Kr decay rate for before purification

Since there was no activity for the liquid scintillator before purification, the number of isotopes can be estimated by decay rate. The decay rate of ^{210}Po and ^{85}Kr ($R_{Po}(t)$ and $R_{Kr}(t)$) for before purification are defined as the following function :

$$\begin{aligned} R_{\mathrm{Po}}(t) &= \frac{N^0_{\mathrm{Pb}}(t_0)}{\tau_{\mathrm{Pb}} - \tau_{\mathrm{Po}}} \left[\exp\left(-\frac{t-t_0}{\tau_{\mathrm{Pb}}}\right) - \exp\left(-\frac{t-t_0}{\tau_{\mathrm{Po}}}\right) \right] \\ R_{\mathrm{Kr}}(t) &= N^0_{\mathrm{Kr}}(t_0)\ \exp\left(-\frac{t-t_0}{\tau_{\mathrm{Kr}}}\right) \end{aligned} \tag{6.1}$$

where t_0 is a time offset which is assumed the start time of the liquid scintillator filling, May 2001. τ_{Po}, τ_{Pb} and τ_{Kr} are life time ($T_{1/2}$ / $\ln 2$) of ^{210}Po, ^{210}Pb and ^{85}Kr defined 32.2 years, 199.7 days and 388.1 days, respectively. $N^0_{Pb}(t)$ and $N^0_{Kr}(t)$ are the number of isotopes as a function of time. Figure 6.6 shows the monthly-averaged ^{210}Po, ^{210}Bi and ^{85}Kr rate. By fitting on the assumption of $R_{Po}(t_0) = 0$ and no supply of ^{210}Pb, $N_{Pb}(t_0)$ is estimated to be about 1.05×10^{11}. The fitted results are in good agreement with the half life of ^{210}Pb (22.3 years) and ^{85}Kr (10.76 years).

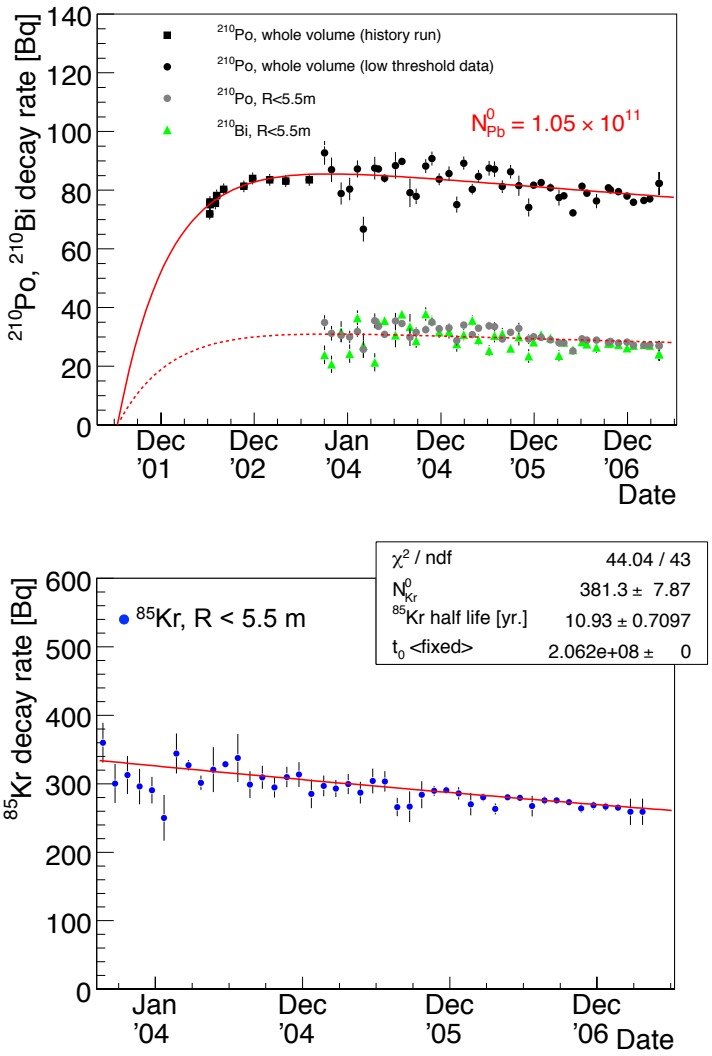

Figure 6.6: Monthly-averaged rates of ^{210}Po, ^{210}Bi and ^{85}Kr.
(Top) Monthly-averaged rates of ^{210}Po, ^{210}Bi. The black points show the ^{210}Po rate in whole volume, the gray points show the ^{210}Po rate within 5.5 m radius, and the green points show the ^{210}Bi rate within 5.5 m radius. At the start of the data taking, the whole volume ^{210}Po rate is estimated by using history runs which have only PMT hit information (black square). In this case, ^{210}Po rate is estimated from NsumMax distribution by fitting gaussian + linear function. The red line shows the fitting function (Eq. (6.1)) for whole volume ^{210}Po rate, where the free parameters are time offset t_0 and the number of initial ^{210}Po, N^0_{Pb}; and the half life of ^{210}Pb and ^{210}Po are fixed. From this fitting result, t_0 can be estimated. And N^0_{Pb} is estimated about 1.05×10^{11}. Then, the red dot line shows the fitting function for 5.5 m radius ^{210}Po rate with fixed t_0. ^{210}Bi rate is found to be in good agreement with ^{210}Po rate and confirms that they are in equilibrium.
(Bottom) Monthly-averaged rates of ^{85}Kr within 5.5 m radius. The red line shows the fitting function (Eq. (6.1)) where the free parameters are the number of initial ^{85}Kr, N^0_{Kr} and half life and t_0 value is fixed at the start of KamLAND liquid scintillator filling. ^{85}Kr half life is in good agreement with expected, 10.76 years.

6.3 Spallation Events Study

6.3.1 Neutron Production

The neutrons produced by muons are captured on proton or ^{12}C within several hundred μsec emitting a 2.22457 MeV γ-ray or 4.9649 MeV γ-ray, respectively. These events are observable by the simple selection criteria using time difference from muons and the NsumMax, which means the maximum number of hits when trigger was issued. The time difference after muon is selected with a cut $150 < \Delta T_{\mathrm{muon}} < 1000$ μsec. In order to reduce the effect of the missing waveform, the good event selection cut is applied.

$$\text{Nhit (number of PMT hits)} \geq \text{NsumMax}$$

Some parameters are checked to improve the efficiency of the neutron capture event selection.

- NsumMax Distribution
  Figure 6.7 shows the NsumMax distribution of neutron capture events on proton and ^{12}C applying the time difference cut. The ratio of the proton capture event and ^{12}C capture events is good agreement with the expected ratio, 99.45 % and 0.55 % from their respective capture cross section. From the on-time histogram, the neutron events capture on proton can be selected with a $350 <$ NsumMax < 550 cut.

- Good Event Selection Cut
  As described above, the good event cut is applied to reduce the effect of missing waveform. Figure 6.8 shows the correlation between the time difference from last muon and the ratio of Nhit to NsumMax. This ratio typically should be more than 1.0, but because of missing waveform, there are events which have a ratio less than 1.0. Figure 6.9 shows the survival events ratio after applying this good event selection cut, Nhit $\geq$ NsumMax.

- Energy Distribution
  Figure 6.10 shows the visible energy distribution with and without the good event selection cut within 6.0 m fiducial radius. The neutron capture events on proton and ^{12}C produce clear pecks around 2.22 MeV and 4.59 MeV. As described in Section 3.3.3 (P.70), these neutron capture events are useful for checking the energy and vertex reconstruction quality. Furthermore, using the uniform distribution in the detector, fiducial volume is estimated as described in Section 3.4.1.

The production rate of neutrons is estimated by the neutron capture time distribution. Figure 6.11 shows the distribution of the time difference from last muon with and without the good event selection cut. From fitting result, the neutron production rate is estimated to be 2846.0 ± 131.1 event/day/kton.

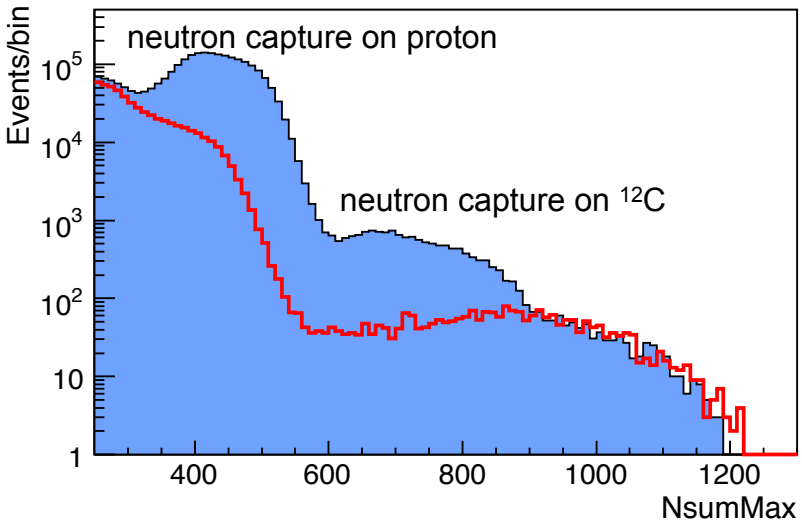

Figure 6.7: NsumMax distribution of neutron capture events on proton and ^{12}C. The blow shaded histogram shows the events within on-time window, $150 < \Delta T_{muon} < 1000$ μsec. The neutron capture events clear distribute around NsumMax $\sim$ 400. Events within $\Delta T_{muon} < 150$ μsec are rejected due to the electronics noise. The red line shows the events within off-time window, $2150 < \Delta T_{muon} < 3000$ μsec. From the on-time histogram, the neutron events capture on proton can be selected with a 350 $<$ NsumMax $<$ 550 cut.

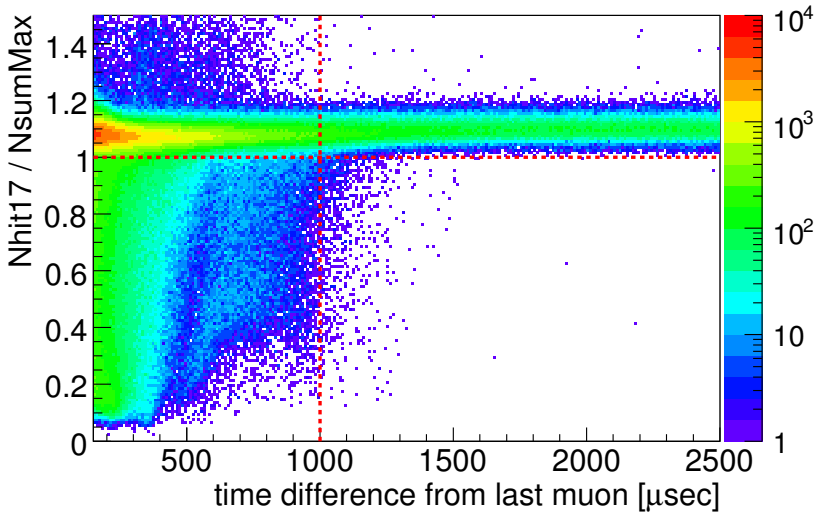

Figure 6.8: Correlation between the time difference from last muon and the ratio of Nhit to NsumMax. Nhit is the number of recorded waveforms and NsumMax is the maximum number of triggered 17-inch PMTs. The ratio typically should be more than 1.0, but there are events which have the ratio less than 1.0 because of missing waveform especially just after muon events. The good events selection cut is set to be Nhit $\geq$ NsumMax.

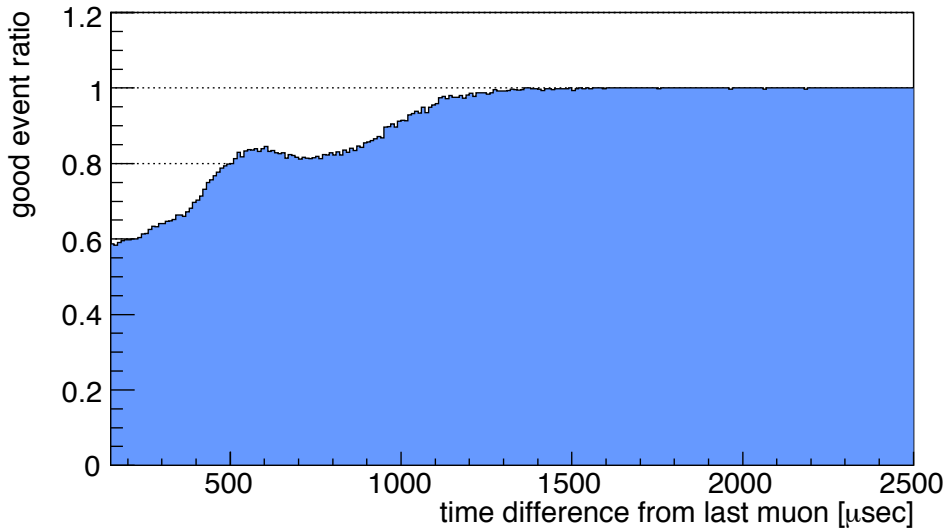

Figure 6.9: Survival event ratio after applying the good event selection cut as a function of the time difference from last muon. Some PMT waveforms are lost within 1200 μsec.

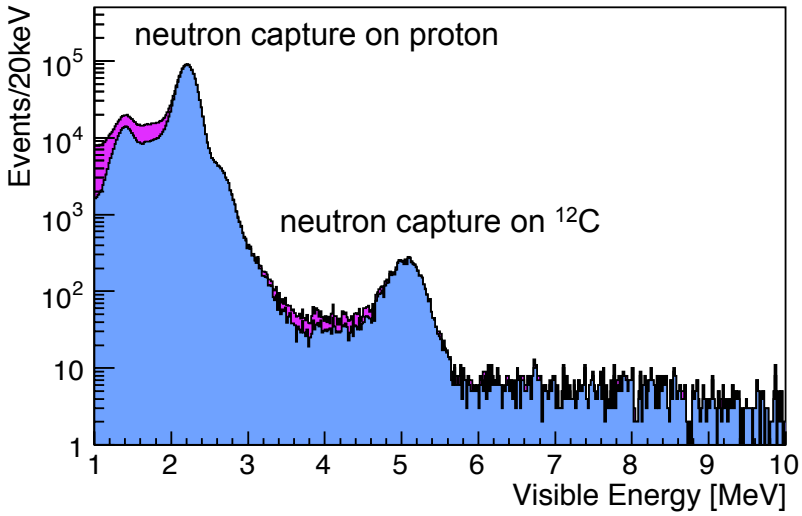

Figure 6.10: Visible energy distribution of the neutron capture events with (blue) and without (magenta) the good event selection cut. The on-time selection $150 < \Delta T_{muon} < 1000$ μsec is applied to both histograms. There are two clear pecks, corresponding to the neutron capture on proton events (2.22 MeV γ) and on ^{12}C events (4.95 MeV γ). Since these events have the uniform vertex distribution in the detector and constant production rate, these are useful for full-volume energy and vertex reconstruction studies.

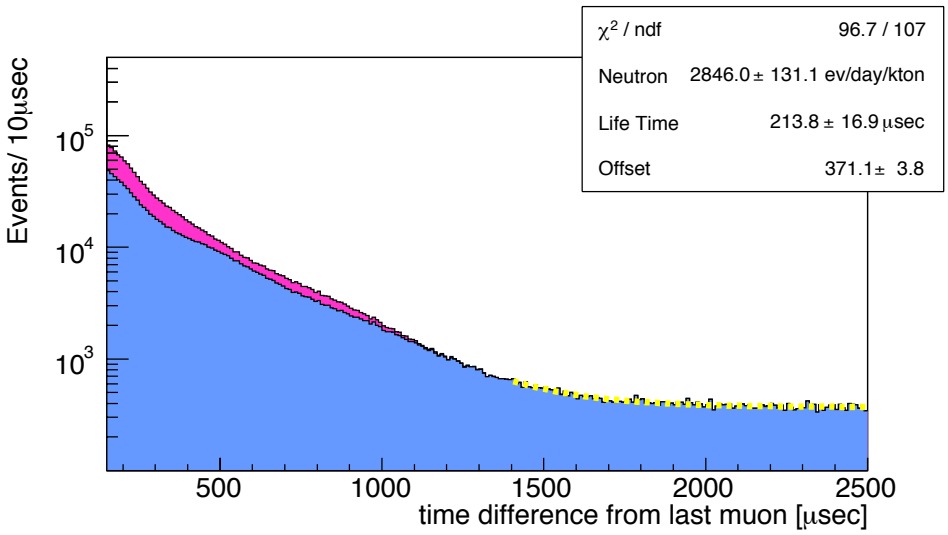

Figure 6.11: Neutron capture time distribution with (blue) and without (magenta) the good event selection cut within 6.0 m fiducial radius. NsumMax cut (350 < NsumMax < 550) is applied to select the neutron capture events on proton. The yellow line shows the exponential fitting result only using larger time events (ΔT_{muon} > 1400 μsec) in order to reduce the unknown effect. From the fitting result, the production rate for the neutron capture events on proton is estimated to be 2846.0 ± 131.1 event/day/kton.

6.3.2 ^{12}B/^{12}N Production

^{12}B and ^{12}N are produced by muons in the liquid scintillator and decay via β decay. The life time and Q value are summarized in Table 6.6. These events are not a background for the anti-neutrino analysis because they do not emit neutrons via β decay. As described in Section 3.4.1, the uniform distribution of ^{12}B/^{12}N production events can be used for estimation of the fiducial volume uncertainty. Figure 6.12 shows the time correlation between muons and ^{12}B or ^{12}N events. Since the Q value of ^{12}N is higher than that of ^{12}B, ^{12}N events are selected with an energy cut E >14.0 MeV. The fit results indicate that the ^{12}B production rate is 60.8 $\pm$ 2.1 events/day/kton and ^{12}N production rate is 2.2 $\pm$ 0.1 events/day/kton. Figure 6.13 shows the energy spectrum for each period.

Table 6.6: Summary for spallation product of ^{12}B/^{12}N

Isotope	Life Time	Q Value	Production Rate [events/day/kton]
^{12}B	29.1 msec	13.4 MeV (β^-)	60.8 $\pm$ 2.1
^{12}N	15.9 msec	17.3 MeV (β^+)	2.2 $\pm$ 0.1

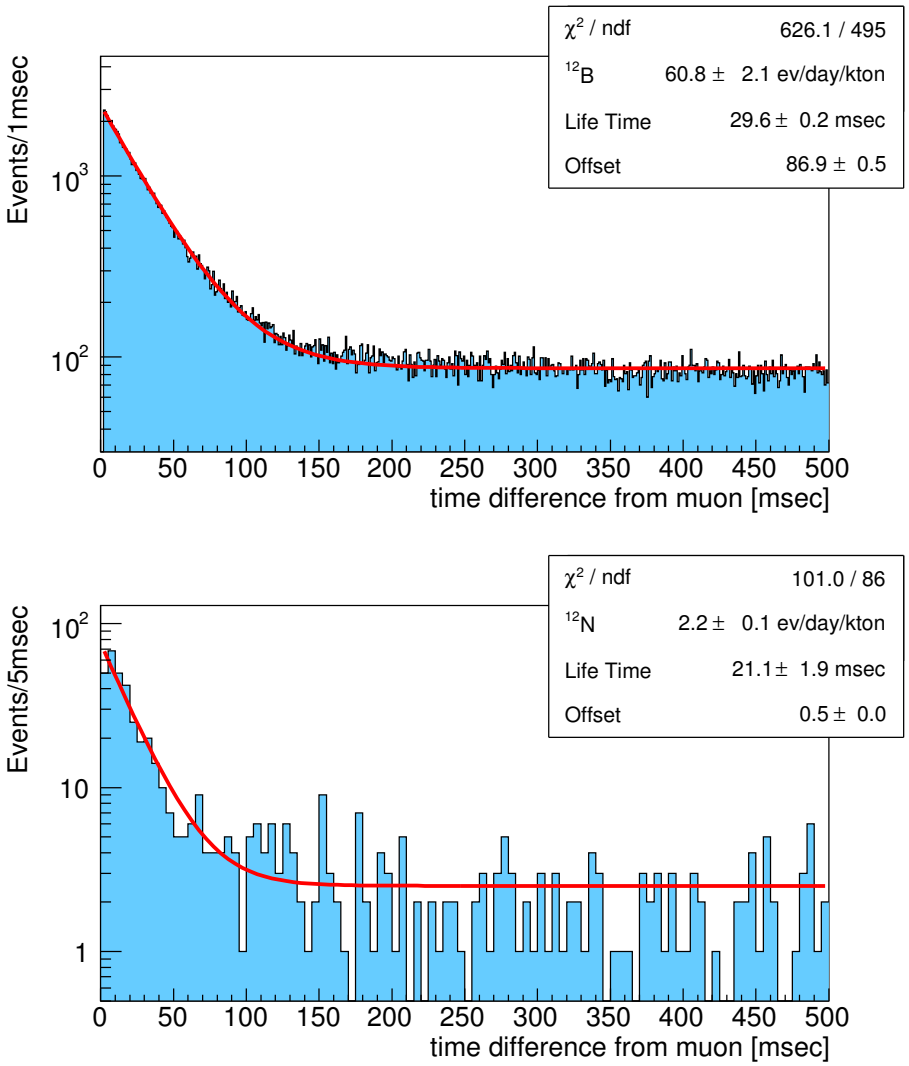

Figure 6.12: Time correlation between muons and ^{12}B (top) or ^{12}N (bottom) events within 6.0 m fiducial radius. ^{12}B events are selected with an energy cut 4.0 MeV $<$ E, and ^{12}N events are set an energy threshold as 14.0 MeV because of high Q value, 17.3 MeV. The red lines shows fitting functions, and estimated life time is consistent with expectation. (^{12}B : 29.6 $\pm$ 0.2 msec (29.1 msec), ^{12}N : 21.1 $\pm$ 1.9 msec (15.9 msec)). From these fitting results, the production rate of ^{12}B and ^{12}N events are estimated to be 60.8 $\pm$ 2.1 events/day/kton and 2.2 $\pm$ 0.1 events/day/kton, respectively.

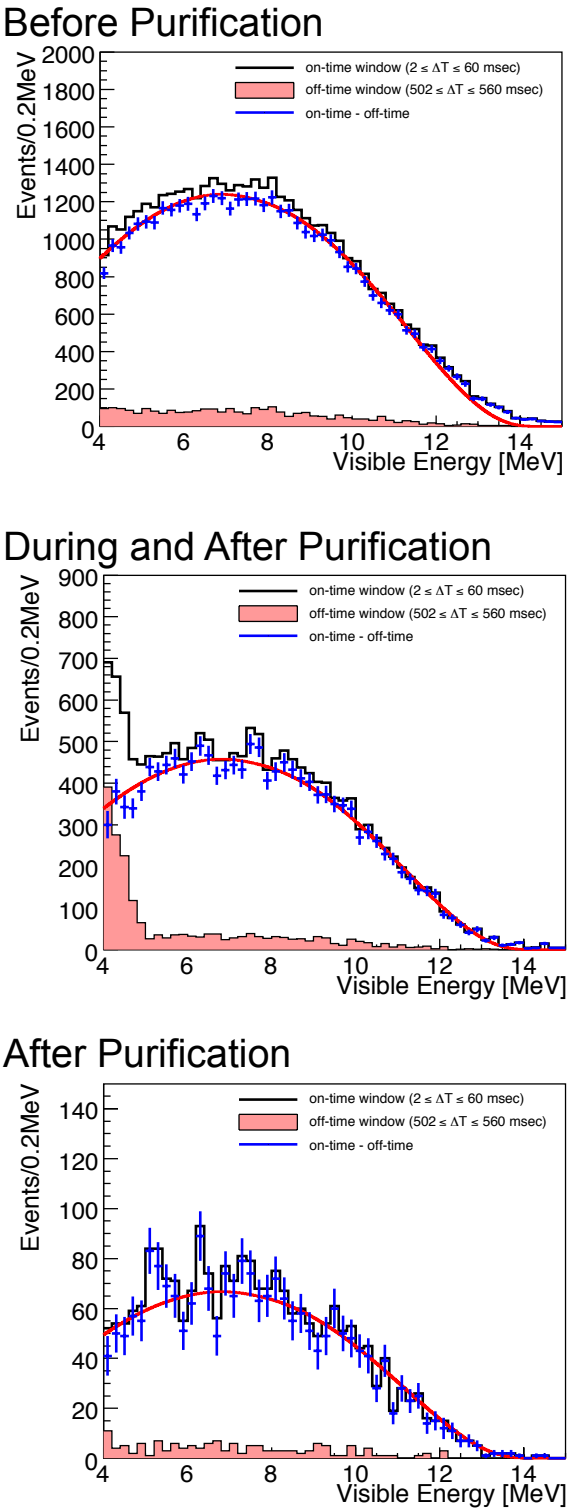

Figure 6.13: ^{12}B/^{12}N events energy spectrum within 6.0 m fiducial radius for before purification (top), during and after purification (middle) and only after purification (bottom). The black histogram shows the events within on-time window $2 \leq \Delta T_{muon} \leq 60$ msec, and the pink shaded histogram shows the events within off-time window $502 \leq \Delta T_{muon} \leq 560$ msec. The blue points show the energy distribution after subtraction of off-time events. The red line shows the expected spectrum from their production rate and energy resolution for each period. In the middle histogram, there is an effect of accidental background around 4 MeV.

6.3.3 ^{8}He/^{9}Li Production

There are several nuclei produced by interaction with cosmic ray muons which emit neutron after β decay, and the emitted neutron has possibilities of creating a signal that mimics the anti-neutrino seventies. In this reaction, the fake prompt signal is the β-ray, and the fake delayed signal is neutron capture. In Table 6.7, the isotopes which emit β-ray and a neutron are listed. The main reactions are dominated by the spallation of ^{12}C. Since these isotopes have long life time, these events are more critical for delayed coincidence analysis. The backgrounds from short life time isotopes are easily rejected by the spallation cut.

The selection criteria for emitting β-ray and a neutron are almost same as that of $\bar{\nu}_e$ selection without the spallation cut as summarized in Table 6.8. The time correlation between these delayed coincidence events and muons are shown in Figure 6.14. This time correlation is used to estimate the number of events, the ^{8}He/^{9}Li event ratio and the number of background events in the anti-neutrino analysis. From fitting by exponential function plus constant background, the total number of events are estimated to be 1852.06 $\pm$ 45.24 events and 377.08 $\pm$ 24.82 events for showering muon and non-showering muon, respectively. Figure 6.15 shows the allowed region from extended likelihood analysis for the number of ^{8}He and ^{9}Li events vs the ratio of ^{9}Li. The decay time of ^{8}He and ^{9}Li are fixed ti the each life time, 171.7 msec and 257.2 msec respectively. The best-fit parameters indicate that the contribution of ^{8}He events is negligible compared to the ^{9}Li events.

^{8}He/^{9}Li background for the anti-neutrino analysis

The muon veto criteria for the anti-neutrino analysis are as follows :
· all μ : 2 msec whole volume veto
· showering μ, bad reconstructed μ : 2 sec whole volume veto
· non-showering μ : 2 sec 3 m cylinder volume veto along μ track
Firstly, to estimate the number of ^{8}He/^{9}Li background for the anti-neutrino analysis, the efficiency of the track cut is estimated from spallation neutron events. Figure 6.16 shows the distribution of distance from muon track. For non-showering muon, which has lower residual charge dQ $< 10^{6}$ p.e., 3.0 m cylindrical cut along the muon track are applied for 2 sec. The efficiency of the muon tracking within 3.0 m is estimated to be 93.8 % as shown in the figure. It means 6.2 % of total spallation events remain after applying 3.0 m cylinder cut. Therefore, the background events are events which survives more the 2 sec and events with a distance from the muon track being larger than 3.0 m. The number of background events for each case is as follows :

- showering muons
  $\Delta T_{\text{showering muon}} > 2$ sec : $(1852.06 \pm 45.24) \times e^{-2.0/\tau_{^{9}\text{Li}}} = 0.777 \pm 0.019$
- non-showering muons
  $\Delta T_{\text{non-showering muon}} > 2$ sec : $(377.08 \pm 24.82) \times e^{-2.0/\tau_{^{9}\text{Li}}} = 0.158 \pm 0.010$
  distance from muon track > 3.0 m : $(377.08 \pm 24.82) \times \dfrac{(1 - 0.958)}{0.958}$
  $= 25.87 \pm 1.70$

where $\tau_{^{9}\text{Li}}$ is the life time of ^{9}Li, 257.2 msec. The total number of backgrounds events is 26.81 $\pm$ 1.70 events.

Table 6.7: Isotopes which emit β-ray and neutron

Isotope	Production Reaction	Life Time [msec]	Decay Mode	Energy [MeV]	Fraction
^{8}He	^{12}C(γ, 4p), ^{12}C(π^-, n3p)	171.7	β^-	10.7	0.84
			β^-+n		0.16
^{9}Li	^{12}C(γ, 3p), ^{12}C(π^-, n2p)	257.2	β^-	13.6	0.52
			β^-+n		0.48
^{11}Li	^{12}C(γ, 2π^+p), ^{12}C(π^-, π^+p)	12.3	β^-	20.6	0.07
			β^-+xn		0.92
^{12}Be	^{12}C(γ, 2π^+), ^{12}C(π^-, π^+)	16.4	β^-	11.7	-
			β^-+n		-

Table 6.8: Selection criteria for ^{8}He/^{9}Li events

Parameters	Criteria
Prompt Energy	$0.9 < E_p < 15$ MeV
Delayed Energy	$1.8 < E_d < 2.6$ MeV
Space Correlation	$\Delta R < 2.0$ m
Time Correlation	$0.5 < \Delta T < 1000$ μsec
Fiducial Volume	$R < 6.0$ m
Muon Veto	2.0 msec veto after muon

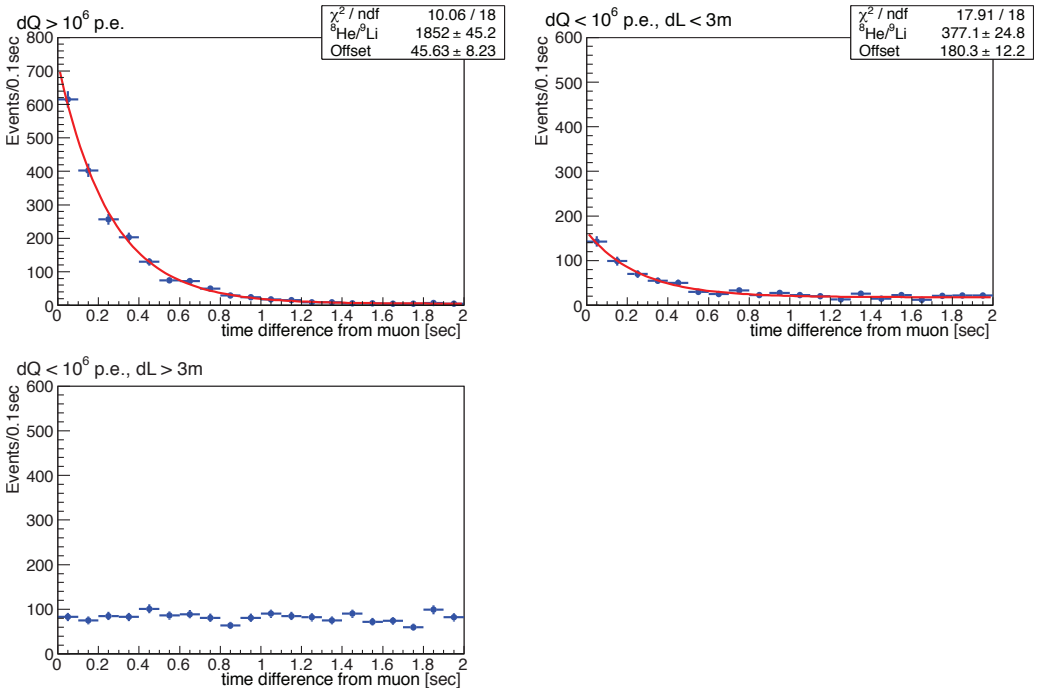

Figure 6.14: Time correlation between ^{8}He/^{9}Li delayed coincidence events and muons for showering muon (top-left), non-showering muon within 3.0 m from muon track (top-right), and non-showering muon which has longer distance from muon track than 3.0m (bottom). The red lines show the fitting function of ^{9}Li decay and constant background contribution. From tese fitting results, the number of backgrounds are estimated to be 1852.06 $\pm$ 45.24 events and 377.08 $\pm$ 24.82 events for showering muon and non-showering muon, respectively.

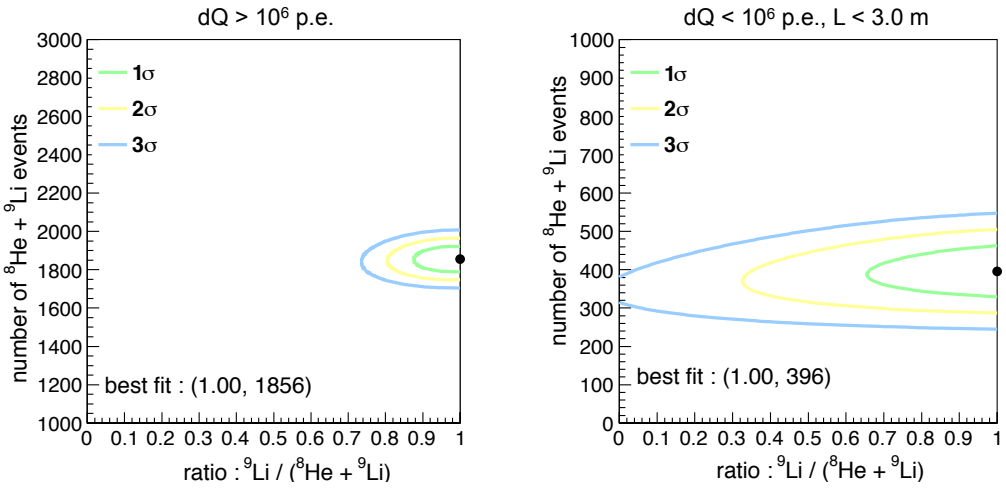

Figure 6.15: Allowed region from extended likelihood analysis of the number of ^{8}He and ^{9}Li events v.s. the ration of ^{9}Li for showering muon (left) and non-showering muon (right). The life time of ^{8}He and ^{9}Li are fixed in this analysis. The best-fit parameters indicate that the contribution of ^{8}He events is negligible compared to the ^{9}Li events.

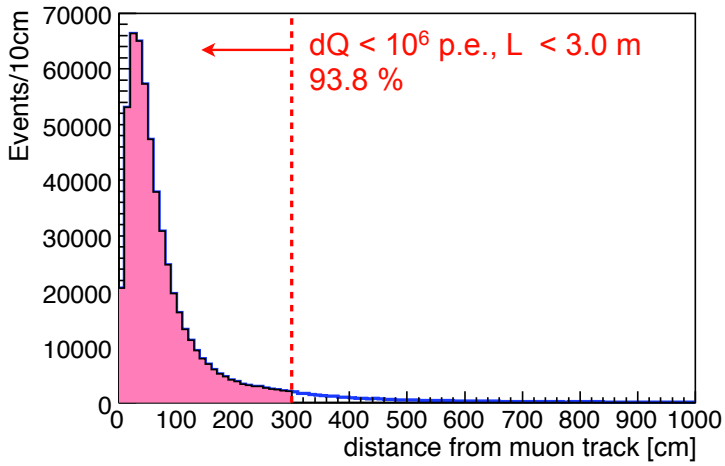

Figure 6.16: Track correlation of spallation neutron events for non-showering muons. The efficiency of the muon tracking within 3.0 m is estimated to be 93.8 %.

6.3.4 Fast Neutrons

Most of cosmogenic neutrons produced by muons are shielded by the rock surrounding the detector and the pure water buffer region of the OD, and tagged using OD signals. If these cosmogenic muons go through the OD insensitive regions, they enter the fiducial volume without making an OD signal. These events are categorized as "fast neutrons". Fast neutrons mimic delayed coincidence because it interacts proton and the recoiled proton emits scintillation light and the neutron are finally captured by proton and emit 2.22 MeV γ-rays. There are two possibilities to make fast neutron background :

- muons go through the OD inefficiency regions
- muons that pass through the rock just outside of the OD and producing neutrons that enter the liquid scintillator

To estimate the fast neutron background, the OD inefficiency is evaluated by using simulation data which reproduce the process of cosmogenic neutron production and the reaction in the detector.

Firstly, the muon flux at KamLAND area is calculated using the MUSIC [66] simulation code. Figure 6.17 shows the distribution of the muon track angle, and the simulation results are in good agreement with KamLAND data [67]. Furthermore, the reaction in the detector including photon generation processes are simulated using GEANT4 [24] to know what kind of muons producing the fast neutron background. From these results, the OD inefficiency is estimated to be 0.12 % for muon passing through the OD and 40 % for muon passing through the rock just outside the OD. Finally the upper limit of the first neutron background estimated to be less than 13.2 events considering estimated OD inefficiency. Figure 6.18 shows the energy spectrum of fast neutron. In this analysis energy region between 0.9 MeV and 8.5 MeV, the energy spectrum is assumed to be flat.

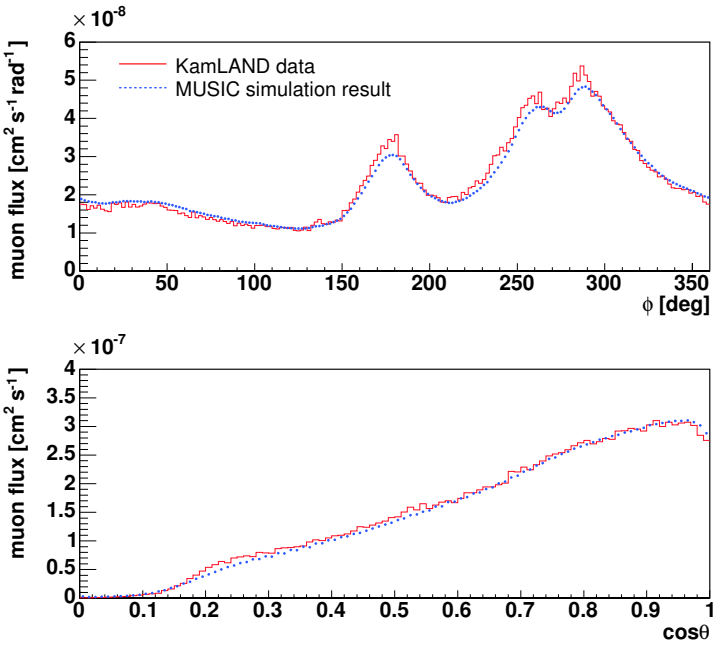

Figure 6.17: The distribution of the muon track direction comparing with simulation (blue dot line) and KamLAND (red line) data [67]. Phi (top) and cosθ (bottom) distributions are simulated using the MUSIC [66] simulation code.

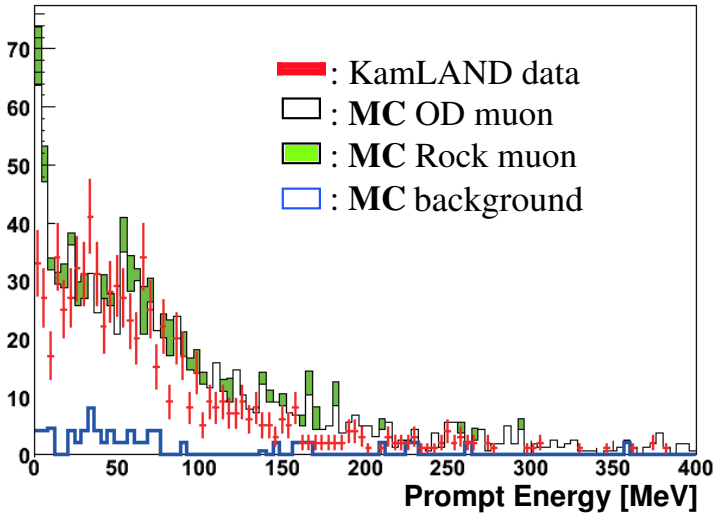

Figure 6.18: Prompt energy spectrum of fast neutron [67]. The red points show the KamLAND data, the green histogram shows the MC result from rock passing muon, the white histogram shows the MC result for muons passing through the OD, and the blue histogram shows the MC result of fast neutron background candidates, which have NhitOD < 5.

6.4 Accidental Backgrounds

As already described in Section 5.6.2, the accidental backgrounds do not have time correlation between the prompt signal and the delayed signal, and these events are estimated by same cut as $\bar{\nu}_e$ selection criteria except for the different time window. The collected accidental events are applied in the likelihood selection cut, and the number of survival events scaled by the anti neutrino analysis time window is used for the anti-neutrino analysis. Figure 6.19 shows the energy spectrum of the accidental backgrounds for various period normalized with livetime. During 1st and 2nd purification, the accidental events which have about 4.0 MeV prompt energy increased. The number of accidental background for the anti-neutrino analysis is estimated to be 108.3 $\pm$ 0.1 events.

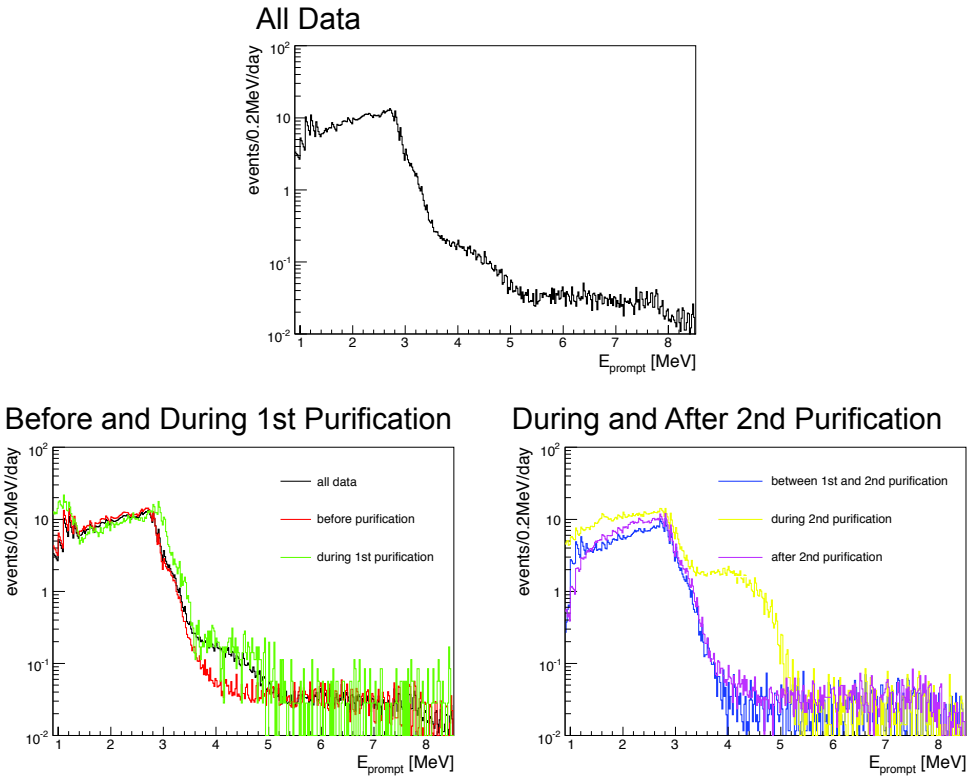

Figure 6.19: Prompt energy spectrum of the accidental backgrounds for various period normalized with livetime. The top figure shows the prompt energy distribution of all data set, and bottom two figures show that for various period. During 1st and 2nd purification, the accidental events which have about 4.0 MeV prompt energy increased.

6.5 (α, n) Interaction

Neutrons which emitted via (α, n) interaction also can be background for the anti-neutrino analysis. There are various radioactivities which emit α particle in the detector. From background study, α decays are dominated by ^{210}Po (Section 6.2). The ^{210}Po is produced by the decay of ^{210}Pb. The ^{210}Pb results from the decay of ^{222}Rn, which was introduced into the detector during the liquid scintillator filling process. The ^{210}Pb has accumulated due to its long half life of 22.3 years.

The target nuclei of (α, n) interaction are listed in Table 6.9. The contribution from the target which has large energy threshold or small natural abundance is negligible. Figure 6.20 shows the total cross sections of (α, n) interaction, and their cross sections are normalized with number of target, which calculated from the composition of KamLAND liquid scintillator and their natural abundance. While the dominant α energy is 5.304 MeV emitted from ^{210}Po, interactions other than ^{13}C(α, n)^{16}O interaction are negligible. The expected background spectrum from ^{13}C(α, n)^{16}O interaction is estimated by the number of ^{210}Po decays, the ionization energy loss of α particles in the liquid scintillator, the reaction cross section, the angular distribution of emitted neutrons, and the KamLAND detector responses.

Table 6.9: Target nuclei of (α,n) interaction

Isotopes	Q Value [MeV]	Threshold [MeV]	Natural Abundance [%]
^{1}H	-23.68	115.4	99.985
^{2}H	-4.190	12.50	0.015
^{3}H	-4.783	11.12	-
^{12}C	-8.502	11.34	98.90
^{13}C	2.216	0	1.10
^{14}C	-1.818	2.337	-
^{14}N	-4.735	6.088	99.634
^{15}N	-6.419	8.131	0.366
^{16}N	1.526	0	-
^{16}O	-12.13	15.17	99.762
^{17}O	5.867	0	0.038
^{18}O	-0.6962	0.8510	0.200
^{19}O	5.713	0	-

6.5.1 ^{13}C(α, n)^{16}O Interaction

As shown in Figure 6.21, the ^{13}C(α, n)^{16}O reaction may populate states in ^{16}O at 6.049 MeV (spin parity : 0^+), 6.130 MeV (3^-), 6.617 MeV (2^+) and 7.117 MeV (1^-). The 6.049 MeV state decays by pair emission and the other three states by γ-emission. Figure 6.22 shows the cross section of ^{13}C(α, n)^{16}O. For 5.304 MeV α particle from ^{210}Po, there are three candidates of the reaction.

- grand state : ^{13}C(α, n)^{16}O
- 1st excited state : ^{13}C(α, n)^{16}O* (6.049 MeV)

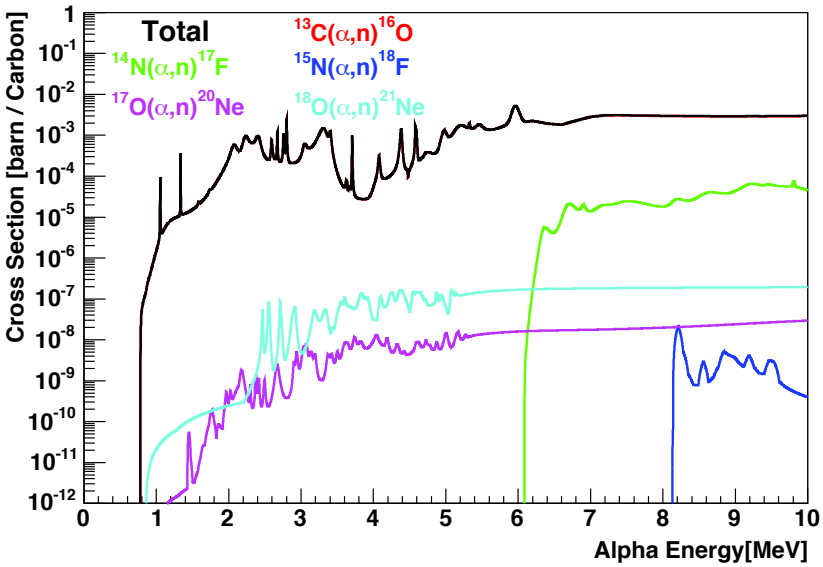

Figure 6.20: Total cross section of (α, n) interaction for various target nuclei in KamLAND based on JENDL calculation (2003) [68]. The cross sections are normalized to the natural carbon abundance and considering the chemical composition of the KamLAND liquid scintillator. The dominant interaction is ^{13}C(α, n)^{16}O at the α energy 5.304 MeV, which emitted from ^{210}Po.

- 2nd excited state : ^{13}C(α, n)^{16}O* (6.130 MeV)

^{13}C(α, n)^{16}O interaction process in the liquid scintillator is shown in Figure 6.23. The prompt signals are the recoiled proton 4.428 MeV γ, 6.046 MeV e^+ e^- from first excited state, and 6.129 MeV γ from second excited state. The delayed signal is 2.22 MeV γ from the neutron capture on proton.

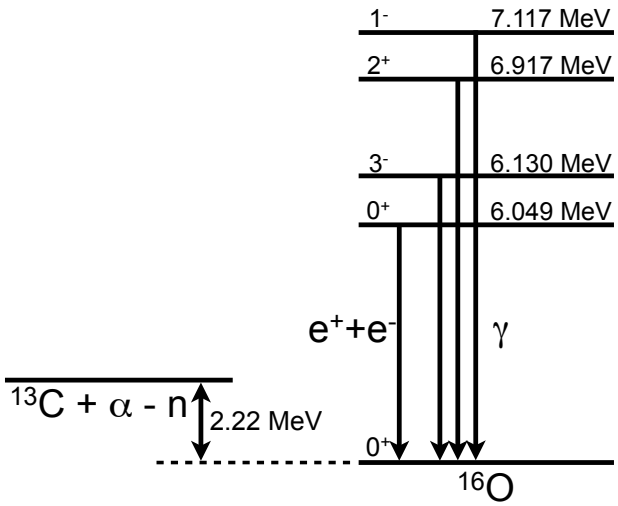

Figure 6.21: Energy level of ^{16}O.

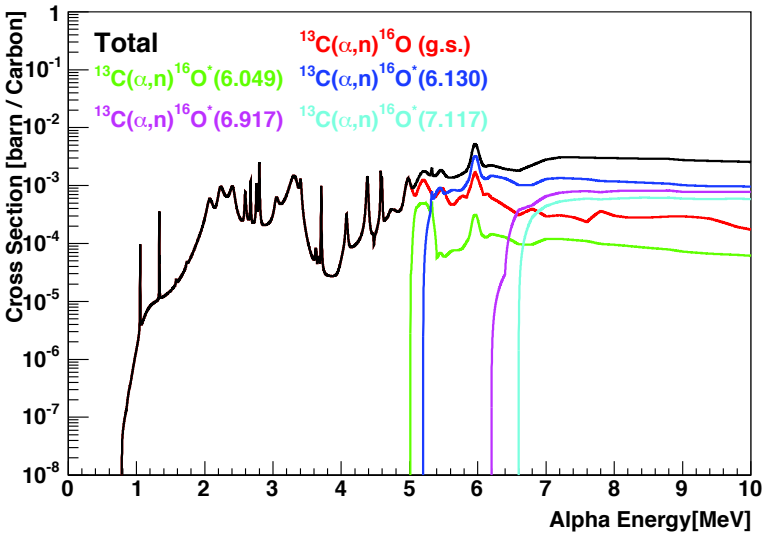

Figure 6.22: Total cross section of ^{13}C(α, n)^{16}O interaction based on JENDL calculation (2003)[68]. Considering 5.304 MeV ^{210}Po α particle, the grand state (red), the first excited state (green) and the second excited state (blue) are candidates interaction.

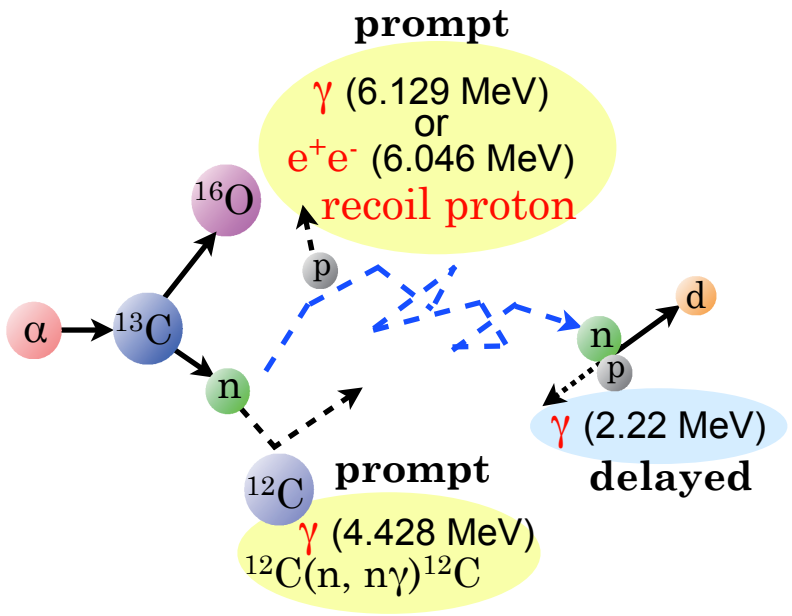

Figure 6.23: ^{13}C(α, n)^{16}O reaction in the liquid scintillator. The prompt signals are the recoiled proton 4.428 MeV γ, 6.046 MeV e^+ e^- from first excited state, and 6.129 MeV γ from second excited state. The delayed signal is 2.22 MeV γ from the neutron capture on proton.

Cross Section Calculation

The cross section of ^{13}C(α, n)^{16}O is calculated based on two types of data base, JENDL calculation (2003) [68] and S. Harissopulos et al. calculation (2003) [69].

- JENDL (2003) :
  · 20 % accuracy in total cross section calculation
  · cross sections are calculated for all states separately
- S. Harissopulos et al. (2005) :
  · 4 % accuracy in total cross section calculation
  · specify only total cross section

To improve the uncertainty of cross section calculation, the excited state cross sections from JENDL (2003) are subtracted from the total cross section from S. Harissopulos et al. (2005). The cross section to grand state is calculated as follows :

$$\begin{aligned}
\sigma_{grand}(E_\alpha) &= \sigma_{total}(E_\alpha) - \sigma_{1st}\frac{\eta(E_{n1})}{\eta(E_{n0})} - \sigma_{2nd}\frac{\eta(E_{n2})}{\eta(E_{n0})} \\
\eta(E_n) &= a_1 + a_2(E_n - a_3)\exp(-a_4E_n) + a_5(E_n + a_6)\exp(-a_7E_n) \\
a_1 &= 0.79042 \\
a_2 &= 0.01073 \\
a_3 &= 513.1884 \\
a_4 &= 6.0439 \\
a_5 &= 0.1607 \\
a_6 &= 247.0738 \\
a_7 &= 0.11416
\end{aligned} \tag{6.2}$$

$\eta(E_n)$ is the neutron detection efficiency shown in Figure 6.24 [70].

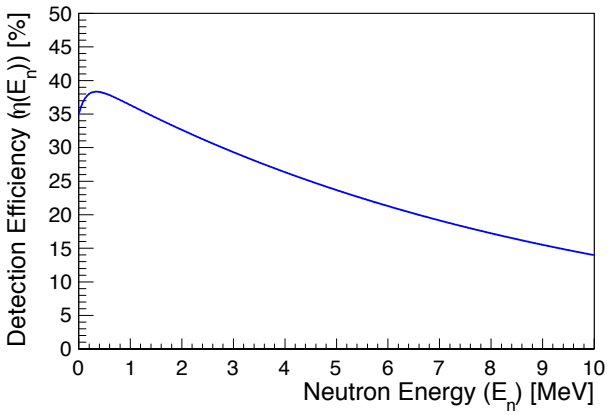

Figure 6.24: Neutron detection efficiency as a function of neutron energy [70].

Neutron Expected Spectrum Calculation

The number of ^{13}C(α, n)^{16}O interaction is calculated as follows :

$$\begin{aligned} N &= \int_{E_0}^{0} dE_\alpha \left(-\frac{dN}{dE_\alpha}\right) \\ -\frac{dN}{dE_\alpha} &= n_{\text{target}} I_{\text{surce}}\ \sigma(E_\alpha) \left(-\frac{dX}{dE_\alpha}\right), \end{aligned} \tag{6.3}$$

where

N : number of neutrons
E_α : α energy
E_0 : initial α energy
n_{target} : number of target nuclei of ^{13}C per unit volume of the liquid scintillator
I_{source} : source intensity
$\sigma(E_\alpha)$: (α, n) cross section
$\frac{dX}{dE_\alpha}$: stopping power

The stopping power in the KamLAND liquid scintillator can be estimated with the MC. The neutron energy depends on the scattering angle. In the lab frame, the momentum of the neutron p_{n} is as follows :

$$\begin{aligned} p_{\text{n}}^{\text{lab}} &= \sqrt{(\gamma\beta E_{\text{n}}^{\text{cm}} + \gamma p_{\text{n}}^{\text{cm}} \cos\theta_{\text{cm}})^2 + (p_{\text{n}}^{\text{cm}} \sin\theta_{\text{cm}})^2} \\ \beta &= \frac{p_\alpha^{\text{lab}} + p_{\text{C}}^{\text{lab}}}{E_\alpha^{\text{lab}} + E_{\text{C}}^{\text{lab}}} (p_{\text{C}}^{\text{lab}} \approx 0, E_{\text{C}}^{\text{lab}} \approx M_{\text{C}}) \\ \gamma &= \frac{1}{\sqrt{1-\beta^2}} \end{aligned} \tag{6.4}$$

The angular distribution of neutron can be expressed a Legendre-polynomial [71] [72]. Finally, the neutron energy spectrum is calculated as follows :

$$\begin{aligned} n(E^{\text{lab}}) &= \int_{E_0}^{0} dE_\alpha \int d\Omega\ \delta(\Omega, E_\alpha, E_{\text{n}}) n_{\text{target}} I_{\text{source}} \frac{d\delta}{d\Omega} \left(-\frac{dX}{dE_\alpha}\right) \\ \frac{d\delta}{d\Omega} &= \sum_l A_l P_l(\cos\theta), \end{aligned} \tag{6.5}$$

where,

E_{n} : neutron energy
Ω : scattering solid angle
$\delta(\Omega, E_\alpha, E_{\text{n}})$: 1 (conservation of momentum) or 0
A_l : coefficients of Legendre-polynomial
$P_l(\cos\theta)$: Legendre-polynomial

Figure 6.25 shows the neutron energy spectrum of ^{13}C(α, n)^{16}O interaction.

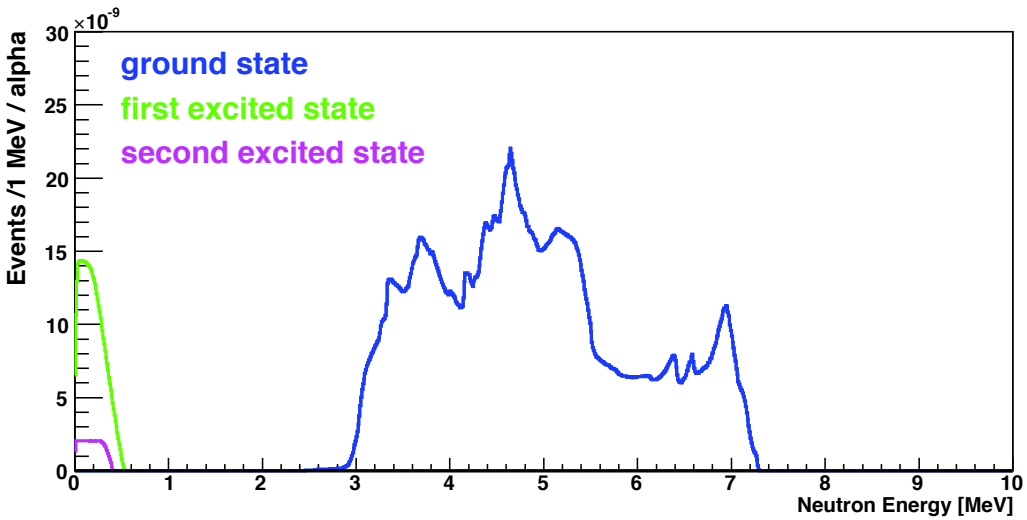

Figure 6.25: Neutron energy distribution of ^{13}C(α, n)^{16}O interaction.

6.5.2 Improvement of Uncertainties

Precise Measurement of Proton Quenching Factor

The prompt signal of ^{13}C(α, n)^{16}O interaction is the recoil of the proton in the neutron-proton elastic scattering. To improve the uncertainty of the neutron energy spectrum in this interaction, it is important to measure the proton quenching factor at different proton energies. The proton quenching factor was precisely measured at the OKTABIAN Facility, Osaka University [73] using a monochromatic neutron beam. Figure 6.26 shows the schematic view of the detector setup of the OKTABIAN Facility. A collimated 14.1 MeV neutron beam is produced by ^{3}H(d, n)^{4}He reactions, and its energy is changed by changing scattering angle θ. These neutrons are scattered by nuclei in the target liquid scintillator, and its light output responses are measured. The target liquid scintillator was taken from the center of KamLAND detector using a specialized sampling devise. In general, the light output response of liquid scintillator depends on its chemical composition as well as its temperature, oxygen content, and water content. Thus the target liquid scintillator was maintained carefully to avoid the affect from them. The temperature of the target liquid scintillator was kept at 9.0 $\pm$ 1.0 °C throughout the course of the experiment. The oxygen content in the actual KamLAND liquid scintillator has been measured to be less than 3 ppm. The oxygen content in the target liquid scintillator was set at 13 $\pm$ 3 and 78 ppm in two independent sets of measurements, and no significant difference was obtained in the light output responses. To prevent oxygen being mixed into the target liquid scintillator, the liquid scintillator sample was kept in an air tight stainless steel container, and was later carefully transferred to the detector cylinder under a nitrogen environment. As a result of these precautions the water content in the target liquid scintillator is expected to be very close to that in KamLAND, $\sim$20 ppm.

As discussed in Section 3.4.2, Birk's formula [25] is popular to estimate the contribution of the quenching effect in the liquid scintillator.

$$\frac{dL}{dx} = \frac{S\left(\frac{dE}{dx}\right)}{1 + kB\left(\frac{dE}{dx}\right)} \tag{6.6}$$

where k_B is Birk's constant, L is the luminescence, and S is the absolute scintillation efficiency. This Birk's formula well describes the quenching phenomena observed for heavier charged particles, and it successfully reproduces the experimental data of the light output responses. Chou [74] proposed an empirical extension of the Birk's formula to better reproduce to observed light output at low energies,

$$\frac{dL}{dx} = \frac{S\left(\frac{dE}{dx}\right)}{1 + kB\left(\frac{dE}{dx}\right) + C\left(\frac{dE}{dx}\right)^2}, \tag{6.7}$$

where C is an adjustable constant for higher-order correction. Furthermore, the generalized Birk's formula to account for the steep increase of quenching factor at low energy region [75]. It was pointed out that energy loss was attributed to two terms : nuclear energy loss and electronic energy loss.

$$\frac{dL}{dx} = \frac{S_e\left(\frac{dE}{dx}\right)_e + S_{\rm n}\left(\frac{dE}{dx}\right)_{\rm n}}{1 + kB_e\left(\frac{dE}{dx}\right)_e + kB_{\rm n}\left(\frac{dE}{dx}\right)_{\rm n}}, \tag{6.8}$$

Here this generalized Birk's formula is extended by introducing the higher-order correction as Chou's extension in Eq. (6.7) :

$$\frac{dL}{dx} = \frac{S_e \left(\frac{dE}{dx}\right)_e + S_{\rm n} \left(\frac{dE}{dx}\right)_{\rm n}}{1 + kB_e \left(\frac{dE}{dx}\right)_e + C_e \left(\frac{dE}{dx}\right)_e^2 + kB_{\rm n} \left(\frac{dE}{dx}\right)_{\rm n}}, \tag{6.9}$$

Figure 6.27 shows the proton quenching factor as a function of the scattered proton energy. In this figure, the data points and two kinds of fitting function Eq. (6.6) (dotted line), Eq. (6.7) (dashed line). The solid line shows the calculated Eq. (6.9) line using the best-fit parameters estimated by Eq. (6.7) fitting. As shown in Figure 6.27, since the fraction of the nuclear energy loss for protons is relative small and negligible in the measured recoil energy range, the generalized Birk's formula of Eq. (6.7) successfully gives a simultaneous description of the light output responses for protons in the KamLAND liquid scintillator. From the fitting results, the accuracy of the measured proton quenching factor is suppressed 2.0 %. This data is used for the ^{13}C(α, n)^{16}O prompt energy simulation.

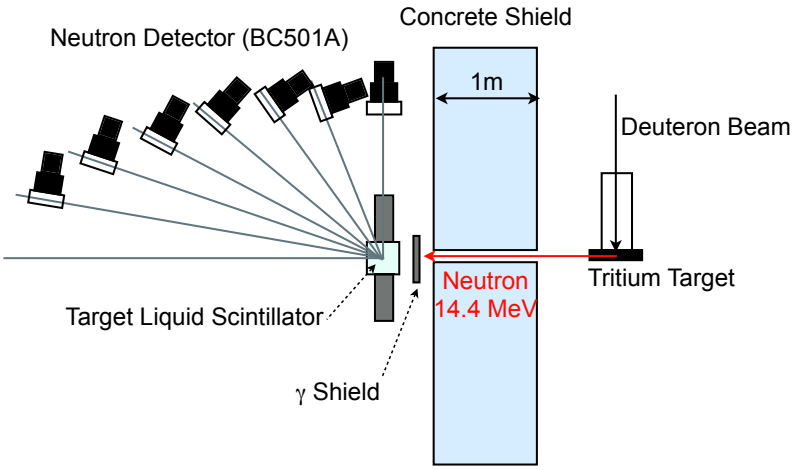

Figure 6.26: Schematic view of the detector setup of the OKTABIAN Facility.

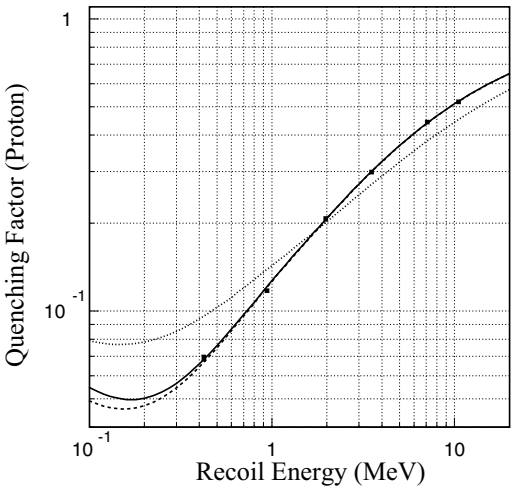

Figure 6.27: Proton quenching factor as a function of the scattered proton energy [73]. The dotted curve represents the Birk's formula of Eq. (6.6) with the best-fit parameter $kB = 1.34 \times 10^{-2}$ g/cm^2/MeV. The dashed line shows the best-fit function using Eq. (6.7) with $kB = 7.79 \times 10^{-3}$ g/cm^2/MeV and $C = 1.64 \times 10^{-5}$ (g/cm^2/MeV)^2. The solid line shows the calculated line of Eq. (6.9) using the best-fit parameters given by the carbon data, $S_e/S_{\rm n} = 0.371$. The nuclear energy loss term in Eq. (6.9) does not largely affect the response curve.

^{210}Po^{13}C Source Calibration

Uncertainties for (α, n) background are estimated by the difference between simulated events and the real data. Using the neutron energy spectrum (Figure 6.25) and proton quenching factor (Figure 6.27), the prompt signal can be simulated using GEANT4 [24]. However, there remains uncertainty about the branching ratio to the excited state of ^{16}O. In the reference model [68], 100 % errors are assigned to the excited states since their cross sections use model calculations.

To improve this branching ration uncertainty, a ^{210}Po^{13}C calibration source was deployed in the KamLAND. Figure 6.28 shows the geometry of the ^{210}Po^{13}C source. The source was constructed by filling the capsule with approximately 0.3 g of ^{13}C powder, dripping a Polonium solution into the carbon powder, and allowing the whole to dry throughly before tamping the powder with a Delrin spacer and closing the system. Figure 6.29 shows the delayed coincidence analysis results of data corrected with ^{210}Po^{13}C source at the center of the detector. Comparing between the prompt energy spectrum and expected spectrum, scaling factors can be estimated for each state.

- first excited state : the expected spectrum agrees with the calibration data if sealed by 0.6

- second excited state : the rate is consistent with the expected rate from Ref [68]

- grand state : the expected spectrum after the subtraction of the scaled first excited state and second excited state, is in good agreement with the calibration data if scaled by 1.05

Figure 6.30 shows the comparison between the expected spectrum and the calibration data. The expected spectrum is good agreement with the calibration data.

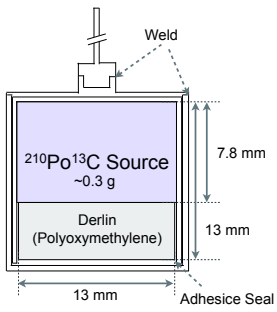

Figure 6.28: Geometry of the ^{210}Po^{13}C source.

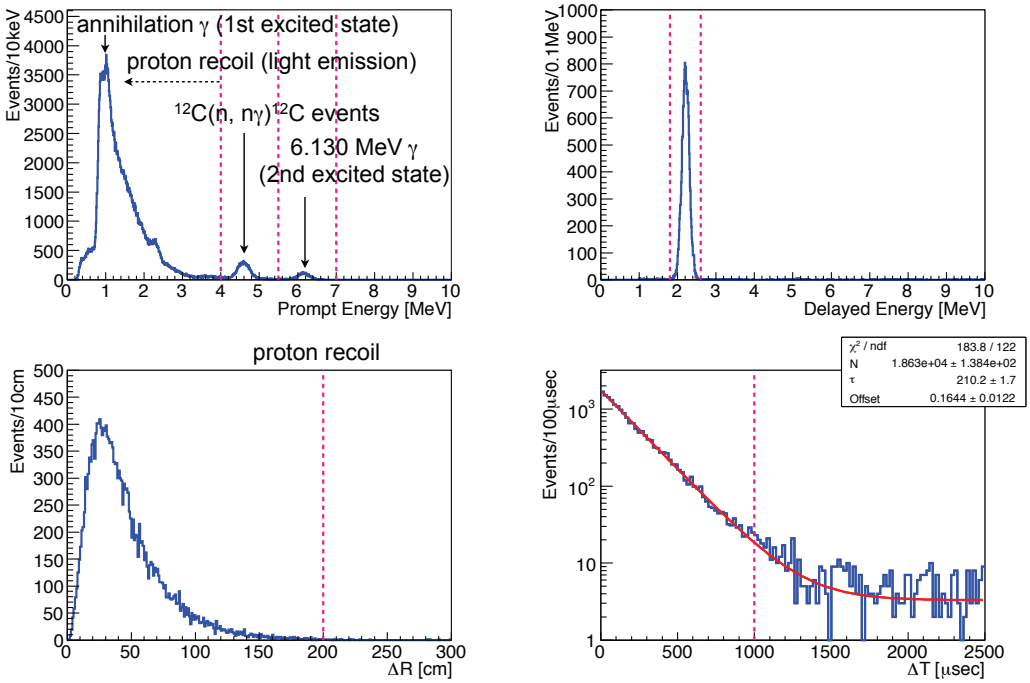

Figure 6.29: Delayed coincidence events of ^{210}Po^{13}C calibration data at the center of the detector. Each spectrum shows prompt energy (top left), delayed energy (top right), space correlation (bottom left) and time correlation distribution (bottom right). In the prompt energy spectrum, the peak at ∼6 MeV corresponds to the 6.130 MeV γ-ray from the second excited state of ^{16}O. The peak at ∼4.4 MeV corresponds to the γ-ray emission from the first excited state of ^{12}C. The peak at ∼1.022 MeV shows the annihilation γ from the first excited state of ^{16}O. The energy spectrum below 4.0 MeV shows the light emission from proton recoil by ^{13}C(α, n)^{16}O grand state. In the time correlation spectrum, the fitted result shows that the neutron capture time is 210.2 ± 1.7 μsec. It is consistent with other analysis, such as AmBe calibration data and spallation neutron data.

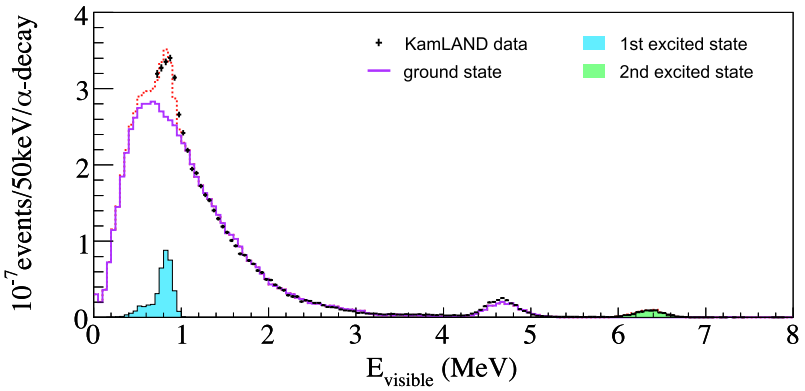

Figure 6.30: Comparison between ^{210}Po^{13}C calibration data and the expected spectrum.

6.5.3 Uncertainties and Number of Background

Uncertainties

The uncertainties of (α, n) interaction come from the ^{210}Po decay rate and the difference between the simulated expected spectrum and the data.

- Uncertainty of ^{210}Po Decay Rate
  The uncertainty of the α-source mainly comes from the ^{210}Po decay rate estimation. As discussed in Section 6.1, the radioactive background rate which comes from the balloon or the outside of the detector is extremely high around the balloon surface. In order to estimate ^{210}Po decay rate accurately, the ^{210}Po decay rate in the 6.0 m fiducial radius is estimated based on single spectrum fitting result of 5.5 m for the anti-neutrino analysis. The uncertainty of the ^{210}Po decay rate comes from the difference between the rate within 5.5 m radius and that within 6.0 m radius.

  There is one consideration of the uncertainty estimation: an effect from vertex resolution. There is a possibility that the ^{210}Po events around the balloon surface are reconstructed inside due to the vertex resolution, and make an effect on the uncertainty estimation. Since ^{210}Po in the liquid scintillator was successfully reduced by the purification campaign (Figure 6.5), the vertex resolution effect get larger than before purification. Figure 6.31 shows the ^{210}Po rate as a function of the fiducial radius for each period. Before purification, the ^{210}Po rate distributes almost flat. On the other hand, after 1st and 2nd purification, the rate increases near the balloon surface. To prevent the vertex resolution effect, ^{210}Po events are generated by MC within the uncertainty of the vertex resolution, and the uncertainty is evaluated by comparing with ^{210}Po rate after subtracting the MC events. Figure 6.32 shows the fiducial radius dependent ^{210}Po rate with MC event rate.

  Finally, the uncertainty of ^{210}Po decay rate is summarized in Table 6.10 for each period, and evaluated by combination of the fiducial volume uncertainty (Section 3.4.1) and its fiducial volume dependence. Figure 6.33 shows the time variation of ^{210}Po decay rate fiducial volume dependence. Before purification, the ^{210}Po decay rate fiducial volume dependence is estimated by comparing with data at 5.5 m radius and 6.0 m radius using the low threshold runs. After 1st and 2nd purification, the ^{210}Po decay rate fiducial volume dependence is estimated using normal run data and MC as described above.

Table 6.10: Uncertainties of ^{210}Po decay rate.

Sources	Before Pur.	After 1st Pur.	After 2nd Pur.
Fiducial Volume Uncertainty	1.8 %	2.5 %	2.5 %
Fiducial Volume Dependence	1.0 %	0.8 %	2.0 %
Total	2.1 %	2.6 %	3.2 %

- Uncertainty of Difference between Simulation and Data
  As discussed in Section 6.5.2, the uncertainty of the cross section of ^{13}C(α,

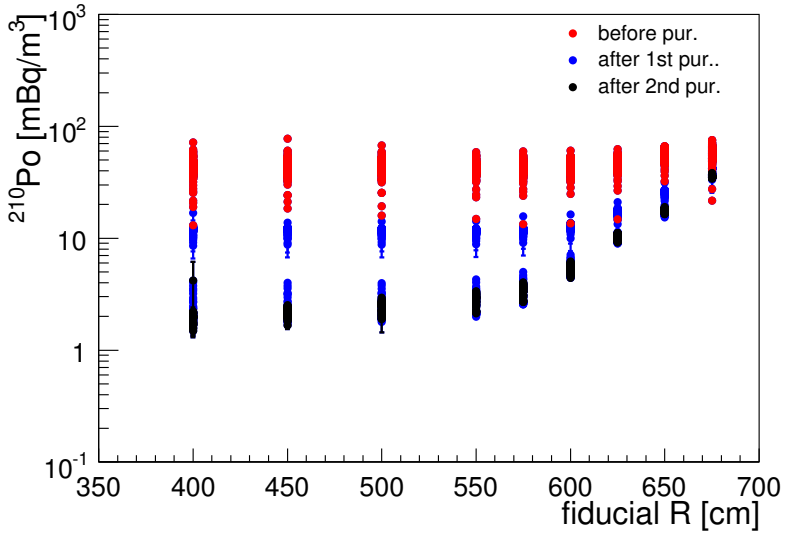

Figure 6.31: Fiducial radius dependence of ^{210}Po decay rate. The red, blue and black points show the ^{210}Po decay rate before purification, after 1st purification, and after 2nd purification, respectively. Before purification, the ^{210}Po decay rates distribute almost flat. On the other hand, after 1st and 2nd purification, the ^{210}Po decay rate increase around the balloon surface.

n)^{16}O interaction was improved by the precise measurement of proton quenching factor in the KamLAND liquid scintillator. Furthermore, the uncertainty of the branching ratio to the excited state of ^{16}O was improved by analyzing the ^{210}Po^{13}C source calibration data at the center of the detector. From these improvement, the uncertainty of the difference between simulation and actual data is suppressed 10 % and 20 % for the grand state and the excited state, respectively.

Table 6.11: Uncertainties of (α, n) background.

Sources	Before Pur.	After 1st Pur.	After 2nd Pur.
^{210}Po Decay Rate	2.1 %	2.6 %	3.2 %
Difference between Simulation and Data	10 % / 20 % (grand state / 1st excited state)		
Total	10.2 % / 20.1 %	10.3 % / 20.2 %	10.5% / 20.3 %

Number of ^{13}C(α, n)^{16}O Background

Finally, the number of ^{13}C(α, n)^{16}O background is estimated as shown in Table 6.12. The total number of ^{13}C(α, n)^{16}O delayed coincidence pairs remaining in the full data set after applying the likelihood selection is 200.4 $\pm$ 23.7. DS-2, which ben-

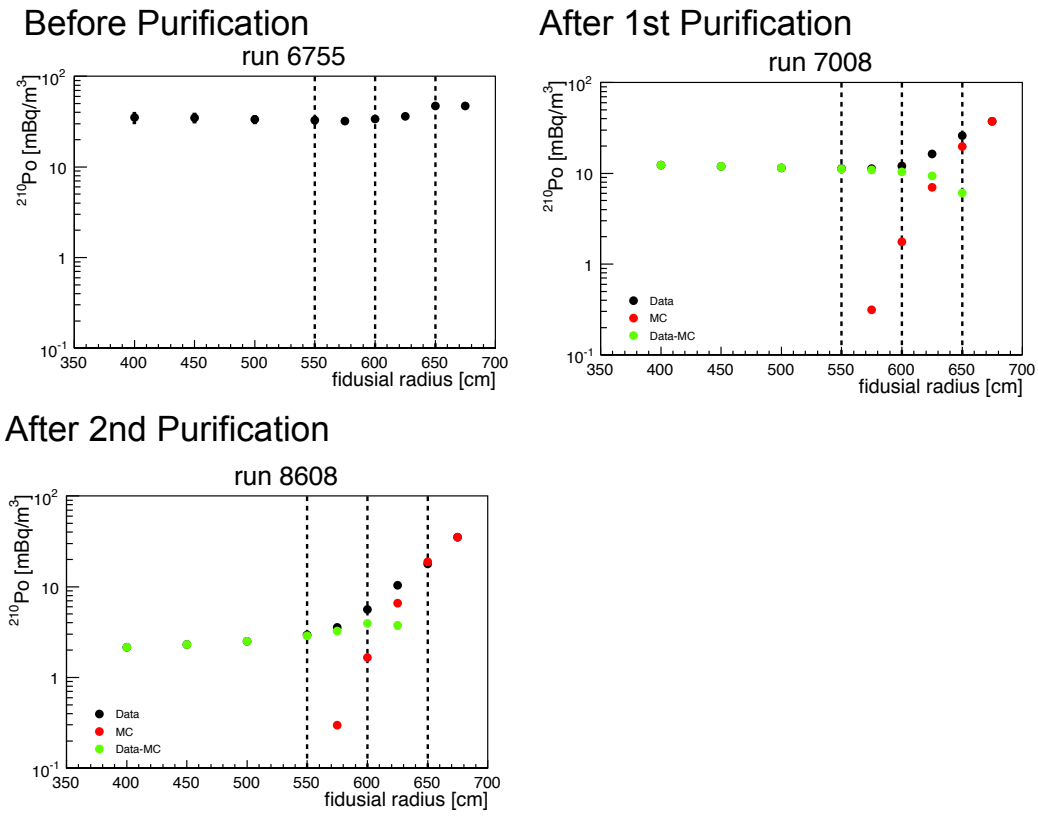

Figure 6.32: Fiducial radius dependence of ^{210}Po decay rate comparing with MC for before purification (top left), after 1st purification (top right) and after 2nd purification (bottom). The black points show the ^{210}Po decay rate of the data analysis results, the red points show the MC within the uncertainty of the vertex resolution, and the green points show the data after subtracted MC results. Comparing between the ^{210}Po decay rate within 5.5 m radius and that within 6.0 m radius, ^{210}Po decay rate of the fiducial volume dependence can be estimated.

efited from reduced ^{210}Po contamination due to the liquid scintillator purification, contributes only 7 % of the total number of ^{13}C(α, n)^{16}O events.

Table 6.12: Number of (α, n) background.

Background	Contribution
^{13}C(α, n)^{16}O$_{\text{g.s.}}$, np $\rightarrow$ np	173.3 $\pm$ 18.8
^{13}C(α, n)^{16}O$_{\text{g.s.}}$, ^{12}C(n, n$'$)^{12}C* (4.4 MeV γ)	7.4 $\pm$ 0.8
^{13}C(α, n)^{16}O, 1st e.s. (6.05 MeV e$^+$e$^-$)	16.0 $\pm$ 3.4
^{13}C(α, n)^{16}O, 2nd e.s. (6.13 MeV γ)	3.7 $\pm$ 0.6
Total	200.4 $\pm$ 23.7

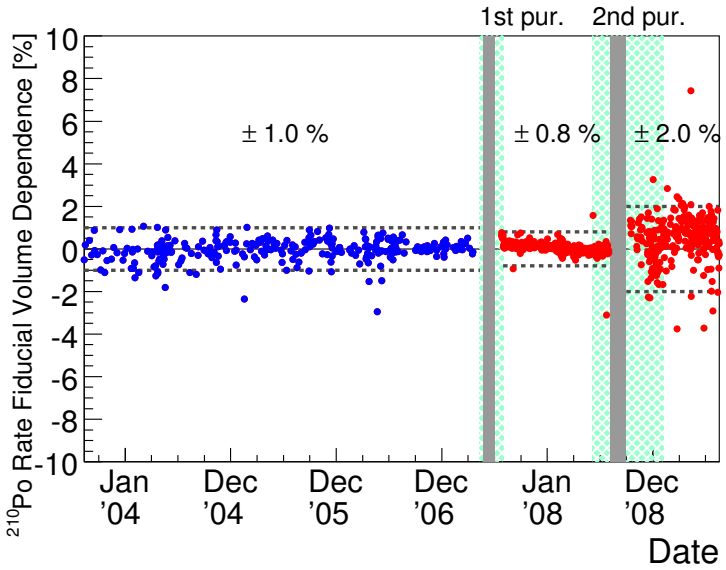

Figure 6.33: Time variation of the fiducial volume dependence of ^{210}Po decay rate. The blue points show the fiducial volume dependence of before purification estimated by low threshold run. The red points show the fiducial volume dependence of after purification using tithe data and MC. The fiducial volume dependence of ^{210}Po decay rate are estimated to be 1.0 % (before purification), 0.8 % (after 1st purification), and 2.0 % (after 2nd purification), respectively.

6.6 Other Negligible Backgrounds

6.6.1 Atmospheric Neutrino

The atmospheric neutrinos consist of the electron and muon neutrinos and their anti-neutrinos. These events come from the decay of particles produced in the atmosphere from cosmic-rays. They interact with nuclei in the liquid scintillator via charged current and neutral current. In the anti-neutrino analysis, the atmospheric neutrino is a background at the low energy regions. The reaction in the liquid scintillator are as follows :

- charged current quasi-elastic interaction : $\nu(\bar{\nu})$ N $\rightarrow l^{\pm}$ N$^{'}$
- charged current single-pion production through Δ resonance : $\nu(\bar{\nu})$ N $\rightarrow l^{\pm}$ π N$^{'}$
- charged current multi-pion production : $\nu(\bar{\nu})$ N $\rightarrow l^{\pm}$ (mπ) N$^{'}$ (m $\geq$ 1)
- neutral current quasi-elastic interaction : $\nu(\bar{\nu})$ N $\rightarrow \nu(\bar{\nu})$ N$^{'}$
- neutral current single-pion production through Δ resonance : $\nu(\bar{\nu})$ N $\rightarrow \nu(\bar{\nu})$ πN$^{'}$
- neutral current multi-pion production : $\nu(\bar{\nu})$ N $\rightarrow \nu(\bar{\nu})$ (mπ) N$^{'}$ (m $\geq$ 1)

Some reactions emit the neutrons, which produce the mimic delayed signals.

The number of the atmospheric neutrino background is estimated using two kinds of simulation tool. Firstly, the atmospheric neutrino flux in Kamioka is simulated with NUANCE [76]. Figure 6.34 shows the atmospheric neutrino fluxes in Kamioka [77] using for NUANCE simulation. Then kinematics for daughter particles and the response in the detector are simulated with GEANT4 [24]. In the GEANT 4 simulation, the atmospheric neutrino events are simulated in 10-years livetime and 5.5 m fiducial radius, and the prompt energy spectrum is assumed to be flat distribution in the analysis energy window between 0.9 MeV and 8.5 MeV, same as for the fast neutron background. Considering both fast neutrons and atmospheric neutrinos, the upper limit of fast neutron and atmospheric neutrino backgrounds is estimated to be less than 9 events in the data set. This value is consistent with the observed events in the high energy region between 8.5 MeV and 30.0 MeV. In this high energy region, observed events are assumed to be fast neutrons or atmospheric neutrinos. Since there are 15 events in this high energy region, the number of expected events are calculated by scaling the energy-window size. The number of atmospheric neutrinos and fast neutrons are expected to be 13.2 events in the reactor neutrino analysis (0.9 MeV $\sim$ 8.5 MeV).

6.6.2 Spontaneous Fission

There are several spontaneous fission isotopes in the U, Th, Ac and Np series, and some of them can become background to the anti-neutrino analysis. This reaction produces a γ-ray ($\sim$6 MeV) as the prompt event and several neutrons as delayed event. In the anti-neutrino analysis, the multiple coincidence events are rejected. Therefore, only single neutron events contribute as a background.

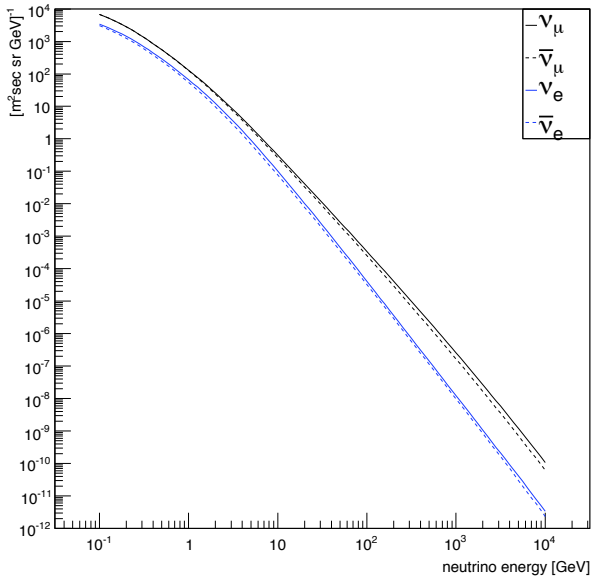

Figure 6.34: Atmospheric neutrino flux [77] using for NUANCE simulation. Each line corresponds to each (anti-)neutrino type.

- U-series (^{238}U, ^{234}U, ^{230}Th)
  ^{238}U spontaneous fission can be estimated by ^{234}Pa events assuming the radiation equilibrium. Figure 6.35 shows the fitted result of ^{234}Pa in the liquid scintillator for all dataset. The cylinder cut is applied to remove events coming from a thermometer, which had been installed at the center of the detector to April 2004. The upper limit of ^{234}Pa events is estimated to be 1.2×10^7 decays in total dataset. Considering ^{238}U branching ratio 5.45×10^{-5} %, the upper limit of the ^{238}U spontaneous fission background is 6.6 events. Since other isotope branching ratio in U-series are $4 \sim 6$ oder smaller than ^{238}U, these contribution is negligible.

- Th-series (^{232}Th, ^{228}Th, ^{225}Ra)
  ^{212}Bi-^{212}Po delayed coincidence is used for ^{232}Th estimation assuming radiation equilibrium. The decay rate is estimated to be 2.2×10^4 decays in total dataset. The branching ratio of each isotope are $< 1.8 \times 10^{-9}$ %, 1.813×10^{-11} % and $< 4.3 \times 10^{-9}$ % for ^{232}Th, ^{228}Th and ^{225}Ra, respectively. Totally, Th-series spontaneous fission is estimated to be less than 1.3×10^{-6} events.

- Ac-series, Np-series
  These series do not exit in nature. The contribution from them is negligible.

For these estimations, the total spontaneous fission is less than 6.6 events in all dataset.

According to Ref [78], the average number of neutrons emitted in spontaneous fission is 2 with a sigma of 1. In the anti-neutrino analysis, only single neutron events become background, and its probability os estimated to be 24.5 % from simple gaussian approximation. From this information, the number of spontaneous fission

backgrounds are less than 1.6 events. Therefore, the contribution of spontaneous fission is negligible.

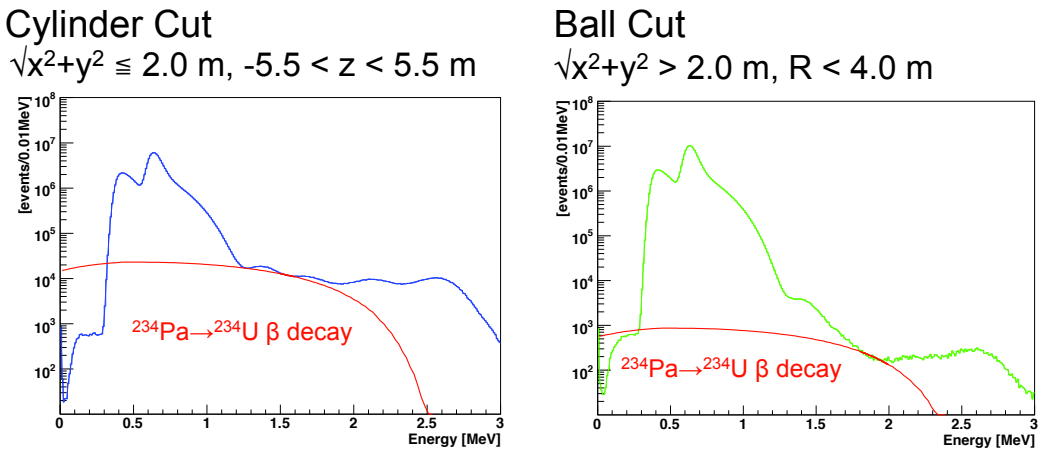

Figure 6.35: Energy spectrum below 3.0 MeV for ^{234}Pa estimation. The left figure shows the energy distribution after applying "Cylinder Cut", -5.5 m $\leq$ z $\leq$ 5.5 m and 2.0 m cylindrical region along z-axis. The right figure shows the energy distribution after applying "Ball Cut", 4.0 m fiducial radius and 2.0 m cylindrical cut around z-axis. The red lines show ^{234}Pa β spectrum, and blue (left) and green (right) histogram show the observed data. The upper limit of ^{234}Pa decay within 6.0 m fiducial radius is estimated to be 5.45×10^5 events in all dataset by scaling fiducial volume and livetime.

6.7 Summary of Backgrounds

The number of various backgrounds for reactor anti-neutrino analysis are summarized in Table 6.13, and that for geo anti-neutrino analysis are summarized in Table 6.14.

For the reactor anti-neutrino analysis, the dominant background is ^{13}C(α,n)^{16}O events. Figure 6.36 shows the time variation of the neutrino event rate and the background event rate with prompt energies between 0.9 and 8.5 MeV including the neutrino oscillation effect. In recent times the reactor $\bar{\nu}_e$ flux was significantly reduced because of an extended shutdown of the Kashiwazaki-Kariwa nuclear power station following an earthquake in July 2007. Figure 6.37 shows the correlation between the observed rate and the expected rate in the KamLAND, using the binning with approximately equal $\bar{\nu}_e$ flux. The slope indicates the reactor correlated signal and the intercept as the reactor independent constant background rate. The fitted result is

$$\mathrm{N_{obs}} = (0.846 \pm 0.098)\mathrm{N_{exp}} + (0.187 \pm 0.090). \tag{6.10}$$

In the geo-neutrino analysis, the dominant background is reactor anti-neutrinos. Figure 6.38 shows the time variation of observed event and expected event in 0.9 $\sim$ 2.6 MeV energy region, and Figure 6.39 represents the correlation between the observed rate and the expected rate. The fitted result is

$$\mathrm{N_{obs}} = (0.949 \pm 0.164)\mathrm{N_{exp}} + (0.075 \pm 0.053). \tag{6.11}$$

The estimated number of events is used for neutrino oscillation analysis and geo neutrino analysis described in Chapter 7 and Chapter 8.

Table 6.13: Summary of signal and backgrounds for reactor anti-neutrinos

	0.9 MeV threshold	2.6 MeV threshold
Expected reactor $\bar{\nu}_e$ without oscillation	3089.6	2211.5
Observed events	2249	1349
Background Events		
Accidental	108.3 ± 0.1	27.2 ± 0.1
^{9}Li/^{8}He	26.8 ± 1.7	23.6 ± 1.5
^{13}C(α,n)^{16}O	200.4 ± 23.7	33.0 ± 5.5
Fast neutron and atmospheric $\bar{\nu}_e$	< 13.2	< 10.3
Geo neutrino	free parameters	negligible
Total	335.5 ± 27.2	83.7 ± 11.8

Table 6.14: Summary of signal and backgrounds for geo anti-neutrinos

	0.9 < E < 8.5 MeV	0.9 < E < 2.6 MeV
Observed events	2249	900
Background Events		
Reactor neutrino	1795.1 ± 98.3	498.9 ± 27.3
Accidental	108.3 ± 0.1	81.1 ± 0.1
^{9}Li/^{8}He	26.8 ± 1.7	2.0 ± 0.1
^{13}C(α,n)^{16}O	200.4 ± 23.7	167.4 ± 18.4
Fast neutron and atmospheric $\bar{\nu}_e$	< 13.2	< 2.8
Total	2130.6 ± 102.0	749.4 ± 33.0

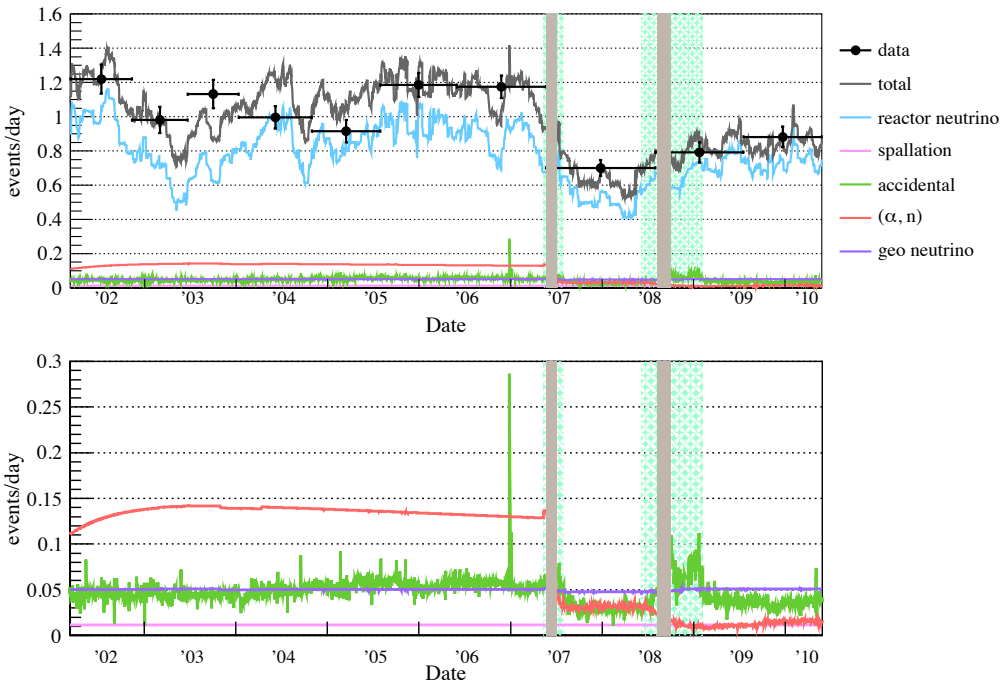

Figure 6.36: Time variation of the neutrino events and the background events with prompt energies between 0.9 and 8.5 MeV including the neutrino oscillation effect. The black points show the event rate observed in KamLAND, and the other lines show expected background event rates. The two vertical gray lines correspond to the low-data-quality period due to the purification activity (green shaded regions). The bottom panel shows mainly background rates.

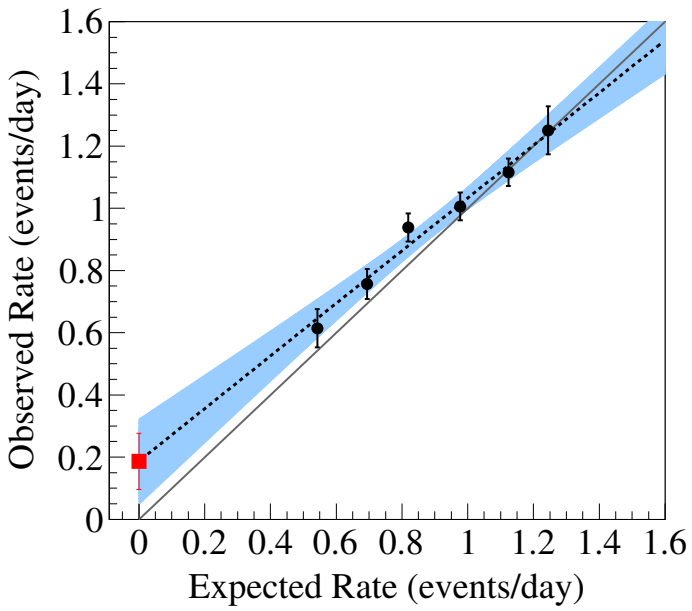

Figure 6.37: Observed anti-neutrino event rate versus event rates without geo-neutrino for $0.9 \sim 8.5$ MeV analysis. The black points show the data, corresponding to intervals of approximately equal $\bar{\nu}_e$ flux. The black dotted line is a fit with a linear function floating both slope and offset, and the 1 σ C.L. region is in the shaded region.

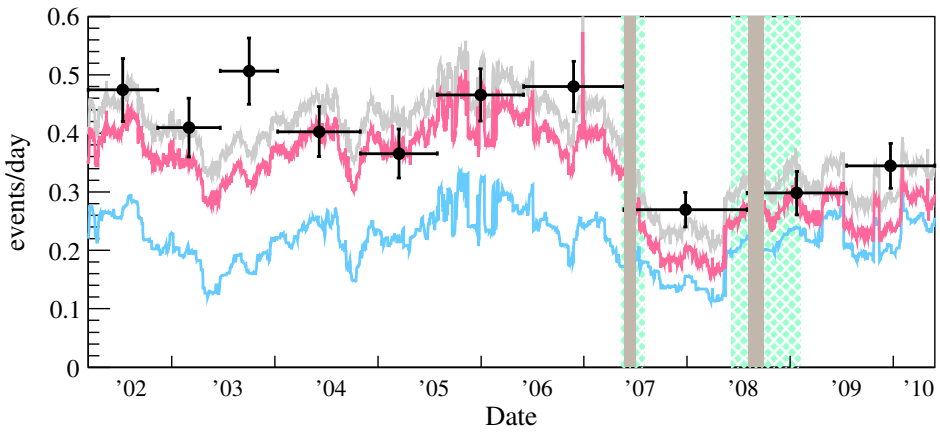

Figure 6.38: Event rate of the neutrino events with prompt energies between 0.9 and 2.6 MeV including neutrino oscillation effect. The black points show data, the blue line shows estimated time variation of only reactor neutrino contribution, the pink line shows the reactor neutrino and background contribution, and the top gray line shows the total event rate including the geo-neutrino events.

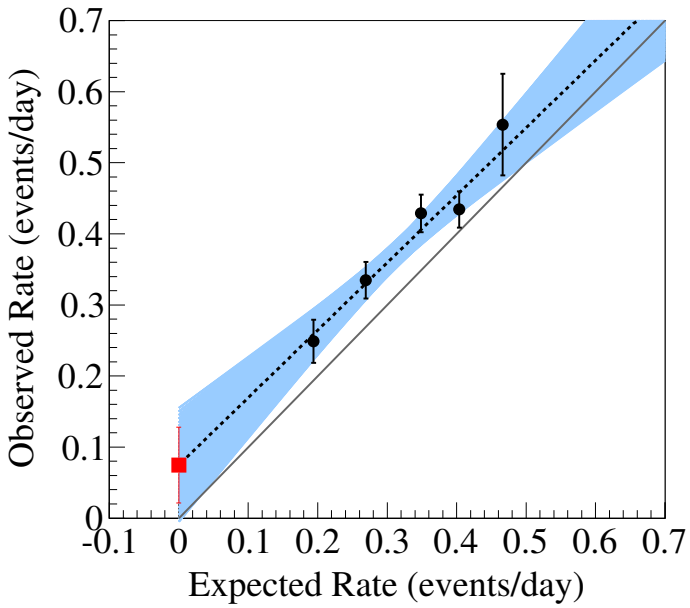

Figure 6.39: Observed rate versus the estimated reactor neutrino and background rate. The gray line represents the expectation without geo-neutrino contribution, and the black dashed line is a best-fit result. The 1 σ C.L. region is shown as blue shaded area. The excess attributed to geo-neutrinos is evident over the entire running period.

Chapter 7

Analysis; Reactor Neutrino

7.1 Neutrino Oscillation Analysis in 2 Generation

The neutrino oscillation analysis in 2 generation scheme is assuming only two flavor mixing between the electron and different flavor of anti-neutrinos ($\bar{\nu}_e$, $\bar{\nu}_x$). This assuming is good approximation in $\theta_{13} \sim 0$ case.

Neutrino oscillation affects not only neutrino disappearance but it also affects the energy spectral distortion. Its survival probability is a function of some parameters, such as mixing angle, mass difference, energy and flight length of $\bar{\nu}_e$. These properties of neutrino oscillation allow detailed investigation of the oscillation parameters. The KamLAND data is analyzed based on unbind maximum-likelihood methods by using the energy spectrum shape distortion of $\bar{\nu}_e$, the observed $\bar{\nu}_e$ rate and the time information. In this analysis, several free parameters are used in the χ^2 and chosen in such a way as minimize the χ^2 for each oscillation parameter.

Rate+Shape Analysis

In the Rate + Shape analysis, the χ^2 is defined as follows :

$$\begin{aligned}
\chi^2(\theta_{12}, \Delta m^2_{21}) &= \chi^2_{\rm rate} + \chi^2_{\rm shape} \\
&= \chi^2_{\rm rate}(\theta_{12}, \Delta m^2_{21}) \\
&\quad - 2\ln L_{\rm shape}(E; \theta_{12}, \Delta m^2_{21}, N_{\rm BG1\to5}, N^{\rm geo}_{\rm U,Th}, \alpha_{1\to4}) + \chi^2(N_{\rm BG1\to5}) + \chi^2(\alpha_{1\to4}) \\
\chi^2_{\rm rate}(\theta_{12}, \Delta m^2_{21}) &= \frac{(N_{\rm observed} - n_{\rm reactor} - N_{\rm BG})^2}{\sigma^2_{stat.}}
\end{aligned} \tag{7.1}$$

The terms are, in order :

1. χ^2 contribution for the total rate
2. χ^2 prompt energy spectrum shape
3. a penalty term for backgrounds
4. a penalty term for systematic uncertainties

$N_{\rm BG1\to5}$ are the expected background levels, and $N^{\rm geo}_{\rm U,Th}$ are the contributions expected from U and Th geo neutrino. $N^{\rm geo}_{\rm U,Th}$ are treated as free parameters for the

independent analysis from the Earth model. $\alpha_{1\to4}$ parametrize the uncertainties on the reactor $\bar{\nu}_e$ spectra and energy scale, the event rate, and the energy dependent efficiencies.

Figure 7.1 shows the allowed region from Rate + Shape analysis. In this analysis of the solar neutrino data, we include the rates in the chlorine [79] and gallium [80] experiments, Borexino [81], SNO III [82], the zenith spectra in Super-Kamiokande phase I [83], and the day-night spectra in SNO phase I and II [84]. The measured fluxes are compared with the high-metallicity standard solar model predictions (GS98) [85]. The more detail analysis from the solar neutrino data is described in Section 7.3. The best-fit oscillation parameters are,

$$\begin{aligned}(\tan^2\theta_{12}, \Delta m^2_{21}) &= (0.476^{+0.077}_{-0.070}, 7.68^{+0.25}_{-0.22}\times10^{-5}[\mathrm{eV}^2])(\text{KamLAND only})\\ (\tan^2\theta_{12}, \Delta m^2_{21}) &= (0.444^{+0.031}_{-0.036}, 7.66^{+0.26}_{-0.22}\times10^{-5}[\mathrm{eV}^2])(\text{KamLAND + Solar})\end{aligned} \tag{7.2}$$

The combined analysis of the solar and KamLAND data is assuming CPT invariance. In this figure, the allowed region from the solar data is in agreement with the KamLAND data, and small tension between the two-flavor best-fit values of θ_{12}.

Rate+Shape+Time Analysis

In the Rate + Shape + Time analysis, the χ^2 is defined as follows :

$$\begin{aligned}\chi^2(\theta_{12}, \Delta m^2_{21}) &= \chi^2_{\mathrm{rate}} + \chi^2_{\mathrm{shape}}\\ &= \chi^2_{\mathrm{rate}}(\theta_{12}, \Delta m^2_{21})\\ &\quad - 2\ln L_{\mathrm{shape}}(E, T; \theta_{12}, \Delta m^2_{21}, N_{\mathrm{BG1}\to5}, N^{\mathrm{geo}}_{\mathrm{U,Th}}, \alpha_{1\to4}) + \chi^2(N_{\mathrm{BG1}\to5}) + \chi^2(\alpha_{1\to4})\\ \chi^2_{\mathrm{rate}}(\theta_{12}, \Delta m^2_{21}) &= \frac{(N_{\mathrm{observed}} - n_{\mathrm{reactor}} - N_{\mathrm{BG}})^2}{\sigma^2_{stat.}}\end{aligned} \tag{7.3}$$

The prompt energy spectrum likelihood term is evaluated as a function of the candidate event time. The detailed knowledge of the time evolution of the total reactor $\bar{\nu}_e$ spectrum and effective baseline, afforded by the Japanese reactor operators, is thus fully utilized in the analysis.

Figure 7.2 shows the allowed region from Rate + Shape + Time analysis. The best-fit oscillation parameters are,

$$\begin{aligned}(\tan^2\theta_{12}, \Delta m^2_{21}) &= (0.500^{+0.083}_{-0.069}, 7.48^{+0.21}_{-0.18}\times10^{-5}[\mathrm{eV}^2])(\text{KamLAND only})\\ (\tan^2\theta_{12}, \Delta m^2_{21}) &= (0.444^{+0.031}_{-0.029}, 7.48^{+0.20}_{-0.22}\times10^{-5}[\mathrm{eV}^2])(\text{KamLAND + Solar})\end{aligned} \tag{7.4}$$

As seen in this figure, the has-splitting sensitivity is dominated by KamLND data. The lower LMA region (LMA 0) and the upper LMA region (LMA II) are significantly disfavored in 5.8 σ and 8.7 σ, respectively. Furthermore, the full-mixing is also disfavored by KamLAND data in 2.9 σ.

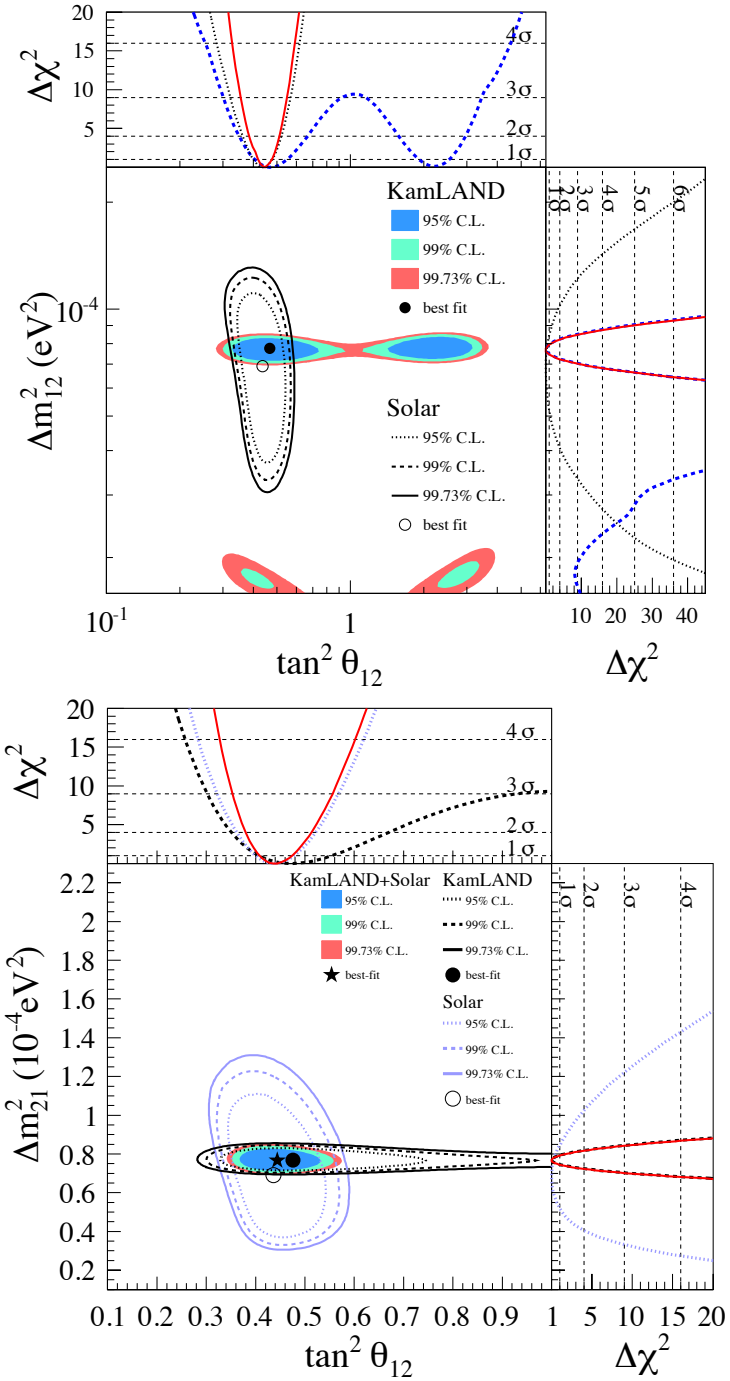

Figure 7.1: Allowed region and $\Delta\chi^2$ distribution from Rate + Shape analysis projected in the $(\tan^2\theta_{12}, \Delta m^2_{21})$ plane. The results of combined oscillation analysis of the solar and KamLAND data under the assumption of CPT invariance.

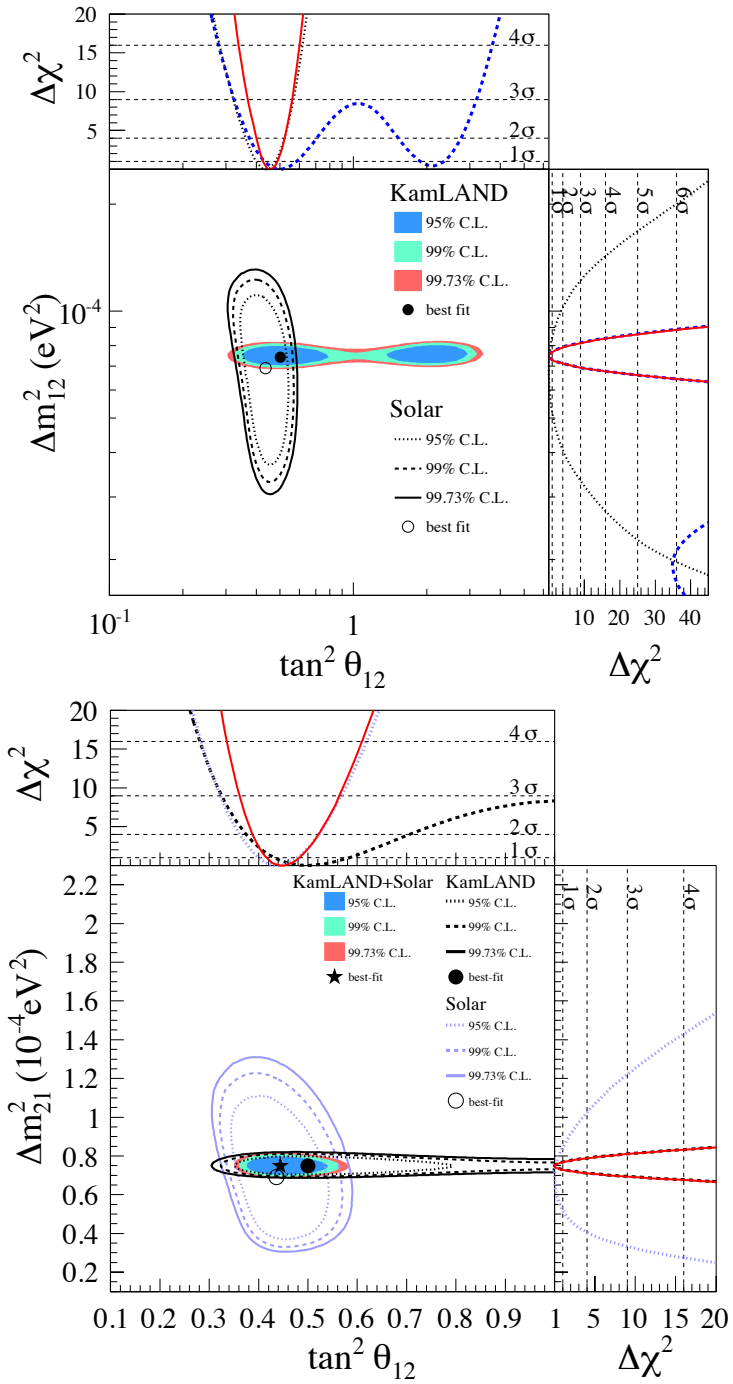

Figure 7.2: Allowed region and $\Delta\chi^2$ distribution from Rate + Shape + Time analysis projected in the ($\tan^2\theta_{12}$, Δm^2_{21}) plane.

7.2 Neutrino Oscillation Analysis in 3 Generation

Previous KamLAND results [86] were based on a two-flavor (ν_1-ν_2) oscillation formalism which assumes $\theta_{13} = 0$. For the length scales relevant to reactor neutrino oscillation at KamLAND and solar neutrino oscillation in the LMA-MSW solution, the dependence of the more general three-flavor phenomenology on the larger ν_1-ν_3 mass splitting ($|\Delta m^2_{31}| \sim |\Delta m^2_{32}| \gg \Delta m^2_{21}$) averages out and the three-flavor survival probability ($P^{3\nu}_{ee}$), including matter effects, may be approximated as

$$P^{3\nu}_{ee} = \cos^4\theta_{13}\widetilde{P}^{2\nu}_{ee} + \sin^4\theta_{13}\ . \tag{7.5}$$

$\widetilde{P}^{2\nu}_{ee}$ has the same form as the survival probability in matter for ν_1-ν_2 mixing but with the electron density (N_e) modified: $\widetilde{N}_e = N_e\cos^2\theta_{13}$ [87]. Since $\sin^2\theta_{13} \ll 1$, the survival probability can be further approximated as $P^{3\nu}_{ee} \sim (1 - 2\sin^2\theta_{13})\widetilde{P}^{2\nu}_{ee}$. Thus for KamLAND and the solar experiments, ν_1-ν_3 mixing would give rise to an energy-independent suppression of the survival probability relative to the $\theta_{13} = 0$ case.

For solar neutrino oscillation in the LMA-MSW solution, coherent mixing can be safely ignored due to the long distance between the Sun and the Earth. The two-neutrino survival probability is simply expressed as

$$\widetilde{P}^{2\nu}_{ee} = P^{\odot}_1 P_{1e} + P^{\odot}_2 P_{2e}\ , \tag{7.6}$$

where $P^{\odot}_i$ and P_{ie} are, respectively, the probability of the $\nu_e \to \nu_i$ transition in the Sun and the probability of the $\nu_i \to \nu_e$ transition in the Earth with the modified electron density $\widetilde{N}_e$. Neutrino propagation in the Sun and Earth is calculated following the analytical procedure of [88] [89], and the resulting survival probabilities agree well with numerical calculations. The details of solar neutrino oscillation are discussed later in Section 7.3.2.

Rate+Shape Analysis

In the Rate + Shape analysis, the χ^2 is defined as follows :

$$\begin{aligned}
\chi^2(\theta_{12},\theta_{13},\Delta m^2_{21}) &= \chi^2_{\rm rate} + \chi^2_{\rm shape} \\
&= \chi^2_{\rm rate}(\theta_{12},\theta_{13},\Delta m^2_{21}) \\
&\quad - 2\ln L_{\rm shape}(E;\theta_{12},\theta_{13},\Delta m^2_{21},N_{\rm BG1\to5},N^{\rm geo}_{\rm U,Th},\alpha_{1\to4}) + \chi^2(N_{\rm BG1\to5}) + \chi^2(\alpha_{1\to4}) \\
\chi^2_{\rm rate}(\theta_{12},\theta_{13},\Delta m^2_{21}) &= \frac{(N_{\rm observed} - n_{\rm reactor} - N_{\rm BG})^2}{\sigma^2_{stat.}}
\end{aligned} \tag{7.7}$$

Figure 7.3 and Figure 7.4 show the results from three-flavor Rate + Shape analysis. The best-fit oscillation parameters are,

$$\begin{aligned}
(\tan^2\theta_{12},\sin^2\theta_{13},\Delta m^2_{21}) &= (0.404^{+0.104}_{-0.085}, 0.038^{+0.037}_{-0.037}, 7.66^{+0.24}_{-0.24}\times10^{-5}[{\rm eV}^2])({\rm KamLAND\ only}) \\
(\tan^2\theta_{12},\sin^2\theta_{13},\Delta m^2_{21}) &= (0.444^{+0.036}_{-0.031}, 0.018^{+0.020}_{-0.021}, 7.66^{+0.23}_{-0.22}\times10^{-5}[{\rm eV}^2])({\rm KamLAND + Solar})
\end{aligned} \tag{7.8}$$

The reduction of the best-fit value of $\tan^2\theta_{12}$ for the three-flavor KamLAND-only analysis relative to the two-flavor oscillation analysis follows the anti correlation

apparent in the KamLAND contours, Figure 7.4. The correlation between θ_{12} and θ_{13} in the solar data is slight and the difference between the best-fit value of θ_{12} from the two-flavor and there-flavor analyses of the solar-only data is small.

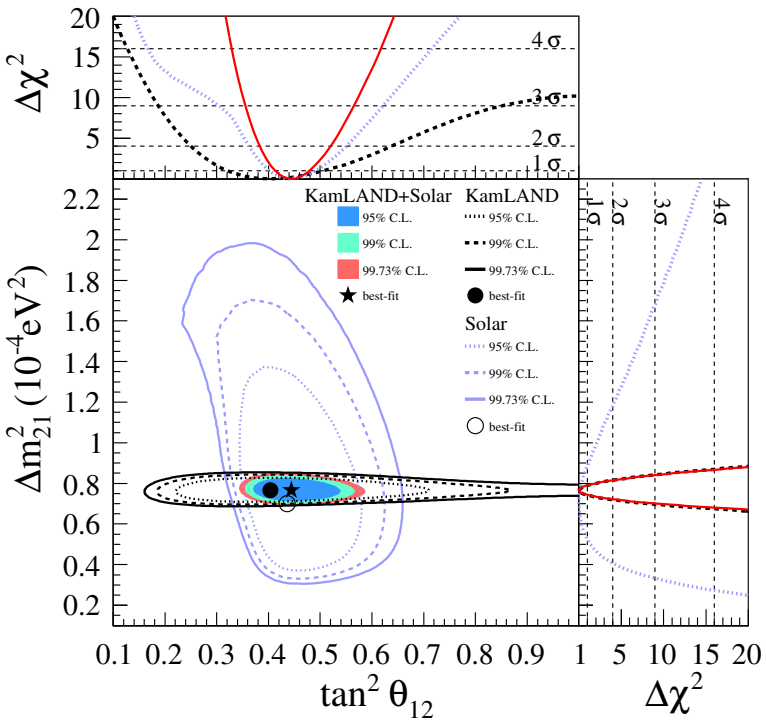

Figure 7.3: Allowed region and $\Delta\chi^2$ distribution from Rate + Shape analysis projected in the $(\tan^2\theta_{12},\ \Delta m^2_{21})$ plane. This is the three-flavor oscillation analysis result, where θ_{13} is a free parameter.

Rate+Shape+Time Analysis

In the Rate + Shape + Time analysis, the χ^2 is defined as follows :

$$\begin{aligned}\chi^2(\theta_{12},\theta_{13},\Delta m^2_{21}) &= \chi^2_{\rm rate} + \chi^2_{\rm shape} \\ &= \chi^2_{\rm rate}(\theta_{12},\theta_{13},\Delta m^2_{21}) \\ &\quad - 2\ln L_{\rm shape}(E,T;\theta_{12},\theta_{13},\Delta m^2_{21},N_{\rm BG1\to5},N^{\rm geo}_{\rm U,Th},\alpha_{1\to4}) + \chi^2(N_{\rm BG1\to5}) + \chi^2(\alpha_{1\to4}) \\ \chi^2_{\rm rate}(\theta_{12},\theta_{13},\Delta m^2_{21}) &= \frac{(N_{\rm observed} - n_{\rm reactor} - N_{\rm BG})^2}{\sigma^2_{stat.}}\end{aligned} \tag{7.9}$$

Figure 7.5 and Figure 7.6 show the results from three-flavor Rate + Shape analysis. The best-fit oscillation parameters are,

$$\begin{aligned}(\tan^2\theta_{12},\sin^2\theta_{13},\Delta m^2_{21}) &= (0.444^{+0.098}_{-0.084}, 0.032^{+0.037}_{-0.032}, 7.48^{+0.19}_{-0.20}\times10^{-5}[{\rm eV}^2])({\rm KamLAND\ only}) \\ (\tan^2\theta_{12},\sin^2\theta_{13},\Delta m^2_{21}) &= (0.452^{+0.034}_{-0.030}, 0.020^{+0.015}_{-0.018}, 7.48^{+0.19}_{-0.19}\times10^{-5}[{\rm eV}^2])({\rm KamLAND + Solar})\end{aligned} \tag{7.10}$$

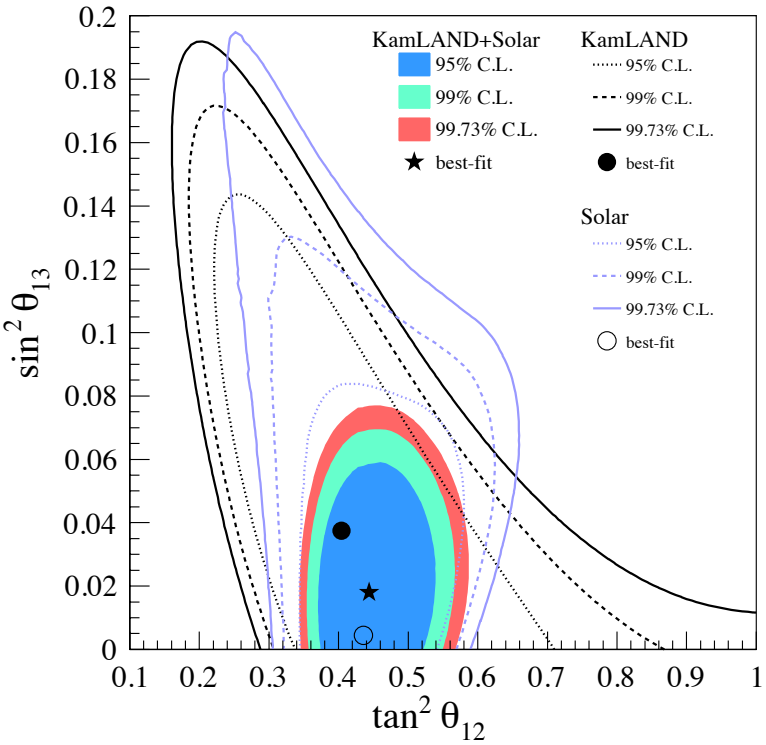

Figure 7.4: Allowed region from Rate + Shape analysis projected in the ($\tan^2\theta_{12}$, $\sin^2\theta_{13}$) plane for the three-flavor analysis. The KamLAND data analysis gives the result of positive $\sin^2\theta_{13}$, $0.038^{+0.037}_{-0.037}$.

Using these best-fit results, the expected prompt energy spectrum is shown in Figure 7.7.

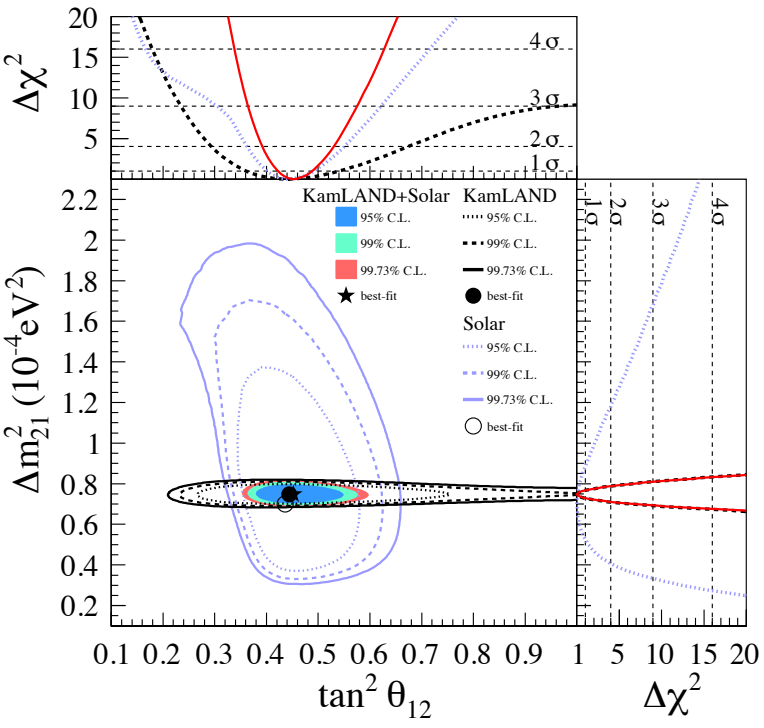

Figure 7.5: Allowed region and $\Delta\chi^2$ distribution from Rate + Shape + Time analysis projected in the ($\tan^2\theta_{12}$, Δm^2_{21}) plane. This is the three-flavor oscillation analysis result, where θ_{13} is a free parameter.

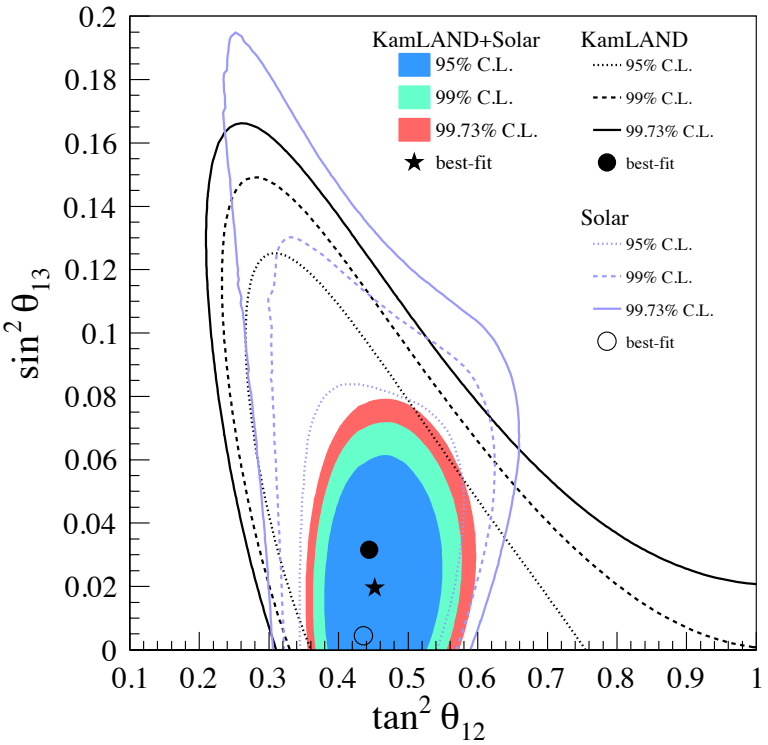

Figure 7.6: Allowed region from Rate + Shape analysis projected in the ($\tan^2\theta_{12}$, $\sin^2\theta_{13}$) plane for the three-flavor analysis. The KamLAND data analysis gives the result of positive $\sin^2\theta_{13}$, $0.032^{+0.033}_{-0.033}$.

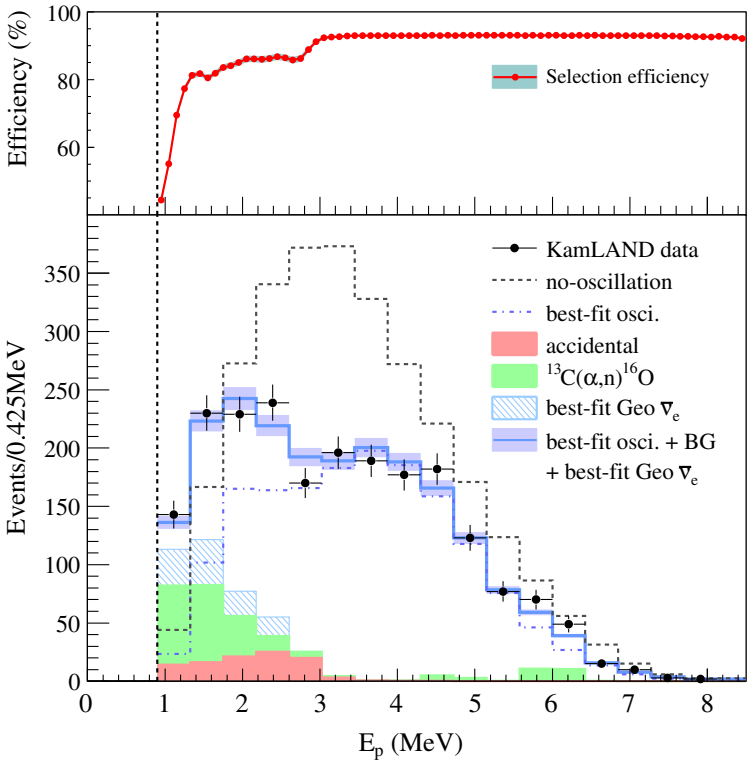

Figure 7.7: Prompt energy spectrum of anti-neutrino candidates above 0.9 MeV energy threshold. The data together with the background and reactor $\bar{\nu}_e$ contributions fitted from an unbind maximum-likelihood there-flavor oscillation analysis are shown in main panel. The number of geo-$\bar{\nu}_e$'s is unconstrained in the fit. The shaded background histograms are cumulative. The top panel shows the energy-dependent selection efficiency; each point is the weighted average over the five time periods.

7.2.1 Global 3 Generation Analysis

Figure 7.8 shows the $\Delta\chi^2$-profiles projected onto the $\sin^2\theta_{13}$ axis for different combinations of the data. The combined analysis of CHOOZ, atmospheric, and long-baseline accelerator (i.e., T2K and MINOS) experiments presented in [90], and the result is used for this global analysis. The difference data sets are listed as follows :

- KamLAND (constraint on Δm^2_{21}, θ_{12}, θ_{13})
  The full data set is used in this analysis. The other parameters, $\tan^2\theta_{12}$ and Δm^2_{21} are floated.

- solar (constraint on Δm^2_{21}, θ_{12}, θ_{13})
  The flux measurement results from the chlorine and gallium experiments, Borexino and SNO III, are used. And SK zenith energy spectra data, and the day-night spectra in SNO phase I and II are also included.

- CHOOZ (constraint on Δm^2_{31}, θ_{31})
  The CHOOZ experiment had an average value $L/E \sim 300$ ($L \sim 1$ km, $E \sim 3$ MeV), and the data shows the reactor $\bar{\nu}_e$ deficit as well as those distortion [14].

- atmospheric (constraint on Δm^2_{31}, θ_{23}, θ_{31})
  In [90], the atmospheric neutrino data of SK-I, SK-II and SK-III [91] are included. The data shows the correlation of the disappearance of the muon type neutrino for nonzero θ_{13} and deviation of $\sin^2\theta_{23}$ from 0.5. No distortions of the neutrino flux consistent with nonzero θ_{13} are found and both neutrino mass hierarchy hypotheses are in agreement with the data. The data are best fit at $\Delta m^2_{31} = 2.1 \times 10^{-3}$ eV^2, $\sin^2\theta_{13} = 0.0$, and $\sin^2\theta_{23} = 0.5$.

- long baseline (constraint on Δm^2_{31}, θ_{23}, θ_{31})
  In the $\nu_\mu \rightarrow \nu_\mu$ disappearance channel, K2K analysis [92] and MINOS spectrum analysis [16] are used in [90]. And, in the appearance channel $\nu_\mu \rightarrow \nu_e$, MINOS results and the recent result from T2K experiment [15] are analyzed.

The results of this global analysis are summarized in Table 7.1. In the global analysis, there is a clear evidence in favor of $\sin^2\theta_{13} > 0$ at a confidence level of 3.12 σ. Remarkably, the data sets sensitive to Δm^2_{21} (solar + KamLAND) and Δm^2_{31} (CHOOZ+Atmospheric+LBL) agree very well. Since the T2K appearance results alone account for more than 2 σ, the bounds from global analysis appear to be currently dominated by Δm^2_{31}-sensitive experiments. Figure 7.9 shows the $\pm 1\sigma$ ranges of $\sin^2\theta_{13}$ in a different data set.

Table 7.1: Summary of the global analysis of $\sin^2\theta_{13}$

	best-fit	90 % C.L.	95 % C.L.	$\sin^2\theta_{13} > 0$
solar	0.006 +0.029/-0.029	0.053	0.062	0.26 σ
KamLAND	0.032 +0.037/-0.032	0.093	0.106	0.90 σ
solar + KamLAND	0.020 +0.015/-0.018	0.047	0.052	1.13 σ
CHOOZ + Atmospheric + LBL	0.020 +0.009/-0.007	0.034	0.037	2.92 σ
global	0.020 +0.007/-0.007	0.033	0.035	3.12 σ

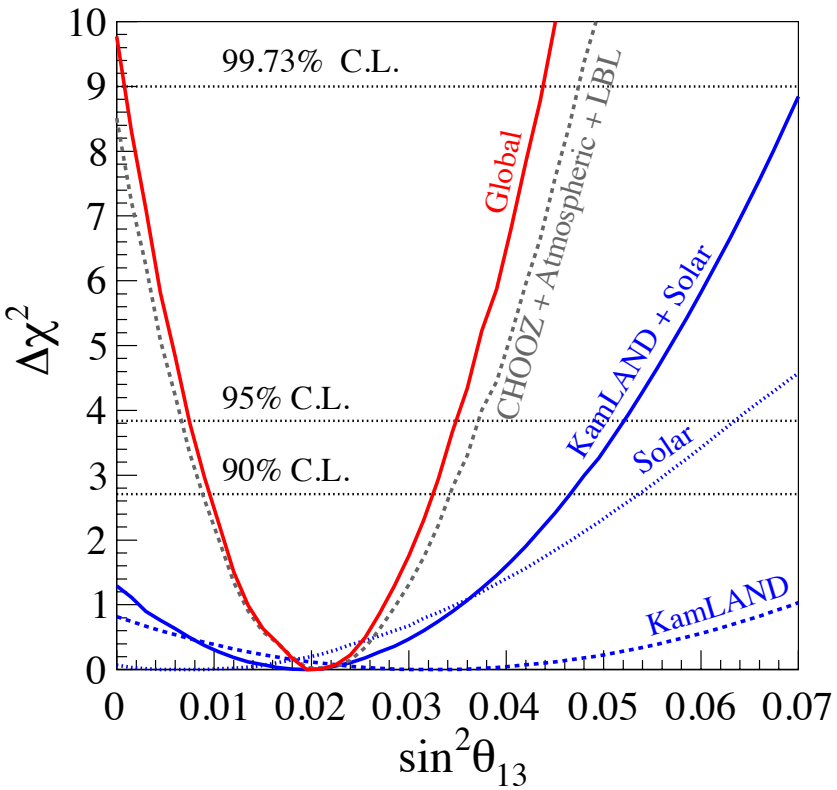

Figure 7.8: $\Delta\chi^2$-profiles projected onto the $\sin^2\theta_{13}$ axis for different combinations of the oscillation data floating the undisplayed parameters ($\tan^2\theta_{12}$, Δm^2_{21}). For CHOOZ + Atmospheric + LBL data (gray dashed line), the combined analysis from [90] is used. In the global analysis (red line), there is a clear evidence in favor of $\sin^2\theta_{13} > 0$ at a confidence level of 3.12 σ.

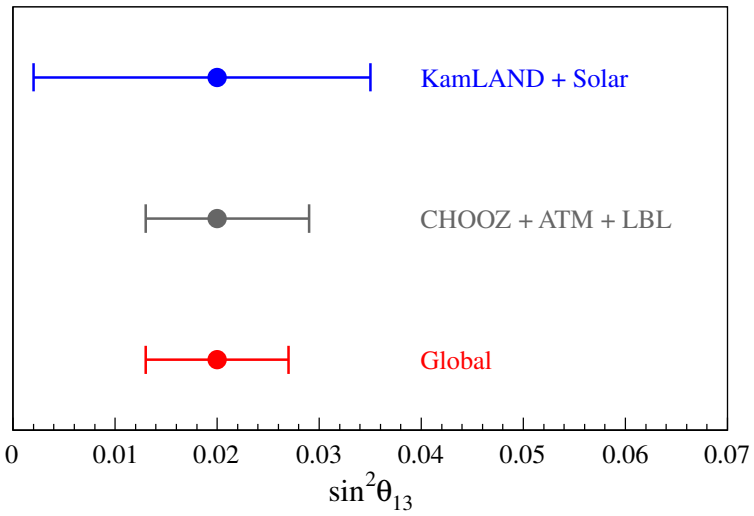

Figure 7.9: $\pm 1\sigma$ ranges of $\sin^2\theta_{13}$ in a different data set.

7.2.2 Visualization of the survival probability

L_0/E Plot

The L_0/E can clearly illustrate the oscillation behavior. Figure 7.10 shows the distribution of the survival probability. The data points are ratio of the observed reactor $\bar{\nu}_e$ spectrum to that expected in the case of no oscillation plotted as a function of L_0/E. L_0 is the flux-weighted effective baseline, and is fixed as180 km. The oscillatory structure arising from the $\sin^2(1.27\Delta m^2_{21}L/E)$ term is clear, but is distorted because the reactor sources are distributed across multiple baselines. Two peaks are clearly seen in this figure and the KamLAND data is excellent agreement with the oscillation scenario.

The expected oscillation curves based on the best-fit parameters from the two-flavor and the three-flavor oscillation analysis also overlaid. The suppression of the oscillation amplitude is slightly larger for the three-flavor oscillation case.

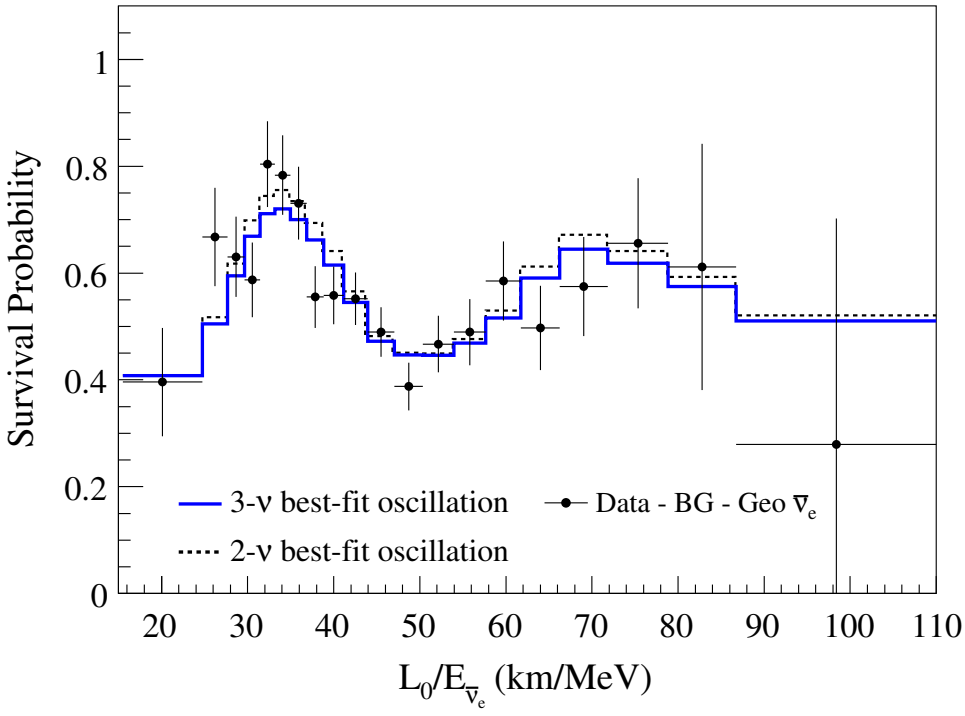

Figure 7.10: L_0/E plot. The vertical axis represents the ratio of the observed $\bar{\nu}_e$ spectrum to the expected spectrum for no-oscillation. This ratio is plotted as a function of L_0/E, where $L_0 = 180$ km is the flux-weighted average reactor baseline. The two- (gray dashed line) and three-flavor (blue line) expected histograms are also overlaid using the best-fit parameter values. Tow pearls are clearly displayed in this figure, and the KamLAND data points (black points) is good agreement with the oscillation scenario.

Survival Probability

Figure 7.11 also illustrates different aspects of the survival probability for the KamLAND data. To focus on θ_{12} and θ_{13} effects in the data, a parameter $x(E_{\rm p}, t)$ is defined by as follows :

$$x(E_{\rm p}, t) = \frac{1}{\sin^2 2\hat{\theta}_{12}} \left[\frac{1}{N_{\text{no-osc}}(E_{\rm p}, t)} \sum_i^{\text{reactors}} \int {\rm d}E \ \sin^2 2\hat{\theta}_{12M} \sin^2 \left(\frac{1.27 \Delta \hat{m}^2_{21M} L_i}{E} \right) P_{\rm R}(E_{\rm p}, t, E) \frac{S_i(E,t)}{4\pi L_i^2} \right] \quad (7.11)$$

$$\equiv \frac{1}{\sin^2 2\hat{\theta}_{12}} \left\langle \sin^2 2\hat{\theta}_{12M} \sin^2 \left(\frac{1.27 \Delta \hat{m}^2_{21M} L}{E} \right) \right\rangle , \quad (7.12)$$

where $N_{\text{no-osc}}(E_{\rm p}, t)$ is the number of candidates with prompt energy $E_{\rm p}$ expected in the absence of neutrino oscillation from all reactors at time t at KamLAND, described as follows :

$$N_{\text{no-osc}}(E_{\rm p}, t) = \sum_i^{\text{reactors}} \int {\rm d}E \ P_{\rm R}(E_{\rm p}, t, E) \frac{S_i(E,t)}{4\pi L_i^2} \quad (7.13)$$

i : labels of the reactor source
L_i : baseline of reactor i
$S_i(E,t)$: neutrino spectrum at time t of reactor i
$P_{\rm R}(E_{\rm p}, t, E)$: probability that a $\overline{\nu}_e$ with energy E will be detected at KamLAND
$(\hat{\theta}_{12M}, \Delta\hat{m}^2_{21M})$, $(\hat{\theta}_{12}, \Delta\hat{m}^2_{21})$: best-fit values from two-flavor analysis with and without matter effect

$P_{\rm R}$ includes the number of target protons, the inverse beta-decay cross section, and the time-dependent detector response function. The angle bracket notation in Eq. (7.12) indicates the weighted average over reactor baselines L_i and neutrino emission energies E, written explicitly in Eq. (7.11). For the region of $(\Delta m^2_{21}, \theta_{12}, \theta_{13})$ parameter space close to $\Delta\hat{m}^2_{21}$, all the information about the reactors, detector-related effects, and matter modification is contained in the parameter x. With this definition, the survival probability may be written as a linear function of x,

$$P(E_{\rm p}, t) = A - B \cdot x(E_{\rm p}, t), \quad (7.14)$$

where

$$A = (\cos^4\theta_{13} + \sin^4\theta_{13})$$
$$B = \cos^4\theta_{13} \sin^2 2\theta_{12}$$

θ_{13} effects are predominately encoded in A whereas θ_{12} effects dominate the slope B.

This linear relationship is illustrated in Figure **??**. The points there are the survival probability for KamLAND events binned as a function of x. Also shown

are lines where A and B have been calculated using the best-fit values from the two- and three-flavor unbinned maximum-likelihood analyses of the KamLAND data. The axis intercept at $x = 0$ of the best-fit 3-ν line is less than one, illustrating the slight indication of positive θ_{13} from the unbinned likelihood analysis. Any further improvement in the significance of the θ_{13} investigation with KamLAND requires reduced systematic uncertainties on the reactor flux and increased detector exposure.

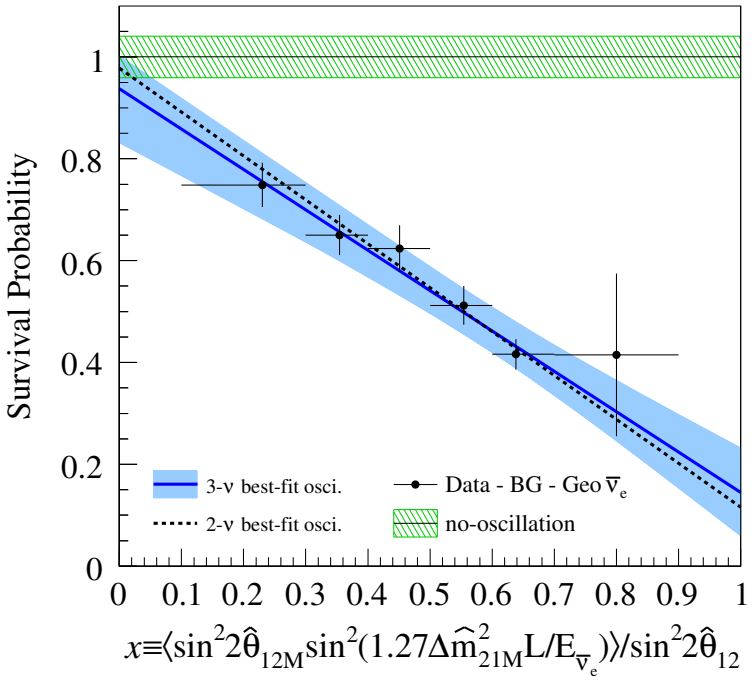

Figure 7.11: Survival probability of reactor $\overline{\nu}_e$ versus x. ($x \equiv \langle \sin^2 2\hat{\theta}_{12M} \sin^2(1.27\Delta \hat{m}^2_{21M} L/E) \rangle / \sin^2 2\hat{\theta}_{12}$) The angle bracket indicates the weighted average over reactor baseline (L_i) and original neutrino energies (E). The points are the survival probability for the KamLAND data. The 3-ν line and 1σ C.L. region are calculated using the unbinned maximum-likelihood fit to the KamLAND data. The 2-ν line is calculated from the two-flavor unbinned maximum-likelihood KamLAND analysis. The 1σ C.L. band for the 2-ν case is not shown but is similar in magnitude to the no-oscillation case shown at $P = 1.0$.

7.3 Solar Neutrino Oscillation Analysis

For the global analysis, the χ^2 of the solar neutrino experiments is calculated. In this analysis, we include the following results.

- observed rate
  the chlorine [79] and gallium [80] experiments, Borexino [81], SNO III [82]
- spectra
  the zenith spectra in Super-Kamiokande phase I [83], and the day-night spectra in SNO phase I and II [84]

The χ^2 is calculated using "pull approach", which embeds the effect of each independent k-th source of systematics through a shift of the difference R_n^{expected} - $R_n^{\text{theoretical}}$. The definition of χ^2 for solar neutrino experiments is as follows :

$$\chi^2_{\text{pull}} = \min_{\{\xi_k\}} \left[\sum_{n=1}^{N} \left(\frac{R_n^{\text{expted}} - R_n^{\text{theorerical}} - \sum_{k=1}^{K} \xi_k c_n^k}{u_n} \right)^2 + \sum_{k=1}^{K} \xi_k^2 \right] \tag{7.15}$$

7.3.1 2 Generation Oscillation Analysis

The figure shows the result of solar neutrino data analysis projected in the ($\tan^2\theta_{12}$, Δm^2_{21}) plane for the two-flavor oscillation analysis. Global result is dominated by SNO's result.

7.3.2 3 Generation Oscillation Analysis

The survival probability of solar neutrinos in the framework of three neutrino oscillation can be written as :

$$P_{ee}^{3\nu} = \cos^4\theta_{13} \widetilde{P}_{ee}^{2\nu}(\Delta m^2_{21}, \theta_{12}) + \sin^4\theta_{13} \tag{7.16}$$

Since $L_{31}^{\text{o/c}} = 4\pi E/\Delta m^2_{31}$ is much shorter than the distance between the Sun and the Earth, the oscillations related to L_{31}^{osc} are averaged. In presence of matter effects $P_{ee}^{2\nu}(\Delta m^2_{21}, \theta_{12})$ should be calculated taking into account the evolution in an effective matter density $\widetilde{N}_e = N_e \cos^2\theta_{13}$. For $10^{-5} \leq \Delta m^2$ / eV^2 $\leq 10^{-4}$,$P_{ee}^{2\nu}(\Delta m^2_{21}, \theta_{12})$ presents the following asymptotic behaviors [87]:

$$P_{ee}^{2\nu}(\Delta m^2_{21}, \theta_{12}) \simeq 1 - \frac{1}{2} \sin^2(2\theta_{12}) \qquad \text{for } E_\nu \leq \text{few} \times 100 \text{ keV} \tag{7.17}$$

$$P_{ee}^{2\nu}(\Delta m^2_{21}, \theta_{12}) \simeq \sin^2(\theta_{12}) \qquad \text{for } E_\nu \geq \text{few} \times 1 \text{ MeV} \tag{7.18}$$

Figure 7.13 shows the allowed regions in the (Δm^2_{21}, θ_{12}) plane as obtained from the analysis of low-energy (radiochemical and Borexino) and high-energy and high-energy (SK and SNO) solar experiments, for different value of θ_{13}. As described in Eq. (7.16), for fixed values of Δm^2_{21} and θ_{12}, the inclusion of a small value of θ_{13} results into a decrease on the predicted rate at a given solar neutrino experiment. This decrease can be compensated by a shift of Δm^2_{21} and θ_{12} which lead to an increase of $P_{ee}^{2\nu}$. However the sign of the shift strongly depends on the characteristic energy of the detected neutrinos. For experiments detecting neutrinos with energies

low enough for matter effects to be irrelevant (such as Chloerine and Gallium experiments) $P_{ee}^{2\nu}$ is given by Eq. (7.17) and increases as θ_{12} decreases. Conversely, for experiments detecting neutrinos mostly in the regime of adiabatic matter oscillations (such as SK and SNO) $P_{ee}^{2\nu}$ is given by Eq. (7.18) and increases as θ_{12} increases. Consequently the combined fit worsens with θ_{13}.

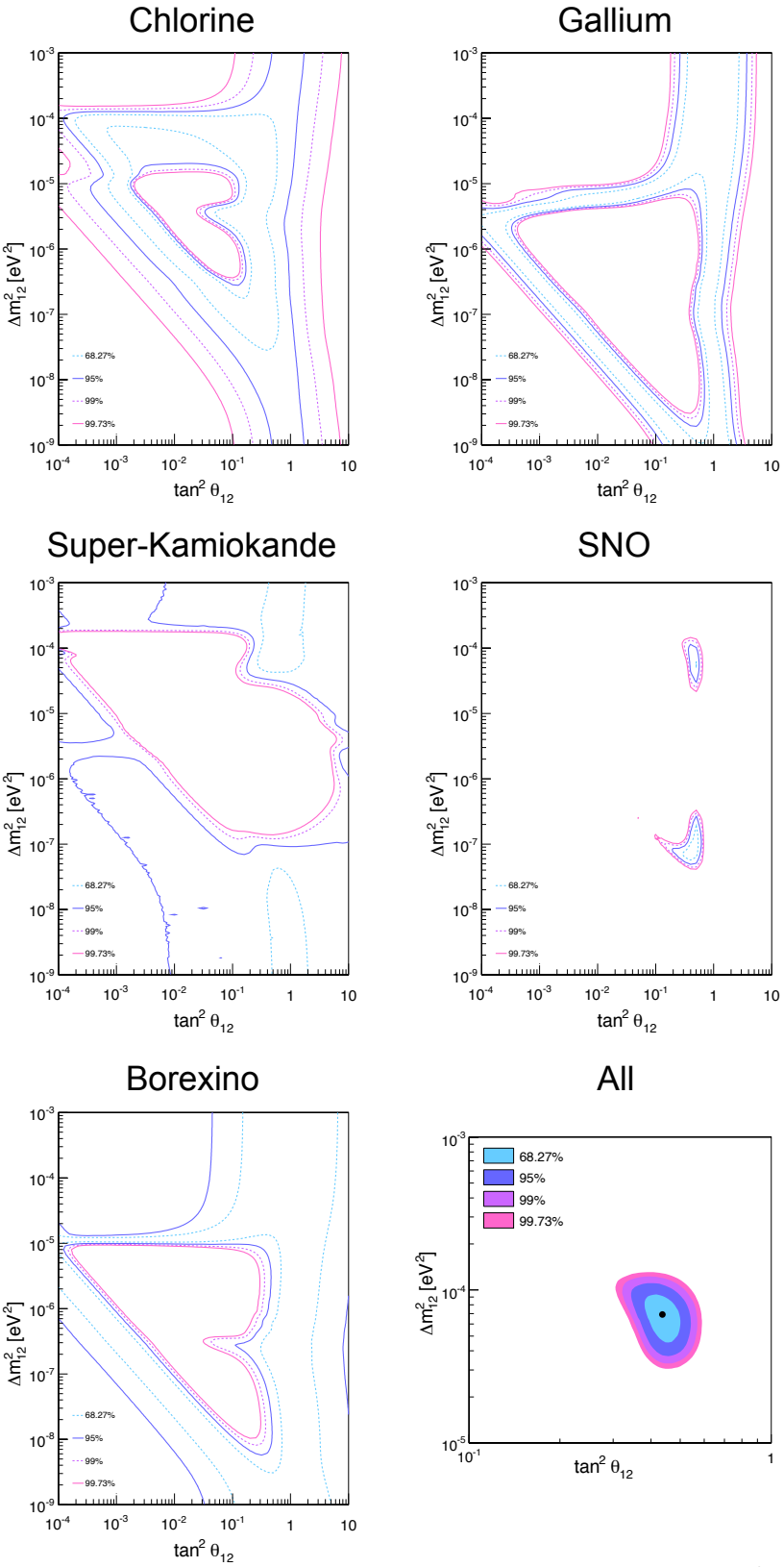

Figure 7.12: Result of solar neutrino data analysis projected in the ($\tan^2\theta_{12}$, Δm^2_{21}) plane for the two-flavor oscillation analysis. Chlorine (top-left), Gallium (top-right), Super-Kamiokande (middle-left), SNO (middle-right), and Borexino (bottom-left) are shown respectively. The bottom-light figure shows the global analysis result, which is dominated by SNO's result.

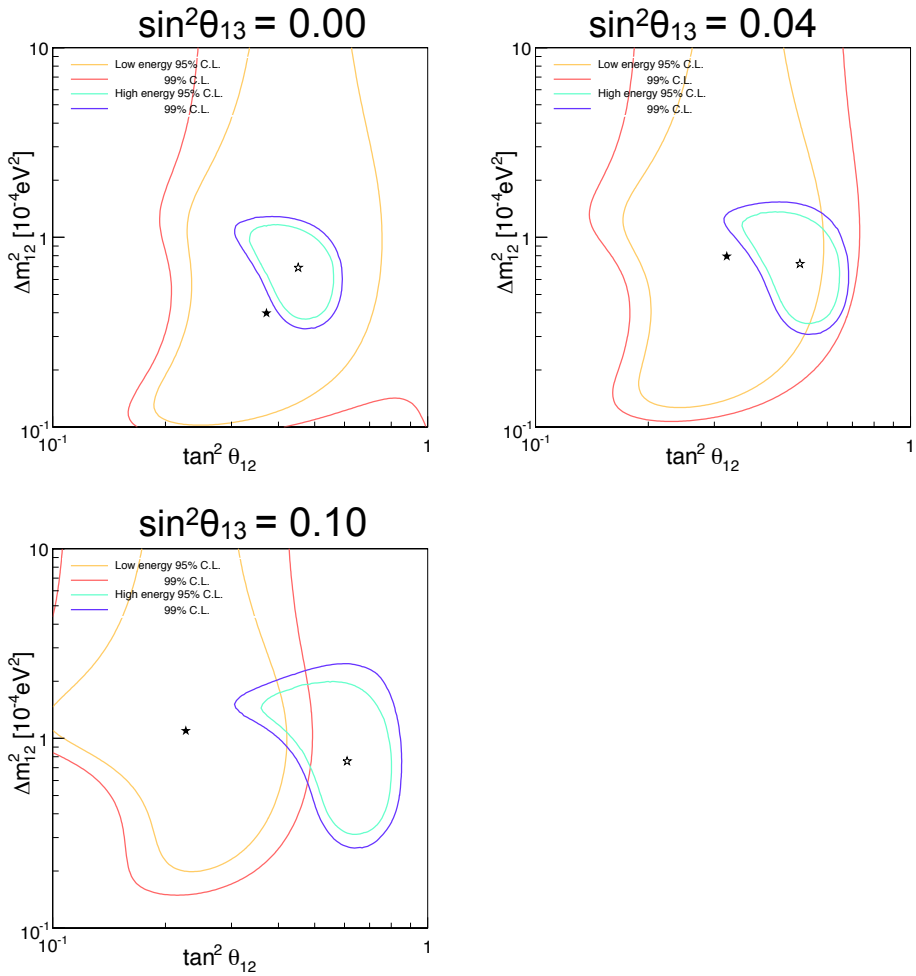

Figure 7.13: Dependence on θ_{13} of the allowed (Δm^2_{21}, θ_{12}) regions from the partial analysis of the "Low energy" (such as Ghloerinen, Gallium and Borexino) and "High energy" (such as SK and SNO) solar neutrino data.

Chapter 8

Analysis; Geo Neutrino

8.1 Rate Analysis

The significance of geo-neutrinos signal positivity is examined by testing a null hypothesis estimated parameters, such as the number of background events, that of expected events and the systematic uncertainties. In Table 8.1, various estimated parameters are listed for $0.9 \sim 2.6$ MeV energy region. The number of total expected events is calculated as follows :

$$\begin{aligned} N^{\rm exp} &= \left[\left\{N^{\rm exp}_{\rm geo} + (N_{\rm reactor} \pm \sigma_{\rm reactor})\right\} \pm \sigma_{\rm detector}\right] \pm (N_{\rm BG} \pm \sigma_{\rm BG}) \\ &= (N^{\rm exp}_{\rm geo} + N_{\rm reactor} + N_{\rm BG}) \\ &\pm \left[\left\{(N^{\rm exp}_{\rm geo} + N_{\rm ractor}) \times \sigma_{\rm detector}\right\} \oplus (N_{\rm reactor} \times \sigma_{\rm reactor}) \oplus (N_{\rm BG} \times \sigma_{\rm BG})\right] \\ &\equiv \mu_{\rm exp} \pm \sigma_{\rm exp} \end{aligned} \tag{8.1}$$

where $N^{\rm exp}_{\rm geo}$ is the number of expected geo-neutrino events. $N_{\rm reactor}$ and $\sigma_{\rm reactor}$ are the number of estimated reactor neutrino events and its uncertainties. $N_{\rm BG}$ and $\sigma_{\rm BG}$ are the number of estimated non-neutrino background events and its uncertainties. The geo-neutrino events and reactor neutrino events share most of detector related systematic error ($\sigma_{\rm detector}$) such as errors on fiducial volume and detection efficiencies. When estimate the significance if geo-neutrino positivity, $N^{\rm exp}_{\rm geo}$ is set to be zero, corresponding that $N^{\rm exp}$ represents the number of background. Under the null hypothesis, the probability that the number of observed events is larger than the number of actual observed events is calculated, considering the Gaussian systematic errors of background and signal estimation,

$$P(N \geq N^{\rm obs}) = \int_0^\infty \left\{ \frac{1}{\sqrt{2\pi\sigma^2_{\rm hyp}}} \exp\left(-\frac{(x-\mu_{\rm hyp})^2}{2\sigma^2_{\rm hyp}}\right)\right\} \times \left\{ \frac{1}{\sqrt{2\pi(\sqrt{x})^2}} \exp\left(-\frac{(N-x)^2}{2(\sqrt{x})^2}\right)\right\} dx \tag{8.2}$$

where $N^{\rm obs}$ is the number of actually observed events, $\mu_{\rm hyp}$ is the number of expected events under the null hypothesis (i.e. the number of background) and $\sigma_{\rm hyp}$ is the systematic uncertainty of $\mu_{\rm hyp}$ estimation.

If the number of geo-neutrino events is converted into geo-neutrino flux $F_{\rm geo}$ in the TNU unit (the number of events with 10^{32} targets, 1 year observation, 100 % efficiency), the number of expected geo-neutrino events $N^{\rm exp}_{\rm geo}$ for the events within

Table 8.1: Summary of geo-neutrino analysis in $0.9 \sim 2.6$ MeV region. Uncertainties for all dataset are weighted average over the two time periods.

	DS-1	DS-2	All
Livetime [days]	1485.7	810.3	2296.0
Reactor neutrino	356.4 ± 19.5	142.5 ± 7.8	498.9 ± 27.3
Accidental	59.0 ± 0.1	22.1 ± 0.1	81.1 ± 0.1
^{9}Li/^{8}He	1.4 ± 0.1	0.6 ± 0.1	2.0 ± 0.1
^{13}C(α,n)^{16}O	155.0 ± 17.1	12.6 ± 1.4	167.4 ± 18.4
Fast neutron	< 2.0	< 0.8	< 2.8
Total	571.8 ± 26.0	177.8 ± 8.0	749.4 ± 33.0
(without Reactor $\bar{\nu}_e$)	215.4 ± 17.2	35.3 ± 1.6	250.5 ± 18.6
Observed	658	242	900
Excess	86	64	150
Detector related uncertainty	2.97 %	3.53 %	3.17 %
Reactor related uncertainty	3.34 %	3.38 %	3.35 %

6.0 m fiducial radius and all dataset is given as

$$N_{\rm geo}^{\rm exp} = \frac{5.979 \times 10^{31}}{10^{32}} \cdot \frac{2296.01[\rm days]}{365.2425[\rm days]} \cdot \frac{F_{\rm geo}}{[\rm TNU]} \tag{8.3}$$

where 5.979×10^{31} is the number of target proton in the 6.0 m fiducial radius. For each given $F_{\rm geo}$, the probability of observing N events is calculated with including statical error,

$$P(N; F_{\rm geo}) = \int_0^\infty \left\{ \frac{1}{\sqrt{2\pi\sigma_{\rm exp}^2}} \exp\left(-\frac{(x-\mu_{\rm exp})^2}{2\sigma_{\rm exp}^2} \right) \right\} \times \left\{ \frac{1}{\sqrt{2\pi(\sqrt{x})^2}} \exp\left(-\frac{(N-x)^2}{2(\sqrt{x})^2} \right) \right\} dx \tag{8.4}$$

Under a hypothesis that the geo-neutrino flux $F_{\rm geo}$, an interval [$N_{\rm lower}$, $N_{\rm higher}$] of N at 68.3 % C.L. (1 σ two side) is given as follows :

$$\int_{N_{\rm lower}}^{N_{\rm upper}} P(N; F_{\rm geo}) dN = 0.683 \tag{8.5}$$

And in the analysis for 99 % C.L. one side,

$$\int_{N'_{\rm lower}}^{\infty} P(N; F_{\rm geo}) dN = 0.99 \tag{8.6}$$

is used. Figure 8.1, 8.2 and 8.3 show the confidence interval for geo-neutrino flux. The significance of positive signal, estimated geo-neutrino flux and the upper limit of geo-neutrino flux are checked for each data taking period, and summarized in Table 8.2.

Table 8.2: Summary of rate analysis.

	DS-1	DS-2	All
significance of positive signal	99.5095 %	99.9979 %	99.9875 %
estimated geo $\bar{\nu}_e$ flux [TNU]	$44.1^{+18.4}_{-17.4}$	$77.9^{+22.8}_{-20.9}$	$54.2^{+16.3}_{-15.4}$
geo $\bar{\nu}_e$ flux upper limit (99 % C.L.) [TNU]	87.9	133.3	93.0

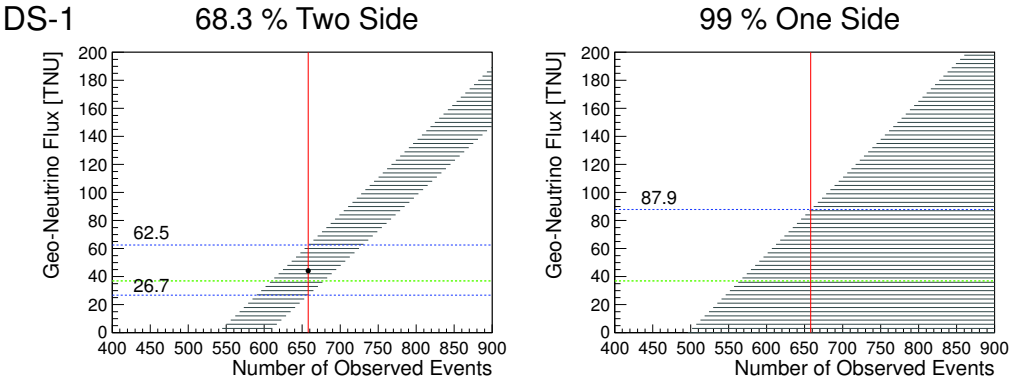

Figure 8.1: Confidence interval of geo-neutrino flux for DS-1. The data was corrected before purification, corresponding to include the higher background period. The left figure shows the 1 σ two side analysis, and the right figure shows the 99 % C.L. one side analysis. The red vertical line shows the number of observed events (658 events), the green horizontal line shows the geo-neutrino flux estimated from reference earth model (36.9 TNU), and the blue lines shows the estimated geo-neutrino flux (left figure) and the estimated geo-neutrino flux upper limit (right figure). The black point in the left figure shows the best-fit parameters in this rate analysis.

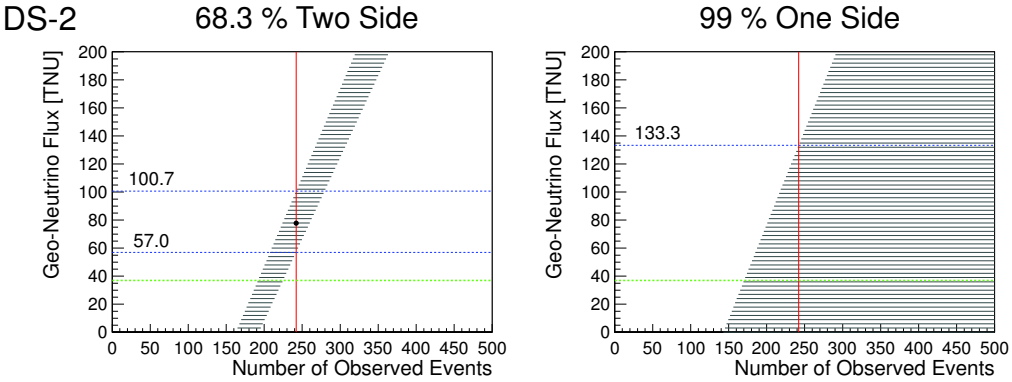

Figure 8.2: Confidence interval of geo-neutrino flux for DS-2. This analysis is done based on the low background period, which corrected after purification.

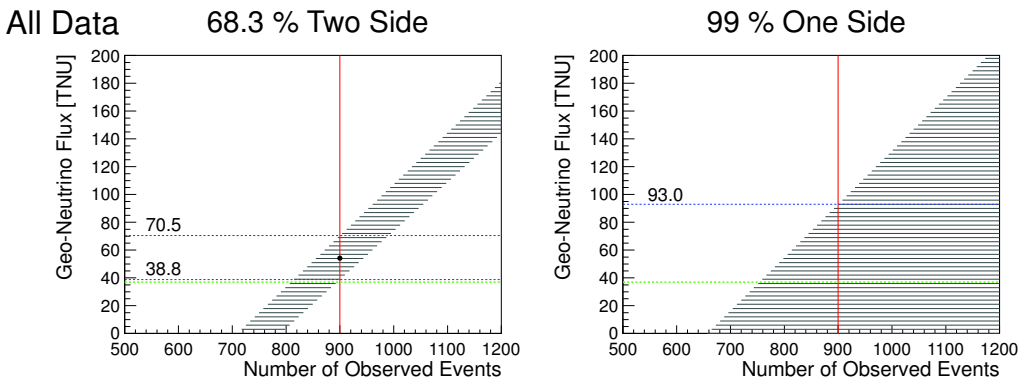

Figure 8.3: Confidence interval of geo-neutrino flux for all dataset.

8.2 Rate + Shape Analysis

A more sensitive analysis is performed using an unbind maximum-likelihood fit which takes into account the event rate and energy information in the energy range 0.9 MeV $< E_{\rm p} <$ 8.5 MeV, and which simultaneously fits geo-neutrinos and reactor $\bar{\nu}_e$'s including the effect of neutrino oscillation. (As described in Section 8.1, the Rate analysis is using only 0.9 MeV $< E_{\rm p} <$ 2.6 MeV region.)

The χ^2 definition in the Rate + Shape analysis is as follows :

$$\begin{aligned}\chi^2(\theta_{12}, \Delta m^2_{21}) &= \chi^2_{\rm rate} + \chi^2_{\rm shape} \\ &= \chi^2_{\rm rate}(\theta_{12}, \Delta m^2_{21}, n_{\rm U}, n_{\rm Th}) \\ &\quad - 2\ln L_{\rm shape}(E; \theta_{12}, \Delta m^2_{21}, n_{\rm U}, n_{\rm Th}, N_{\rm BG1\to5}, \alpha_{1\to4}) \\ &\quad + \chi^2(N_{\rm BG1\to5}) + \chi^2(\alpha_{1\to4}) + \chi^2_{\rm solar} \\ \chi^2_{\rm rate}(\theta_{12}, \Delta m^2_{21}, n_{\rm U}, n_{\rm Th}) &= \frac{(N_{\rm observed} - n_{\rm geo} - n_{\rm reactor} - N_{\rm BG})^2}{\sigma^2_{\rm stat.}}\end{aligned} \tag{8.7}$$

The terms are, in order :

1. χ^2 contribution for the total rate
2. χ^2 prompt energy spectrum shape
3. a penalty term for backgrounds
4. a penalty term for systematic uncertainties
5. χ^2 for several solar neutrino experiments

where $n_{\rm geo}$ and $n_{\rm reactor}$ are variable parameters as the number of geo- and reactor neutrinos. $N_{\rm BG1\to5}$ are the expected background levels, and $\alpha_{1\to4}$ parametrize the uncertainties on the geo-neutrino (U and Th spectrum), the reactor $\bar{\nu}_e$ spectra and energy scale, the event rate, and the energy dependent efficiencies. The $\chi^2_{\rm solar}$ is the sum of rate and shape analysis of several solar neutrino experiments in two-flaver oscillation case, whose details are described in Section 7.3. In the rate term, it includes χ^2 values of the neutrino oscillation parameters, θ_{12} and Δm^2_{21}. These are taken from a estimation based on a global two-flavor analysis of the KamLAND reactor neutrino measurement and the solar neutrino observation, and its best-fit values are $(\sin^2 2\theta_{12},\ \Delta m^2_{21}) = (0.84\pm0.03,\ 7.50^{+0.019}_{-0.020} \times 10^{-5}\ [\mathrm{eV}^2])$.

Using the χ^2 presented above, distribution of $\chi^2(N_{\rm U}, N_{\rm Th})$ is calculated with the observed data set. Figure 8.4 shows the allowed region for the observed geo-neutrino event rate of Rate + Shape analysis. The best-fit yields 71 and 43 geo-neutrino events from ^{238}U and ^{232}Th, respectively, when the contributions of the two isotopes are left free to vary independently. Figure 8.7 shows the $\Delta\chi^2$-profiles projected onto the $N_{\rm U}$ or $N_{\rm Th}$ axis.

From geophysical or geochemical point of view, the total flux is of particular interest, while U/Th ratio is well determined from cosmo-chemical arguments. Behaviors of Uranium and Thorium in the Earth are quite similar to each other, and their ratio in various Earth components is fairly stable. Hence it is interesting to display the 2-parameter χ^2 contour in a way that the total flux and the U/Th ratio are separated. Figure 8.6 shows the distribution of χ^2 displayed in a ($N_{\rm U}$+$N_{\rm Th}$)

v.s. $(N_{\mathrm{U}}\text{-}N_{\mathrm{Th}})/(N_{\mathrm{U}}+N_{\mathrm{Th}})$ plane. The vertical axis shows the total flux and the horizontal axis shows the U/Th flux ratio. Fixing the Earth's U/Th ratio at 3.9, as observed chondritic meteorites, the total number of excess events is 127^{+32}_{-31} events from geo-neutrinos, as shown in Figure 8.7, and the null hypothesis is rejected at the 4.39 σ C.L.

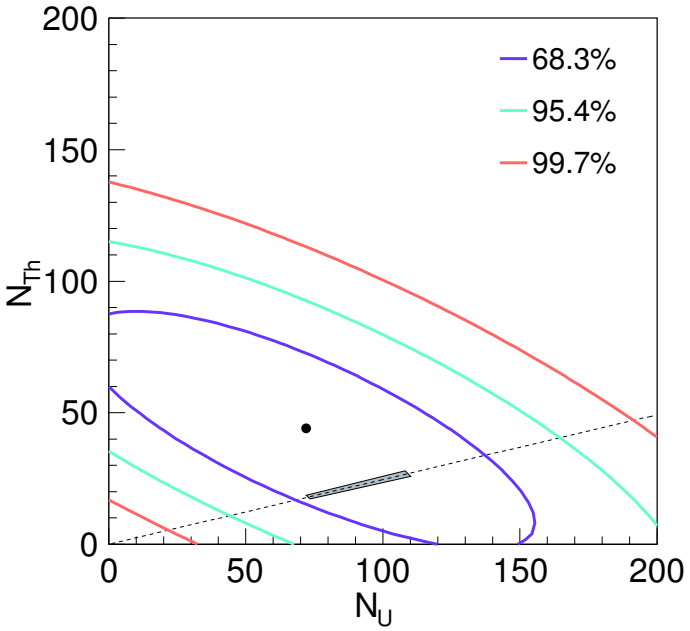

Figure 8.4: Allowed region for the observed geo-neutrino event rate from Rate + Shape analysis. The small shaded region is favored by the reference model, and the dashed line is the locus of points excepted from chondritic meteorite abundance, U/Th = 3.9. The black point shows the best-fit, (U, Th) = (71, 43).

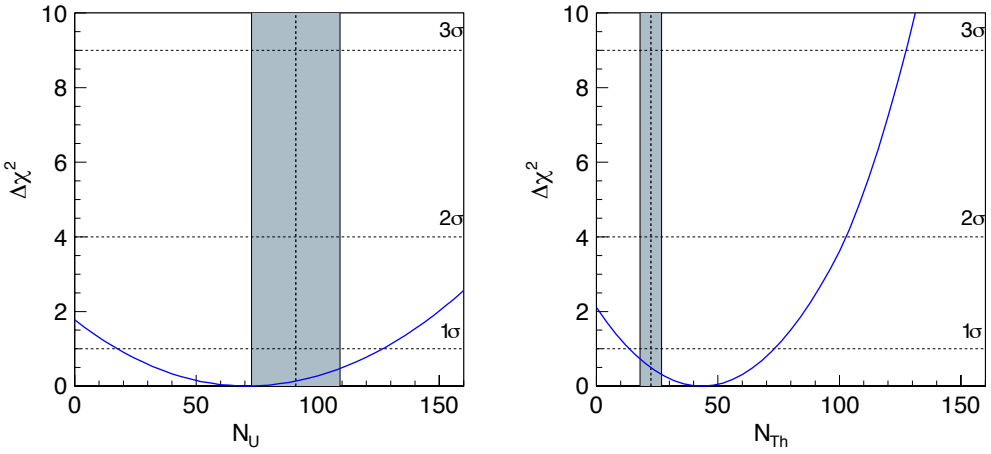

Figure 8.5: $\Delta\chi^2$-profiles projected onto the N_{U} (left) or N_{Th} (right) axis from Rate + Shape analysis. The shaded region corresponds to the expected number of events from the reference model.

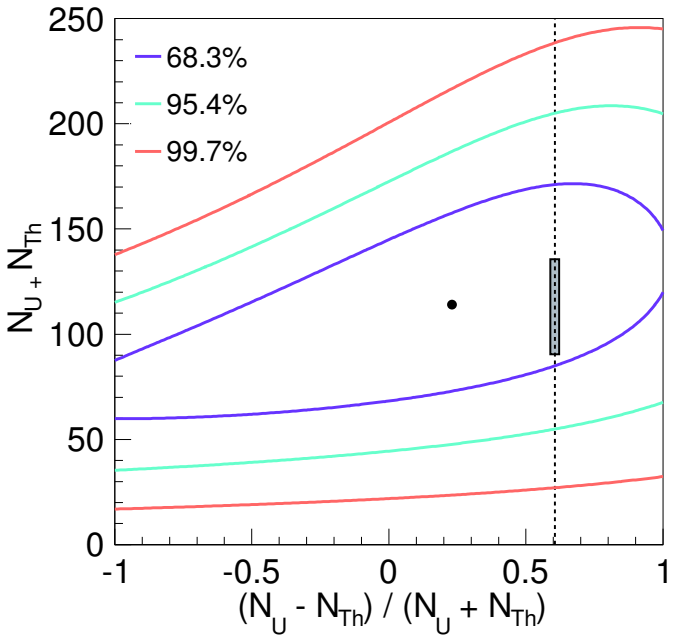

Figure 8.6: χ^2 displayed in a $(N_{\rm U}+N_{\rm Th})$ v.s. $(N_{\rm U}\text{-}N_{\rm Th})/(N_{\rm U}+N_{\rm Th})$ plane from Rate + Shape analysis. The small shaded region is favored by the reference model, and the dashed line is the locus of points excepted from chondritic meteorite abundance, U/Th = 3.9. The black point shows the best-fit.

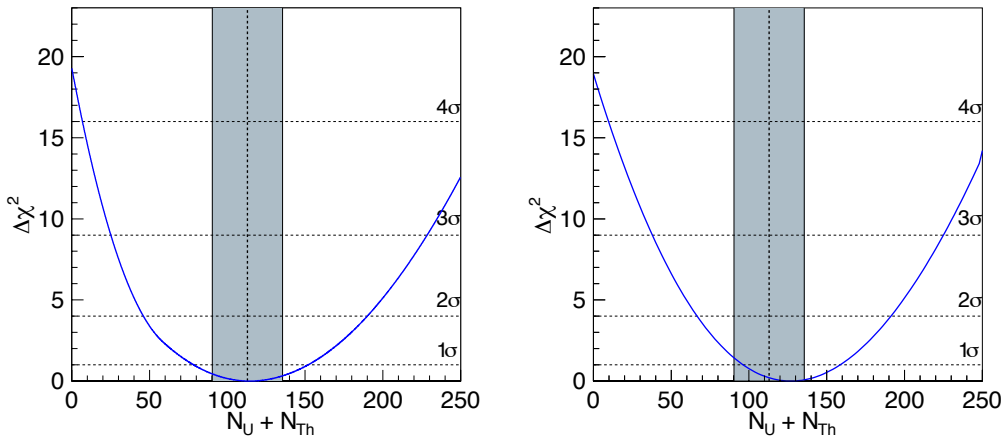

Figure 8.7: $\Delta\chi^2$-profiles projected onto the $N_{\rm U}+N_{\rm Th}$ axis from Rate + Shape analysis. Left figure shows the U/Th ratio floated result, and the right figure corresponds to $\Delta\chi^2$ along the geochemical constraint line. The shaded regions show the expected number of events from the reference model. The best-fit values are as follows :
U/Th ratio floated : 115^{+37}_{-36}
U/Th ratio fixed : 127^{+32}_{-31}

8.3 Rate + Shape + Time Analysis

As described in Section 8.2, the reactor $\bar{\nu}_e$ is analyzed together with the geo-neutrinos. In KamLAND, the reactor $\bar{\nu}_e$ represents the largest background in the present measurement since their energy spectrum partially overlaps that of geo-neutrinos. The differences in energy spectra and the fact that the reactor $\bar{\nu}_e$ rate varies with the output of the power plants while the geo-neutrino rate can be taken as constant over the time scale of the experiment are exploited in a simultaneous fit to both sources, thereby providing substantial discrimination between the two. Thus the time information is effective to suppress the background for geo-neutrinos.

The χ^2 definition in the Rate + Shape + Time analysis is as follows :

$$\begin{aligned}
\chi^2(\theta_{12}, \Delta m^2_{21}) &= \chi^2_{\rm rate} + \chi^2_{\rm shape} \\
&= \chi^2_{\rm rate}(\theta_{12}, \Delta m^2_{21}, n_{\rm U}, n_{\rm Th}) \\
&\quad - 2\ln L_{\rm shape}(E, T; \theta_{12}, \Delta m^2_{21}, n_{\rm U}, n_{\rm Th}, N_{\rm BG1\to5}, \alpha_{1\to4}) \\
&\quad + \chi^2(N_{\rm BG1\to5}) + \chi^2(\alpha_{1\to4}) + \chi^2_{\rm solar} \\
\chi^2_{\rm rate}(\theta_{12}, \Delta m^2_{21}, n_{\rm U}, n_{\rm Th}) &= \frac{(N_{\rm observed} - n_{\rm geo} - n_{\rm reactor} - N_{\rm BG})^2}{\sigma^2_{\rm stat.}}
\end{aligned} \tag{8.8}$$

Figure 8.8 shows the allowed region projected in the ($N_{\rm U}$, $N_{\rm Th}$) plane for the Rate + Shape + Time analysis. The best-fit values are in good agreement with the expected event rate from the reference model, (U, Th) = (97, 21). Figure 8.11 shows the $\Delta\chi^2$ distribution profiled onto U or Th axis. The distribution of χ^2 displayed in a ($N_{\rm U}$+$N_{\rm Th}$) v.s. ($N_{\rm U}$-$N_{\rm Th}$)/($N_{\rm U}$+$N_{\rm Th}$) plane is also checked in the Rate + Shape + Time analysis, as shown in Figure 8.10. As shown in Figure 8.11, the total number of excess events is 117^{+29}_{-28} events from geo-neutrinos when the U/Th ratio is fixed to 3.9. Finally, zero-signal geo-neutrino is rejected at the 4.49 σ C.L.

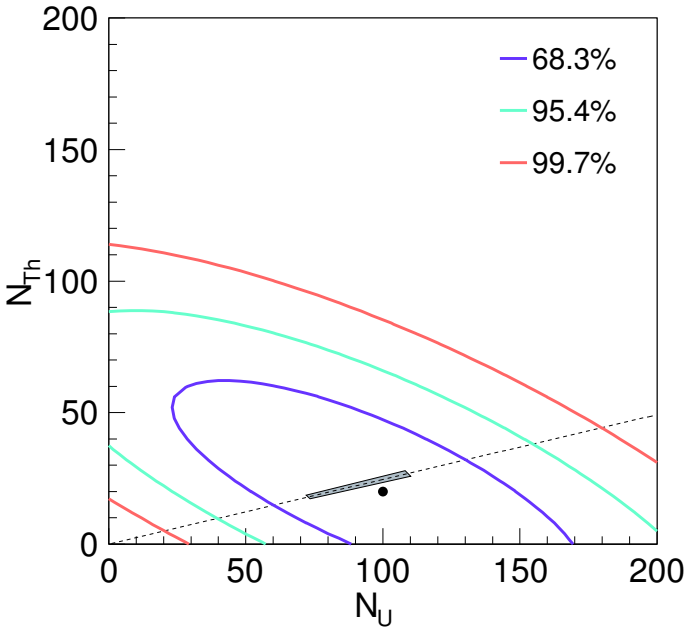

Figure 8.8: Allowed region for the observed geo-neutrino event rate from Rate + Shape analysis. The small shaded region is favored by the reference model, and the dashed line is the locus of points excepted from chondritic meteorite abundance, U/Th = 3.9. The black point shows the best-fit, (U, Th) = (97, 21).

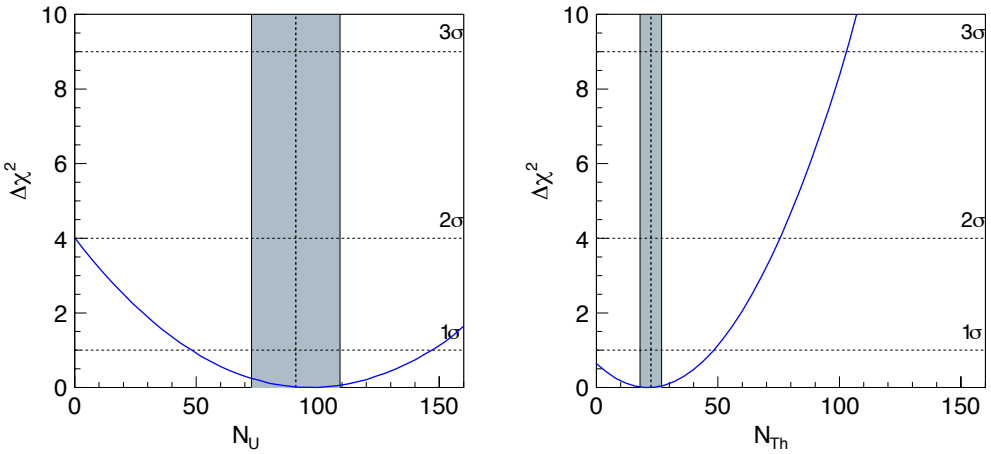

Figure 8.9: $\Delta\chi^2$-profiles projected onto the N_{U} (left) or N_{Th} (right) axis from Rate + Shape + Time analysis. The shaded region corresponds to the expected number of events from the reference model.

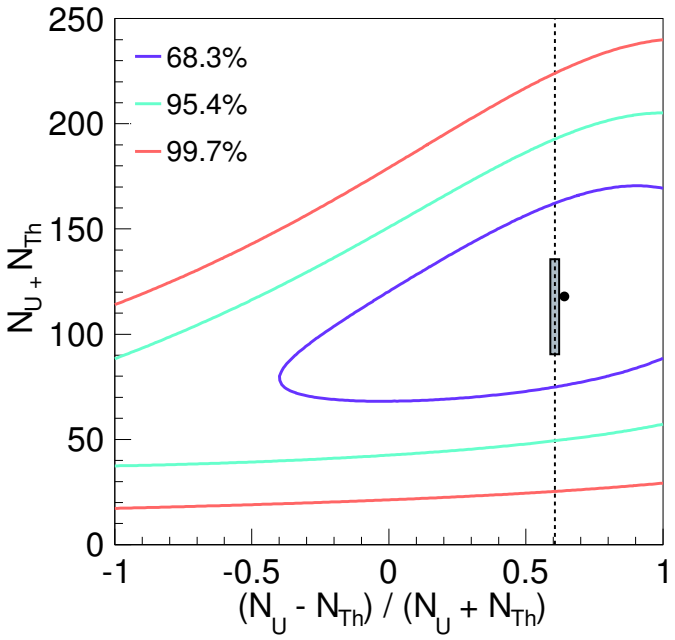

Figure 8.10: χ^2 displayed in a ($N_{\rm U}$+$N_{\rm Th}$) v.s. ($N_{\rm U}$-$N_{\rm Th}$)/($N_{\rm U}$+$N_{\rm Th}$) plane from Rate + Shape + Time analysis. The small shaded region is favored by the reference model, and the dashed line is the locus of points excepted from chondritic meteorite abundance, U/Th = 3.9. The black point shows the best-fit.

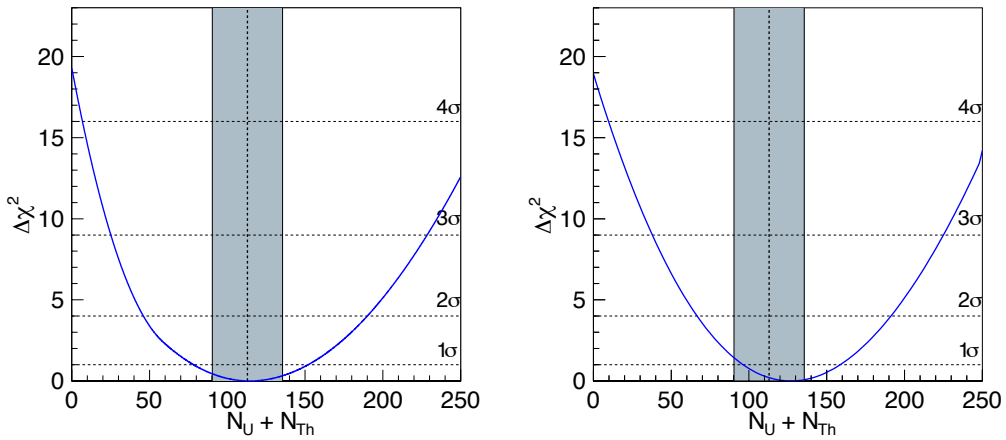

Figure 8.11: $\Delta\chi^2$-profiles projected onto the $N_{\rm U}$+$N_{\rm Th}$ axis from Rate + Shape + Time analysis. Left figure shows the U/Th ratio floated result, and the right figure corresponds to $\Delta\chi^2$ along the geochemical constraint line. The shaded regions show the expected number of events from the reference model. The best-fit values are as follows :

U/Th ratio floated : 118^{+34}_{-33}

U/Th ratio fixed : 117^{+29}_{-28}

8.4 Summary of Geo-Neutrino Analysis

The analysis results from Rate + Shape analysis and Rate + Shape + Time analysis are summarized in Table 8.3. The best-fit parameters and these errors are shown in unit of events par all data set. Furthermore, the results in unit of TNU and flux are summarized in Table 8.4. Geochemistry predicts that the ratio of geo-neutrino flux (N_U/N_{Th}) is ∼3.9 with 20 % error. In the two tables, the constraint results are also listed as "fixed" lines. It's striking that the significance of zero geo-neutrino signals is excluded at 4.49 σ (99.9993 %) from Rate + Shape + Time analysis.

The Figure 8.12 and 8.13 show the comparison between each analysis and the expectation from chomdritic meteorite abundances. The analysis results are appropriate with the geochemical predication within the errors. The uncertainty of the number of U + Th geo-neutrino events are as follows :

- Rate + Shape : (U/Th free, U/Th fixed) = (32.2 %, 25.1 %)
- Rate + Shape + Time : (U/Th free, U/Th fixed) = (28.8 %, 24.8 %)

The Rate + Shape + Time analysis can conduce to better results than the Rate + Shape analysis.

Table 8.3: Summary of geo-neutrino analysis. The best-fit parameters and these errors are shown in unit of events per all data set.

	Mass ratio	U [events]	Th [events]	U + Th [events]	U/Th	non-zero geo $\bar{\nu}_e$
Rate+Shape	free	71^{+55}_{-53}	44^{+30}_{-30}	115^{+37}_{-36}	$11.6^{+3.8}_{-9.4}$	4.39 σ
	fixed	102^{+36}_{-32}	25^{+26}_{-25}	127^{+32}_{-31}	(3.9)	4.39 σ
Rate+Shape+Time	free	97^{+50}_{-40}	21^{+27}_{-21}	118^{+34}_{-33}	$4.4^{+2.2}_{-3.8}$	4.49 σ
	fixed	94^{+53}_{-46}	23^{+25}_{-20}	117^{+29}_{-28}	(3.9)	4.49 σ
Reference Earth model	-	91	22	113	3.9	-

Table 8.4: Summary of geo-neutrino analysis. The results are summarized in unit of TNU and flux.

	Mass ratio	Unit	U	Th	U + Th
Rate + Shape	free	TNU	$25.6^{+19.8}_{-19.1}$	$15.8^{+10.8}_{-10.8}$	$41.4^{+13.3}_{-13.0}$
		$10^6 cm^{-2}s^{-1}$	$2.0^{+1.5}_{-1.5}$	$3.9^{+2.7}_{-2.7}$	$5.9^{+1.9}_{-1.8}$
	fixed	TNU	$36.7^{+13.0}_{-11.5}$	$9.0^{+13.0}_{-9.0}$	$45.7^{+11.5}_{-11.2}$
		$10^6 cm^{-2}s^{-1}$	$2.8^{+9.9}_{-8.8}$	$2.2^{+3.2}_{-2.2}$	$5.1^{+1.3}_{-1.2}$
Rate + Shape + Time	free	TNU	$34.9^{+18.0}_{-14.4}$	$7.6^{+9.7}_{-7.6}$	$42.5^{+12.2}_{-11.9}$
		$10^6 cm^{-2}s^{-1}$	$2.7^{+1.4}_{-1.1}$	$1.9^{+2.4}_{-1.9}$	$4.6^{+1.3}_{-1.3}$
	fixed	TNU	$33.8^{+19.1}_{-16.6}$	$8.3^{+9.0}_{-7.2}$	$42.1^{+10.4}_{-10.1}$
		$10^6 cm^{-2}s^{-1}$	$2.6^{+1.5}_{-1.3}$	$2.1^{+2.2}_{-1.8}$	$4.7^{+1.2}_{-1.1}$
Reference Earth model	-	TNU	32.8	8.1	40.9
	-	$10^6 cm^{-2}s^{-1}$	2.5	2.0	4.5

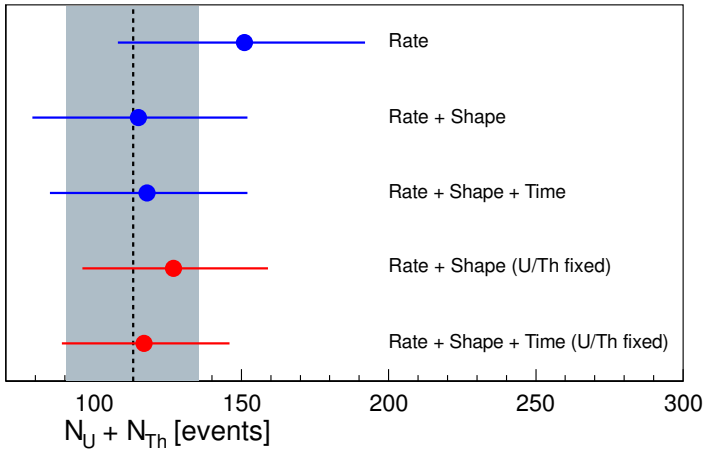

Figure 8.12: $\pm 1\sigma$ ranges of the number of U and Th geo-neutrinos in different analysis. The blue points show the analysis results of U/Th ratio floated, and the red points show the that of fixing at geochemical prediction. The shaded band represents the expected event rate from BSE model with 20 % error.

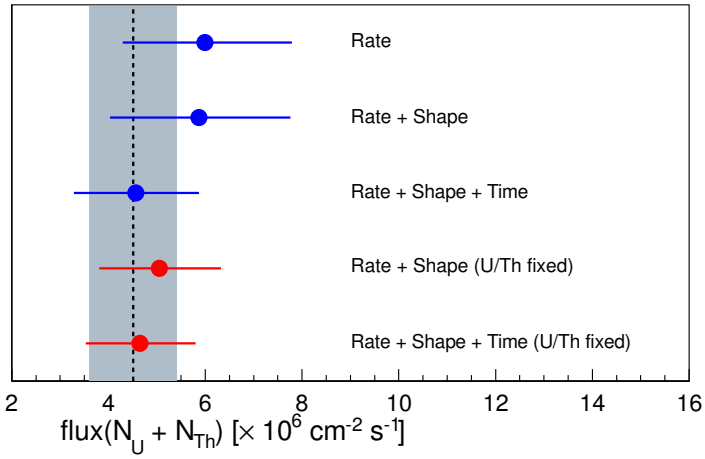

Figure 8.13: $\pm 1\sigma$ ranges of the number of U and Th geo-neutrinos in different analysis. The blue points show the analysis results of U/Th ratio floated, and the red points show the that of fixing at geochemical prediction. The shaded band represents the expected event rate from BSE model with 20 % error.

8.4.1 Best-Fit Spectrum

The best-fit parameters are summarized in Table 8.5 for Rate + Shape + Time analysis. In this analysis, the events whose prompt energy within 0.9 MeV $< E_{\rm p} <$ 8.5 MeV are used to improve the sensitivity of geo-neutrinos.

Finally, the energy spectra calculated with the Rate + Shape + Time best-fit parameters are shown in Figure 8.14. That results are for the fit with U/Th ratio fixed to 3.9 based on geochemical constraints. Observed spectrum is also shown by a histogram with 0.2 MeV bins from 0.9 MeV to 2.7 MeV. The upper panel shows the background-subtructed energy spectrum. The observed data points are consistent with the expected spectrum within these error.

Table 8.5: The best-fit of each parameter for U/Th ratio free and fixed analysis.

	Signals		Osci. parameters	
	U	Th	$\sin^2 2\theta_{12}$	Δm^2_{21}
U/Th free	96.8	21.4	0.854	7.49×10^{-5}
U/Th fixed	93.8	23.2	0.854	7.49×10^{-5}

	Backgrounds				
	Reactor	^{13}C(α, n)^{16}O	Accidental	^{9}Li/^{8}He	Fast neutron
U/Th free	1785.0	219.6	108.3	26.8	0.0
U/Th fixed	1786.8	219.6	108.3	26.8	0.0

	Errors			
	$\sigma_{\rm reactor}$	$\sigma_{\rm geo}$	$\sigma_{\rm efficiency}$	$\sigma_{\rm energy\ scale}$
U/Th free	-0.79	-0.02	-0.15	0.64
U/Th fixed	-0.77	-0.01	-0.15	0.64

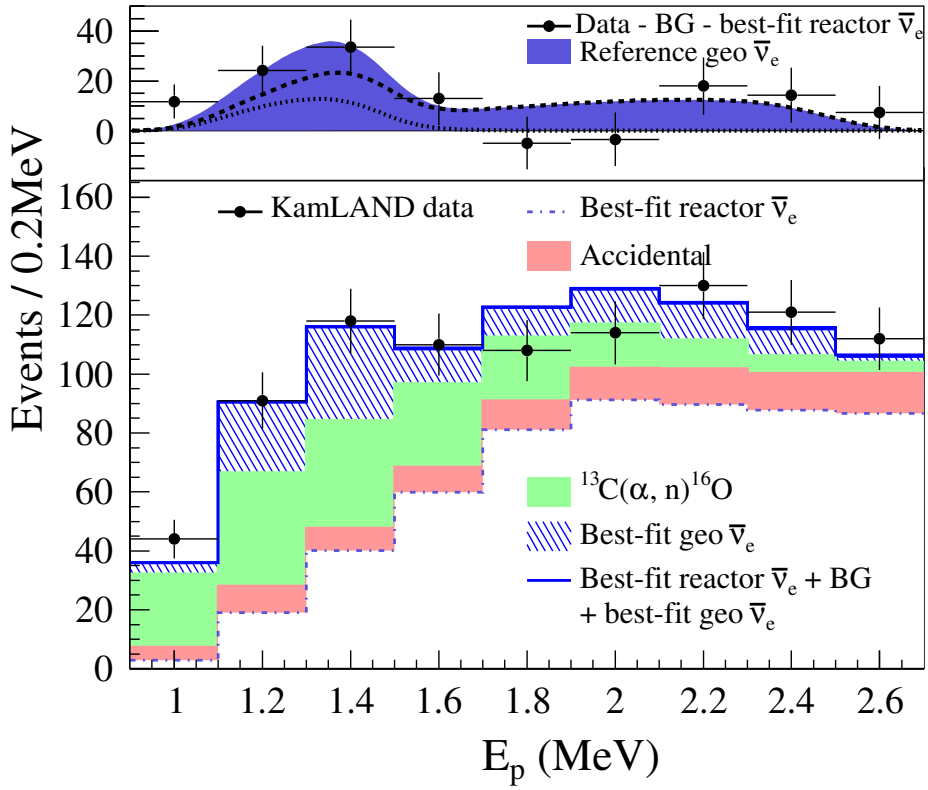

Figure 8.14: Prompt energy spectrum for geo-neutrino energy region, 0.9 MeV $< E_p <$ 2.7 MeV. The histograms indicate the backgrounds, while the best-fit (including geo-neutrinos) is shown in blue. The upper panel shows the background-subtructed energy spectrum. The blue shade spectrum is the expectation for the reference model, consisting the contributions from U (dashed curve) and Th (dotted curve). Statistical uncertainties are shown for the data in the bottom panel, and uncertainties on the background estimation are added in the upper panel.

8.5 Constraints on Geophysical Models

The radioactive decays inside the Earth are considered as the primary heart budget. Their quantitive estimation is important and effective way to understand the planet's formation and evolution. The radiogenic heat can be evaluated by measuring the geo-neutrino, however, prior results, such as [93] and [10], were not enough to constrain geophysical models. As shown in Section 8.4, 117^{+29}_{-28} events excess is observed in the geo-neutrino energy region. Its uncertainty, 24.8 %, is improved about factor 3 compared with [93] result (25^{+19}_{-18}). In this section, the first constrains to radiogenic heat models is provided using the results of geo-neutrino estimation.

Figure 8.15 shows the comparison between the measured geo-neutrino fluxes at the Kamioka and Gran Sasso experimental sites and the predictions of model. The procedure to interpret this figure is described as follows :

1. Calculate the model prediction
   For calculating model predictions, the U/Th ratio for each contributing layer is fixed at the standard BSE model value of 3.9 [38]. The composition of the crust is derived from a BSE model that incorporates the crust and a detailed description of the local geology [63]. Furthermore, as a primary hypothesis, U and Th are assumed to be uniform distributed in the mantle. If geo-neutrino can be measured at the Hawaii experimental site, the contribution from the crust is significantly smaller than continental site as shown in the Hawaii column. The geo-neutrino flux measured by KamLAND is good agreement with the BSE model prediction.

2. Estimate the radiogenic heat in the Earth from the geo-neutrino flux
   The radiogenic heat estimation from the geo-neutrino flux depends on the modelling of the geology.

   - Uncertainties of U and The content in the crust
     In this analysis, we account for crustal uncertainties by assuming 17 % and 10 % error for the U and Th content, including correlated errors as suggested in [94].

   - Crustal model
     We use the crustal model pointed out in [48]. This model assumes independent errors for each layer (upper, middle and lower crust), and include extra contributions from the error in the mass distribution and the fractional uncertainty in the U/Th ratio [94].

   Since the modelling uncertainties are applies for the crust, the crust contribution is subtracted for clarity in the right figure of 8.15. The radiogenic heat contribution from ^{238}U and ^{232}Th is estimated to be $20.1^{+9.1}_{-9.1}$ TW by both KamLAN and Borexino data.

3. Constraints on geophysical models
   The red lines show the model predictions from a fully radiogenic model. It is constructed by uniformely introducing U and Th in the mantle (homogeneous hypothesis) and, alternatively, by locating all the U and Th at the mantle-core interface ("sunken layer" hypothesis). Comparing between the measured data

and the model prediction, this model is constrained by the actual data. If we use the recent heat emission rate of 44.2 ± 1.0 TW [52], the fully radiogenic model is excluded at 97.9 % C.L. using KamLAND and Borexino data, or the 98.3 % C.L. using KamLAND data alone.

As discussed above, the radiogenic heat production in the Earth by ^{238}U and ^{232}Th is estimated to be $20.1^{+9.1}_{-9.1}$ TW combining the KamLAND and Borexino results. This measurement result derives that the radiogenic heat contribution is evidently smaller than the heat emission rate (44.2 ± 1.0 TW) from the Earth surface, even adding the heat emission from ^{40}K and ^{235}U decays (predicted about 4.3 TW). This is the first practical direct estimates of the radiogenic heat with geo-neutrinos, revealing a partial radiogenic model for the Earth.

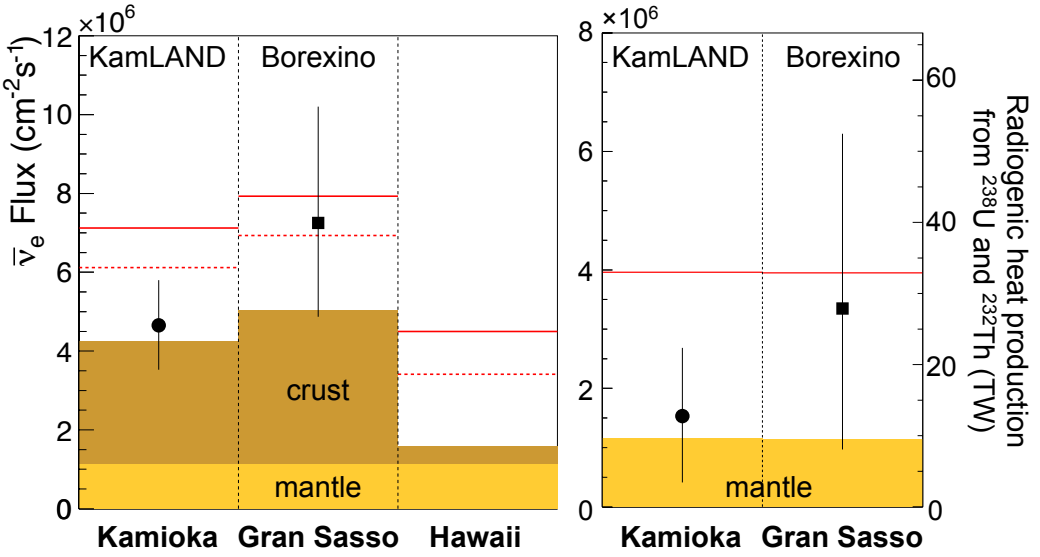

Figure 8.15: Measured geo-neutrino flux and models.
(Left) Measured geo-neutrino flux at Kaimoka and Gran Sasso experimental sites, and expected fluxes at these sites and Hawaii based on the reference model and knowledge of the local geology. The solid and dashed red lines represent the fluxes for a fully radiogenic model assuming the homogeneous and sunken layer hypotheses. (Right) Measured geo-neutrino flux at Kamioka and Gran Sasso after subtracting the estimated crustal contributions. The right axis shows the total radiogenic heat production assuming a homogeneous mantle, The solid red line indicated the fully radiogenic model where the contributions from the crust (7.0 TW) and the other isotopes (4.3 TW) [60] [63] are subtracted from the total heat flow (44.2 TW) [52].

Part III

High Energy Anti-Neutrino

Chapter 9

High Energy Anti-neutrino Sources

There are several conceivable sources which would lead to an anti-neutrino signal at KamLAND. As discussed in Chapter 4, in the low energy region, the anti-neutrinos mainly come from the Earth's internal or man-made reactors. The geo-neutrinos have energies below ~ 3.4 MeV and the energy region below ~ 8 MeV is dominated by the reactor anti-neutrinos. On the other hand, the extremely high energy region, which means above a few tens of MeV, is dominated by neutrinos generated from the decays of muons and pions produced by cosmic-ray interactions in the atmosphere. The remaining energy region between 8 MeV to 15 MeV is useful to study exotic generation mechanisms of extraterrestrial neutrinos, such as conversions of solar neutrinos into anti neutrinos or light dark matter annihilation. In this chapter, the candidates of the high energy anti-neutrinos are listed.

9.1 Solar Anti-neutrinos

There is no direct production of $\bar{\nu}_e$'s in the Sun. However, if the neutrino has a non-zero magnetic moment, it could be converted into an antineutrino in the strong solar magnetic field. This mechanism was originally proposed as a solution to the solar neutrino problem [**?**] and was later revisited in [95].

9.1.1 Neutrino Magnetic Moment

In the framework of the standard Weinberg-Salam theory, neutrino magnetic dipole moment for Dirac neutrinos is induced by radiative corrections and in calculated to be [96] :

$$\mu_\nu \equiv \frac{3eG_F}{8\sqrt{2}\pi^2} m_\nu = 3 \times 10^{-19} \mu_B \left(\frac{m_\nu}{1\mathrm{eV}}\right), \tag{9.1}$$

where μ_B is the Bohr magneton ($= e/2m_e = 5.788 \times 10^{-9}$ eV/Gauss). The order of the neutrino magnetic dipole moment is not enough to be detected directly. Majorana neutrinos cannot have the magnetic dipole moment because of CPT invariant. However, the transition moment, which is relevant to $\nu_i \to \nu_j$, may exist for both Dirac and Majorana neutrinos. If the magnetic moment would be found to have a value beyond Eq.(9.1), it would imply new physics, such as interactions

which violate chirality conservation beyond the standard model. The experimental measurement results are listed as follows :

- $\bar{\nu}_e$ flux measurement from reactor (MUNU experiment, [97])

$$\mu_{\bar{\nu}_e} < 1.0 \times 10^{-10}\mu_B \qquad (90\%\text{C.L.})$$

- ν_e, ν_μ and ν_τ from accelerator-based experiment [98] [99] [100]

$$\mu_{\nu_e} < 10.8 \times 10^{-10}\mu_B \qquad (90\%\text{C.L.})$$
$$\mu_{\nu_\mu} < 6.8 \times 10^{-10}\mu_B \qquad (90\%\text{C.L.})$$
$$\mu_{\nu_\tau} < 3.9 \times 10^{-7}\mu_B \qquad (90\%\text{C.L.})$$

- $\bar{\nu}_e$ from the GEMMA spectrometer [101], current best limit

$$\mu_{\bar{\nu}_e} < 3.2 \times 10^{-11}\mu_B \qquad (90\%\text{C.L.})$$

9.1.2 Resonant Spin Flavor Precession

The Homestake experiment reported the anti-correlation between the neutrino flux and the sunspot numbers [102], as shown in Figure 9.1. The neutrino capture rate at ^{37}Ar seems to be changed with a change of the sunspot number in 22 year's period of the change of the magnetic field. Furthermore, several authors ([103], [104]) proposed that a magnetic moment of neutrino can cause the resonant transition of neutrino helicity like the MSW effect in the sun. This effect is called Resonant Spin Flavor Precession (RSFP). This RSFP model can explain the time variation of the neutrino capture rate reported by Homestake experiment with a very large magnetic mordent such as $10^{-10}\mu_B$. However such large magnetic moment was excluded by phenomenological limit. In addition, the Kamiokande 2079 days data presented that the neutrino capture rate for not have the correlation to the sunspot number within the errors [105]. Figure 9.2 shows the result of the Kamiokande experiment.

The defect of the simple RSFP model is compensated by inducing the hybrid model which is including the MSW effect in the sun simultaneously with RSFP. The propagation equation of Dirac neutrino under the hybrid model is :

$$i\frac{d}{dt}\begin{pmatrix}\nu_{eL}\\ \nu_{\mu L}\\ \nu_{eR}\\ \nu_{\mu R}\end{pmatrix} = \begin{pmatrix} \frac{G}{\sqrt{2}}(2N_e - N_n) & \frac{\Delta m^2}{4E}\sin 2\theta & \mu_{ee}B & \mu_{e\mu}B \\ \frac{\Delta m^2}{4E}\sin 2\theta & -\frac{G}{\sqrt{2}}N_n + \frac{\Delta m^2}{2E}\cos 2\theta & \mu_{\mu e}B & \mu_{\mu\mu}B \\ \mu_{ee}B & \mu_{e\mu}B & 0 & 0 \\ \mu_{\mu e}B & \mu_{\mu\mu}B & 0 & \frac{\Delta m^2}{2E}\cos 2\theta \end{pmatrix}\begin{pmatrix}\nu_{eL}\\ \nu_{\mu L}\\ \nu_{eR}\\ \nu_{\mu R}\end{pmatrix} \tag{9.2}$$

In a Dirac neutrino case, there are no weak interactions by ν_{eR} and $\nu_{\mu R}$ because they are sterile. Neutrino flavor mixing is considered only for left-handed neutrino. In a Majorana neutrino case, the transition is $\nu_{iL} \to \nu^c_{jL}$ $(\bar{\nu}_j)$ which are not sterile. The propagation equation of the Majorana neutrino is :

$$i\frac{d}{dt}\begin{pmatrix}\nu_{e}\\ \nu_{\mu}\\ \bar{\nu}_e\\ \bar{\nu}_\mu\end{pmatrix} = \begin{pmatrix} \frac{G}{\sqrt{2}}(2N_e - N_n) & \frac{\Delta m^2}{4E}\sin 2\theta & 0 & \mu B \\ \frac{\Delta m^2}{4E}\sin 2\theta & -\frac{G}{\sqrt{2}}N_n + \frac{\Delta m^2}{2E}\cos 2\theta & -\mu B & 0 \\ 0 & -\mu B & -\frac{G}{\sqrt{2}}(2N_e - N_n) & \frac{\Delta m^2}{4E}\sin 2\theta \\ \mu B & 0 & \frac{\Delta m^2}{4E}\sin 2\theta & \frac{G}{\sqrt{2}}N_n + \frac{\Delta m^2}{2E}\cos 2\theta \end{pmatrix}\begin{pmatrix}\nu_{e}\\ \nu_{\mu}\\ \bar{\nu}_e\\ \bar{\nu}_\mu\end{pmatrix} \tag{9.3}$$

Neutrino flavor mixing is also considered for anti-neutrino and solar $\bar{\nu}_e$ production can be expected [106]. There are essentially two ways in which $\bar{\nu}_e$'s can be produced.

- The originally produced solar ν_e first oscillate into $\bar{\nu}_\mu$, and then converted into $\bar{\nu}_e$ by RSFP
$$\nu_e \xrightarrow{\text{osci.}} \nu_\mu \xrightarrow{\text{RSFP}} \bar{\nu}_e$$
- solar ν_μ are first converted to $\bar{\nu}_\mu$ and oscillated into $\bar{\nu}_e$
$$\nu_e \xrightarrow{\text{RSFP}} \bar{\nu}_\mu \xrightarrow{\text{osci.}} \bar{\nu}_e$$

The conversion probability for the two processes is defined as follows :

$$P(\nu_{eL} \to \bar{\nu}_{eR}) \simeq 1.8 \times 10^{-10} \sin^2 2\theta_{12} \left[\frac{\mu}{10^{-12}\mu_B} \frac{B_T(0.05R_\odot)}{10\text{kG}} \right]^2, \qquad (9.4)$$

where B_T is the transverse solar magnetic field in the region of neutrino production, $R_\odot$ is the solar radius, and μ is the neutrino magnetic moment in Bohr magneton (μ_B). Very little os known about the magnitude of magnetic fields in the solar interior, nut values up to 3×10^7 G are permitted based on SOHO observation [107]. The present best-limit for the probability of neutrino-to-antineutrino conversion is less than 1.3×10^{-4} from the Borexino experiment [108].

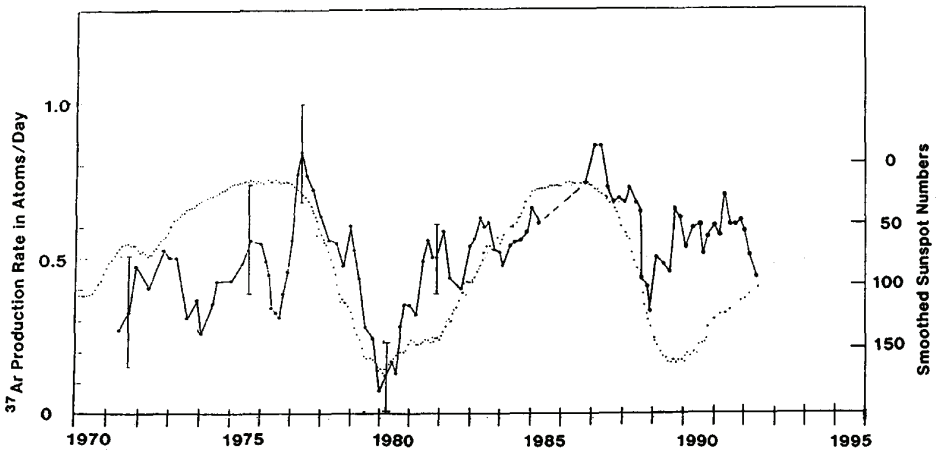

Figure 9.1: Time variation of ^{37}Ar production rate (solid line) and sunspot number (dotted line) [102]. A cycle of these rates were estimated to be 22 years.

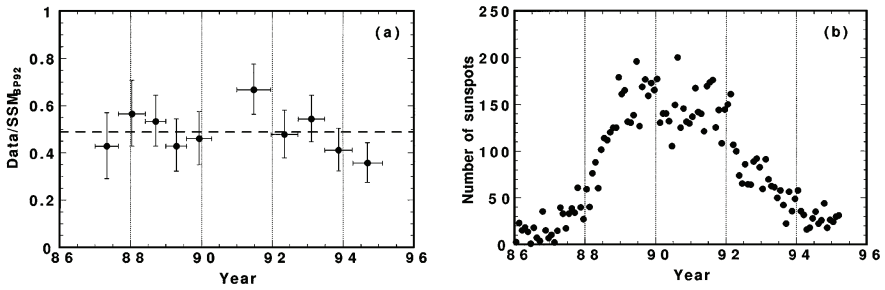

Figure 9.2: Time variation of the observed solar neutrino flux in Kamiokande (left) and sunspot (right) [105].

9.2 Diffuse Supernova Neutrino Flux

During a core-collapse supernova, approximately 10^{53} ergs of energy are released, about 99% of which are in the form of neutrinos. To date, the only time that a burst of such neutrinos has been detected was in the case go supernova SN1987A [18] [109]. However, it is generally believed that core-collapse supernovae have occurred throughout the universe since the formation of stars. Thus, there should exist a diffuse background of neutrinos originating from all supernovae that have ever occurred. Discussion of these supernova relic neutrinos would offer insight about the history of star formation and supernovae explosions in the universe.

Only upper limits for the diffuse supernova neutrino flux (DSNF) have been set. Super-Kamiokande found the upper limit of 1.2 cm^{-2} s^{-1} with an energy grater than 19.3 MeV [110]. And an upper limit on the flux in the energy range of 22.9 MeV $< E_\nu <$ 36.9 MeV of 70 cm^{-2} s^{-1} at the 90 % C.L. presented by SNO experiment [111]. Because the diffuse $\bar{\nu}_e$ energy is lowered by redshift, the spectral shape is closely connected to the history of star formation. Various supernova and cosmological models predict difference shapes, and should be confronted with data.

9.3 Dark Matter Annihilation

Self-annihilation of light (MeV-scale) dark matter in the universe could create a mono-energetic signal in the detector. The Super-Kamiokande data provides the best-limit on the rate of such annihilation for dark matter mass (m_χ) above 15 MeV. Assuming an annihilation model in the Galactic halo [112], the limit can be translated into a velocity-dependent averaged cross section ($\langle \sigma_{A^\nu} \rangle$) for data matter particles.

Chapter 10

Background Estimation

The event selection criteria for extraterrestrial electron anti-neutrinos are listed in this section. This analysis used the data in the energy range 8.3 MeV $< E_{\bar{\nu}_e} <$ 30.8 MeV, and the estimated backgrounds are also described.

10.1 Event Selection

In 2004, the results of high-energy anti-neutrino analysis were presented using KamLAND data [113]. The total live time was 185.5 days, and the fiducial radius was set within 5.5 m. The data was used to search for $\bar{\nu}_e$'s energy range 8.3 MeV $< E_{\bar{\nu}_e} <$ 14.8 MeV. This analysis presents a study of extraterrestrial anti-neutrinos based on data collected from March 5, 2002 to July 23, 2010, corresponding to 2343 live-days, corresponding to 12.5 times longer than the last analysis. The selection criteria are summarized in Table 10.1. To improve the statical uncertainty, the fiducial volume was enlarged from 5.5 m radius to 6.0 m radius. Furthermore, the upper limit of prompt energy was changed from 14.8 MeV to 30.8 MeV. Spallation cuts were used to reduce backgrounds from long-lived isotopes, such as ^{9}Li (τ = 237 ms, Q = 13.6 MeV), that are generated by cosmic muons passing through the detector. The overall selection efficiency of the candidates is 92 %, which is evaluated from a Monte Carlo simulation.

Table 10.1: Event selection criteria for extraterrestrial anti-neutrinos.

Paramaters	Criteria
Prompt Energy (E_p)	$7.5 < E_p < 30.0$ MeV
Delayed Energy (E_d)	$1.8 < E_d < 2.6$ MeV
Space Correlation (ΔR)	$\Delta R < 1.6$ m
Time Correlation (ΔT)	$5 < \Delta T < 1200$ μsec
Off Time Window	$0.5 < \Delta T < 1000$ μsec
Fiducial Cut	$R_d < 6.0$ m

10.2 Backgrounds for Extraterrestrial Anti-Neutrinos

The backgrounds for the extraterrestrial anti-neutinos are summarized in Table 10.2.

Table 10.2: Summary of the estimated backgrounds for extraterrestrial anti-neutrinos with prompt energy between 7.5 MeV and 30.0 MeV.

Backgrounds	Number of Events
Random Coincidences	0.22 ± 0.01
Reactor $\bar{\nu}_e$	2.2 ± 0.7
^{9}Li	4.0 ± 0.3
Atmospheric ν (CC)	0.9 ± 0.2
Atmospheric ν (NC)	16.4 ± 4.7
Fast-neutron	3.2 ± 3.2
Total	26.9 ± 5.7

Chapter 11

Analysis and Interpretation

As described in Section 10.1, the various cuts are applied to the data set, and we observed 25 events after these cuts. The estimated number of backgrounds for $\bar{\nu}_e$ detection is 26.9 $\pm$ 5.7 events as summarized in Section 10.2. In this section, the final interpretations using these observed events and estimated backgrounds are described.

11.1 Energy Spectrum

Figure 11.1 shows the prompt energy spectrum for the selected energy window 7.5 MeV $< E_{\bar{\nu}_e} <$ 30.0 MeV. The data set presented here contains 16 times more statistics then the first KamLAND publication on this subject **??**.

The data is analyzed using an unbind maximum likelihood fit to the event spectrum. The χ^2 definition is as follows :

$$\begin{aligned}
\chi^2 &= -2\ln L + \chi^2_{BG} \\
\ln L &= n \ln \nu(N_{BG_{1\sim6}}, N_{^8B_{\bar{\nu}_e}}) - \nu(N_{BG_{1\sim6}}, N_{^8B_{\bar{\nu}_e}}) + \sum_{i=1}^{n} \ln f(E_i; N_{BG_{1\sim6}}, N_{^8B_{\bar{\nu}_e}}) \\
\chi^2_{BG} &= \sum_{j=1}^{3} \frac{(N_{BG_j} - N^{\text{expected}}_{BG_j})^2}{\sigma^{2}{}_{BG_j}},
\end{aligned} \tag{11.1}$$

where n is the number of observed events, 25, f is the normalized probability density function. $\mathrm{N}_{BG_{1\sim6}}$ are the expected number of backgrounds, and they are treated as follows :

- BG_1 : Atmospheric ν, CC
- BG_2 : Fast neutron
- BG_3 : Random coincidence
- BG_4 : ^{9}Li
- BG_5 : Reactor $\bar{\nu}_e$
- BG_6 : Atmosphericν, NC

Since the estimate for ^{9}Li and reactor $\bar{\nu}_e$ are rather robust, these parameters are fixed to estimated number of events. On the other hand, reliable data for neutral current interactions in the energy range of interest do not exist and the method we used to calculate this background contribution has large uncertainties. To avoid possible bias from modeling in the NC background calculation, the normalization of the NC events is a free parameter in the spectral fits.

From this fitting result, the allowed region for the NC background and the probability of solar neutrino conversion is shown in Figure 11.2. For the NC-floated normalization analysis, the upper limit for neutrino conversion is 5.3×10^{-5} at 90 % C.L., which corresponds to a solar $\bar{\nu}_e$ flux of 93 $\mathrm{cm}^{-2}\mathrm{s}^{-1}$ above the energy threshold, 8.3 MeV. This limit is a factor 2.5 improvement over the previous limit (760 $\mathrm{cm}^{-2}\mathrm{s}^{-1}$) [108]. The fitted NC background assuming zero solar $\bar{\nu}_e$ events is $14.8^{+5.8}_{-5.4}$ events, which is in good agreement with the calculation (16.4 ± 4.7 events) within its uncertainties.

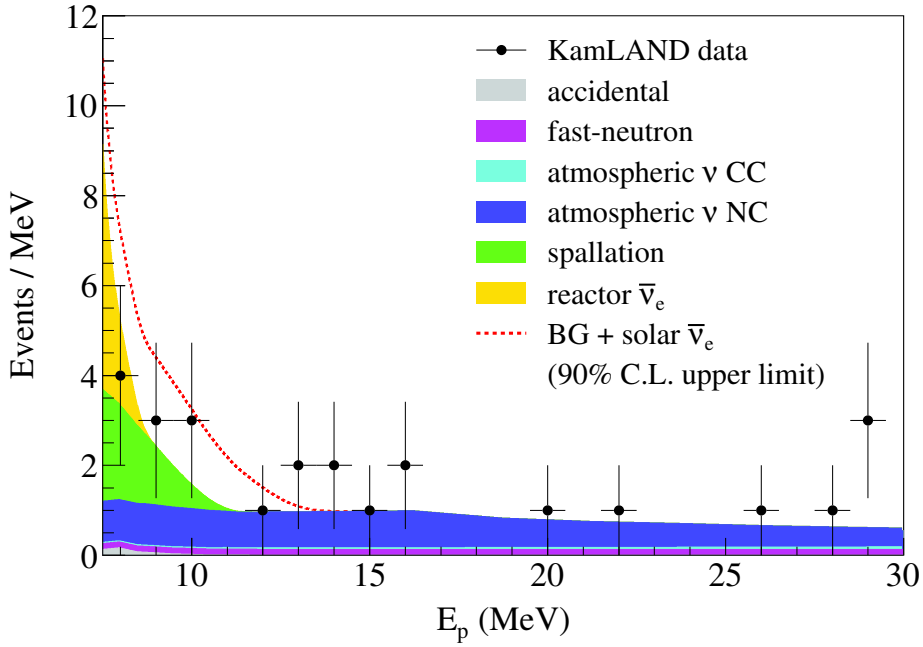

Figure 11.1: Prompt energy spectrum of solar $\bar{\nu}_e$ analysis. The black points shows the KamLAND datas, the filled spectra show the best-fit backgrounds, and red dashed line shows the upper limit of solar $\bar{\nu}_e$ at 90 % C.L. The background histograms are cumulative.

11.2 Neutrino Magnetic Moment

The probability for solar neutrino conversion can be predicted by the models of spin flavor precession and MSW-LMA oscillations in the Sun. If the conversion model for ^{8}B neutrinos of Eq. (9.4) is assumed, we can obtain the following limit on the product of the neutrino magnetic moment (μ) and the transverse component of the

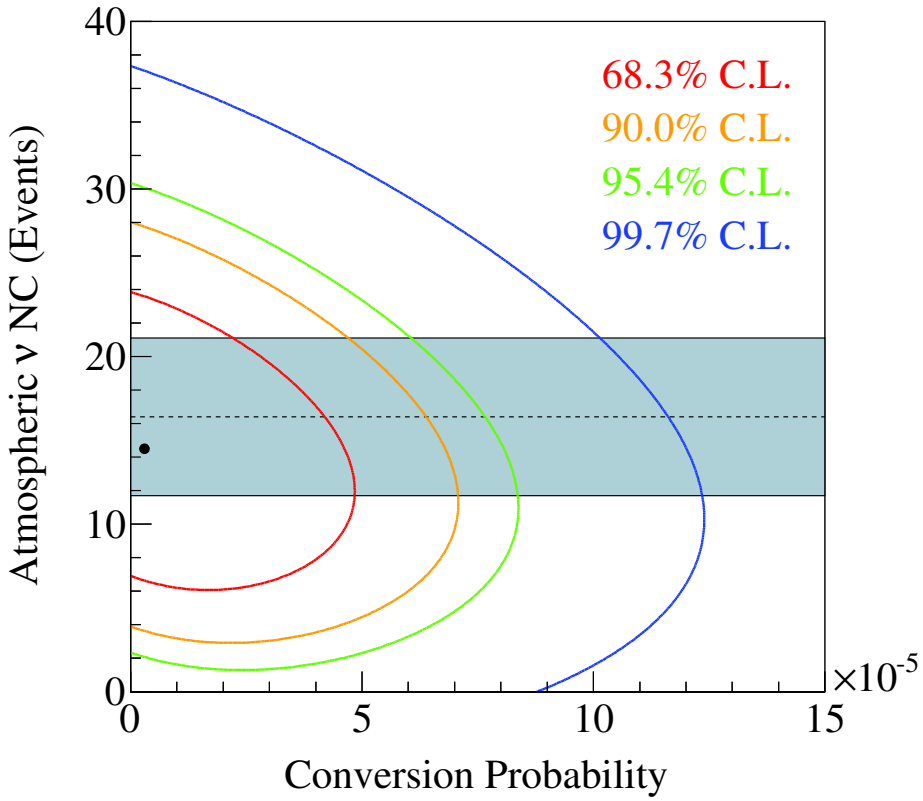

Figure 11.2: Allowed region from the maximum likelihood analysis projected in the (NC background, conversion probability) panel in the energy range of 8.3 MeV $< E_{\bar{\nu}_e} <$ 30.8 MeV. The confidence level is shown for two degrees of freedom. The gray shaded region indicates the $\pm 1\sigma$ prediction from the NC background calculation. The black point shows the best fit value.

magnetic field (B_T) in the Sun at a radius of $0.05 R_\odot$:

$$\frac{\mu}{10^{-12}\mu_B}\frac{B_T(0.05R_\odot)}{10\mathrm{kG}} < 5.9 \times 10^2, \tag{11.2}$$

using the value of 34° for the mixing angle, θ_{12} [114].

The current best limit on the neutrino magnetic moment is from the GEMMA spectrometer, $\mu_{\bar{\nu}_e} < 3.2 \times 10^{-11}\ \mu_B$ at 90 % C.L. [101]. Lack of knowledge of the value of B_T limits KamLAND sensitivity to the neutrino magnetic moment.

11.3 Other Extraterrestrial Anti-Neutrinos

This analysis results also tests other potential extraterrestrial anti-neutrinos.

11.3.1 Diffuse Supernova $\bar{\nu}_e$

If we assume an energy spectrum calculated from a cosmological model, an upper limit for the diffuse supernova can be conduced. To define a confidence interval for the diffuse supernova flux, a probability density function $P(N)$ is defined as follows :

$$P(N) = \int_0^{\inf} \frac{1}{2\pi\sigma^2} \exp\left(-\frac{(N^{\exp} - \nu)^2}{2\sigma^2}\right) \frac{\nu^N}{N!} e^{-\nu} d\nu, \tag{11.3}$$

where $N^{\exp}$ is number of total expected event ($= N_{\mathrm{DSNF}}$(number of unknown diffuse supernova events) + N_{BG} (number of observed background)), σ is the total uncertainties

$$\sigma = \sqrt{(N_{\mathrm{DSNF}} \cdot \sigma_{\mathrm{syst}})^2 + (N_{\mathrm{BG}} \cdot \sigma_{\mathrm{BG}})^2} \tag{11.4}$$

Flux of diffuse supernova ($f(E_\nu)$) is defined from reference model [115] as follows :

$$\begin{aligned}
f(E_\nu) &= \frac{c}{H_0} \int_0^{z_{\max}} R_{\mathrm{SN}}(z) \frac{dN_\nu(E'_\nu)}{dE'_\nu} \frac{dz}{\sqrt{\Omega_m(1+z)^3 + \Omega_\Lambda}} \\
R_{\mathrm{SN}(z)} &= \frac{\int_{8M_\odot}^{125M_\odot} dm \phi(m)}{\int_0^{125M_\odot} dm\ m\phi(m)} \psi_*(z) = 0.0122 M_\odot^{-1} \psi_*(z) \\
\psi_*(z) &= 0.32 f_* h_{70} \frac{e^{3.4z}}{e^{3.4z} + 45} \frac{\sqrt{\Omega_m(1+z)^3 + \Omega_\Lambda}}{(1+z)^{3/2}} M_\odot \mathrm{year}^{-1} \mathrm{Mpc}^{-3} \\
\frac{dN_\nu}{dE_\nu} &= \frac{(1+\beta_\nu)^{1+\beta_\nu} L_\nu}{\Gamma(1+\beta_\nu) \bar{E}_\nu^2} \left(\frac{E_\nu}{\bar{E}_\nu^2}\right)^{\beta_\nu} \exp\left(-\frac{(1+\beta_\nu)E_\nu}{\bar{E}_\nu^2}\right)
\end{aligned} \tag{11.5}$$

The upper limit for the diffuse supernova $\bar{\nu}_e$ flux is estimated to be 139 $\mathrm{cm}^{-2}\mathrm{s}^{-1}$ st 90 % C.L. by Eq.(11.3). This limit is weaker than our solar $\bar{\nu}_e$ flux limit due to the strong anti correlation between the signal and NC background events amplified by the summary in their spectral shape. This flux limit corresponds to about 36 times the model prediction [115], indicating poor statistical power in constraining the cosmological models using the current KamLAND data.

11.3.2 Dark Matter Annihilation Cross Section

The upper limit for the monochromatic $\bar{\nu}_e$ flux at each energy can be translated to a limit for the dark matter annihilation cross section [112]. The dark matter annihilation limit varies weakly over the dark matter mass range due to limited statistics. As shown in Figure 11.3, we obtain $\langle\ \gamma_A^\nu\ \rangle$ < (1-3) $\times$ 10^{-24} cm^3 s1 at 90 % C.L. in the mass range 8.3 MeV < m_χ < 30.8 MeV. This is most stringent constraint on the annihilation cross section below 15 MeV.

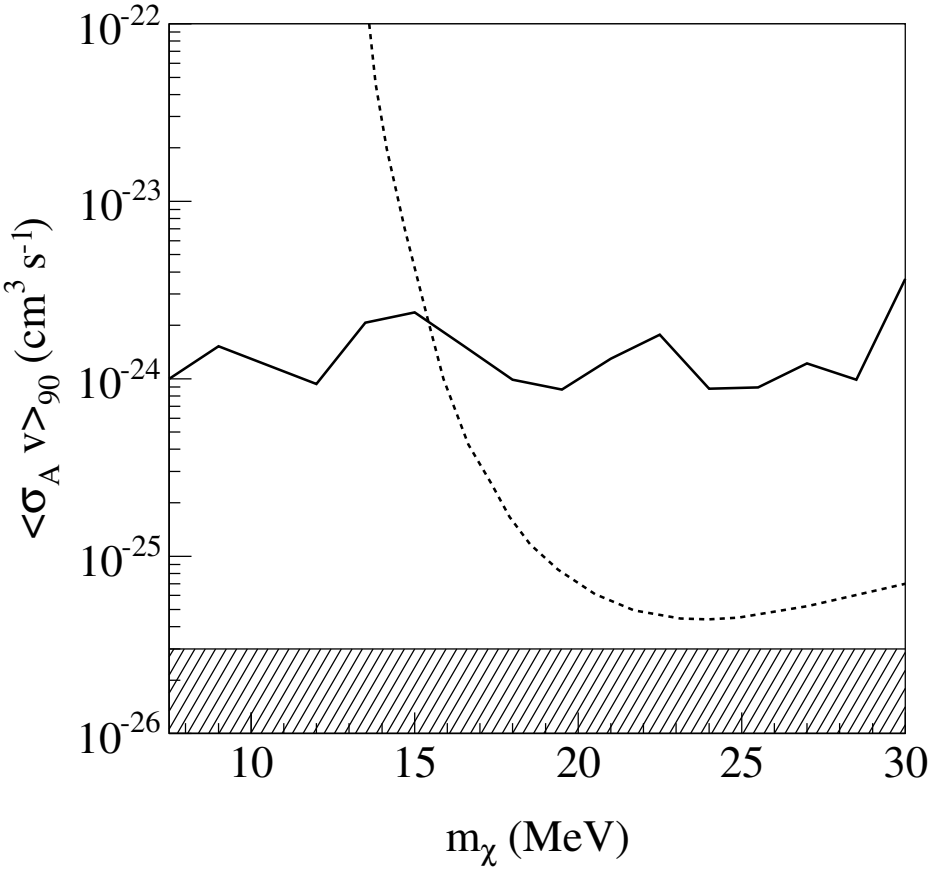

Figure 11.3: 90 % C.L. band of dark matter annihilation cross section. The solid line shows the upper limit from KamLAND, and the dashed line shows that from Super-Kamiokande [112]. The shaded curve shows the natural scale of the annihilation cross section. The KamLAND limit is most stringent constraint below 15 MeV.

11.4 $\bar{\nu}_e$ Flux

Figure 11.4 shows model-independent upper limit for $\bar{\nu}_e$ flux. The limits are given at 90 % C.L. based on the rate analysis using the Feldman-Cousins approach [116] with 1 MeV energy bins, including all the constraints on the energy range 8.3 MeV $< E_{\bar{\nu}_e} <$ 18.3 MeV, owing to the efficient $\bar{\nu}_e$ detection by the delayed coincidence method and lawge exposure. Given that data are background limited, mainly from the atmospheric neutrino NC interactions, accumulation of additional statistics is unlikely to improve this limit significantly.

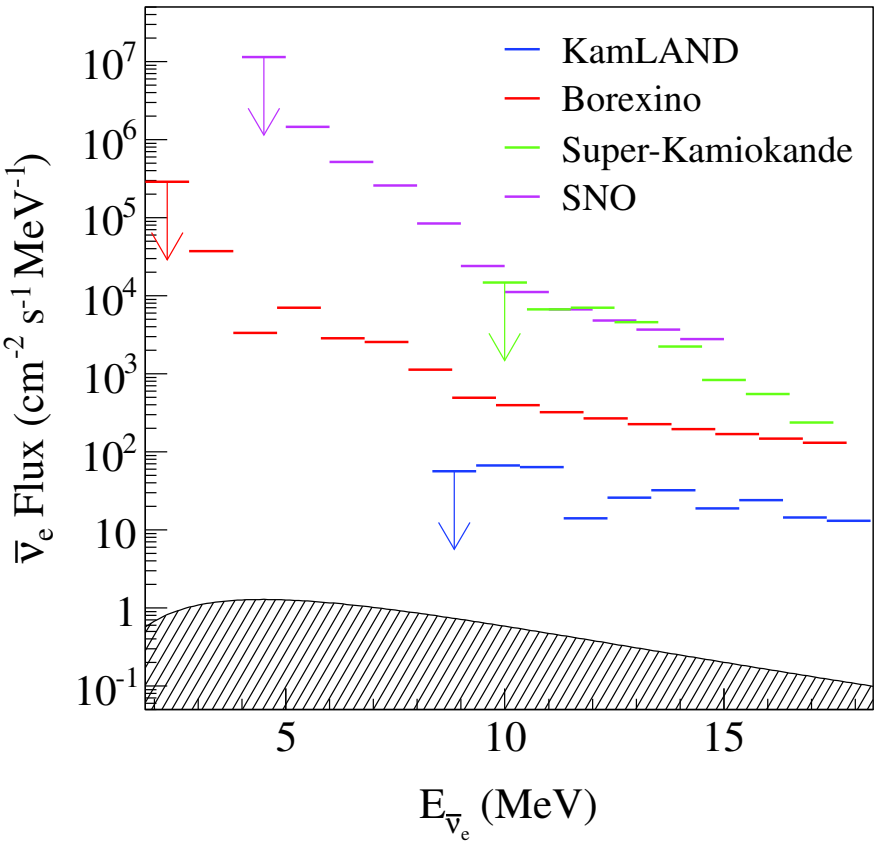

Figure 11.4: Model independent upper limits at 90 % C.L. on the $\bar{\nu}_e$ flux from KamLAND (blue line), Borexino (red line) [108], Super-Kamiokande (green line) [117], and SNO (magenta line) [118]. The shaded curve shows the diffuse supernova $\bar{\nu}_e$ flux for the reference model prediction [115].

Part IV

Discussions and Conclusions

Chapter 12

Discussions and Conclusions

The KamLAND experiment has addressed investigation of anti-neutrino signals. The analysis presented in this dissertation includes several mentions about anti-neutrino studies, such as reactor $\bar{\nu}_e$, geo $\bar{\nu}_e$ and extraterrestrial $\bar{\nu}_e$.

12.1 Reactor $\bar{\nu}_e$

Based on the data acquired from March 2002 to May 2009, corresponding to 2296.0 days livetime, a new constrains on the neutrino oscillation parameters Δm^2_{21}, θ_{12}, and θ_{13} from a three-flavor analysis are presented. The $\bar{\nu}_e$ candidate events within 6.0 m fiducial radius are selected by the likelihood selection to increase the ratio of signal to accidental backgrounds. The primary improvements from KamLAND previous result [86] are

1. The high-quality data corrected after purification accounts for 30.5 % of the total livetime. The radioactive backgrounds were efficiently reduced by the liquid scintillator purification as described in Section 6.2. Especially the number of ^{13}C(α, n)^{16}O background after purification contributions only 7 % of total number of them.

2. To utilize the variation in the accidental backgrounds, the full data set is divided into five periods and the probability density function for the accidental backgrounds is computed for each.

The observed number of events is 2249 events for 0.9 MeV energy threshold, and the expected number of reactor anti-neutrinos without neutrino oscillation is 3089.6 events.

A two-flavor analysis ($\theta_{13} = 0$) of the KamLAND data gives the best-fit values $\tan^2\theta_{12} = 0.500^{+0.083}_{-0.069}$ and $\Delta m^2_{21} = 7.48^{+0.21}_{-0.18} \times 10^{-5}$ eV^2; a three-flavor analysis with θ_{13} as a free parameter gives the best-fit values $\tan^2\theta_{12} = 0.444^{+0.098}_{-0.084}$, $\Delta m^2_{21} = 7.48^{+0.19}_{-0.20} \times 10^{-5}$ eV^2, and $\sin^2\theta_{13} = 0.032^{+0.037}_{-0.032}$. These results are consistent with the previous results [86]. As shown in Figure 7.2, The lower LMA region (LMA 0) and the upper LMA region (LMA II) are significantly disfavored in 5.8 σ and 8.7 σ, respectively. LMA I is only remained. Furthermore, the full-mixing is also disfavored by KamLAND data in 2.9 σ.

The global analysis provides 3.12 σ evidence for nonzero θ_{13}. Remarkably, the data set sensitive to Δm^2_{21} (solar neutrino experiments, and KamLAND) and Δm^2_{31}

(CHOOZ, Atmospheric and LBL) agree very well in the range $\sin^2\theta_{13} \simeq 0.01$-$0.04$ range at 2 σ. Most recently, the Double Chooz experiment presented a first result of a search for evidence of a non-zero θ_{13} [17]. They found $\sin^2\theta_{13} = 0.022 \pm 0.010$ (stat) $\pm$ 0.008 (syst), or at 90 % C.L., $0.004 < \sin^2\theta_{13} < 0.04$. This result is also consistent with past limits. If nonzero θ_{13} is confirmed, the evidence for $\sin^2\theta_{13} \sim$ few % would open the door to CP violation searches in the neutrino sector, with profound implications for our understanding of the mater-antimatter asymmetry in the universe.

12.2 Geo $\bar{\nu}_e$

The geo-neutrino analysis results are presented in this dissertation based on 2296.0 days livetime data set, which is 3.1 times more than that of the previous result [9]. The primary improvements from KamLAND previous result [9] are

1. The newly constructed energy estimator has better energy resolution in the low energy region than that of old one.

2. The dominant backgrounds for geo-neutrino detection in KamLAND, such as reactor $\bar{\nu}_e$ and ^{13}C(α, n)^{16}O reaction, are significant reduced. Since July 2007, the 25 GWth Kashiwazaki nuclear plant has been shut down due to damage from an earthquake, which resulted in about 25% of the reduction of reactor $\bar{\nu}_e$ signal in KamLAND when it is fully operational. Furthermore, the liquid scintillator purification produced dramatical decrease of ^{13}C(α, n)^{16}O reaction rate. The data set corrected after purification is high quality to search the geo-neutrino signals.

3. The time dependence likelihood selection method was used to improve the selection efficiency.

900 events are observed as candidate $\bar{\nu}_e$ between 0.9 MeV and 2.6 MeV energy window, whereas the predicted number of backgrounds are 749.4 ± 33.0. To improve the sensitivity, we performed the analysis using an unbinned maximum-likelihood fit in the energy 0.9 MeV $< E_{\rm p} <$ 8.5 MeV. The Rate + Shape + Time analysis was performed. Fixing the Earth's U/Th ratio at 3.9, as observed chondritic meteorites, the total number of excess events is 117^{+29}_{-28} from geo-neutrinos, corresponding to a geo-neutrino flux of $4.7^{+1.2}_{-1.1} \times 10^6 \mathrm{cm}^{-2}\mathrm{s}^{-1}$. This results are consistent with model prediction, and the significance of zero geo-neutrinos is excluded at 4.49 σ.

The radiogenic heart can be evaluated by geo-neutrino, however, the prior result [9] was not enough to constrain geophysical model. In this dissertation, we provide the first constraints to radiogenic heat models. The radiogenic heart production in the Earth by ^{238}U and ^{232}Th is estimated to be $20.1^{+9.1}_{-9.1}$ TW combining the KamLAND and Borexino results. This measurement result derives that the radiogenic heat contribution is evidently smaller than the heat emission rate (44 ± 1 TW) from the Earth surface, even adding the heat emission from ^{40}K and ^{235}U decays (predicted about 4.3 TW). This is the first practical direct estimation of the radiogenic heat with geo-neutrinos, revealing a partial radiogenic model from the Earth.

12.3 Extraterrestrial $\bar{\nu}_e$

In the low energy region, the anti-neutrinos mainly come from the Earth's interior or man-made reactors. The analysis results using these sources are described as above. The search for $\bar{\nu}_e$'s in the energy range 7.5 MeV $< E_{\bar{\nu}_e} <$ 30.0 MeV has been done for the 2343 days data, and 25 candidate events were found. In 2004, the results of high-energy anti-neutrino analysis were presented using KamLAND data [113]. Current data set is 12.5 times longer than the previous data set, and we enraged the analysis energy range (8.3 MeV $< E_{\bar{\nu}_e} <$ 14.8 MeV $\rightarrow$ 7.5 MeV $< E_{\bar{\nu}_e} <$ 30.0 MeV) and the fiducial radius (5.5 m $\rightarrow$ 6.0 m).

The background 26.9 $\pm$ 5.7 events are estimated. The data is analyzed using unbinned maximum likelihood fit to the event spectrum. For NC-floated normalization analysis, the upper limit of neutrino conversion probability is estimated to be 5.3 $\times$ 10^{-5} at 90 % C.L., which corresponds to a solar $\bar{\nu}_e$ flux of 98 cm^{-2} s^{-1}. This limit is factor 2.5 improvement over the previous limit by Borexino experiment [108]. Assuming that an energy spectrum calculated from a cosmological model, an upper limit for the diffuse supernova flux can be calculate, and that to be 139 cm^{-2} s^{-1} 90 % C.L. Furthermore, the monochromatic $\bar{\nu}_e$ flux can be translated to be a dark matter annihilation cross section. We obtain $\langle\, \sigma_A^{\nu} \,\rangle <$ (1-3) $\times$ 10^{-24} cm^3 s^{-1} at 90 % C.L. This is most stringent constraint on the annihilation cross section below 15MeV.

Bibliography

[1] W. Pauli. Letter to L. Meitner and her colleagues (letter open to the participants of the conference in Tubingen). 1930.

[2] E. Reines and C. L. Cowan Jr. Detection of the Free Neutrino. *Phys. Rev.*, 92:830–831, 1953.

[3] C. L. Cowan Jr. et al. Detection of the Free Neutrino: a confirmation. *Science*, 124(3212):123–124, 1956.

[4] R. Davis et al. Search for Neutrinos from the Sun. *Phys. Rev. Lett.*, 20:1205–1209, May 1968.

[5] Z. Maki et al. Remarks on the Unidied Model of Element Particles. *Prog. Theor. Phys.*, 28:870–880, 1962.

[6] K. Hirata et al. Results from one thousand days of real-time, directional solar-neutrino data. *Phys. Rev. Lett.*, 65:1297–1300, Sep 1990.

[7] Y. Fukuda et al. Evidence for Oscillation of Atmospheric Neutrinos. *Phys. Rev. Lett.*, 81:1562–1567, Aug 1998.

[8] K. Eguchi et al. First Results from KamLAND: Evidence for Reactor Antineutrino Disappearance. *Phys. Rev. Lett.*, 90:021802, Jan 2003.

[9] T. Araki et al. Experimental investigation of geologically produced antineutrinos with KamLAND. *Nature*, 436:499–503, 2005.

[10] G. Bellini et al. Observation of Geo-Neutrinos. *Phys. Lett. B*, 687:299–304, 2010.

[11] L. Wolfenstein. Neutrino oscillations in matter. *Phys. Rev. D*, 17:2369–2374, May 1978.

[12] S. Mikheyev and A. Smirnov. Resonance enhancement of oscillations in matter and solar neutrino spectroscopy. *Sov. J. Nucl. Phys.*, 42:913–916, 1985.

[13] T. Schwetz et al. Three-flavour neutrino oscillation update. *arXiv:0808.2016v3*, 2010.

[14] A. Apollonio et al. Search for neutrino oscillations on a long base-line at the CHOOZ nuclear power station. *Eur. Phys. J. C*, 27(3):331–374, 2003.

[15] K. Abe et al. Indication of Electron Neutrino Appearance from an Accelerator-Produced Off-Axis Muon Neutrino Beam. *Phys. Rev. Lett.*, 107:041801, Jul 2011.

[16] P. Adamson et al. Measurement of the Neutrino Mass Splitting and Flavor Mixing by MINOS. *Phys. Rev. Lett.*, 106:181801, May 2011.

[17] Y. Abe et al. Indication for the disappearance of reactor $\bar{\nu}_e$ in the Double Chooz experimenthooz experiment. *arXiv:/hep-ex/1112.6353v2*, 2011.

[18] K.S. Hirata et al. Observation in the Kamiokande-II detector of the neutrino burst from supernova SN1987A. *Phys. Rev. D*, 38(2):448–458, 1988.

[19] O.Tajima. Master thesis. 2000.

[20] O.Tajima. Doctor thesis. 2003.

[21] T.Araki et al. Measurement of Neutrino Oscillation with KamLAND: Evidence of Spectral Distortion. *Phys. Rev. Lett. 94, 081801*, 94(081801), 2005.

[22] P. Vogel and J. F. Beacom. Angular distribution of neutron inverse beta decay, $\bar{\nu}_e + \mathrm{p} \rightarrow e^+ + \mathrm{n}$. *Phys. Rev. D*, 60(053003), 1999.

[23] P. Vogel. Analysis of the antineutrino capture on protons. *Phys. Rev. D*, 29(9), 1984.

[24] S. Agostinelli. G4–a simulation toolkit. *Nuclear Instruments and Methods in Physics Research Section A*, 506:250–303, 2003.

[25] J. B. Birks. Scintillations from organic crystals : Specific fluorescence and Relative Response to Different Radiationselative Response to Different Radiations. *Proceedings of the Physical Society. Section A*, 64 (10):874–877, 1951.

[26] EFPC. the Federation of Electric Power Companies of Japan available at http://www.fepc.or.jp/.

[27] INSC. the International Nuclear Safety Center available at http://www.insc.anl.gov/. 2010.

[28] K. Nakajima et al. A simple model of reactor cores for reactor neutrino flux calculations for the KamLAND experiment. *Nucl. Instr. and Methods.*, A(569):837–844, 2006.

[29] K. Schreckenbach et al. Determination of the antineutrino spectrum from ^{235}U thermal neutron fission products up to 9.5 MeV. *Phys. Lett. B*, 160(4-5):325–330, 10 1985.

[30] A. A. Hahn et al. Antineutrino spectra from ^{241}Pu and ^{239}Pu thermal neutron fission products. *Phys. Lett. B*, 218(3):365–368, 2 1989.

[31] P. Vogel et al. Reactor antineutrino spectra and their application to antineutrino-induced reactions II. *Phys. Rev. C*, 24(4):1543–1553, 1981.

[32] B. Achker et al. Comparison of anti-neutrino reactor spectrum models with the Bugey 3 measurements. *Phys. Lett. B*, 374(1-3):243–248, 5 1996.

[33] S. Enomoto. Doctor thesis. 2005.

[34] A. M. Dziewonski and D. L. Anderson. Preliminary reference Earth model. *Phys. Earth Planet. Interiors*, 25:297–356, 1981.

[35] C. Bassin et al. The Current Limits of Resolution for Surface Wave Tomography in North America available at http://igppweb.ucsd.edu/∼gabi/rem.html. *EOS Trans AGU*, 81(897), 2000.

[36] D. Zhao et al. Seismic velocity structure of the crust beneath the Japan Islands. *Tectonophysics*, 212:289–301, 1992.

[37] W. Hofmann. Just add water. *Nature*, 425:24–25, 2003.

[38] W. F. McDonough and S. s. Sun. The composition of the Earth. *Chem. Geol.*, 120:223–253, 1995.

[39] S. R. Taylor and S. M. McLennan. *The Continental Crust: it Composition and Evolution.* Blackwell Scientic, Oxford, 1985.

[40] S. R. Hart and A. Zindler. In search of a bulk-Earth composition. *Chem. Geol.*, 57:247–267, 1986.

[41] A. W. Hofmann. Chemical differentiation of the Earth: the relationship between mantle, continental crust, and oceanic crust. *Earth and Planet. Sci. Lett.*, 90:297–314, 1988.

[42] M. Javoy. *Chemical earth models*, volume 329 of *537–555.* C. R. Acad. Sco. Paris, 1999.

[43] H. Palme and H. S. C. O′Neil. *Treatise on Geochemistry: Cosmochemical estimates of mantle composition*, volume 2 of *1-38.* Pergamon Press, Oxford, 2003.

[44] T. Lyubetskaya and J. Korenaga. Chemical composition of Earth's primitive mantle and its variance. *J. Geophys. Res*, 112(B03211), 2007.

[45] S. R. Taylor and S. M. McLennan. The geochemical evolution of the continental crust. *Rev. Geophys.*, 33:241–265, 1995.

[46] K. H. Wedepohl. The composition of the continental crust. *Geochimi. Cosmochimi. Acta*, 59(7):1217–1232, 1995.

[47] R. L. Rudnick and D. M. Fountain. Nature and composition of the continental crust: A lower crustal perspective. *Rev. Geophys.*, 33(3):267–309, 1995.

[48] R. L. Rudnick et al. *Treatise on Geochemistry: Composition of the Continental Crust*, volume 3 of *1-64.* Pergamon Press, Oxford, 2003.

[49] W. F. McDonough. *Earth's Core: The Encyclopedia of Geochemistry.* 151–156. Kluwer Academic Publ., Amsterdam, 1999.

[50] S. M. McLennan et al. *Earth's Continental Crust: The Encyclopedia of Geochemistry.* 145–150. Kluwer Academic Publ., Amsterdam, 1999.

[51] V. Rama Murthy et al. Experimental evidence that potassium is a substantial radioactive heat source in planetary cores. *Nature*, 423:163–165, 2003.

[52] H. N. Pollack et al. Heat flow from the Earth's interior: Analysis of the global data set. *Rev. Geophys.*, 31(3):267–280, 1993.

[53] A. M. Hofmeister and R. E. Criss. Earth's heat flux revised and linked to chemistry. *Tectonophysics*, 395:159–177, 2005.

[54] J. H. Davies and D. R. Davies. Earth's surface heat flux. *Solid Earth*, 1:5–24, 2010.

[55] D. L. Anderson. Energetics of the Earth and the Missing Heat Source Mystery available at http://www.mantleplumes.org/Energetics.html. 2009.

[56] D. L. Williams and R. P. von Herzen. Heat Loss from the Earth: New Estimate. *Geology*, 2:327–328, 1974.

[57] G. F. Davies. Review of oceanic and global heat flow estimates. *Rev. Geophys.*, 18(3):718–722, 1980.

[58] J. G. Sclater et al. The heat flow through oceanic and continental crust and the heat loss of the Earth. *Rev. Geophys.*, 18(1):269–311, 1980.

[59] C. Jaupart and S. Labrosse. *Treatise on Geophysics: Temperatures, Heat and Energy in the Mantle of the Earth*, volume 7 of *253–303*. Elsever, Amsterdam, 2007.

[60] R. Jr. Arevalo et al. The K/U ratio of the silicate Earth: Insights into mantle composition, structure and thermal evolution. *Earth Planet. Sci. Lett.*, 278:361–369, 2009.

[61] J. Korenaga. Urey ratio and the structure and evolution of Earth's mantle. *Rev. Geophys.*, 46(RG2007), 2009.

[62] T. Plank and C. H. Langmuir. The chemical composition of subducting sediment and its consequences for the crust and mantle. *Chem. Geol.*, 145:325–394, 1998.

[63] S. Enomoto et al. Neutrino geophysics with KamLAND and future prospects. *Earth and Planet. Sci. Lett.*, 258:147–159, 2007.

[64] T. Hagner et al. Muon-induced production of radioactive isotopes in scintillation detectors. *Astroparticle Physics*, 14(1):33–47, 2000.

[65] V.G.Aleksankin et al. Handbook, "Beta and Antineutrino Radiation of Radioactive Nuclei". *Edited by P.M.Rubzov , Moscow, Energoatomizdat*, 1989.

[66] P.Antonioli et al. A three-dimensional code for muon propagation through the rock: MUSIC. *Astroparticle Physics*, 7(4):357–368, 1997.

[67] Y. Minekawa. Master thesis. 2007.

[68] JENDL. (α, n) Reaction Data File. *JAERI*, 2003.

[69] S. Harissopulos et al. Cross section of the $^{13}C(\alpha,n)^{16}O$ reaction: A background for the measurement of geo-neutrinos. *Phys. Rev. C*, 72:062801, 2005.

[70] H.W. Becker. private communication.

[71] R.B. Walton et al. Interaction of Neutrons with Oxygen and a Study of the $C^{13}(\alpha, n)O^{16}$ Reaction. *Phys. Rev.*, 107:1065–1075, Aug 1957.

[72] G.W. Kerr et al. Energy levels of ^{17}O from $^{13}C(\alpha, \alpha 0)^{13}C$ and $^{13}C(\alpha,n)^{16}O$. *Nucl. Phys.*, A(110):365, 1968.

[73] S. Yoshida et al. Light output response of KamLAND liquid scintillator for protons and ^{12}C nuclei. *Nucl. Instr. and Methods.*, A(622):574, 2010.

[74] C.N. Chou. The Nature of the Saturation Effect of Fluorescent Scintillators. *Phys. Rev.*, 87:904–905, Sep 1952.

[75] J. Hong et al. The scintillation efficiency of carbon and hydrogen recoils in an organic liquid scintillator for dark matter searches. *Astropart. Phys.*, 16:333–338, 2002.

[76] D. Casper. The nuance Neutrino Physics Simulation, and the Future. *arXiv:hep-ph/0208030v1*, 2002.

[77] M. Honda et al. Comparison of 3-dimensional and 1-dimensional schemes in the calculation of atmospheric neutrinos. *Phys. Rev. D*, 64:053011, Aug 2001.

[78] E. Cheifetz et al. Prompt Neutrons from Spontaneous Fission of ^{257}Fm. *Phys. Rev. C*, 3:2017–2021, May 1971.

[79] B. T. Cleveland et al. Measurement of the Solar Electron Neutrino Flux with the Homestake Chlorine Detector. *Astrophys. J.*, 496:505–526, 1998.

[80] J. N. Abdurashitov et al. Measurement of the solar neutrino capture rate with gallium metal. iii. results for the 2002-2007 data-taking period. *Phys. Rev. C*, 80(1):015807, 07 2009.

[81] C. Arpesella et al. Direct Measurement of the ^{7}Be Solar Neutrino Flux with 192 Days of Borexino Data. *Phys. Rev. Lett.*, 101:091302, 2008.

[82] B. Aharmim et al. Independent Measurement of the Total Active ^{8}B Solar Neutrino Flux Using an Array of ^{3}He Proportional Counters at the Sudbury Neutrino Observatory. *Phys. Rev. Lett.*, 101(11):111301, 09 2008.

[83] J. Hosaa et al. Solar neutrino measurements in Super-Kamiokande-I. *Phys. Rev. D*, 73(11):112001, 06 2006.

[84] B. Aharmim et al. Low-energy-threshold analysis of the Phase I and Phase II data sets of the Sudbury Neutrino Observatory. *Phys. Rev. C*, 81(5):055504, 05 2010.

[85] N. Grevesse et al. Standard Solar Composition. *Space Sci. Rev.*, 85(1):161–174, 1998.

[86] S. Abe et al. Precision Measurement of Neutrino Oscillation Parameters with KamLAND. *Phys. Rev. Lett.*, 100(22):221803, 2008.

[87] S. Goswami et al. Solar neutrinos and 1-3 leptonic mixing. *Phys. Rev. D*, 72(5):053011, 09 2005.

[88] Stephen J. Parke. Nonadiabatic Level Crossing in Resonant Neutrino Oscillations. *Phys. Rev. Lett.*, 57(10):1275, 09 1986.

[89] E. Lisi et al. Earth regeneration effect in solar neutrino oscillations: An analytic approach. *Phys. Rev. D*, 56(3):1792, 08 1997.

[90] G.L. Fogli et al. Evidence of $\theta_{13} > 0$ from global neutrino data analysis. *arXiv:hep-ph/1106.6028v1*, 2011.

[91] R. Wendell et al. Atmospheric neutrino oscillation analysis with subleading effects in Super-Kamiokande I, II, and III. *Phys. Rev. D*, 81:092004, May 2010.

[92] E. Aliu et al. Evidence for Muon Neutrino Oscillation in an Accelerator-Based Experiment. *Phys. Rev. Lett.*, 94:081802, Mar 2005.

[93] T. Araki et al. Experimental investigation of geologically produced antineutrinos with KamLAND. *Nature*, 436:499–503, July 2005.

[94] G.L. Fogli et al. Geo-neutrinos: A systematic approach to uncertainties and correlations. *Earth, Moon and Planets*, 99:111–130, 2006.

[95] E. Kh. Akhmedov and J. Pulido. Solar neutrino oscillations and bounds on neutrino magnetic moment and solar magnetic field. *Phys. Lett. B*, 553:7–17, 2003.

[96] K. Fujikawa and R. E. Shrock. Magnetic Moment of a Massive Neutrino and Neutrino-Spin Rotation. *Phys. Rev. Lett.*, 45:963–966, Sep 1980.

[97] Z. Daraktchieva et al. Limits on the neutrino magnetic moment from the MUNU experiment. *Phys. Lett. B*, 564:190–198, 2003.

[98] D. A. Krakauer et al. Limits on the neutrino magnetic moment from a measurement of neutrino-electron elastic scattering. *Phys. Lett. B*, 252(1):177–180, 1990.

[99] L. B. Auerbach et al. Measurement of electron-neutrino electron elastic scattering. *Phys. Rev. D*, 63:112001, May 2001.

[100] R. Schwienhorst et al. A new upper limit for the tau-neutrino magnetic moment. *Phys. Lett. B*, 513:23–29, 2001.

[101] A. G. Beda et al. Upper limit on the neutrino magnetic moment from three years of data from the GEMMA spectrometer. *arXiv:hep-ph/1005.2736v2*, 2010.

[102] R. Davis. A review of the Homestake solar neutrino experiment. *Prog. Part. Nucl. Phys.*, 32:13–32, 1994.

[103] A. Cisneros. Effect of neutrino magnetic moment on solar neutrino observations. *Astrophys. Space. Sci*, 10:87–92, 1971.

[104] L. B. Okun et al. On the electric dipole moment of the neutrino. *Sov. J. Nucl. Phys.*, 44:440, 1986.

[105] Y. Fukuda et al. Solar neutrino data covering solar cycle 22. *Phys. Rev. Lett.*, 77:1683–1686, Aug 1996.

[106] C. S. Lim et al. Resonant spin-flavor precession of solar and supernova neutrinos. *Phys. Rev. D*, 37:1368–1373, Mar 1988.

[107] S. Couvidat et al. Solar seismic models and the neutrino predictions. *Astrophys. J.*, 599:1434–1448, 2003.

[108] G. Bellini et al. Study of solar and other unknown anti-neutrino fluxes with Borexino at LNGS. *Phys. Lett. B*, 696(3), 191–196 2011.

[109] C. B. Bratton et al. Angular distribution of events from SN1987A. *Phys. Rev. D*, 37:3361–3363, Jun 1988.

[110] M. Malek et al. Search for Supernova Relic Neutrinos at Super-Kamiokande. *Phys. Rev. Lett.*, 90:061101, Feb 2003.

[111] B. Aharmim et al. A search for Neutrinos from the Solar hep Reaction and the Diffuse Supernova Neutrino Background with the Sudbury Neutrino Observatory. *Astrophys. J.*, 653(2):1545–1551, 2006.

[112] S. Palomares-Ruiz and S. Pascoli. Testing Mev dark matter with neutrino detectors. *Phys. Rev. D*, 77:025025, Jan 2008.

[113] K. Eguchi et al. High Sensitivity Search for anti-electron-neutrino's from the Sun and Other Sources at KamLAND. *Phys. Rev. Lett.*, 92(071301):1–4, 2004.

[114] A. Gando et al. Constraints on θ_{13} from a three-flavor oscillation analysis of reactor antineutrinos at KamLAND. *Phys. Rev. D*, 83:052002, Mar 2011.

[115] S. Ando and K. Sato. Relic neutrino background from cosmological supernovae. *New. J. Phys.*, 6(170), 2004.

[116] G. J. Feldman and R. D. Cousins. Unified approach to the classical statistical analysis of small signals. *Phys. Rev. D*, 57:3873–3889, Apr 1998.

[117] Y. Gando et al. Search for $\bar{\nu}_e$ from the Sun at Super-Kamiokande-I. *Phys. Rev. Lett.*, 90:171302, May 2003.

[118] B. Aharmim et al. Electron antineutrino search at the Sudbury Neutrino Observatory. *Phys. Rev. D*, 70:093014, Nov 2004.